

Design tools for low noise gear transmissions

Citation for published version (APA):

Roosmalen, van, A. N. J. (1994). *Design tools for low noise gear transmissions*. [Phd Thesis 1 (Research TU/e / Graduation TU/e), Mechanical Engineering]. Technische Universiteit Eindhoven.
<https://doi.org/10.6100/IR423648>

DOI:

[10.6100/IR423648](https://doi.org/10.6100/IR423648)

Document status and date:

Published: 01/01/1994

Document Version:

Publisher's PDF, also known as Version of Record (includes final page, issue and volume numbers)

Please check the document version of this publication:

- A submitted manuscript is the version of the article upon submission and before peer-review. There can be important differences between the submitted version and the official published version of record. People interested in the research are advised to contact the author for the final version of the publication, or visit the DOI to the publisher's website.
- The final author version and the galley proof are versions of the publication after peer review.
- The final published version features the final layout of the paper including the volume, issue and page numbers.

[Link to publication](#)

General rights

Copyright and moral rights for the publications made accessible in the public portal are retained by the authors and/or other copyright owners and it is a condition of accessing publications that users recognise and abide by the legal requirements associated with these rights.

- Users may download and print one copy of any publication from the public portal for the purpose of private study or research.
- You may not further distribute the material or use it for any profit-making activity or commercial gain
- You may freely distribute the URL identifying the publication in the public portal.

If the publication is distributed under the terms of Article 25fa of the Dutch Copyright Act, indicated by the "Taverne" license above, please follow below link for the End User Agreement:

www.tue.nl/taverne

Take down policy

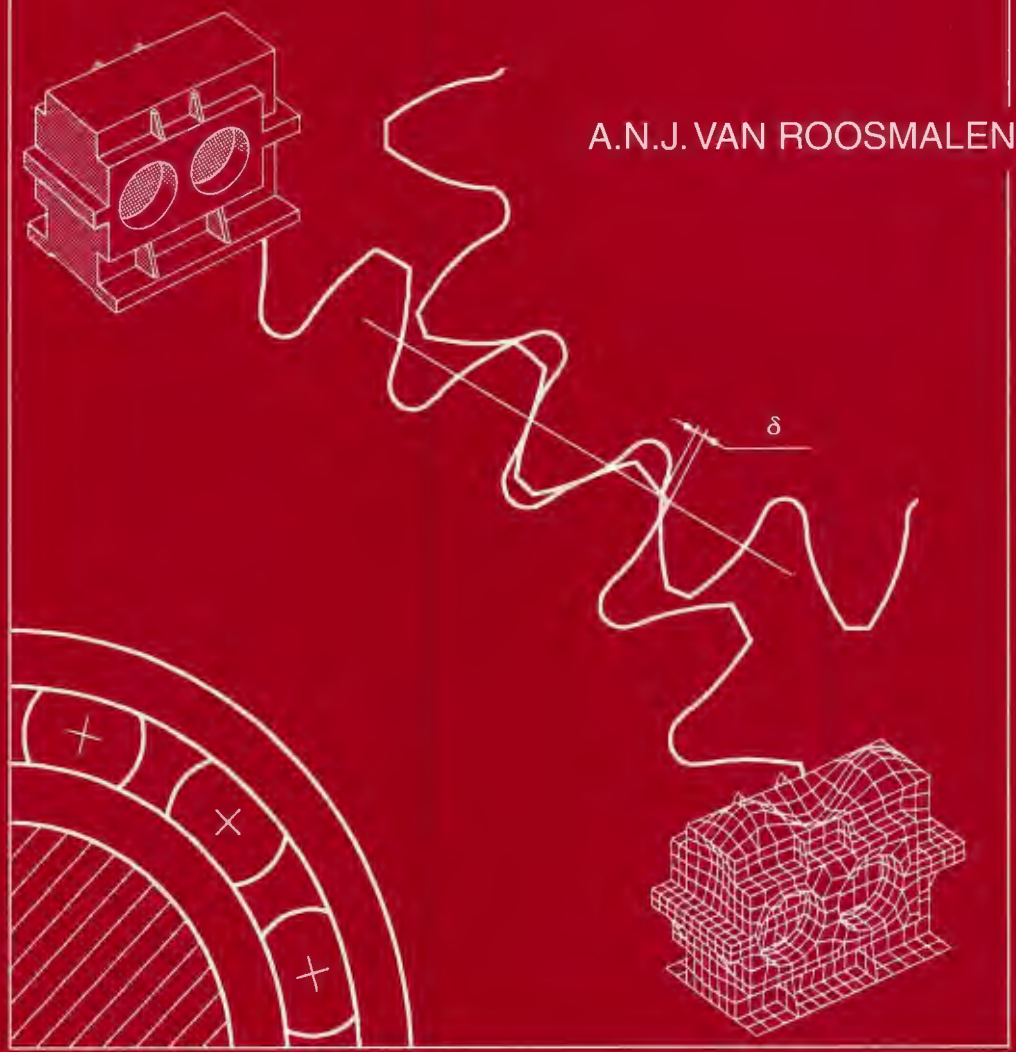
If you believe that this document breaches copyright please contact us at:

openaccess@tue.nl

providing details and we will investigate your claim.

DESIGN TOOLS FOR LOW NOISE GEAR TRANSMISSIONS

A.N.J. VAN ROOSMALEN



DESIGN TOOLS FOR LOW NOISE GEAR TRANSMISSIONS

A.N.J. van Roosmalen
Eindhoven University of Technology
Faculty of Mechanical Engineering
Power Transmissions and Tribology Laboratory
Eindhoven
October 21, 1994

CIP-DATA KONINKLIJKE BIBLIOTHEEK, DEN HAAG

Roosmalen, Arnoldus Nicolaas Josephus van

Design tools for low noise gear transmissions / Arnoldus
Nicolaas Josephus van Roosmalen. - Tilburg : Gianotten
Thesis Eindhoven. - With ref. - With summary in Dutch.
ISBN 90-6663-030-2

Subject headings: gear transmissions / mechanical
engineering / sound insulation.

DESIGN TOOLS FOR LOW NOISE GEAR TRANSMISSIONS

PROEFSCHRIFT

ter verkrijging van de graad van doctor aan de
Technische Universiteit Eindhoven, op gezag van
de Rector Magnificus, prof.dr. J.H. van Lint,
voor een commissie aangewezen door het College
van Dekanen in het openbaar te verdedigen op
vrijdag 21 oktober 1994 om 14.00 uur

door

ARNOLDUS NICOLAAS JOSEPHUS VAN ROOSMALEN

geboren te Bommel

Dit proefschrift is goedgekeurd
door de promotoren:

prof.dr.ir. J.W. Verheij

prof.dr.ir. M.J.W. Schouten

Aan mijn vader en moeder
Aan Ingrid, mijn aanstaande

CONTENTS

SYMBOLS	IV
1. GENERAL INTRODUCTION	
1.1 Field of interest covered by this thesis	1
1.2 Vibration source	2
1.3 Vibration transmission through bearings	4
1.4 Housing dynamics and noise radiation	6
1.5 Outline of the study	9
2. VIBRATION SOURCE	
2.1 Introduction	11
2.2 Deflections	14
2.2.1 Tooth deflection	16
2.2.2 Hertzian deflection δ_{Hertz}^*	26
2.2.3 Deflection due to bending of the gear shafts δ_{bend}^*	26
2.2.4 Deflections due to torsion of the gear wheels $\delta_{\text{torsion}}^*$	28
2.3 Force distribution along the line of contact	30
2.4 Tooth stiffness of spur and helical gears	31
2.5 Dynamic behaviour of the gearbox interior	33
2.6 Engagement and disengagement shock	38
2.7 Profile corrections and their influence on L_w	42
2.8 Summary	48
3. VIBRATION TRANSFER THROUGH BEARINGS	
3.1 Introduction	51
3.2 Stiffness matrix of ball bearings	53
3.2.1 Bearing load-displacement relations	55
3.2.2 Bearing stiffness matrix $[K]_{\text{bm}}$	56
3.3 Stiffness matrix of roller bearings	59
3.3.1 Stiffness matrix according to Lim /3.1/	59
3.3.2 Improvement on Lim's theory	61
3.4 Experimental verification of a calculated stiffness matrix	64
3.5 Stiffness and damping matrices of fluid film bearings	67
3.6 Summary	71

4. VIBRATIONAL BEHAVIOUR AND SOUND RADIATION OF GEARBOX HOUSINGS	
4.1 Introduction	73
4.2 Unsupported simple box-like structure	76
4.3 Supported simple box-like structure	82
4.4 Two assembled box halves	85
4.5 Empty gearbox model	89
4.6 Gearbox model with shafts and ball bearings	94
4.7 Sound radiation	101
4.8 Summary	109
5. EXPERIMENTS	
5.1 Introduction	111
5.2 The test rig	112
5.3 Angular velocity level $L_w(f)$ at the gears	116
5.4 Velocity level $L_v(f)$ at the gearbox housing surface	121
5.5 Sound power level $L_w(f)$ of the test gearbox	123
5.6 Scatter in sound power levels for a single gearbox variant	127
5.7 Profile corrections and their influence on L_w	130
5.8 Rolling element bearings	134
5.9 Double helical gears with roller bearings and fluid film bearings	138
5.10 Summary	143
6. EVALUATION	
6.1 Theoretical achievements	147
6.1.1 Prediction of gear vibrations	147
6.1.2 Vibration transmission from gears to the housing	148
6.1.3 Sound radiation from the housing surface	150
6.2 Practical results	151
6.2.1 Tooth profile corrections	151
6.2.2 Bearing variants	152
SUMMARY	153
SAMENVATTING	157
APPENDICES:	
A. Contents of the Schmidt-matrix	161

B. Tooth profile form of involute gears	165
C. Stiffness matrix and other variables of the lumped parameter model of Chapter 2	169
D. Contents of the rolling element bearing stiffness matrix	173
E. Radiation efficiency of two gearbox housings	177
F. Geometry and profile corrections of five test gear sets	181
REFERENCES	187
DANKBETUIGING	194
CURRICULUM VITAE	196

SYMBOLS

The symbol definitions are tabulated below. Symbols that are used only in passing are not included. The meaning of subscripts is given for only a few cases.

Roman capitals:

A_0	unloaded relative distance between inner and outer bearing raceway
A_j	loaded relative distance between inner and outer bearing raceway
B	face width
C	compliance function
F	tooth force
\bar{F}^2	mean square force
$H(f)$	frequency response function
I	moment of inertia
J	polar moment of inertia
$[K]_{bm}$	mean bearing stiffness matrix (6x6)
K_n	effective bearing stiffness coefficient
$L_F(f)$	force level
L_S	area level
$L_v(f)$	surface-averaged mean square velocity level of the gearbox housing
$L_w(f)$	sound power level
$L_\omega(f)$	angular velocity level at the gears
$L_\sigma(f)$	radiation index
M	torque; mass matrix
N	number of contact points; plate stiffness
P	point load force
\mathcal{P}	sound power
Q_j	normal bearing element load
S	surface area; stiffness matrix
\mathcal{S}	tooth stiffness per unit width
\bar{S}_P	mean plate surface area
$S_t(t)$	time variable tooth stiffness
T	torque; time period
T_{60}	60 dB decay time
TF_F	Transfer function with force input
TF_M	Transfer function with moment input
TF_ω	Transfer function with angular velocity input

U perimeter
W force distribution along the line of contact

Lower-case Roman letters:

a acceleration; radius of a baffled piston
c speed of sound in air ≈ 344 m/s
 c_0 tooth curvature factor
d gear shaft diameter; pitch diameter
f tooth deflection function; frequency
 f_{band} centre frequency of a (1/3-)octave band
 f_c critical frequency
 f_p transitional frequency of a baffled piston
 f_s transitional frequency of a sphere
 f_{tooth} tooth frequency
 $\{f\}_{\text{bm}}$ mean bearing load vector
h plate thickness
 h_a addendum coefficient
 h_d dedendum coefficient
i integer; transmission gear ratio
j integer; $\sqrt{-1}$
k integer; addendum reduction factor
 k_{bij} bearing stiffness component of $[K]_{\text{bm}}$
 ℓ length of profile correction (measured along the line of contact)
m module; mass
n bearing exponent; rotational speed
 $\bar{p}^2(f)$ mean square sound pressure
 p_t transverse pitch
 $\{q\}_{\text{bm}}$ mean bearing displacement vector
 r_L bearing radial clearance
 v velocity
 $\bar{v}^2(f)$ surface-averaged mean square velocity
 v_R velocity at the surface of a pulsating sphere
x,y coordinates in Cartesian coordinate system
 \dot{x} velocity in Cartesian coordinate system
 \ddot{x} acceleration in Cartesian coordinate system
 x_1, x_2 addendum modification factor of pinion respectively wheel
z number of teeth; number of rolling bearing elements
 z_1, z_2 number of teeth of pinion respectively wheel

Lower-case Greek letters:

α	material factor; pressure angle
α_0, α_j	unloaded and loaded bearing contact angle
α_t	transverse pressure angle
β	helix angle; angular displacement in bearing Cartesian coordinate system
β_b	base helix angle
δ	deflection
ϵ_{tot}	total contact ratio
ϵ_α	transverse contact ratio
ϵ_β	overlap ratio
γ	deflection ratio factor; rotation angle of roller element bearing
η	loss factor
ψ_j	angle in bearing Cartesian coordinate system
λ	wave length
ω	angular velocity
$\tilde{\omega}^2(f)$	mean square angular velocity
ρ	density of air $\cong 1.2 \text{ kg/m}^3$
σ	radiation efficiency
ξ	coordinate along the line of contact; damping coefficient = $\eta/2$

1. GENERAL INTRODUCTION

This chapter presents a general introduction to modeling of gearbox vibrations and noise and an outline of the study of this thesis.

1.1 Field of interest covered by this thesis

The airborne and structureborne noise produced by gearboxes is a well known problem to gearbox users. Especially high power gearboxes can give rise to high noise levels. The demand for less noisy gearboxes has led to many investigations all over the world. None of them has given a complete solution to the problem.

This thesis presents new contributions to the modeling of the sound generating and transmission mechanisms of a gearbox with parallel shafts. Attention is paid to the gears as the primary source of vibrations and noise and to the transmission chain between the gears and the surrounding air. The bearings will be investigated thoroughly, being important components in this transmission chain. Also the computational modeling of the vibration response of the housing is studied and the sound radiation by the housing. A combination of theoretical and experimental work is reported, resulting into guidelines for designing less noisy gearboxes in a cost effective way.

Fig. 1.1 shows the model scheme which is used in this thesis. The sound generation mechanism is modeled as depicted by the three separate blocks. The first block describes the dynamical behaviour of the gears. The second block describes the vibration transmission from the gears via the shafts

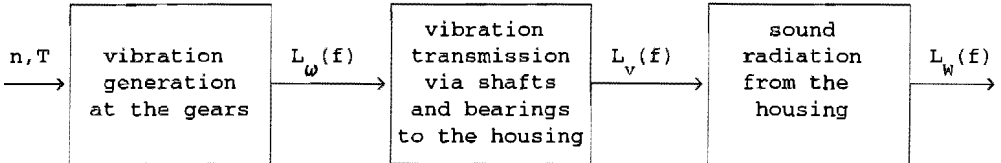


Figure 1.1:

Sound generation scheme of a gear transmission.

n and T are the speed [rev/min] and the applied torque [Nm] of the gearbox, $L_{\omega}(f)$ is the angular velocity level at the gears, $L_v(f)$ is the velocity level at the surface of the gearbox, and $L_w(f)$ is the sound power level.

and bearings and resulting in the velocity response of the housing. The third block quantifies the sound radiation process by which the housing vibrations are converted into sound.

This thesis does not pretend to cover the complete field of gears which consists of many different types. The gearboxes of interest here have parallel shafts with spur, helical and double helical gears. For simplicity only single stage gearboxes are taken into consideration. Gearboxes with more than one stage are somewhat more complex to describe mathematically, but from a fundamental point of view there is no great difference with single stage gearboxes.

The gearboxes of interest have a power range from 10 up to 2000 kW and are heavily loaded. These are industrial gearboxes, as mentioned in the VDI 2159 guideline /1.1/, which are mainly in use for applications where an electric motor has to be connected to some kind of machinery. The gearbox acts as a transmission of torque and rotational speed.

In this thesis only the vibrations and noise of a gearbox are considered that are caused by the meshing of the gears. Vibrations due to external machinery (i.e. outside the gearbox) are neglected. Also vibrations caused by internal unbalance, squeezing of oil between the gear teeth and bearing noise are neglected.

The most important assumption is the limitation to high quality gears with high tooth loads because for them the dynamic consequences of the tooth deflections are much greater than those due to the tooth errors which are permitted by the DIN or AGMA standards (Chapter 2 of this thesis).

1.2 Vibration source

The dynamic deformations of the teeth even under a constant torque load are the main cause of vibrations. The change of the tooth deflections is a result of the changing positions of the teeth that are in contact with each other. Under the given assumptions a totally rigid gear pair without tooth errors would result in a noiseless gearbox. However, because such rigid structures do not exist, every gearbox makes some noise. In practice the sound power levels of gearboxes are often unacceptable.

Noise measurements of many gearboxes have shown that the sound power level decreases when the gear quality is increased (/1.2/, /1.3/). However, even high quality gears may produce too much noise. It was recognized that due

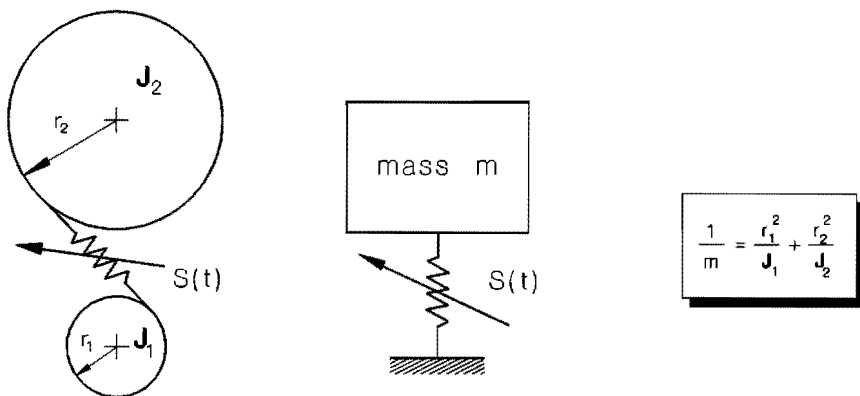


Figure 1.2:
Analogy with time variable stiffnesses.

to the bending of the teeth an engagement shock is introduced because the next tooth pair to come into contact will meet a fraction too early. This can be ameliorated by introducing a tooth profile correction. This profile correction or tip relief, which generally is not greater than 50 microns (/1.4/, /1.5/, /1.6/), prevents the engagement shock when the load is applied for which it was designed.

Nevertheless, an optimal tip relief does not take away all the vibrations. First of all a tip relief is only optimal for one tooth load /1.7/. Secondly, the variation in tooth stiffness, which under the given assumptions is a periodical function of time, is another source of vibration. This thesis studies both vibration sources, i.e. engagement shock and tooth stiffness variations.

Fig. 1.2 shows the analogy between the variation of a tooth stiffness in a gearbox with constant torque load and the variation of a spring stiffness with a constant load. In both cases the variation of the stiffness causes the system to vibrate even when the load is constant. In order to minimize these vibrations the stiffness variations have to be as small as possible. This can be done by choosing suitable gear parameters such as tooth width, helical angle and modulus. These parameters determine the overlap ratio ϵ_{β} . According to the literature (see e.g. /1.8/) for values of $\epsilon_{\beta} = 1$ or greater the variation of tooth stiffness will be significantly smaller than

for values smaller than one.

A new method to get small variations of tooth stiffness and of engagement shocks is a three dimensional profile correction, which can be produced by highly advanced so called topological or 3-D grinding machinery relatively recently developed.

1.3 Vibration transmission through bearings

The vibrations that are produced at the gears are transmitted to the gear shafts and reach the bearings. The bearings transmit the vibrations into the gearbox housing. Apart from the vibration transmission through bearings, the bearings themselves produce vibrations and noise. But as stated before, those contributions to the gearbox vibrations do not form part of this study and will be carefully excluded during measurements. Pittroff /1.9/ states that bearing noise will become noticeable when no other strong time varying forces are present. This is the case, for example, in some electric motors, but not in gearboxes where tooth forces are predominant.

The vibration transmission through bearings can be described by the stiffness matrices and if necessary also the damping matrices of these bearings. This thesis deals with rolling element bearings and fluid film bearings for which the stiffness matrices are calculated. In the literature many investigations were made to calculate the bearing stiffness of rolling element bearings. White /1.10/ describes a method to calculate the radial stiffness of rolling element bearings. It is concluded that the bearing stiffness is dependent on the bearing load. Especially when the applied load is small the stiffness is highly dependent on that load. Here, a slight increase in load will produce a large change in stiffness. At higher loads this effect is less. Under high loads where the noise problem has to be considered, the stiffness may be linearised in order to simplify further calculations.

White /1.10/ also states that for a bearing with a relatively small clearance, the number of rolling elements present in the load zone at any instant has an insignificant effect on the bearing nonlinear stiffness characteristics. Therefore, in this thesis the bearing stiffness is assumed not to be affected by the changing numbers of elements rolling through the load zone during bearing operation.

Gargiulo /1.11/ presents formulas to approximate radial and axial bearing stiffnesses of different types of bearings. Ophrey /1.12/ measured radial stiffnesses of ball bearings in the frequency domain. It was concluded that the radial stiffness of a ball bearing can be calculated accurately with the methods as described in the above mentioned references. Kraus et al. /1.13/ presented a method for the extraction of rolling element bearings characteristics (stiffness and damping) under operating conditions. In essence, they came to the same conclusions and also found very small influence of running speed on bearing stiffness. Bearing stiffness varies very little between static and dynamic conditions. Thus it is sufficient, for practical purposes, to use the static bearing stiffness when modeling the vibration transmission properties.

Lim /1.14/ has shown that radial and axial bearing stiffnesses are not sufficient to describe the vibration transmission through bearings correctly. For example, a shaft connected with a bearing perpendicular to a casing plate with a force on the shaft in the plane of the plate, will not be able to cause bending waves in the plate according to the simple mathematical bearing model. However, in practice, the casing plate motion is primarily flexural. Lim introduces moment stiffnesses which can be used for analysis as well as design studies of rotating mechanical systems with multiple shafts and gear pairs or multi-staged rotors. He describes a complete bearing stiffness matrix in six degrees of freedom /1.15/.

Fluid film bearings can be described mathematically in a similar way as rolling element bearings. The stiffness and damping coefficients for plain cylindrical bearings are widely published in the literature on rotor dynamics, see e.g. /1.16/, /1.17/, /1.18/ and /1.19/. Because of the need to validate these theoretical models of bearings, much work took and takes place on measurement of bearing stiffness and damping. Stiffness coefficients have mostly been measured by the application of static loads only /1.20/, but usually the damping coefficients are required too for rotor dynamic applications. This necessitates the application of a dynamic load to the bearing /1.21/. The major difficulty encountered in obtaining accurate experimental results is that the equations needed to process the measured data are ill-conditioned, so that small inaccuracies of measurements can result in substantial differences in the observed values of stiffness and damping. Nevertheless, radial and axial stiffnesses and

damping coefficients can be easily derived from graphs in the references mentioned. In contrast, literature for deriving the moment stiffness and damping coefficients is extremely scarce. Kikuchi /1.22/ and Mukherjee and Rao /1.23/ have created graphs for that purpose, but these are not widely used. Probably moment stiffness and damping coefficients are usually considered to be of negligible influence on rotor dynamic behaviour. However, analysis of vibration transmission through fluid film bearings requires the moment stiffness coefficients and possibly also damping coefficients in order to predict out-of-plane vibrations on a gearbox. In this thesis the graphs of Kikuchi and of Mukherjee and Rao will be used.

1.4 Housing dynamics and noise radiation

A number of publications contain experimental data on gear housing vibration due to gear excitation at the mesh frequencies and their multiples. Most of these give the acceleration spectra of the housing plates. Although extensive experimental studies were undertaken, attempts to correlate these test results with computational predictions were limited. One reason may be the complexity of the housing geometry involved. The modeling of gear housing vibration can be grouped as Experimental Modal Analysis (EMA), Finite Element Method computations (FEM), and Statistical Energy Analysis (SEA).

The Experimental Modal Analysis technique has been widely used not only in dynamic analysis of gearboxes but also of many other mechanical systems. Modal analysis may be defined as the characterization of the dynamic properties of an elastic structure through the identification of its mode shapes and natural frequencies. The general steps involved are measurements of force and response signals, determination of frequency response functions using Fourier Transforms, and curve fitting to obtain natural frequencies, mode shapes, damping and transmissibility from one point to another. Van Haven et al. /1.24/ used the Experimental Modal Analysis technique to characterize a gear-motor housing which radiated excessive noise. They claimed that the fundamental frequency coincided with one of the gear mesh frequencies, and by ribbing the housing interior the natural frequency was shifted away from the excitation frequency.

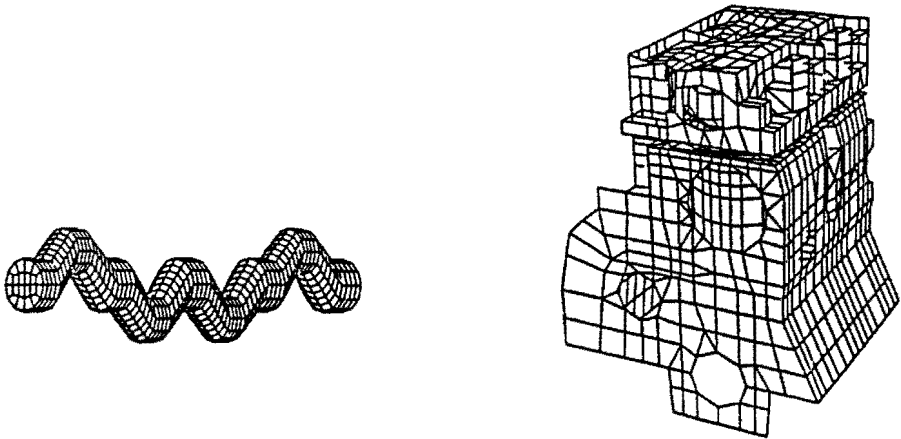


Figure 1.3:

Finite Element Models of engine block and crankshaft /1.26/.

The Finite Element Method is widely used due to the availability of general purpose finite element programs such as NASTRAN, ANSYS, ABAQUS, COSMOS, etc. In the few cases that are known from literature, the gear housing is modeled independently from the geared transmission. These FEM-models of empty gearboxes are used to calculate natural frequencies. The reason for independent modeling and analysis of gearbox and gears lies in the fact that this reduces the model size, which has a favourable effect on time and memory consumption of the finite element programs used. However, the steady increase of computing power leads to an increase of cases that analyze a complete system.

Kato et al. /1.25/ used 480 plate elements to obtain the vibration modes and natural frequencies of a simple gearbox with two gears. A similar approach was undertaken by Sung and Nefske /1.26/ to model an engine block with a crankshaft connected to each other by bearings. Fig. 1.3 shows the finite element models of engine block and crankshaft.

Not only natural frequencies and vibration modes were calculated, but also a prediction was made of the surface-averaged mean square velocity, up to 2000 Hz, due to cylinder combustion excitation. The regions of the engine block with the highest levels of vibration were stiffened, and this led to a significant predicted noise reduction (about 10 to 20 dB) for a wide frequency range above 400 Hz. However, the coupling of the crankshaft to the engine block was done by using simple radial springs.

Another way to pinpoint the areas that should be stiffened is to use strain energy methods with the above mentioned finite element models to calculate the strain energy density for each troublesome vibration mode. The structural elements with the highest strain energy per unit volume can be determined as the best choice for structural modification. Drago (/1.27/) applies this method to a helicopter transmission. However, no mention is made of the sound radiation efficiency of the structure. Apparently it is assumed to be equal to unity. As will be seen later in Chapter 4 of this thesis, only in that case the proposed method leads with certainty to noise reduction.

The Statistical Energy Analysis method has been used to analyze power flow in marine geared transmissions from the gears to the housing (/1.28/, /1.29/). This SEA approach is valid when a large number of vibration modes takes part in the vibration transmission. A complex system like a gearbox can be divided into many subsystems. Energy flow balance equations are then formulated for the entire system by considering energy stored, energy loss to the environment and energy transfer from one subsystem to another. The response of each subsystem is computed in terms of the average and standard deviation of the rms response in a frequency band.

Lu et.al. /1.29/ summarized that the SEA method is suitable for determining the averaged response in the high frequency range where enough vibration modes are present in each frequency band considered and also for averaging over a certain speed range because of the tonal force spectrum of a gear transmission. On the other hand, the Finite Element Method was recommended for estimating the response in the lower frequency range due to the detailed model information available. In the postprocessing, for example, this information can be too detailed and may be reduced by spatial averaging and by summation over frequency bands.

Gearbox noise radiation models have been semi-empirical in nature due to the complexity of the interactions between a vibrating box structure, such as a gearbox housing and its surroundings. An analytical solution to a sound radiation problem has been restricted to simple sound sources and highly idealized environment. Examples are pulsating and oscillating spheres, cylinders and ellipsoids (/1.30/, /1.31/). The noise radiation of more complex structures can be calculated numerically with the Boundary Element Method (BEM). However, with increasing frequency the element mesh

becomes finer and computational time becomes very large.

There have been many attempts in the past to characterize and correlate gearbox noise spectra with the structural vibration spectra using semi-empirical prediction formulas, for example /1.32/ and /1.33/. Most have concluded that the noise prediction is quite complicated and hence an analysis requires many assumptions. A rather common approach is the use of the so-called radiation efficiency.

The radiation efficiency relates structural vibrations and radiated sound power. Modal radiation efficiencies can be calculated mathematically for such idealized structures as simply supported rectangular plates and cylinders. However, generally speaking analytical expressions for complex structures like gearbox structures are not available. Fortunately, above a certain frequency, the so-called critical frequency, the radiation efficiency becomes unity. Approximate estimation of this critical frequency seems not too difficult even for rather complex structures. Therefore, above a certain frequency the modeling of the relation between structural vibrations and radiated sound power becomes very simple.

1.5 Outline of the study

This thesis pays attention to all previously mentioned parts of the vibration and noise model of a gearbox as shown in Fig. 1.1. In Chapter 2 an analytical model is developed and experimentally tested for modeling the vibration source of a gearbox. The model describes the time variable tooth stiffness and the engagement and disengagement shocks which are considered to be the main vibration sources in high quality gearboxes. The purpose of the analytical model is to create a fast calculation method as an alternative to the often used time consuming Finite Element Method computations.

Chapter 3 describes the vibration transmission through bearings. Bearing stiffnesses of various types of rolling element bearings are predicted and these predictions are to some extent verified by experiments. The bearing stiffness consists of a stiffness matrix for six degrees of freedom which is considerable more complex than the commonly used radial and axial stiffness coefficient of a bearing. New contributions are made for roller bearing and for tapered roller bearing stiffness calculations. It will be shown that especially the bearing moment stiffness plays an important role in the vibration transmission from shaft to gearbox housing.

Chapter 4 studies Finite Element Modeling (FEM) of several simple gearbox structures. The surface-averaged mean square velocity of simple gearbox-like structures is predicted and those predictions are verified by Experimental Modal Analysis. A step by step approach is used to investigate the usefulness of FEM for very simple up to complex structures such as a gearbox housing with shafts and bearings. Special attention is paid to the connection of bearings to the gearbox housing in the finite element model and to the influence of the bearing stiffness matrix. The purpose of this chapter is to verify by experiments the results of the FEM calculations and thereby to increase the knowledge of a proper modeling of the structure for practical use. Chapter 4 also studies analytical and statistical models for the relationship between housing vibration and radiated noise.

In Chapter 5 a gearbox test rig is described on which vibration and sound power levels have been measured. The test rig contains a single stage gearbox in which different sets of single helical and double helical gears with different profile corrections have been used. Also various kinds of bearings have been used to measure their effects on vibrations and sound power levels.

In this chapter the synthesis of the developed theories is tested. The complete mathematical model containing the analytical description of the vibration source, the stiffness matrices of the bearings, the finite element model of the gearbox housing and the model of the radiation efficiency is used to predict vibration and sound power levels. Special attention is paid to different kinds of profile corrections used. Part of the experiments is used to investigate the practical value of the proposed theories of the previous chapters. This forms a new contribution to the analysis of the noise problem of gear transmissions because no such complete investigations are known from the literature. Furthermore, this chapter investigates the influence on the vibration and sound production of several practical design measures such as bearing choice and the change from single helical to double helical gears.

A final evaluation of this study is found in Chapter 6. The proposed theories of this thesis are discussed and design guidelines for noise and vibration control of gearboxes are presented. The influence on the sound power level of gearboxes of bearing choice, tooth profile corrections and the use of double helical gears are the most important ones.

2. VIBRATION SOURCE

An analytical method is developed to calculate the tooth stiffness of an involute gear pair. The method is valid for spur gears, helical gears and double helical gears with parallel shafts. The deflections due to the flexible shafts (torsion and bending) are taken into account as well. A lumped parameter model of the gearbox interior (i.e. the rotating elements) with the time variable tooth stiffness and the engagement shocks gives the frequency dependent vibration levels at the gears. This vibration level will be used later as input for further calculations of the vibration transmission through bearings to the gearbox housing.

The proposed analytical modeling is a low cost alternative for tooth profile designing with the Finite Element Method and includes the modeling of 2-D and 3-D profile corrections.

2.1 Introduction

The basic source of noise and vibration inside a gearbox can be described with the time variable tooth stiffness and the engagement shocks. Fig. 2.1 shows the generation and propagation chain of vibrations and sound of a gear transmission. In this Chapter the first part of this chain is being investigated. Most investigators use the Finite Element Method for calculating the time variable tooth stiffness, see e.g. /2.1/, /2.2/. This proves to be a time and computer storage consuming process. Since for every gear pair a new FEM model has to be made, it looks attractive to look for a faster method. In this chapter an analytical method for calculating the tooth stiffness is developed which is based upon work from Schmidt /2.3/.

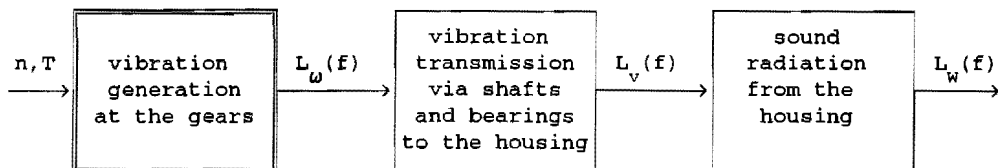


Figure 2.1:

Sound generation scheme of a gear transmission.

n and T are the speed [rev/min] and the applied torque [Nm] of the gearbox, L_{ω} is the angular velocity level at the gears, L_v is the velocity level at the surface of the gearbox, and L_w is the sound power level.

This results in a universal computer program that calculates tooth deflections, tooth force distributions and tooth stiffnesses. It also gives suggestions for an optimum tooth profile correction to achieve smaller engagement shocks.

In contrast to what is stated in the literature, see e.g. /2.1/, it will be shown that profile corrections have no significant effect on the tooth stiffness. However, the commonly used profile corrections have certainly a significant effect on the engagement shock. The vibrations at the gears are a result of both effects, the time variable tooth stiffness and the engagement shocks.

Furthermore, this chapter contains a dynamical model of a single stage gear transmission in order to predict the vibration levels at the gears which are originated by the time variable tooth stiffness and the engagement shocks.

To describe the behaviour of a gearbox as a source of noise and vibration, one has to know the mechanisms that are responsible for the noise generation. Noise and vibration problems in gear technology are concerned less with the strength of gears than with their smoothness of drive, since it is speed variation and the resulting force variation that generates unwanted sound. This imperfect smoothness of drive is called Transmission Error. The Transmission Error is defined as the deviation from the position at which the output shaft of a gear drive would be if the gearbox would be perfect, i.e. without errors or deflections and the actual position of the output shaft when no force is applied. It may be expressed, for example, as an angular rotation from the "correct" position or sometimes more conveniently as a linear displacement along the line of action /2.4/.

The Transmission Error is a resultant of all kind of tooth errors such as pitch errors, helical errors, misalignment errors and once per revolution errors. Since the Transmission Error is measured without any load applied, here a distinction is made between an unloaded Transmission Error and a loaded Transmission Error. The loaded T.E. also contains the deflections of the teeth and the gear shafts due to the gear load. For lightly loaded gears with normal or large pitch errors the difference between the unloaded and loaded T.E. will be insignificant. However, for highly loaded gears with small tooth errors the unloaded T.E. will be very small in comparison with the loaded T.E.. This is the case for the gearboxes which are of interest in this thesis. This means that for these types of high accuracy gearboxes the tooth errors can be neglected for modeling purposes because

the tooth deflections dominate the loaded Transmission Error.

The loaded Transmission Error is caused by the time dependent variation of stiffness of the meshing teeth which is a result of the bending of the teeth and gear shafts. This stiffness variation always occurs even in a perfect gearbox without unloaded Transmission Error. As a consequence of tooth deflection, tooth engagement and disengagement shocks will occur as well. In the computational models in this thesis it is assumed that the Transmission Error and the resulting vibrations and noise are primarily caused by variations in tooth stiffness and by the tooth engagement and disengagement shocks. These errors result from the elasticity of the materials.

High quality gears are often modified by adding some kind of a profile correction. These modifications consist of corrections that generally do not exceed one tenth of a millimeter. In practice such small profile corrections have great influence on the dynamic behaviour of the gears. This supports the assumption that the Transmission Error is mainly determined by the tooth deflection variations and the engagement shocks when high quality gears are used.

In this chapter the tooth stiffness is being calculated as a function of geometrical parameters and as function of the linear displacement along the line of action by the use of analytical formulations of the tooth deflections according to Schmidt /2.3/ and not by the use of Finite Element Method. The same route was followed by Placzek /2.5/ who's work was published at a time where our investigations were completed (Roosmalen /2.6/ and /2.7/). Placzek calculated force distributions along the tooth profiles that were in agreement with our computations. However, he did not calculate the tooth stiffness.

The investigations resulted in a computer program which enables fast calculations by simply downloading the geometrical parameters of the gear transmission such as number of teeth, modulus etc. The gears are supposed to be geometrically perfect (high quality gears). The calculations are valid for involute gears with parallel shafts. The gears can be spur ($\beta = 0$) or helical ($\beta > 0$) and configured single helical or open-V. The tooth stiffness S per unit width is defined as follows:

$$S = \frac{\partial F/B}{\partial \delta} \quad [(N/mm)/\mu m]^1 \quad (2.1)$$

1) throughout this thesis SI-units will be used and for the convenience of the reader they will often be put between brackets

Where F is the total tooth force, B is the tooth width and δ is the tooth deflection in microns measured at the contact points of the mesh in the direction along the line of action (in the transverse plane).

The total tooth force is known as the quotient of torque and radius of one of the gears. The tooth width B is a constant that can be obtained from the drawings of the gears. The tooth deflection δ is the unknown part in the formula of the tooth stiffness S . To obtain the tooth stiffness one has to calculate tooth deflections for two slightly different tooth forces F . By doing this the approximation of the quotient $\partial F/\partial \delta$ can be calculated. The difficulty lies in finding the tooth deflection δ for a given tooth force F and tooth width B . For this purpose it is necessary to take a closer look at the teeth in meshing.

2.2 Deflections

Two involute gears that are meshing make contact in the contact area. The contact consists of straight lines along the teeth. When the applied force F is zero the gears touch one another at these lines. By increasing the force the teeth in contact will bend. The gears will move towards each other by a displacement of δ micron. During this process it is assumed that the displacements are small enough to assume that the contact lines remain the same. This assumption makes it possible to calculate the contact lines in advance and they do not have to be altered as a function of the displacements.

In order to obtain the tooth deflection δ of the entire contact, the contact is divided into N contact points. Each point lies upon a contact line of one of the meshing teeth. The partial deflection of each contact point will be calculated as a function of one point-force. Linearity of the systems makes it possible to add up all the partial deflections to get the total deflection of each point. By dividing the contact lines into N points it should be possible to calculate their deflections by looking at the points separately. The only problem that remains is the calculation of the partial deflections δ_i of the contact points ($i = 1 \dots N$) when one of the points is loaded by a force F_j .

The deflection $\delta_{i,j}^*$ of point i as result of force F_j that is applied on point j can be divided into four parts. These are:

$$\delta_{1,j}^* = \delta_{\text{tooth}}^* + \delta_{\text{Hertz}}^* + \delta_{\text{bend}}^* + \delta_{\text{torsion}}^* \quad [\text{m}] \quad (2.2)$$

with δ_{tooth}^* tooth deflection
 δ_{Hertz}^* Hertzian deflection (if $i = j$)
 δ_{bend}^* deflection due to bending of the gear shafts
 $\delta_{\text{torsion}}^*$ deflection due to torsion of the gear wheels

The total deflections of all N points can then be calculated by summation:

$$\delta_i = \sum_{j=1}^N \delta_{i,j}^* \quad [\text{m}] \quad i = 1, 2, \dots, N \quad (2.3)$$

Now that all N deflections δ_i are calculated the question arises how large the deflection of the entire mesh will be. To answer that question it is necessary to look a little bit closer at the mesh. If one of the gears is supposed to be rigid (which is not true, but is done for simplicity) then the other gear will have to take on all the deflections δ_i . When both gears are fixed to their places the deflections δ_i create space between the teeth. After this the only thing to do, in order to obtain the final position of the gears, is to turn one or both gears towards each other until they touch. If the partial deflections are all different from each other, which is probably the case when a uniform force distribution is assumed, the gears will touch at only one point. All the other points will leave a gap between the teeth. This means that these loose points could not have been loaded by the previously assumed force.

The only conclusion that can be drawn from this is that all partial displacements δ_i have to be equal to one another. This demands a force distribution of a particular kind. One way of obtaining this force distribution is to start with a uniform force distribution over all points and calculate the partial deflections. After this has been done a new force distribution has to be calculated that will result in a uniform deflection distribution. If all four parts of the partial deflections were linear with respect to force this would require only one iteration. However, as will be shown, one of the parts is nonlinear with respect to force. This part is the deflection due to Hertzian contact of both gears.

The Hertzian deflection is for this level of loading only slightly nonlinear with the applied force. Therefore, no large error will be made by assuming the Hertzian deflection linear with respect to force. This

linearisation is only made in order to obtain a new force distribution out of the calculated deflections. This results in an almost perfect force distribution which will produce a uniform deflection over all the contact points. In order to get a better force distribution, this iteration process is put to an end when the difference between minimum and maximum partial deflection is smaller than a specified maximum error.

After this iteration process has come to an end, two things are known. These are the deflection of the teeth (this is the average of all partial deflections) and the force distribution over the contact field. The latter being a by-product to the problem of finding the tooth stiffness.

The tooth deflection δ as function of gear geometry and applied tooth force can be calculated in the manner described above. By repeating this for two slightly different forces the tooth stiffness can be calculated by using Eq. (2.1).

To be able to calculate the tooth deflection the four partial deflections have to be calculated first. The next sections will deal with these four deflections.

2.2.1 Tooth deflection

Schmidt /2.3/ describes a method to calculate deflections of a tooth with a point load. He combines two theories. One that is valid for spur gears /2.8/ and one that describes the deflection of a cantilever plate /2.9/. Schmidt has made a comparison between his calculations and measurements that were made by Hayashi /2.10/. Here it was found that theory and practice are in good agreement with one another. Placzek /2.5/ uses the method described by Schmidt to calculate tooth force distributions and profile corrections but does not calculate the tooth stiffness. This chapter will describe the method of Schmidt and will use it as input for the calculation of the tooth stiffness and for dynamical calculations.

A tooth that makes contact with another tooth will do so along a contact line l with a force distribution $W(\xi)$. See Fig. 2.2. The deflection of the tooth can be described as follows:

$$f_1(x) = \int_0^l C_1(x, \xi) W(\xi) d\xi \quad [m] \quad (2.4)$$

Also a similar equation describes the deflection of the opposite tooth:

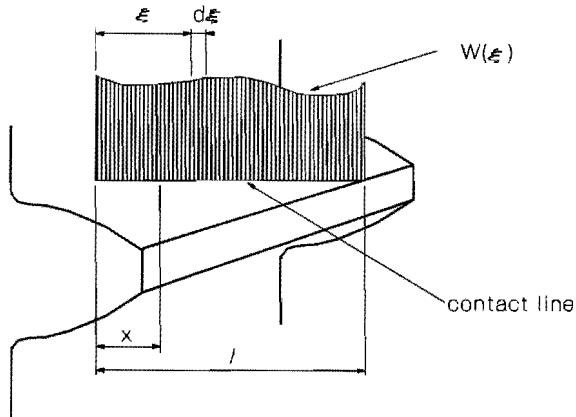


Figure 2.2:
Force distribution along the line of contact.

$$f_2(x) = \int_0^l C_2(x, \xi) W(\xi) d\xi \quad [m] \quad (2.5)$$

The coordinates x and ξ are along the contact line l as is shown in Fig. 2.2. $C_1(x, \xi)$ and $C_2(x, \xi)$ are functions that describe the flexibility of the teeth. $f_1(x)$ and $f_2(x)$ are deflections of both teeth at position x in the direction of the force $W(\xi)$. The flexibility functions describe how much the tooth deflects at position x due to the point force $W(\xi)$ at point ξ . The total deflection of both teeth will then be:

$$\begin{aligned} f(x) = f_1(x) + f_2(x) &= \int_0^l [C_1(x, \xi) + C_2(x, \xi)] W(\xi) d\xi = \\ &= \int_0^l C(x, \xi) W(\xi) d\xi \quad [m] \quad (2.6) \end{aligned}$$

This means that the two contacting teeth can be replaced by one beam that can be described by the compliance function $C(x, \xi)$. This function will be evaluated by putting a point force $P(\xi)$ at the edge of a cantilever plate as is shown in Fig. 2.3. The deflection $f(x)$ due to this load is schematically shown in the figure. These deflections are determined by a differential equation of the following kind /2.8/:

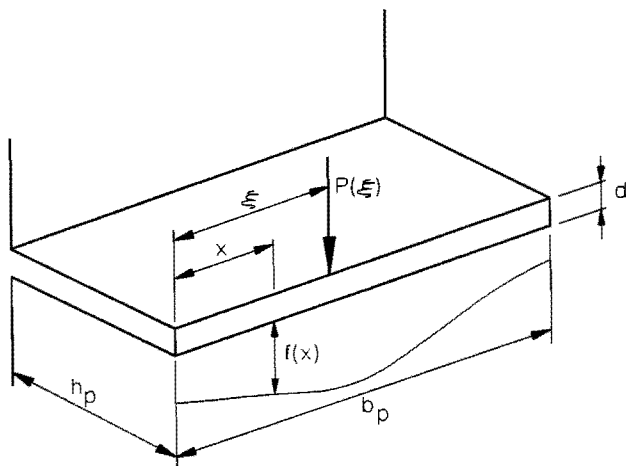


Figure 2.3:

Deflection of a cantilever plate loaded at its free edge.

$$S_1 \frac{d^4 f}{dx^4} - S_2 \frac{d^2 f}{dx^2} + S_3 f = P(\xi) \quad [N] \quad (2.7)$$

In this way the plate is being described by three stiffnesses. S_1 is the bending stiffness of the plate, S_2 is the stiffness against bending at the root of the plate and S_3 is the stiffness against displacements at the root of the plate. These three stiffnesses are being obtained as follows.

$$S_1 = \frac{h N}{\alpha} \quad (2.8)$$

$$S_2 = \frac{2(1-\nu)}{h_p} N \quad (2.9)$$

$$S_3 = \gamma \frac{3N}{h_p^3} \quad (2.10)$$

with	h_p	height of the plate
	$N = \frac{Ed^3}{12(1-\nu^2)}$	plate stiffness
	E	elasticity modulus
	d	thickness of the plate
	ν	poisson's constant

$$\alpha = \frac{12}{(1+2\nu)^2}$$

$$\gamma = \frac{f_e}{f_{\text{etot}}} \quad (2.11)$$

f_e deflection of the plate only,
the foot is rigid
 f_{etot} total deflection of the plate,
with foot-deflection

The differential Equation (2.7) can be solved by setting the right hand side equal to zero. This homogeneous differential equation then describes the deflections $f(x)$ of the unloaded part of the plate. The equation can be written as follows:

$$\frac{d^4 f}{dx^4} - \frac{S_2}{S_1} \frac{d^2 f}{dx^2} + \frac{S_3}{S_1} f = 0 \quad (2.12)$$

or

$$\left(D^4 - \frac{S_2}{S_1} D^2 + \frac{S_3}{S_1} \right) f = 0 \quad (2.13)$$

or

$$(D - \phi)(D + \phi)(D - \psi)(D + \psi) = 0 \quad (2.14)$$

with

$$\phi = \sqrt{\frac{S_2}{2S_1} + \frac{1}{2} \sqrt{\left(\frac{S_2}{S_1}\right)^2 - \frac{4S_3}{S_1}}} \quad (2.15)$$

$$\psi = \sqrt{\frac{S_2}{2S_1} - \frac{1}{2} \sqrt{\left(\frac{S_2}{S_1}\right)^2 - \frac{4S_3}{S_1}}} \quad (2.16)$$

There are two solutions to Eq. (2.14) depending on the values of the three stiffnesses S_1 , S_2 and S_3 .

$$\text{If } \left(\frac{S_2}{S_1} \right)^2 > \frac{4S_3}{S_1} ,$$

then the solution has the form

$$f_e(x) = Ae^{r_1 x} + Be^{-r_1 x} + Ce^{r_2 x} + De^{-r_2 x} \quad (2.17)$$

with

$$r_1 = \frac{1}{h_p} \sqrt{\alpha(1-\nu)} + \frac{1}{2} \sqrt{\left(2\alpha(1-\nu)\right)^2 - 12\alpha\gamma} \quad (2.18a)$$

$$r_2 = \frac{1}{h_p} \sqrt{\alpha(1-\nu)} - \frac{1}{2} \sqrt{\left(2\alpha(1-\nu)\right)^2 - 12\alpha\gamma} \quad (2.18b)$$

The index e indicates that the solution is only correct for the edge of the plate.

$$\text{If } \left(\frac{S_2}{S_1} \right)^2 < \frac{4S_3}{S_1} ,$$

then the solution has the form

$$f_e(x) = e^{px} \left(A'' \cos(qx) + B'' \sin(qx) \right) + e^{-px} \left(C'' \cos(qx) + D'' \sin(qx) \right) \quad (2.19)$$

$$\text{with } p = \frac{1}{\sqrt{2} h_p} \sqrt{\sqrt{3\alpha\gamma} + \alpha(1-\nu)} \quad (2.20)$$

$$q = \frac{1}{\sqrt{2} h_p} \sqrt{\sqrt{3\alpha\gamma} - \alpha(1-\nu)} \quad (2.21)$$

The constants A, B, C, D or A'', B'', C'' and D'' can be derived from the following boundary conditions.

a) to the left of where the point load is applied:

$x = 0$ then the torque $M(0) = 0$ and transverse force $Q(0) = 0$

$$\frac{d^2 f_{el}(0)}{dx^2} = 0 \quad (2.22)$$

$$\frac{d^3 f_{el}(0)}{dx^3} - \frac{2(1-\nu)\alpha}{h_p^2} \frac{df_{el}(0)}{dx} = 0 \quad (2.23)$$

b) to the right of where the point load is applied:

$x = \ell$ then the torque $M(\ell) = 0$ and transverse force $Q(\ell) = 0$

$$\frac{d^2 f_{er}(\ell)}{dx^2} = 0 \quad (2.24)$$

$$\frac{d^3 f_{er}(\ell)}{dx^3} - \frac{2(1-\nu)\alpha}{h_p^2} \frac{df_{er}(\ell)}{dx} = 0 \quad (2.25)$$

c) continuity at the loaded point $x = \xi$

$$f_{el}(\xi) = f_{er}(\xi) \quad (2.26)$$

$$\frac{df_{el}(\xi)}{dx} = \frac{df_{er}(\xi)}{dx} \quad (2.27)$$

d) force and torque equality at the loaded point $x = \xi$

$$\int_{x=0}^{\xi} S_3 f_{el}(x) dx + \int_{x=\xi}^{\ell} S_3 f_{er}(x) dx = P \quad (2.28)$$

$$\int_{x=0}^{\xi} S_3 f_{el}(x) (\xi-x) dx - \int_{x=0}^{\xi} S_2 \frac{df_{el}}{dx} dx = \int_{x=\xi}^{\ell} S_3 f_{er}(x) (x-\xi) dx + \int_{x=\xi}^{\ell} S_2 \frac{df_{er}}{dx} dx \quad (2.19)$$

The calculation of the constants for every point force leads to 8 linear equations because the differential equation has to be solved separately for the left and the right side of the point force. These 8 equations can be solved by introducing a matrix **A** and vectors **b** and **c**;

$$\mathbf{A} \cdot \mathbf{b} = \mathbf{c} \quad (2.30)$$

- A** 8x8 matrix
- b** vector with the eight unknown constants
- c** load vector

Vector **b** can be solved with help of LU-decomposition techniques as described in the literature, e.g. /2.11/. The 64 parts of matrix **A** and vector **b** and **c** can be obtained from Appendix A for both Eqs. (2.17) and (2.19).

The deflection at the edge of the plate can be calculated with the above equations. Deflections at an arbitrary point of the plate can be derived by introducing a function $g(x)$. The deflection at an arbitrary point x due to a force at point ξ can then be calculated like:

$$f(x, \xi) = f_e(x, \xi)g(x)g(\xi) \quad [\text{m}] \quad (2.31)$$

In Eq. (2.31) $f_e(x, \xi)$ stands for the deflection at the edge of the plate. $f_e(x, \xi)$ can be calculated in a way as described above. The functions $g(x)$ and $g(\xi)$ are defined as:

$$g(x) = \sqrt{\frac{f_{\text{tot}}(x)}{f_{\text{etot}}}} \quad \text{and} \quad g(\xi) = \sqrt{\frac{f_{\text{tot}}(\xi)}{f_{\text{etot}}}} \quad (2.32)$$

The three deflections $f_{\text{tot}}(x)$, $f_{\text{tot}}(\xi)$ and f_{etot} are being calculated by using the theory of Weber and Banaschek for spur gears. For that purpose a helical gear will be looked upon as a spur gear. The tooth form is determined by looking at the gears in the normal plane. In Appendix B the formulas to calculate these profile forms are presented. These profile forms of the gears are used to calculate the deflection at the top of the tooth and the deflections at positions x and ξ by applying a unit load of one Newton.

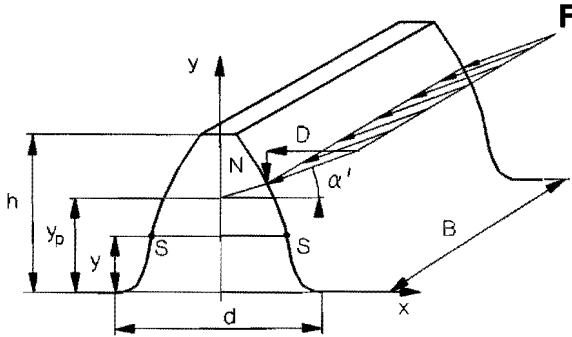


Figure 2.4:
Tooth dimensions.

To be able to calculate the value of stiffness S_3 , the factor γ has to be calculated ($\gamma = f_e / f_{etot}$). This means that the deflection f_e has to be calculated. This also is done by using the theory of Weber and Banaschek. For this purpose the tooth deflection is being divided into two parts. These are: deflection without movement of the root δ_t and deflection due to the root of the tooth without movement of the tooth itself δ_r . Together they add up to the tooth deflection δ_{tooth}^* .

$$\delta_{tooth}^* = \delta_t + \delta_r \quad [m] \quad (2.33)$$

To calculate δ_t and δ_r the boundary between root and tooth has to be defined. See Fig. 2.4. The x-axis makes contact with the tooth profile at the point where the trochoid stops and passes into the root circle. The applied force F stands perpendicular towards the surface of the tooth. It has horizontal and vertical components D and N respectively as can be seen in Fig. 2.4.

$$D = F \cos(\alpha'), \text{ and } N = F \sin(\alpha') \quad [N] \quad (2.34)$$

In an arbitrary section $S - S$ of the tooth a torque $M = D(y_p - y)$ works as well as both forces D and N . To obtain the deflection δ_t at the point where the force acts, the tensile energy inside the tooth is put equal to the

deflective energy $F\delta_t/2$. The tensile energy can be written down for torque M and forces D and N. This yields:

$$\begin{aligned} \frac{1}{2} F\delta_t &= \frac{1}{2} \int_{y=0}^{y_P} \frac{M^2}{\frac{E}{1-\nu^2} \frac{1}{12} B(2x)^3} dy + \frac{1}{2} \int_{y=0}^{y_P} \frac{1.2D^2}{2GBx} dy + \\ &+ \frac{1}{2} \int_{y=0}^{y_P} \frac{N^2}{\frac{E}{1-\nu^2} 2Bx} dy \end{aligned} \quad (2.35)$$

or:

$$\begin{aligned} \delta_t &= \frac{F\cos^2(\alpha')}{EB} \left\{ 12(1-\nu^2) \int_{y=0}^{y_P} \frac{(y_P - y)^2}{(2x)^3} dy + \right. \\ &\left. + \left\{ 2.4(1+\nu) + (1-\nu^2)\tan^2(\alpha') \right\} \int_{y=0}^{y_P} \frac{1}{2x} dy \right\} \end{aligned} \quad (2.36)$$

The root deflection δ_r can be obtained in a similar way. For that purpose the tooth is considered stiff. At the root of the tooth ($y = 0$) a torque $M = F\cos(\alpha')y_P$ and the forces D and N act. Here also deflective energy and tensile energy are used to obtain the deflection at the point where the force acts:

$$\frac{1}{2} F\delta_r = c_{11}M^2 + 2c_{12}MD + c_{22}D^2 + c_{33}N^2 \quad (2.37)$$

The factors c_{11} , c_{12} , c_{22} and c_{33} are obtained after a long process of well chosen assumptions and calculations. For further detail see Weber and Banaschek /2.8/. Eventually it yields:

$$\begin{aligned} c_{11} &= \frac{9(1-\nu^2)}{\pi EBd^2} & c_{12} &= \frac{(1+\nu)(1-2\nu)}{2EBd} \\ c_{22} &= \frac{2.4(1-\nu^2)}{\pi EB} & c_{33} &= \frac{(1-\nu^2)(1-\nu)}{\pi EB} \tan^2(\alpha') \end{aligned} \quad (2.38)$$

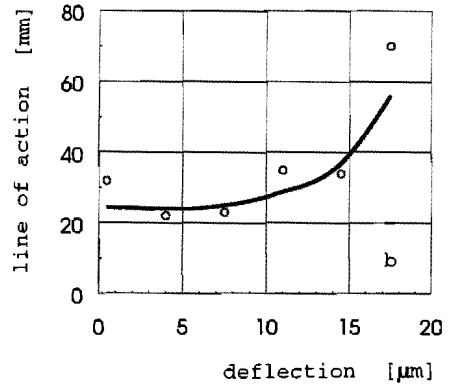
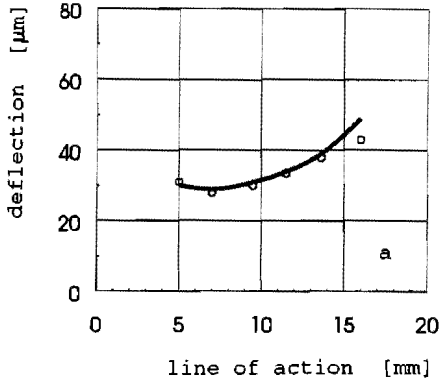


Figure 2.5:

Calculated and measured total deflections of aluminium spur gears /2.6/.

a. 15 teeth, b. 24 teeth (— theory, o measurement).

The root deflection can be calculated as:

$$\delta_r = \frac{F \cos^2(\alpha')}{EB} \left\{ \frac{18(1-\nu^2)}{\pi d^2} y_p^2 + \frac{2(1+\nu)(1-2\nu)}{d} y_p + \frac{4.8}{\pi} (1-\nu^2) \left\{ 1 + \frac{1-\nu}{2.4} \tan^2(\alpha') \right\} \right\} \quad (2.39)$$

The accuracy of these formulas has been tested in Roosmalen /2.6/. Two aluminium spur gears with 15 and 24 teeth respectively with modulus $m = 30$ mm and a tooth width of 20 mm were submitted to a load of 4000 Newton.

Fig. 2.5 shows the calculated and measured total deflections δ_t as function of the position at the line of contact. It is seen that for both cases the deflections increase with the position at the line of contact. This can be expected as the tooth load is applied at the foot of the tooth when this position is zero and at the tooth tip when this position reaches its maximum. The Figure also shows that the calculations are in good agreement with the measurements for any position at the line of contact. Therefore, it is concluded that the given theory for calculating the tooth deflections may be used for further calculations.

2.2.2 Hertzian deflection δ_{Hertz}^*

The Hertzian deflection of two teeth can be compared with two solid cylinders with different radii that make contact along a straight line of length B. The radius of each cylinder is equal to the radius ρ of the tooth at the momentary point of contact. Due to the fact that the theory of Hertz is only valid for two bodies of infinite dimensions it does not apply exactly to the problem of two teeth. This is because the finite thickness of the teeth. Hertz states that the inside stresses will decrease away from the point of contact, but only at an infinite distance they will become zero.

The teeth have a finite thickness, so it is supposed that at a distance t the stresses are equal to zero. Weber and Banaschek chose t to be the distance from the contact point to the point where the contact line intersects with the tooth line of symmetry. For both teeth this yields a different distance t_1 and t_2 . Eventually Weber and Banaschek /2.8/ come to the following formula for the total deflection of both teeth:

$$\delta_{\text{Hertz}}^* = \frac{2F(1-\nu^2)}{\pi EB} \ln \left\{ \frac{t_1 t_2 \pi EB}{2\rho_\nu (1-\nu^2) F} - \frac{\nu}{1-\nu} \right\} \quad (2.40)$$

$$\text{with } \rho_\nu = \frac{\rho_1 \rho_2}{\rho_1 + \rho_2} \quad (2.41)$$

It can be seen that the Hertzian deflection is not linear with respect to the force F.

2.2.3 Deflection due to bending of the gear shafts δ_{bend}^*

Each point force F_j makes the gear shafts bend. To calculate the amount of deflection at positions i in the mesh, it is assumed that the Euler theory of beams can be applied. For this purpose the shaft is divided into three parts with different diameter d_1 , d_2 and d_3 . See Fig. 2.6.

The middle part with diameter d_2 and length ℓ_2 is the gear. At the outer parts the bearings are attached at a distance ℓ_1 and ℓ_3 from the gear. In this section it is assumed that the bearing radial stiffnesses are infinite and that the bearing moment stiffnesses are zero. The deflections at positions i are of interest. These points all are part of the gear.

A distinction has to be made whether point i lies left or right from the point force position j . This is being referred to as $i < j$ (left) and $i > j$ (right). If i is equal to j then both formulas apply.

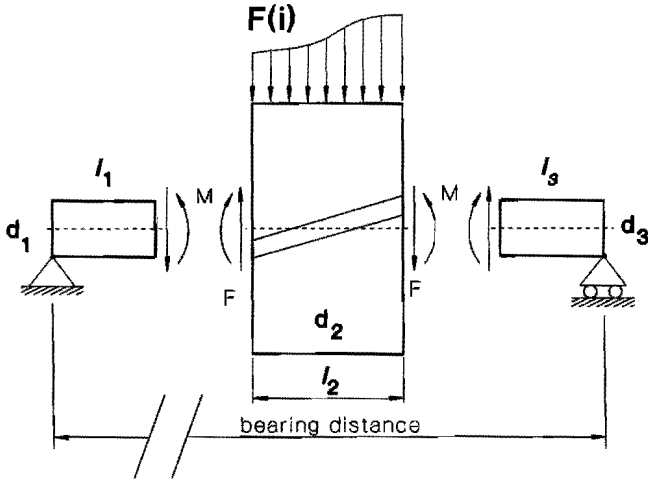


Figure 2.6:
Bending of a shaft.

The formulas are:

$i < j$:

$$\delta_{\text{bend}}^*(x_i) = \delta_B + \varphi_B(x_i - l_1) - \frac{F_j}{6EI_2} \frac{l-l_j}{l} \left\{ 3l_1(x_i^2 - l_1^2) + (x_i - l_1)^3 \right\} \quad (2.42)$$

$i > j$:

$$\delta_{\text{bend}}^*(x_i) = \delta_C + \varphi_C(x_i - l_j) - \frac{F_j}{6EI_2} \frac{l_j}{l} \left\{ 3(l-l_j)(x_i - l_j)^2 - (x_i - l_j)^3 \right\} \quad (2.43)$$

$$\text{with: } \delta_B = \varphi_{A1} l_1 - \frac{F_j l_1^3}{6EI_1} \frac{l-l_j}{l} \quad (2.44)$$

$$\delta_C = \varphi_{A_j} l_j + \frac{F_j}{6EI_1} \frac{l-l_j}{l} \left[\frac{l_1^3 - 3l_1^2 l_j}{I_1} + \frac{-l_j^3 + 3l_j l_1^2 - 2l_1^3}{I_2} \right] \quad (2.45)$$

$$\begin{aligned}
\varphi_A = & - \frac{F_j}{6E\ell} \left[\frac{\ell - \ell_j}{\ell I_1} \left\{ 2\ell_1^3 - 3\ell_1^2 \ell \right\} + \frac{\ell_j}{\ell I_3} \left\{ -2\ell_2^3 \right\} + \right. \\
& + \frac{\ell - \ell_j}{\ell I_2} \left\{ 2\ell_j^3 - 2\ell_1^3 - 3\ell\ell_j^2 + 3\ell_1^2 \ell \right\} + \\
& \left. + \frac{\ell_j}{\ell I_2} \left\{ 2\ell_2^3 - 2\ell^3 + 2\ell_j^3 + \ell^2 \ell_j - \ell\ell_j^2 \right\} \right] \quad (2.46)
\end{aligned}$$

$$\varphi_B = \varphi_A - \frac{F_j \ell_1^2}{2EI_1} \frac{\ell - \ell_j}{\ell} \quad (2.47)$$

$$\varphi_C = \varphi_B - \frac{F_j (\ell_j^2 - \ell_1^2)}{2EI_2} \frac{\ell - \ell_j}{\ell} \quad (2.48)$$

The deflections due to bending are linear with respect to the force F . Hence, the calculation of $\delta_{\text{bend}}^*(x_1)$ is rather straight forward.

2.2.4 Deflections due to torsion of the gear wheels $\delta_{\text{torsion}}^*$

As a rule investigators in the literature pay no attention to the phenomenon of wheel torsion, as they believe it is of no importance to the tooth stiffness. They are right when narrow gears in relation to the diameter are concerned, but in general gear wheel torsion may not be neglected. Deflections due to torsion of the gear wheels are a main source of a non-uniform tooth force load distribution along the tooth width with its influence on the tooth stiffness. Especially for slender gears the following formulations are relevant.

Each wheel has a torque T_1 or T_2 Nm on one side and is torque-free on the other side. Thus the variation in torque along the axis of each wheel makes the wheel deflect due to torsion. This effect will increase when the width of the gears becomes larger. There are two different torque configurations to be considered, see Fig. 2.7.

In the first configuration the torques are situated on the same side of the gearbox. This will lead to high tooth forces on this side with according deflections due to torsion. The second configuration will compensate this effect.

The deflections due to torsion can be calculated when the tooth forces F_j are known. For this we can use the formulas that describe torsion of solid

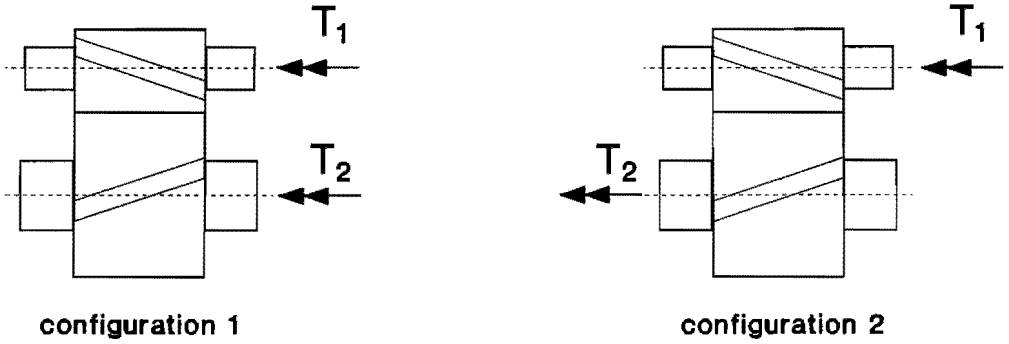


Figure 2.7:
Torque configurations 1 and 2.

shafts. The gears are considered to be solid and the outside diameter is equal to the pitch diameter d_1 or d_2 . The angle ϑ over which the wheel with length ℓ will rotate can be calculated as follows:

$$\vartheta = T\ell / (GI_p) \quad [\text{rad}] \quad (2.49)$$

with

T	torque	[Nm]
ℓ	length	[m]
G	shear modulus	[N/m ²]
$I_p = \pi \cdot r^4 / 2$		[m ⁴]
r	pitch radius	[m]

In the case of the gear wheels with N point forces F_j we obtain:

$$\vartheta(i, j) = \frac{F_j r_b \ell_k}{GI_p} = \frac{F_j r_b}{GI_p} \sum_{q=1}^k \Delta L(q) \quad [\text{rad}] \quad (2.50)$$

with

r_b	radius of the base circle	[m]
$\Delta L(q)$	length at point q	[m]

k :

	configuration 1		configuration 2	
$k =$	wheel 1	wheel 2	wheel 1	wheel 2
$i \leq j$	i	i	i	j
$i \geq j$	j	j	j	i

The deflection $\delta(i,j)$ at point i as a result of force F_j at point j can be calculated from:

$$\delta(i,j) = r_b \theta(i,j) \quad [m] \quad (2.51)$$

The deflections $\delta_{\text{torsion}}^*(i)$ result after a summation of $\delta(i,j)$ over all forces F_j . They can be calculated as follows:

$$\delta_{\text{torsion}}^*(i) = \frac{2r_b^2}{\pi G r^4} \sum_{j=1}^N \left\{ F(j) \sum_{q=1}^k \Delta L(q) \right\} \quad [m] \quad (2.52)$$

2.3 Force distribution along the line of contact

In order to calculate the force distribution along the line of contact the deflections described in the previous section are needed. The deflections δ_{tooth}^* , δ_{Hertz}^* , δ_{bend}^* and $\delta_{\text{torsion}}^*$ can be calculated when the force distribution is known. As pointed out in the beginning of this chapter the problem lies in the fact that this distribution is unknown. This problem can be solved by means of an iterative process. This process is started with a uniform force distribution. This will most likely result in a non-uniform deflection distribution. As stated in the beginning of this chapter one needs to find the force distribution that gives a uniform deflection distribution along the line of contact. In order to be able to choose a better force distribution we make use of the formulas for the deflections. A compliance matrix C is used for this purpose.

$$\delta(i) = \sum_{j=1}^N C(i,j) F(j) \quad [m] \quad (2.53)$$

This means that the deflections $\delta(i)$ are proportional with the tooth forces $F(j)$. This is not completely true because the Hertzian deflection is not proportional with the tooth force. However, to get a better force distribution the assumption is good enough, although it means that the problem has to be solved by iteration. The linear problem to be solved looks as follows:

$$\begin{bmatrix}
 & & & & & & & & -1 \\
 & & & & & & & & \cdot \\
 & & & & & & & & \cdot \\
 & & & & & & & & \cdot \\
 & & & & & & & & \cdot \\
 & & & & & & & & -1 \\
 & & & & & & & & -1 \\
 & & & & & & & & -1 \\
 & & & & & & & & F(1) \\
 & & & & & & & & F(2) \\
 & & & & & & & & \cdot \\
 & & & & & & & & \cdot \\
 & & & & & & & & \cdot \\
 & & & & & & & & \cdot \\
 & & & & & & & & F(N) \\
 & & & & & & & & \bar{\delta} \\
 1 & 1 & 1 & \dots & \dots & \dots & 1 & 1 & 0 \\
 \end{bmatrix}
 *
 \begin{bmatrix}
 F(1) \\
 F(2) \\
 \cdot \\
 \cdot \\
 \cdot \\
 \cdot \\
 F(N) \\
 \bar{\delta}
 \end{bmatrix}
 =
 \begin{bmatrix}
 0 \\
 0 \\
 \cdot \\
 \cdot \\
 \cdot \\
 \cdot \\
 0 \\
 F_{tot}
 \end{bmatrix}
 \tag{2.54}$$

The vector on the left hand side in this equation has unknown elements. F(1) up to F(N) are the point forces and $\bar{\delta}$ is the mean deflection. The problem can be solved with standard numerical techniques. Next, the N forces are used to calculate the exact deflections $\delta(i)$. When the individual differences between these deflections become negligible than the iteration process can be stopped. Then the force distribution F(i) and the mean deflection $\bar{\delta}$ are known.

The tooth stiffness can be obtained by repeating the calculation with a somewhat larger (e.g. 1/10th percent) tooth force F'_{tot} . This results in a mean deflection $\bar{\delta}'$. From this we can calculate the tooth stiffness per unit width **s**:

$$\mathbf{s} = \frac{(F'_{tot} - F_{tot})/B}{(\bar{\delta}' - \bar{\delta})} \quad [(N/mm) / \mu m] \tag{2.55}$$

2.4 Tooth stiffness of spur and helical gears

A single stage gearbox with spur gears is chosen to illustrate the results that can be obtained from Eq. (2.55). Fig. 2.8 shows the tooth stiffness of a spur gear set as function of the position on the line of action. This position is 100 percent when one tooth has passed. Therefore, the function is periodical as it is assumed that the gears are perfect. When the running speed n is known, this horizontal axis could also represent the time axis (position 100 % = $t_{tooth} = 60/nz$).

The variation in tooth stiffness is striking. It resembles a block function with a low and a high stiffness. This is caused by the fact that the number of teeth in contact changes abruptly from one to two and vice versa. This is characteristic for spur gears. When two teeth of each wheel are in contact the tooth deflections are small compared to the situation when only

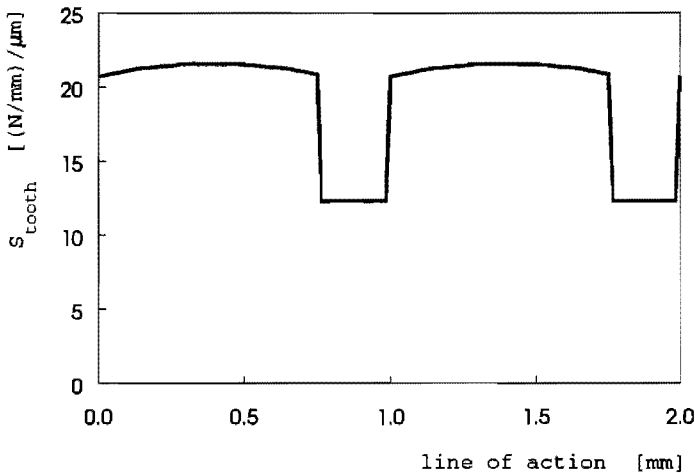


Figure 2.8:
Tooth stiffness of a spur gear set.

one tooth of each gear is in contact. Therefore the tooth stiffness is smaller when only one tooth is in contact.

The temporal variation of the tooth stiffness of helical gears is smoother than that of spur gears. This is due to the fact that helical teeth gradually make contact with each other. The amplitude of the stiffness is smaller than that of spur gears. Therefore, helical gears produce lower vibration levels. Helical gears are used to minimize the produced sound power level of gearboxes. They are designed in such a way that the overlap ratio ϵ_{β} equals an integer. It is believed to be true that a gearbox with an integer overlap ratio will minimize the produced noise. However, Lachenmaier /2.12/ could not confirm this hypothesis in his noise measurements. He only found that the sound power level decreases with increasing overlap ratio.

Another way to look at this phenomenon, is to calculate the tooth stiffnesses of different gear transmissions, and to plot the tooth stiffness amplitude against the overlap ratio. The tooth stiffness amplitude is a measure for the intensity of vibration generation at the gear mesh. Fig. 2.9 shows the result of such a calculation.

The calculations are based upon a gear set with following dimensions:

$z_1 = 18$, $z_2 = 90$, $m = 2.25$ mm, $\alpha = 20$ degr., $h_a = 1$, $h_d = 1$, $c_0 = 0.25$, $x_1 = 0.472$ and $x_2 = -0.110$. The tooth face width B has been varied from 20.25 to 81 mm, with steps of 10.125 mm. Since $d_1 = m \cdot z_1 = 40.5$ mm this

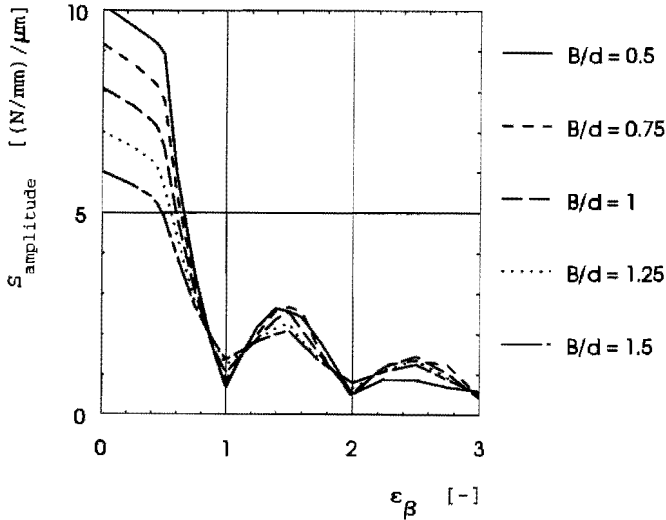


Figure 2.9:
Tooth stiffness amplitude as function of the overlap ratio.

means that B/d_1 was varied from 0.5 to 1.5 with steps of 0.25. The tooth force F was corrected in such a way that F/B remained a constant value of 50 N/mm.

As can be seen from Fig. 2.9, the tooth stiffness amplitude becomes small when the overlap ratio ϵ_β reaches a value of 0.8 or more. There are minima in the figure at integer values of ϵ_β . This means that gear transmissions with an integer overlap ratio will have a smaller loaded Transmission Error than those with a non-integer ϵ_β . But for $\epsilon_\beta > 0.8$ the differences in stiffness amplitude are small, and this probably explains why Lachenmaier could not measure any difference in sound power levels in this area for ϵ_β .

2.5 Dynamic behaviour of the gearbox interior

As a result of the previous sections of this chapter the time variable tooth stiffness of a spur, single helical or double helical gear transmission can be calculated quickly by the use of a computer program which contains the equations needed. As input for this computer program the geometrical dimensions of the gears have to be known after which in a few minutes the time variable tooth stiffness is being calculated. This variation of tooth stiffness is one of the reasons for a gear transmission to generate vibrations and sound. In this section it will be used to predict vibration levels at the gears of a single stage helical gear transmission.

The loaded Transmission Error is influenced by the time variable tooth stiffness and by the (dis)engagement shocks. To make a distinction between these two influences the T.E. will firstly be characterized only by the tooth stiffness. The (dis)engagements shocks will be put into the calculations in later sections of this chapter.

In order to calculate the vibration levels of the gears, the time variable tooth stiffness is used in a lumped parameter model of the gearbox interior (i.e. the rotating elements). For simplicity, the model does not include any exterior machinery. Normally, such a model does not represent the dynamical behaviour of a gearbox. Only when the couplings with the exterior machinery are sufficiently flexible, this model is valid. The test rig of Chapter 5 consists of a (test) gearbox which is connected to another gearbox with long, torsionally weak shafts. In this case the simple lumped parameter model does apply. The following calculations in this section are made for this test gearbox.

The masses and moments of inertia of the gears, gear shafts and couplings are connected by massless springs and dampers. The gears are connected by the time variable tooth stiffness. The gear shafts are connected with the gearbox housing by radial and axial bearing stiffnesses. The gear housing is assumed to be rigid.

Fig. 2.10 shows the lumped parameter model of the gearbox interior. For simplicity, the dampers are not shown in the figure. The dynamics of this system can be described as follows:

$$[M]\ddot{x} + [D]\dot{x} + [S(t)]x = \{F\} \quad [N] \quad (2.56)$$

This matrix equation of dimension 15 contains the following matrices:

$$\text{Mass-matrix } [M] = \text{diag}(m_{g1}, m_{g1}, m_{g1}, I_{xg1}, I_{yg1}, J_{g1}, m_{g2}, m_{g2}, m_{g2}, I_{xg2}, I_{yg2}, J_{g2}, J_{c1}, J_{c2}, 0)$$

$$\text{Damping-matrix } [D(i,j)] = 2\eta \sqrt{\frac{[M(i,i)][M(j,j)]}{[M(i,i)]+[M(j,j)]}} \quad |[S(i,j)]|$$

$$\text{Stiffness-matrix } [S(t)] = [S_{\text{tooth}}(t)] + [S_{\text{shafts}}] + [S_{\text{bearing}}]$$

$$\text{Force vector } \{F\}^T = (0, 0, 0, 0, 0, 0, 0, 0, 0, 0, 0, 0, 0, T_{15})$$

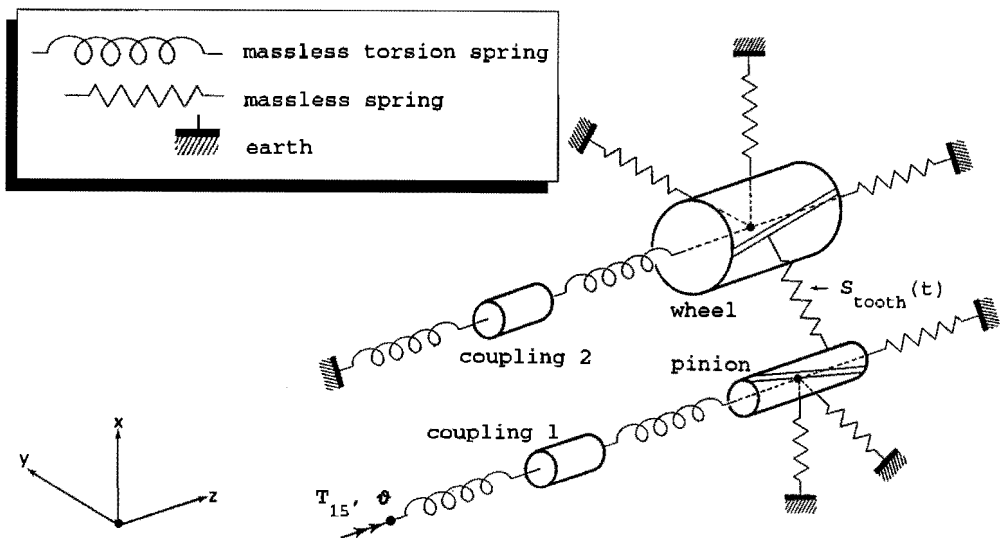


Figure 2.10:
Lumped parameter model of a gearbox.

The elements of the stiffness matrix $[S(t) \cdot B]$ are presented in Appendix C. Degree Of Freedom (DOF) number 15 provides a torsional preload to the system. This preload, which equals the applied torque, is necessary to make the system vibrate by the time variable tooth stiffness $S_{\text{tooth}}(t)$. The 15th DOF consists of an angular displacement ϕ at the far end of shaft number 1, which is calculated at the start of the dynamical calculations and is held constant during the rest of the calculations. This angular displacement has to be calculated in advance to ensure that at this position a prescribed torque T_{15} is present. In the test rig, which will be described in Chapter 5, the torque at position 15 can be varied between 400 and 2000 Nm. For the measurements, the resultant angular displacement ϕ at the test rig is not important, the torque however is what counts. However, this situation is reversed when the dynamical calculations are considered. A prescribed torque will then have to be achieved by an appropriate angular displacement. This is done by using Eq. (2.56) for the situation when all accelerations and velocities are zero, i.e. the static solution.

The time variable tooth stiffness $S_{\text{tooth}}(t)$ is a periodic function. The time of one period T depends on the number of teeth z and the gear running speed n rev/min.

$$T = \frac{60}{n \cdot z} = \frac{1}{f_{\text{tooth}}} \quad [\text{s}] \quad (2.57)$$

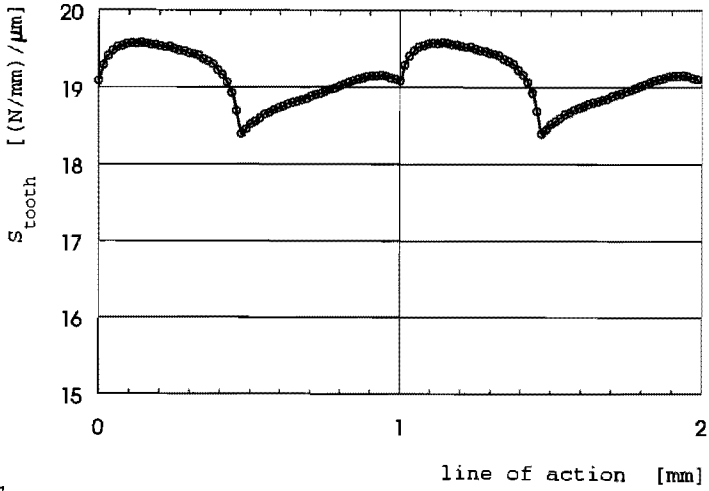


Figure 2.11:
Tooth stiffness of single helical gears.

The high speed gear of the test rig has 24 teeth. The running speed varies from 50 to 1500 rev/min. Thus the period time T becomes respectively 0.05 s and 0.00167 s. The tooth frequency f_{tooth} varies from 20 Hz to 600 Hz. The tooth stiffness $S_{\text{tooth}}(t)$ is obtained from the theory discussed in the previous sections. $S_{\text{tooth}}(t)$ consists of a discrete series S_r with $r = 0, 1, 2, \dots, (N-1)$. In Fig. 2.11 S_r is plotted as dots, the spline through these dots is used as input for the dynamic calculations. This spline can be written as a discrete Fourier transform series X_k :

$$X_k = \frac{1}{N} \sum_{r=0}^{N-1} S_r e^{-j(2\pi kr/N)} \quad k = 0, 1, 2, \dots, (N-1) \quad (2.58)$$

$$X_k = a_k - jb_k \quad (2.59)$$

The time variable tooth stiffness is calculated as follows:

$$S_{\text{tooth}}(t) = \sum_{k=0}^{N-1} X_k e^{j(2\pi kt/T)} \quad (2.60)$$

This procedure guarantees a $S_{\text{tooth}}(t)$ function which can be differentiated at any value of t . Because of this, the differential equations can be solved by using a Runge-Kutta-Merson numerical solution procedure. These numerical procedures are commonly used, and they provide an evenly time spaced solution that can be Fourier transformed by using a FFT routine.

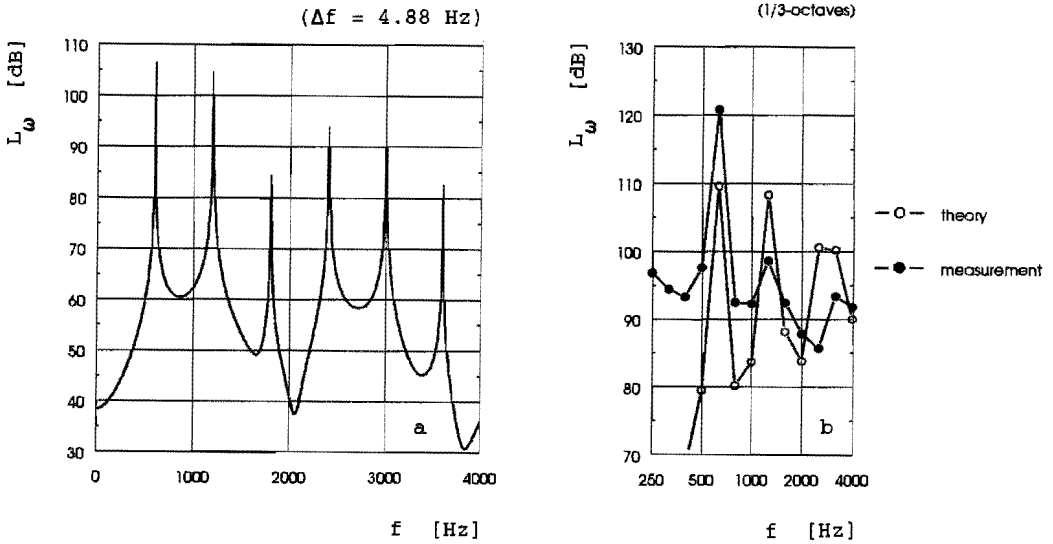


Figure 2.12:

Angular velocity level L_ω of the gear wheel in a narrow-band spectrum (a) and a 1/3-octave band spectrum (b) presentation.

$n = 1500$ rev/min, $T = 2000$ Nm, $f_{\text{tooth}} = 600$ Hz.

As output signal of the dynamic calculations the angular velocity ω of the gear wheel has been chosen, mainly because this velocity is believed to represent the vibration level of the total gearbox interior [2.12]. This angular velocity level of the gear wheel will be measured at the test rig as will be explained in Chapter 5. Comparison between these measurements and the dynamical calculations will be presented in Chapter 5. However, one measurement result is shown in Fig. 2.12-b to verify the dynamical calculations. In this section the theoretical background of the computer program and its results will be emphasized.

The angular velocity level of the gear wheel $L_\omega(f)$ will be presented in the frequency domain. $L_\omega(f)$ is defined as follows:

$$L_\omega(f) = 10 \log \left(\frac{\tilde{\omega}^2(f)}{\omega_0^2} \right) \quad [\text{dB}] \quad (2.61)$$

with $\omega_0 = 5 \cdot 10^{-8}$ rad/s

As result of the periodic tooth stiffness variation, the angular velocity level $L_\omega(f)$ contains high peak levels at the tooth frequency f_{tooth} and its

higher harmonics $2 \cdot f_{\text{tooth}}$, $3 \cdot f_{\text{tooth}}$ et cetera. The actual levels are dependent on the amount of internal damping of the lumped parameter model. Some measurements have been carried out on the test rig to determine the damping loss factor η . It turned out to vary quite a lot between the different resonant frequencies that were investigated. It was decided to take for the calculations an averaged frequency independent damping loss factor of $\eta = 0,1$. This kind of loss factor is also used by other investigators for comparable dynamical calculations.

Fig. 2.12 shows the results of calculations with a frequency resolution of $\Delta f = 2,44$ Hz and with a 1/3-octave band representation. It also shows the measured level of $L_{\omega}(f)$ from which can be seen that the prediction does not completely coincide with the measurement. At the tooth frequency a difference of 12 dB occurs, while at higher frequencies prediction and measurement agree somewhat better.

This phenomenon was observed in all similar calculations for different operational conditions of the gearbox, i.e. for different running speeds and torques.

From this it is clear that the present prediction model which only includes the time variable tooth stiffness does not completely describe the dynamic behaviour of the gearbox interior. The time variable tooth stiffness can not be the only cause of the vibration levels. This confirms the well known fact that the engagement shocks have to be taken into account as well. However, most investigators in the literature incorrectly try to combine these two vibration sources in one model as will be shown in section 2.7. Some investigators use the tooth stiffness model (e.g. /2.1/) and others use the Transmission Error (e.g. /2.4/) as basis for their calculations.

The next section will deal with the implementation of both the time variable tooth stiffness and the engagement shock into the dynamic model. The engagement shock model will be introduced as a new contribution to the modeling of the vibration and sound generating mechanism of gear transmissions.

2.6 Engagement and disengagement shock

The engagement shock occurs due to the bending of the gear teeth. Without any tooth load, geometrically perfect gears rotate smoothly as result of the involute tooth shapes. When a tooth force is applied, the teeth in contact will bend and the teeth that are on the point of coming into

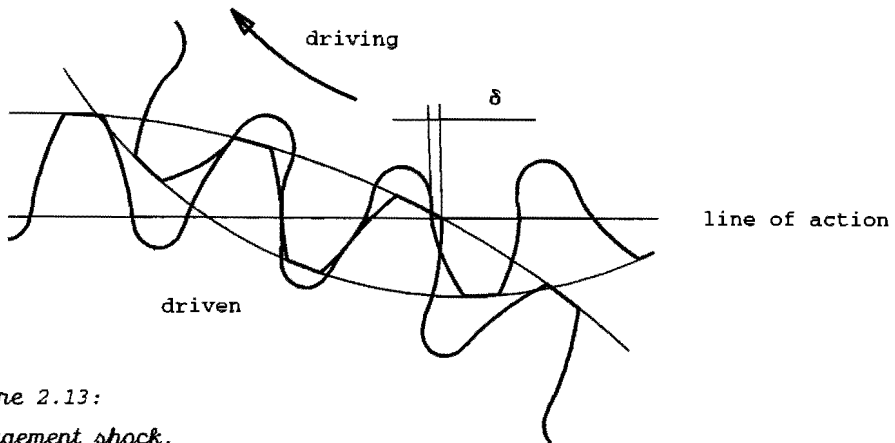


Figure 2.13:
Engagement shock.

contact will do so too early and therefore with a shock. This can be seen in Fig. 2.13 where the teeth come too soon in contact by the amount of δ μm . The tooth that is coming into contact has to deflect by δ almost instantaneously which will produce a shock and resultant vibrations of the gears. At the end of engagement a similar process takes place; the disengagement shock.

The engagement and disengagement shocks will both occur at tooth frequency f_{tooth} . Hence, they will contribute to the vibration level of the gearbox interior especially at f_{tooth} and its higher harmonics. So, these shocks are acting in the same way upon the system as the time variable tooth stiffness. But to describe the shocks mathematically is not straight forward nor known from literature. Therefore a new engagement shock model has to be introduced. This model has to meet certain requirements. It has to be periodical, and it has to depend on the tooth load as well as on the rotational speed of the gears. As will be discussed later on in this chapter, the engagement shock will strongly depend on the chosen profile corrections of the gear and pinion.

Fig. 2.14 shows the teeth in contact between gear and pinion in a schematic way. Every spring in this figure depicts a tooth pair of gear and pinion. The stiffnesses of these springs are all assumed to be equal, in such a way that the total stiffness equals the tooth stiffness $S_{\text{tooth}}(t)$. The distance between the springs equals the distance between the teeth: p_t . The number of teeth in contact is controlled by the total length of contact $\epsilon_{\text{tot}} \cdot p_t$. After $1/f_{\text{tooth}}$ seconds, which is the same as p_t mm in Fig. 2.14, the situation of contact repeats itself. Thus, the requirement for periodic

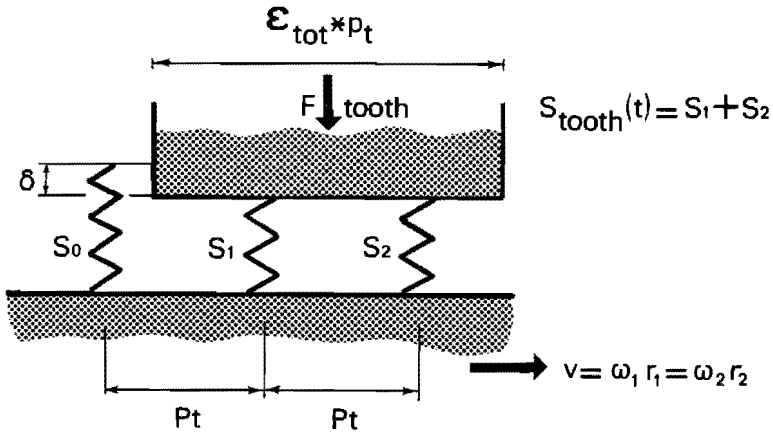


Figure 2.14:
Mathematical model of the engagement shock.

behaviour of the model is satisfied.

The tooth force has its influence on the model by the amount of deflection δ : $\delta = S_{\text{tooth}}(t)/F$. The higher this tooth load will be, the greater the engagement shock is. The dependence on the rotational speed of the gears is controlled by the velocity $v = \omega_1 \cdot r_1$. The engagement shock is implemented in the dynamic model of the gearbox interior by an extra tooth force F_e .

$$F_e = S_{\text{tooth}}(t) \cdot \left(\sum_{i=1}^n \delta_i - \delta_{\text{mean}} \right) / \epsilon_{\text{tot}} \quad [\text{N}] \quad (2.62)$$

with n = number of teeth in contact

This engagement force exists between the teeth of the gears in a direction which is dependent on the transverse pressure angle α'_t and the helix angle at the base circle β_b . The non-zero elements of the force vector $\{F\}$ look like:

$$F(1) = F_e \sin(\alpha'_t) \cos(\beta_b) \quad F(2) = -F_e \cos(\alpha'_t) \cos(\beta_b)$$

$$F(3) = -F_e \sin(\beta_b) \quad F(6) = F_e r_1 \cos(\beta_b)$$

$$F(7) = -F(1), F(8) = -F(2), F(9) = -F(3), F(12) = F(6), F(15) = T_{15}$$

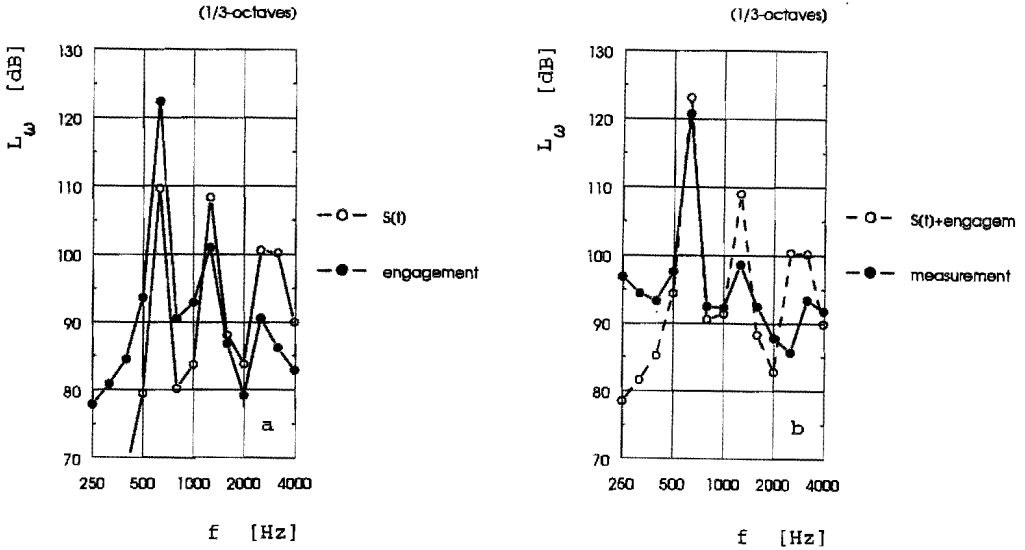


Figure 2.15:

Angular velocity level L_ω of the gear wheel at $n = 1500$ rev/min and with $T_{15} = 2000$ Nm.

The inclusion of these supplementary forces affects the results of the dynamic calculations mainly at tooth frequency f_{tooth} . Fig. 2.15 shows the angular velocity level $L_\omega(f)$ at $n = 1500$ rev/min of the pinion with and without the engagement shock. The calculated angular velocity level with engagement shock is approximating the measured angular velocity level better than without, as is seen when Fig. 2.15-a is compared with Fig. 2.15-b.

From this it can be seen that the engagement shock plays an important role in the dynamic behaviour of the gearbox interior. Time variable tooth stiffness with corresponding tooth deflections as well as the engagement shock have to be taken into account to predict angular velocity levels that will agree with practice. The importance of the separation of the time variable tooth stiffness and the engagement shock in the dynamic calculation model will be further emphasized in the next session when profile corrections are being scrutinized.

2.7 Profile corrections and their influence on L_{ω}

In the previous sections the Transmission Error and the resulting vibration levels at the gears have been characterized by the time variable tooth stiffness and the engagement shocks. In order to be able to reduce the resulting angular velocity level $L_{\omega}(f)$ at the gears, profile corrections are introduced.

In gear technology it is well known that proper profile corrections can have a desirable effect on gearboxes when vibrations and sound pressure levels are concerned. Highly loaded gears of high quality, which are considered in this thesis, are almost without exception provided with some kind of profile correction. Tip and foot relief are well known corrections which can be manufactured on a grinding machine.

The amount of relief is often in the order of a few up to 100 μm . The actual relief is often chosen on basis of experience, but can be calculated by formulas given by Sigg /2.13/. In essence, the amount of correction is optimal when it equals the tooth deflections. This can only be true for one tooth load. When the tooth load varies, due to variable operational conditions of the gearbox, the profile corrections will not be optimal for all conditions. Therefore an optimal profile correction exists only for those situations where the operational conditions stay the same, which form a small percentage of practical applications. However, this does not mean that in all other cases profile corrections are useless. On the contrary, they are very useful because the vibration levels for tooth loads around the optimum load are still smaller than when no corrections are used.

To ameliorate engagement and disengagements shocks, profile corrections have to be added to one or both gears. Normally both gears are being corrected on the tips of the teeth. When the pinion drives the wheel, the tip relief of the wheel ensures that the engagement shock will be weakened and the tip relief of the pinion will do so at the end of engagement. In Fig. 2.16 this is shown in the schematic model of the engagement shock. In practice, both profile corrections of pinion and gear can have different amounts of correction with different correction lengths ℓ_1 and ℓ_2 .

When the amount of correction δ_1 equals the tooth deflection, the tooth pair that comes into contact will do so in a smooth way. The length of correction in combination with the rotational speed of the gears will smoothen the engagement shock even further when they are long respectively slow enough. The same arguments apply for the disengagement shock.

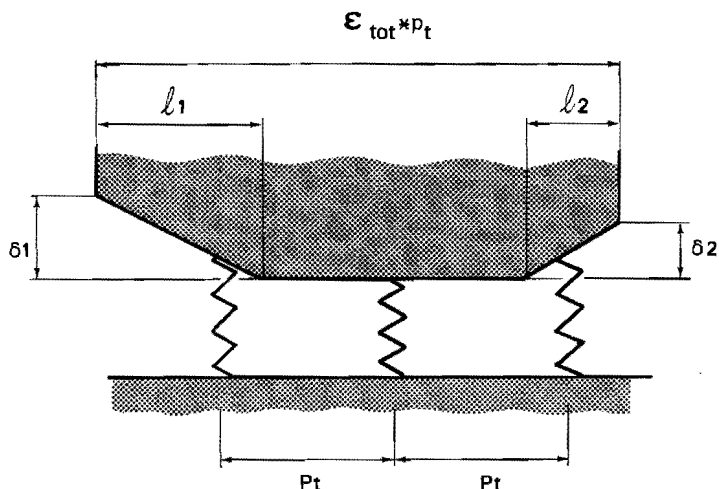


Figure 2.16:
Schematic model of the engagement shock with profile corrections.

Calculations of the time variable tooth stiffness have been performed for a number of profile corrections on the test gears of Chapter 5. These are:

	δ_1	l_1	δ_2	l_2
1. uncorrected	0	0	0	0
2. correction A	31	4,1	13	1,3
3. correction B	40	4,8	15	1,4
4. correction C	18	2,0	0	0
5. correction D	30	5,2	37	6,0
	μm	mm	μm	mm

The gears with the profile corrections A, B, C and D are used for measurements as described in Chapter 5. The uncorrected gears are used as reference and are no part of the measurements since uncorrected gears are not representative when highly loaded precision gears are considered. Correction A has been proposed by 'the gearing industry' and thus is a result of experience of a gear manufacturer. Correction B, C and D have been calculated with the computer program as described in the previous sections of this chapter.

Correction B includes a helical profile correction of the pinion as well as tip relief of both gears. The tip relief of the pinion had to be the same

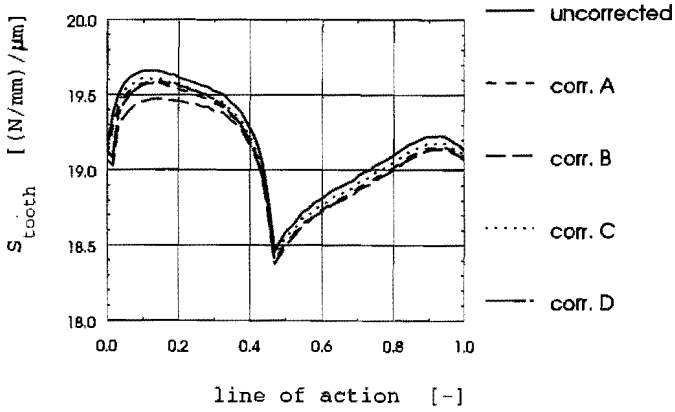


Figure 2.17:
 Calculated tooth stiffnesses for different profile corrections.

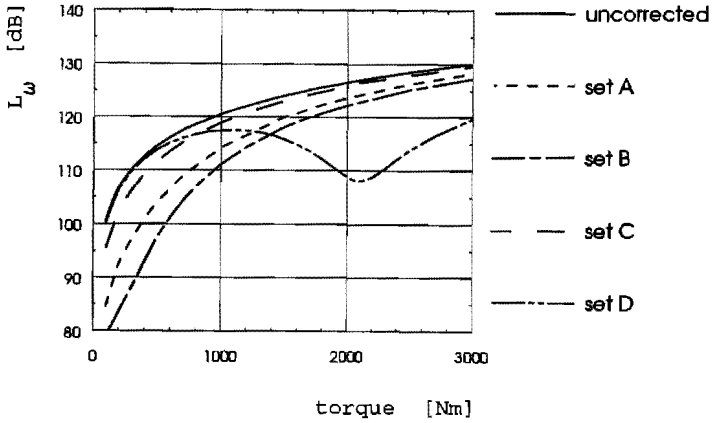


Figure 2.18:
 Calculated angular velocity level L_ω as function of the applied torque at the pinion for different profile corrections ($n = 1500 \text{ rev/min}$).

as the tip relief of the gear namely $40 \mu\text{m}$. But due to manufactural inaccuracies this was not achieved. A too small tip relief was the result. It was not reground because it concerned the disengagement shock which was believed to be of minor importance.

Correction C has only tip relief on the gear wheel. The amount of relief is about half as large as for the other gear pairs. The purpose of this correction is to investigate the influence on vibration and sound of too small a correction.

Correction D is a so called three dimensional profile correction in the shape of triangles on both pinion and gear wheel tooth flanks. This makes it possible to create longer paths of engagement ℓ_1 and ℓ_2 . This would be expected to result in the lowest vibration levels of all gear sets.

With these five different gear sets calculations have been performed with the dynamic model as described before. Fig. 2.17 shows the small differences in tooth stiffnesses that occur for these profile corrections. From this it can be said that profile corrections have a very small influence on the tooth stiffness.

Fig. 2.18 shows the influence of the applied torque on the angular velocity level at the tooth frequency. The uncorrected gear set has the highest level at any torque. This is what one can expect since the engagement shocks will be the greatest for this set. Gear set C shows an angular velocity level that almost equals the curve of the uncorrected set. Because of the very small amount of profile correction on set C, the angular velocity level decreases only a little.

Set A and set B are showing better results due to a proper chosen corrections δ_1 and δ_2 . Set B differs from set A in a positive way, due to an additional profile length correction and somewhat larger corrections. Here it must be stated that according to the computer program, the optimal amount of corrections should be $40 \mu\text{m}$ when a torque of 2000 Nm is being applied at the pinion.

Curve D shows a complete different type of line. At low torques it approximates the uncorrected curve. This is due to the fact that the long correction length in combination with low tooth loads shortens the line of action. This leads to a smaller actual ϵ_{tot} which means that the average number of teeth in contact decreases. As the tooth force stays the same, the tooth deflections will increase and with it the engagement shock.

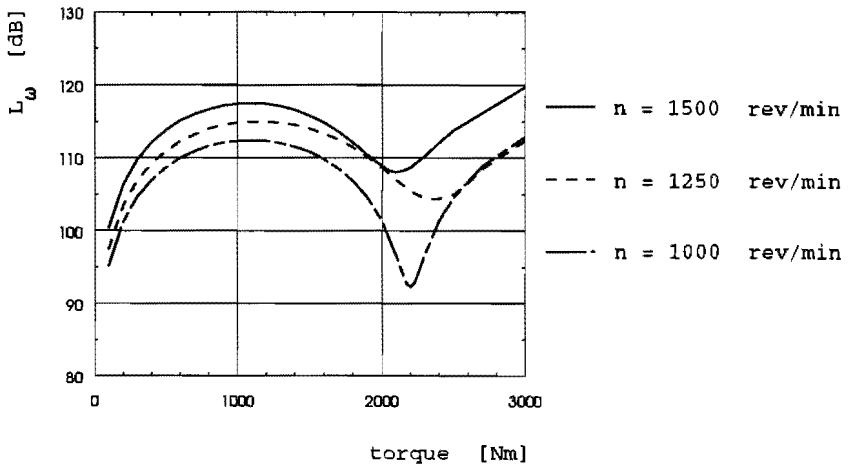


Figure 2.19:

The influence of running speed on the calculated angular velocity level L_{ω} of gear set with 3-Dimensional profile corrections.

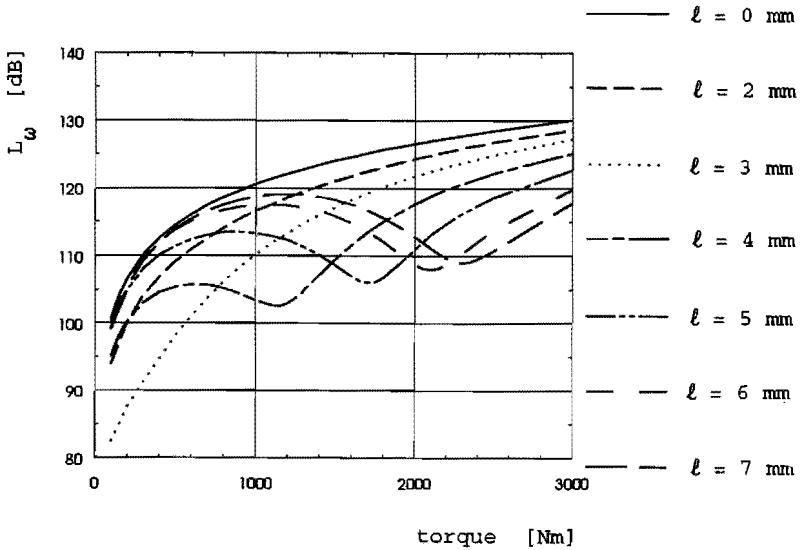


Figure 2.20:

The influence of profile length l on the calculated angular velocity level L_{ω} ($\delta = 40 \mu\text{m}$, $n = 1500 \text{ rev/min}$).

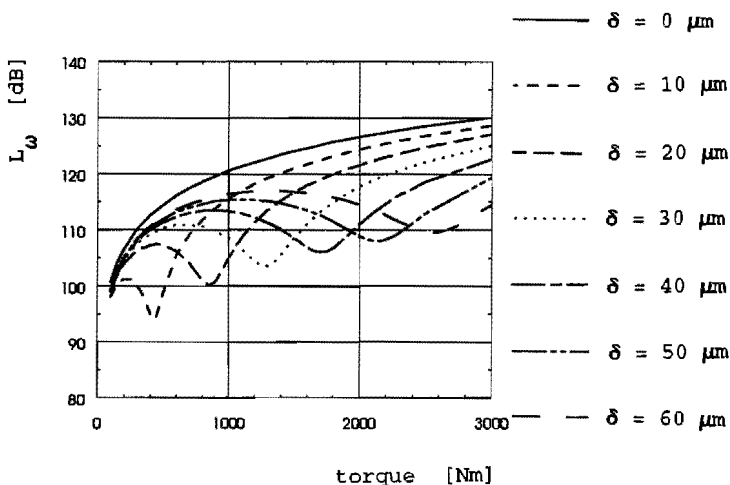


Figure 2.21:

Calculated angular velocity level L_{ω} as function of the amount of correction δ ($l = 5.0$ mm, $n = 1500$ rev/min).

Fig. 2.19 shows the influence of the running speed on the angular velocity level. The level increases with increasing speed for torque loads up to the 'optimum' torque of 2000 Nm. At this torque, the angular velocity level L_{ω} drops considerably as the running speed decreases. This shows the effect of the perfect profile correction for this particular torque load. At higher speeds this effect is less pronounced but the angular velocity level stays low for a large torque area.

The effect of the correction length l of gear set D is shown in Fig. 2.20. The amount of correction is held constant for these calculations at 40 μm , which is about optimal as the tooth deflections are of this magnitude. The uncorrected gears are represented by $l = 0$ and they show the highest levels as would be expected. By increasing l the angular velocity levels decrease considerably. When l reaches 4 mm the curves show the previously mentioned dip at varying torque loads. At low torque loads the angular velocity level approximates the level of the uncorrected gears due to the imperfect meshing of the teeth. When the gears should be operated at a torque load of 2000 Nm, a correction length of 5.5 mm appears to be the best choice. However, when the load will vary between 1000 and 2000 Nm a correction length of 4 or 5 mm should be used.

When the length of correction ℓ is held constant at .5 mm, the influence of the amount of correction δ can be seen from Fig. 2.21. Again, the uncorrected gears ($\delta = 0$) show the highest angular velocity levels for any torque load. Any other δ leads to an angular velocity level optimum at a torque at which the tooth deflections equal the correction. So, when the torque of the gears, i.e. the tooth force, is constant during operation, the amount of correction should be chosen properly to ensure a low angular velocity level of the gears.

2.8 Summary

In this chapter the vibration generation of a gearbox is analyzed. The main cause that makes the gears vibrate is the loaded Transmission Error. This T.E. is caused by the time variable tooth stiffness and the engagement and disengagement shocks. The variable tooth stiffness of spur gears, helical gears and double helical gears can now be calculated as function of the positions of the gears by using a newly developed computer program that is much faster than any of the Finite Element Method programs that are commonly used to achieve the same results. The tooth stiffness is a periodical function of time when the gears rotate at a constant speed. When running, the Transmission Error will excite the gearbox interior, i.e. the gears and shafts. To reduce these vibrations the tooth stiffness variation has to be smoothed as much as possible. This can be done by applying a helix angle to the gear teeth, i.e. increasing the overlap ratio ϵ_{β} . When no helix angle is applied, i.e. spur gears with $\epsilon_{\beta} = 0$, the tooth stiffness will resemble a block function as is shown in this chapter. In contrast, helical gears have the advantage of a smooth take-over of the teeth which results in a much smaller variation of the tooth stiffness. When the overlap ratio $\epsilon_{\beta} \geq 0.8$ the tooth stiffness amplitude is small enough to ensure this favourable effect. In contrast to what is found in the literature, an integer value of ϵ_{β} is not necessarily required.

The engagement and disengagement shocks are a result of the tooth geometry, the tooth load and the elasticity of the gear material. This makes the gear teeth bend under load which leads to an incorrect engagement of the teeth that come into contact. At the end of contact a similar imperfection will occur when the teeth separate.

The engagement and disengagement shocks have been described mathematically in this chapter as part of a computer program for a dynamical model of the

gearbox interior. This computer program predicts angular velocity levels $L_{\omega}(f)$ of the gears. The test gears of chapter 5 are used for illustrative calculations. From this it is predicted that proper profile corrections can decrease the angular velocity level considerably. The amount of correction δ is optimal when it equals the tooth deflections under load. The correction length l over which the correction is applied can be varied as well. When this length reaches a certain value, the angular velocity level shows a minimum at a certain torque load, i.e. tooth force. This enables the gear manufacturer to optimize the gears when the operational conditions are known.

With the help of the available computer programs it is now possible to calculate angular velocity levels $L_{\omega}(f)$ of the gears that will be used as input for further calculations. The angular velocity level of the gears will be used to calculate the velocity level $L_v(f)$ at the surface of the gearbox housing and to calculate the resulting sound power level $L_w(f)$ of the gearbox.

The computational tool developed in this chapter is useful even when quantitative data on other parts of the sound generation scheme of Fig. 2.1 are unknown or prove to be inaccurate. Besides for the calculation of $L_{\omega}(f)$ as a model input it can also be used to obtain optimum profile corrections for a certain tooth load or to calculate the force distribution at the teeth.

3. VIBRATION TRANSFER THROUGH BEARINGS

Gearbox bearings transmit vibrations from the gears to the gearbox housing. The stiffness of the bearing is a main parameter that influences the vibration transmission through the bearing. The bearing damping properties form another parameter that will be assumed negligible for rolling element bearings and will be discussed for fluid film bearings. In this chapter the stiffnesses of rolling element bearings and fluid film bearings are presented. The theory of Lim /3.1/ is used to describe the six dimensional stiffness matrix of ball bearings. As this theory is incorrect for roller bearings, this part is modified so that it now can be applied for these bearings too. Some predictions of this theory are tested using experimental modal analysis on a shaft-bearing test rig.

The stiffness and damping matrices of fluid film bearings will be calculated using numerically derived graphs for determining axial, radial and moment stiffness and damping coefficients. The moment stiffness and damping coefficients are taken from Kikuchi /3.2/ and from Mukherjee and Rao /3.3/.

The moment stiffness coefficients of all type of bearings are of particular interest of this chapter because they are assumed to have a significant influence on the vibration transmission of a gearbox.

3.1 Introduction

In the literature many investigations have been made to calculate the bearing stiffness of rolling element bearings. White /3.4/ describes a method to calculate the radial stiffness of rolling element bearings. He concludes that the bearing stiffness is nonlinear with respect to load or deflection. Especially when the applied load is small, the stiffness is very nonlinear. Here, a slight increase in load will produce a large change in stiffness. At higher loads the effect of nonlinearity is less. When the applied load doesn't change too much, the nonlinear stiffness may be linearised in order to simplify further calculations.

White /3.4/ also states that for a bearing with a relatively small clearance, the number of rolling elements present in the load zone at any instant has an insignificant effect on the bearing stiffness characteristics. Therefore, the bearing stiffness should not be affected by the changing numbers of elements rolling through the load zone during bearing

operation.

Gargiulo /3.5/ presents formulas to approximate radial and axial bearing stiffnesses of different types of bearings. Ophrey /3.6/ measured radial stiffnesses of ball bearings in the frequency domain. He concluded that the radial stiffness of a ball bearing can be calculated accurately with the methods as described in the above mentioned references. Kraus et al. /3.7/ presented a method for the extraction of rolling element bearings characteristics (stiffness and damping) under operating conditions. In essence, they came to the same conclusions and also found very small influence of rotor speed on bearing stiffness. Bearing stiffness varies very little between static and dynamic conditions. Thus it is sufficient, for practical purposes, to use the static stiffness when modeling the vibration transmission properties.

Lim /3.8/ has shown that radial and axial bearing stiffnesses are not sufficient to describe the vibration transmission through bearings correctly. For example, a shaft connected with a bearing perpendicular to a casing plate with a force on the shaft in the plane of the plate, will not be able to cause bending waves in the plate according to the simple mathematical bearing model. However, in practice, the casing plate motion is primarily flexural. Lim introduces moment stiffnesses which can be used for analysis as well as design studies of rotating mechanical systems with multiple shafts and gear pairs or multi-staged rotors. He describes a complete bearing stiffness matrix in six degrees of freedom /3.1/.

Fluid film bearings can be described mathematically in a similar way as rolling element bearings. The stiffness and damping coefficients for plain cylindrical fluid film bearings are widely published in the literature on rotor dynamics, see e.g. /3.9/, /3.10/, /3.11/ and /3.12/. Because of the need to validate these theoretical models of bearings, much work took and takes place on measurement of bearing stiffness and damping. Stiffness coefficients have mostly been measured by the application of static loads only /3.13/, but usually the damping coefficients are required too for rotor dynamic applications. This is also the case when computations for the vibration transmission through fluid film bearings are of interest because the vibration dissipation in fluid film bearings will not be negligible as is assumed here to be the case for rolling element bearings. This necessitates the application of a dynamic load to the bearing in order to measure the damping coefficients /3.14/. The major difficulty encountered in

obtaining accurate experimental results is that the equations needed to process the measured data are ill-conditioned, so that small inaccuracies of measurements can result in substantial differences in the observed values of stiffness and damping.

Nevertheless, radial and axial stiffnesses and damping coefficients can be easily derived from graphs in the references mentioned. In contrast, literature for deriving the moment stiffness and damping coefficients is extremely scarce. Kikuchi /3.2/ and Mukherjee and Rao /3.3/ have created graphs for that purpose, but these are not widely used. Probably moment stiffness and damping coefficients are usually considered to be of negligible influence on rotor dynamic behaviour. However, analysis of vibration transmission through fluid film bearings requires the moment stiffness coefficients and possibly also damping coefficients in order to predict out-of-plane vibrations on a gearbox. In this thesis the graphs of Kikuchi and of Mukherjee and Rao will be used.

3.2 Stiffness matrix of ball bearings

In this section the theory according to Lim /3.1/ will be explained. This theory applies to deep groove ball bearings, angular contact ball bearings and thrust ball bearings. The theory for straight roller bearings and taper roller bearings will be explained in section 3.3.

It is assumed that ball bearings have elliptical contacts between the inner race, rolling elements and outer race when loaded. The bearing stiffness matrix $[K]_{bm}$ can be calculated when the following kinematic and design parameters of the bearing are known. These are the unloaded contact angle α_0 , radial clearance r_L , effective stiffness coefficient K_n for inner ring - single ball - outer ring contacts, angular misalignment, preloads and radius of inner and outer raceway groove curvature centre.

The mean bearing displacements $\{q\}_{bm}^T = (\delta_{xm}, \delta_{ym}, \delta_{zm}, \beta_{xm}, \beta_{ym}, \beta_{zm})$ as shown in Fig. 3.1 are given by the relative rigid body motions between the inner and outer rings. The total bearing displacement vector is given as $\{q\}_b = \{q\}_{bm} + \{q\}_{ba}(t)$ where $\{q\}_{ba}$ is the fluctuation about the mean point $\{q\}_{bm}$ during the steady state rotation. Accordingly one must consider time varying bearing coefficients. However in this analysis, such time varying bearing stiffness coefficients are neglected by assuming very small vibratory motions i.e. $\{q\}_{ba} \ll \{q\}_{bm}$, and high bearing preloads.

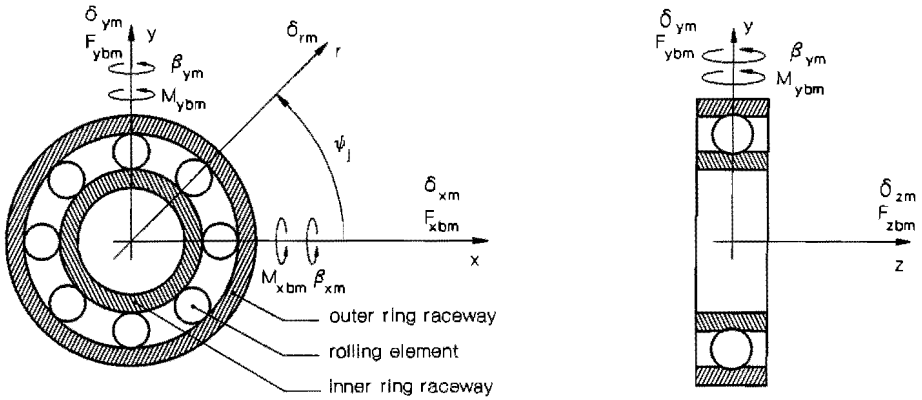


Figure 3.1:
Ball bearing kinematics /3.1/.

Consequently, only the mean bearing preloads and displacements are included in the derivation of $[K]_{bm}$. The basic load-deflection relation for each elastic rolling element is defined by the Hertzian contact stress theory (see for example /3.15/), and the load experienced by each rolling element is described by its relative location in the bearing raceway. Furthermore, it is assumed that the angular position of the rolling elements relative to one another is always maintained due to the rigid cages. Secondary effects such as centrifugal forces and gyroscopic moments (see for example /3.16/) on the bearing are ignored as these effects are evident only at extremely high running speeds. Tribological issues are beyond the scope of this study and hence the analysis assumes bearings to be unlubricated. For this reason the bearing damping properties are assumed to be of the same order as the damping coefficient of the complete structure of which the bearing is a part.

3.2.1 Bearing load-displacement relations

In this section, the relationships between the bearing forces $\{F_{x_{bm}}, F_{y_{bm}}, F_{z_{bm}}\}$ and moments $\{M_{x_{bm}}, M_{y_{bm}}\}$ transmitted through the rolling element bearing, and the bearing displacements $\{q\}_{bm}$ as shown in Fig. 3.1 will be derived. The mean applied loads at the shaft and the bearing preloads generate the mean bearing displacements $\{q\}_{bm}$ and loads $\{f\}_{bm}$. These displacements $\{q\}_{bm}$ are used to derive the resultant elastic deformation $\delta(\psi_j)$ of the j -th rolling element located at angle ψ_j from the x -axis. From the ball bearing kinematics shown in Fig. 3.1 $\delta(\psi_j)$ is

$$\delta(\psi_j) = \begin{cases} A_j - A_0 & , \quad \delta_j > 0 \\ 0 & , \quad \delta_j \leq 0 \end{cases} \quad [\text{m}] \quad (3.1)$$

$$A_j = \sqrt{(\delta_{zj}^*)^2 + (\delta_{rj}^*)^2} \quad [\text{m}] \quad (3.2)$$

$$(\delta_{zj}^*) = A_0 \sin(\alpha_0) + (\delta)_{zj} \quad [\text{m}] \quad (3.3)$$

$$(\delta_{rj}^*) = A_0 \cos(\alpha_0) + (\delta)_{rj} \quad [\text{m}] \quad (3.4)$$

where A_0 and A_j are the unloaded and loaded relative distances between the inner a_i and outer a_o raceway groove curvature centres. Note that $\delta_j \leq 0$ implies that the j -th rolling element is stress free. The effective j -th rolling element displacements in axial $(\delta)_{zj}$ and radial $(\delta)_{rj}$ directions are given in Fig. 3.2 and Eq. (3.5) in terms of the bearing displacements $\{q\}_{bm}$.

$$(\delta)_{zj} = \delta_{zm} + r_j (\beta_{xm} \sin(\psi_j) - \beta_{ym} \cos(\psi_j)) \quad [\text{m}] \quad (3.5)$$

$$(\delta)_{rj} = \delta_{xm} \cos(\psi_j) + \delta_{ym} \sin(\psi_j) - r_L \quad [\text{m}]$$

where r_j is the radial distance of the inner raceway groove curvature centre. Eqs. (3.1) - (3.5) in conjunction with the Hertzian contact stress principle /3.17/ yield the load-deflection relationships for a single rolling element.

$$Q_j = K_n \delta_j^n \quad [\text{N}] \quad (3.6)$$

where Q_j is the resultant normal load on the rolling element, and K_n is the

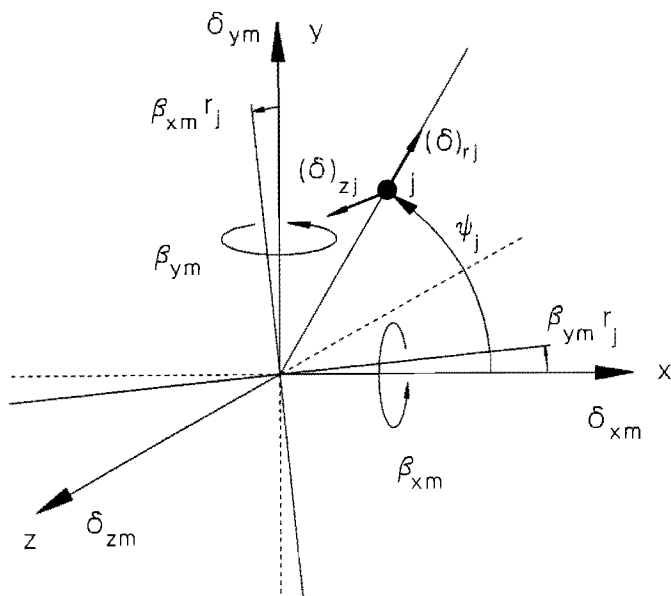


Figure 3.2:

Bearing displacements in the coordinate system /3.1/.

effective stiffness constant for the inner race-rolling element-outer race contacts and it is a function of the bearing geometry and material properties /3.18/. Note that the exponent n is equal to $3/2$ for the ball type with elliptical contacts and $10/9$ for the roller type with rectangular contacts.

The loaded contact angle α_j may alter from the unloaded position α_0 . The sign convention is such that α_j is positive when measured from the bearing x-y plane towards the axial z-axis as shown in Fig. 3.1. For the ball bearing the loaded contact angle α_j is determined by

$$\tan(\alpha_j) = \frac{A_0 \sin(\alpha_0) + (\delta)_{zj}}{A_0 \cos(\alpha_0) + (\delta)_{rj}} \quad (3.7)$$

where $(\delta)_{zj}$ and $(\delta)_{rj}$ are given by Eq. (3.5).

3.2.2 Bearing stiffness matrix $[K]_{bm}$

The proposed bearing stiffness matrix $[K]_{bm}$ is a global representation of the bearing kinematic and elastic characteristics as it combines the effects of z rolling element stiffnesses in parallel given by $\delta_j > 0$.

First, the resultant bearing mean load vector $\{f\}_{bm}$ has to be related to the bearing displacement vector $\{q\}_{bm}$. This can be achieved through vectorial sums $Q_j(\delta_{wm}^*, \beta_{pm}; w = x, y, z \text{ and } p = x, y)$ in Eq. (3.6) for all of the loaded rolling elements which lead to the following bearing forces $\{F_{wbm}\}$ and moments $\{M_{wbm}\}$ as follows

$$\begin{Bmatrix} F_{x_{bm}} \\ F_{y_{bm}} \\ F_{z_{bm}} \end{Bmatrix} = \sum_j^z Q_j \begin{Bmatrix} \cos(\alpha_j) \cos(\psi_j) \\ \cos(\alpha_j) \sin(\psi_j) \\ \sin(\alpha_j) \end{Bmatrix} \quad [N] \quad (3.8)$$

$$\begin{Bmatrix} M_{x_{bm}} \\ M_{y_{bm}} \\ M_{z_{bm}} \end{Bmatrix} = \sum_j^z r_j Q_j \sin(\alpha_j) \begin{Bmatrix} \sin(\psi_j) \\ -\cos(\psi_j) \\ 0 \end{Bmatrix} \quad [Nm]$$

Replacing Q_j by Eq. (3.6) and using $\sin(\alpha_j) = (\delta^*)_{zj}/A_j$ and $\cos(\alpha_j) = (\delta^*)_{rj}/A_j$ as can be seen from Fig. 3.1, yields the following explicit relationship between $\{f\}_{bm}$ and $\{q\}_{bm}$ for ball bearings.

$$\begin{Bmatrix} F_{x_{bm}} \\ F_{y_{bm}} \\ F_{z_{bm}} \end{Bmatrix} = K_n \sum_j^z \frac{(A_j - A_0)^n}{A_j} \begin{Bmatrix} (\delta^*)_{rj} \cos(\psi_j) \\ (\delta^*)_{rj} \sin(\psi_j) \\ (\delta^*)_{zj} \end{Bmatrix} \quad [N] \quad (3.9)$$

$$\begin{Bmatrix} M_{x_{bm}} \\ M_{y_{bm}} \\ M_{z_{bm}} \end{Bmatrix} = K_n \sum_j^z \frac{(A_j - A_0)^n}{A_j} r_j (\delta^*)_{zj} \begin{Bmatrix} \sin(\psi_j) \\ -\cos(\psi_j) \\ 0 \end{Bmatrix} \quad [Nm]$$

Approximate integral forms of Eq. (3.9) are often used instead of the summation forms to eliminate explicit dependence on ψ_j , especially in the case of only one or two degrees of freedom bearings as they are widely used in the literature. The explicit Eq. (3.9) is used to define a symmetric bearing stiffness matrix $[K]_{bm}$ of dimension 6. The index b denotes the bearing and index m denotes the mean displacements, as it is assumed that $\{q\}_{ba} \ll \{q\}_{bm}$.

$$[K]_{bm} = \begin{bmatrix} \frac{\partial F}{\partial \delta_{im}} & \frac{\partial F}{\partial \beta_{im}} \\ \frac{\partial M}{\partial \delta_{im}} & \frac{\partial M}{\partial \beta_{im}} \end{bmatrix} ; \quad w, i = x, y, z \quad (3.10)$$

Here each stiffness coefficient must be evaluated at the mean point $\{q\}_{bm}$. Note that $[K]_{bm}$ is symmetric i.e. $k_{biw} = k_{bwi}$. Explicit expressions for the ball bearing stiffness are presented in Appendix D. All stiffness terms associated with the torsional degree of freedom β_{zm} are zero due to the fact that an ideal bearing allows free rotation about the z-direction. The coefficients k_{biw} are numerically computed after the mean bearing displacement vector $\{q\}_{bm}$ has been calculated. Eq. (3.9) has to be satisfied by $\{q\}_{bm}$. This requires an iterative process, as the equations are nonlinear with respect to displacements. The Newton-Raphson method is chosen for its good convergence characteristic. To implement this method, Eq. (3.8) is rearranged as

$$\begin{Bmatrix} H_1 \\ H_2 \\ H_3 \end{Bmatrix} = \begin{Bmatrix} F_{x_{b_{m}}} \\ F_{y_{b_{m}}} \\ F_{z_{b_{m}}} \end{Bmatrix} - \sum_j^z Q_j \begin{Bmatrix} \cos(\alpha_j) \cos(\psi_j) \\ \cos(\alpha_j) \sin(\psi_j) \\ \sin(\alpha_j) \end{Bmatrix} = \begin{Bmatrix} 0 \\ 0 \\ 0 \end{Bmatrix} \quad (3.11)$$

$$\begin{Bmatrix} H_4 \\ H_5 \end{Bmatrix} = \begin{Bmatrix} M_{x_{b_{m}}} \\ M_{y_{b_{m}}} \end{Bmatrix} - \sum_j^z r_j Q_j \sin(\alpha_j) \begin{Bmatrix} \sin(\psi_j) \\ -\cos(\psi_j) \end{Bmatrix} = \begin{Bmatrix} 0 \\ 0 \end{Bmatrix}$$

where $\{H_k\}$ are functions defined for computational reasons. Using Taylor's series, any function H_k in Eq. (3.11) can be expanded about the solution vector $X = \{q\}_{bm}$ as follows by neglecting second and higher order terms.

$$H_k(X + \delta X) \approx H_k(X) + \sum_j^5 \frac{\partial H_k}{\partial X_j} \delta X_j ; \quad k = 1, 2, 3, 4, 5 \quad (3.12)$$

The solution for the incremental vector δX can be obtained by setting $H_k(X + \delta X) = 0$ in Eqs. (3.11) and (3.12) which yields a set of linear algebraic equations. This vector δX is added to the previously computed vector X given by $H_k(X) = 0$ for the next iteration until the convergence criterion, say that δX is within a specified tolerance, is satisfied.

The numerical scheme starts with a guess for the bearing displacement vector $\{q\}_{bm}$ and a given load vector $\{f\}_{bm}$. Usually, only a few iteration steps are required to satisfy the specified tolerance when the guessed bearing displacement vector $\{q\}_{bm}$ is good enough. For this purpose the Newton-Raphson method for nonlinear systems of equations can be used (/3.19/).

3.3 Stiffness matrix of roller bearings

Roller bearings can be divided into two groups, straight roller bearings and tapered roller bearings. However, the first group is a special case of the more general group of tapered roller bearings. As is shown in Fig. 3.3 the contact angle α_0 can vary between zero and 90 degrees. Straight roller bearings have a contact angle $\alpha_0 = 0$ or $\alpha_0 = 90$ degrees. From this point on, both groups of roller bearings are being referred to as roller bearings.

3.3.1 Stiffness matrix according to Lim /3.1/

It is assumed that roller bearings have rectangular contacts between the inner race, rolling elements and outer race when loaded and that the loaded contact angle α_j remains relatively constant; $\alpha_j \cong \alpha_0$. Furthermore, the same assumptions are made as was done for the ball bearings in section 3.2. The relationships between the bearing forces ($F_{x_{bm}}$, $F_{y_{bm}}$, $F_{z_{bm}}$) and moments

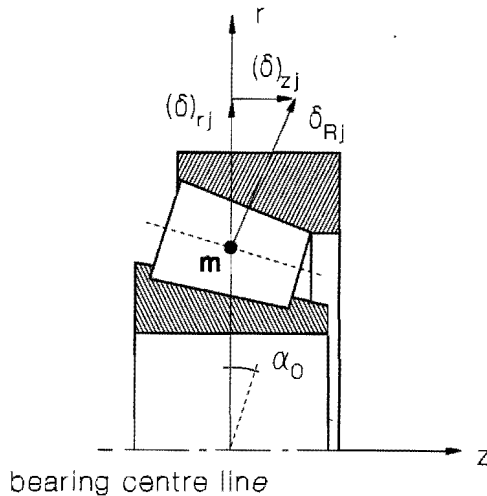


Figure 3.3:
Roller bearing kinematics /3.1/.

$(M_{x_{bm}}, M_{y_{bm}})$ transmitted through the roller bearing, and the bearing displacements $(q)_{bm}$ are derived in a similar fashion as was done in section 3.2. The displacements $(q)_{bm}$ are used to derive the resultant elastic deformation $\delta(\psi_j)$ of the j -th rolling element located at angle ψ_j from the x -axis. From the roller bearing kinematics shown in Fig. 3.3 $\delta(\psi_j)$ is:

$$\delta(\psi_j) = \begin{cases} (\delta)_{rj} \cos(\alpha_0) + (\delta)_{zj} \sin(\alpha_0) & , \delta_j > 0 \\ 0 & , \delta_j \leq 0 \end{cases} \quad (3.13)$$

The effective j -th rolling element displacements in the axial $(\delta)_{zj}$ and radial $(\delta)_{rj}$ directions are given in Fig. 3.2 in terms of the bearing displacements $(q)_{bm}$.

$$(\delta)_{zj} = \delta_{z_m} + r_j (\beta_{x_m} \sin(\psi_j) - \beta_{y_m} \cos(\psi_j)) \quad [m] \quad (3.5)$$

$$(\delta)_{rj} = \delta_{x_m} \cos(\psi_j) + \delta_{y_m} \sin(\psi_j) - r_L \quad [m]$$

where r_j is the pitch bearing radius of the roller bearing. Also, the Hertzian contact stress principle, Eq. (3.6), is used for each rolling element. The resultant bearing mean load vector $(f)_{bm}$ and the bearing displacement vector $(q)_{bm}$ are related to one another through vectorial sums $Q_j(\delta_{w_m}, \beta_{p_m}; w = x, y, z \text{ and } p = x, y)$ for all the rolling elements. This leads to the same bearing moments $(M_{w_{bm}})$ and forces $(F_{w_{bm}})$ as for ball bearings (Eq. (3.8)). This yields the following explicit relationship between $(f)_{bm}$ and $(q)_{bm}$ for roller bearings:

$$\begin{Bmatrix} F_{x_{bm}} \\ F_{y_{bm}} \\ F_{z_{bm}} \end{Bmatrix} = K_n \sum_j^z \{ (\delta)_{rj} \cos(\alpha_0) + (\delta)_{zj} \sin(\alpha_0) \}^n \begin{Bmatrix} \cos(\alpha_0) \cos(\psi_j) \\ \cos(\alpha_0) \sin(\psi_j) \\ \sin(\alpha_0) \end{Bmatrix} \quad (3.14)$$

$$\begin{Bmatrix} M_{x_{bm}} \\ M_{y_{bm}} \\ M_{z_{bm}} \end{Bmatrix} = K_n \sin(\alpha_0) \sum_j^z r_j \{ (\delta)_{rj} \cos(\alpha_0) + (\delta)_{zj} \sin(\alpha_0) \}^n \begin{Bmatrix} \sin(\psi_j) \\ -\cos(\psi_j) \\ 0 \end{Bmatrix}$$

where $(\delta)_{rj}$ and $(\delta)_{zj}$ are functions of $\{\delta_{w_m}, \beta_{p_m}\}$ as defined by Eq. (3.5) and the exponent n is equal to 10/9. The explicit Eq. (3.14) is used to define the symmetric bearing stiffness matrix $[K]_{bm}$ of dimension 6 in an analog way to the ball bearing of section 3.2. Explicit expressions for the

roller bearing stiffness matrix elements are presented in Appendix D.

3.3.2 Improvement on Lim's theory

The theory for roller bearings was derived in a similar way as for ball bearings. This is not completely correct. The load-deflection relationship (3.6) for a single rolling element is only valid when the resultant normal load Q_j on the rolling element is taken into consideration. Ball bearings have point contacts between inner race, ball and outer race which remain point contacts when loaded. Even when the actual positions of point contact move as a result of changing loaded contact angle α_j .

Roller bearings have line contact between inner race, roller and outer race. The load distribution along the line of contact does not have to be uniform as is assumed when using Eq. (3.6). Under the assumption that each rolling element has a uniform load distribution, the elements do not have any resistance against tilting. This can be shown by looking at a straight roller bearing with contact angle $\alpha_0 = 0$ degrees. For this bearing Lim's theory produces a stiffness matrix in which the majority of the stiffness elements is equal to zero. Only k_{bxx} , k_{bxy} and k_{byy} are nonzero. This would suggest that the straight roller bearing can freely rotate around all three axes, which is not the case.

The moment stiffnesses around the x and y-axis are of great importance to the vibration transmission through roller and tapered bearings. Therefore, the theory has to be altered by introducing a line contact over the rolling elements with non-uniform load distributions. This will result in a (more complex) new formulation of the load-deflection relationship (3.6).

The assumptions made are first of all that the rolling elements are cylindrical which is not completely true when tapered roller bearings are taken into account. The inner and outer ring are supposed to be rigid when displacements along the roller are calculated. This means that the cylindrical roller elements will become tapered when submitted to bearing displacements $\{q\}_{bm}$.

Fig. 3.4 introduces the coordinate a along the line of contact of a rolling element. Each element of a roller bearing has length l . The coordinate a is defined between $-l/2$ and $+l/2$. The centre of the unloaded roller element m coincides with $a = 0$. The unloaded centre line lies under the pressure angle α_0 and will rotate over $\gamma/2$ when loaded, where

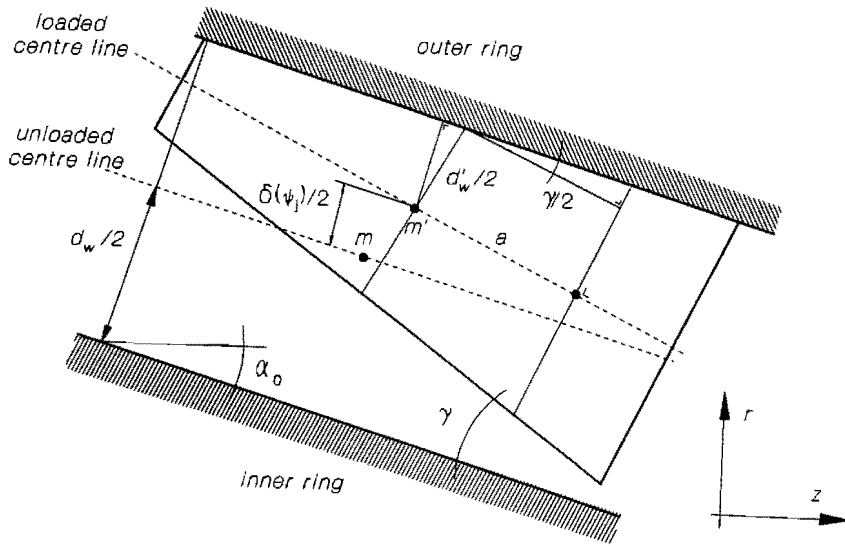


Figure 3.4:
Kinematics of a roller element.

$$\gamma = \beta_{xm} \sin(\psi_j) - \beta_{ym} \cos(\psi_j) \quad [\text{rad}] \quad (3.15)$$

is the angle over which the inner ring rotates while the outer ring stands still, as can be seen from Eq. (3.5). The centre m of the loaded element has moved to m' according to Eq. (3.13) over a distance $\delta(\psi_j)$ in a direction perpendicular to the unloaded centre line. At a distance a from m' the roller element will have moved $\delta(\psi_j, a)$ perpendicular to the loaded centre line. This is the displacement we are looking for.

From Fig. 3.4 it follows:

$$\delta(\psi_j, a) = \frac{\delta(\psi_j) - a \cdot \sin(\gamma/2)}{\cos(\gamma/2)} \quad [\text{m}] \quad (3.16)$$

where $\delta(\psi_j)$ can be obtain by Eqs. (3.13) and (3.5).

The force distribution which satisfies $\delta(\psi_j, a)$ can be calculated by introducing the force-displacement formula which is also used in Chapter 2 to obtain the Hertzian displacements on gear teeth.

$$\delta = \frac{2F(1-\nu^2)}{\pi E(\theta \ell)} \ln \left\{ \frac{t_1 t_2 \pi E(\theta \ell)}{2\rho_v(1-\nu^2)F} - \frac{\nu}{(1-\nu^2)} \right\} \quad [\text{m}] \quad (3.17)$$

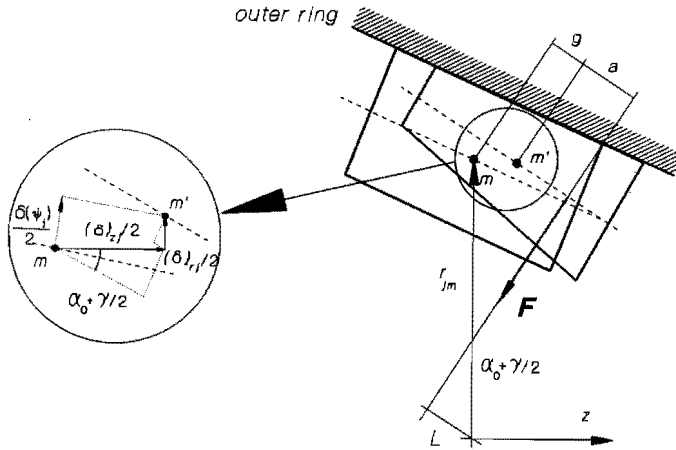


Figure 3.5:

Force and moment on the bearing due to the partial load F .

where θl is the length of the rolling element that belongs to position a and F is the force at this position; $F(\psi_j, a)$. As t_1 and t_2 were set to halve the tooth width in Chapter 2, they are set to halve the roller diameter here. From Eq. (3.17) it is obvious that, with given displacements, the force F has to be calculated iteratively. For this purpose the Newton-Raphson method is used.

In this way, from a mean displacement vector $(q)_{bm}$, the force distribution over all rolling elements can be calculated. These force distributions are correct when the total forces and moments on the complete bearing are (almost) the same as the given load vector $\{f\}_{bm}$. For this purpose the forces and moments on the bearing have to be calculated for each force $F(\psi_j, a)$.

Fig. 3.5 shows the force F at position a of element j . This force acts upon the bearing centre and can be rewritten as F_x , F_y , M_x and M_y . For the calculation of the moments M_x and M_y the length L of Fig. 3.5 has to be known. From this Figure it follows:

$$L = (r_{jm} + (\delta)_{zj}/2) \sin(\alpha_0 + \gamma/2) - g - a \quad [\text{m}] \quad (3.18)$$

or:

$$L = (r_{jm} + (\delta)_{zj}/2) \sin(\alpha_0 + \gamma/2) - (\delta)_{zj}/2 \cos(\alpha_0 + \gamma/2) - a \quad [\text{m}] \quad (3.19)$$

Now all ingredients are known to calculate the total resulting forces and moments which act upon the bearing centre. For this purpose a summation has to be made over all rolling elements and all positions α along the contact of each rolling element. The stiffness coefficients of roller bearings can be calculated in the same manner as is done for the ball bearings, namely by changing the mean displacement vector $\{q\}_{qbm}$ a little so that $\partial F_1 / \partial \delta_1$ can be calculated as Eq. (3.10) shows in the case of ball bearings.

3.4 Experimental verification of a calculated stiffness matrix

Experiments have been carried out to obtain the elements of the stiffness matrix of a rolling element bearing. For this purpose an experimental setup was made as is shown in Fig. 3.6. This setup consisted of a shaft with one ball bearing of which the outer race was connected to a rigid housing. The bearing preloads were applied at three points of the shaft by the use of long (thus relatively low stiffness) piano strings which were lead over pulley-blocks. The force was applied at the ends of the strings with different masses. In this way any given load vector $\{f\}_{bm}$ could be applied to the bearing.

The shaft and the bearing can be modeled as a one-mass-spring system with

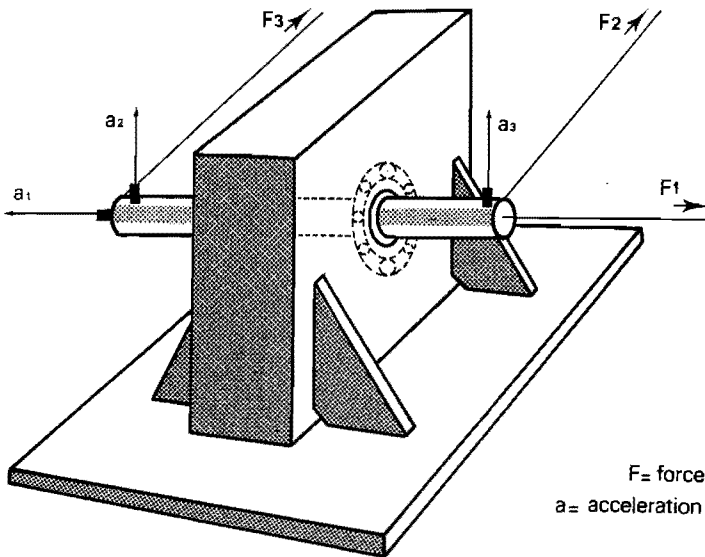


Figure 3.6:

Experimental setup for the determination of the stiffness matrix of a rolling element bearing.

five degrees of freedom. The rotational stiffness around the shaft axis is assumed to be zero. The stiffness matrix can be calculated when all transfer functions are measured. Each transfer function describes the relationship between a displacement or rotation of a certain degree of freedom and an applied force spectrum at another degree of freedom. This results in a 5x5 matrix of transfer functions which all have to be measured.

The calculation of the stiffness matrix out of these measured transfer functions is based upon the equation of motion of the shaft-spring system:

$$\underline{M} \ddot{q} + \underline{B} \dot{q} + \underline{K} q = u \quad (3.20)$$

The diagonal mass matrix \underline{M} contains the mass m and the moment of inertia I of the shaft:

$$\underline{M} = \text{diag.}\{m, m, m, I, I\} \quad (3.21)$$

The damping matrix \underline{B} contains the damping coefficients which will be assumed unknown just like the stiffness coefficients of the stiffness matrix \underline{K} . The displacement vector $q^T = \{x, y, z, \beta_x, \beta_y\}$ and the force vector u will be measured. The transfer function matrix \underline{H} is defined as the matrix containing all transfer functions $H = q/u$ and can be expressed as follows:

$$\underline{H} = [-\omega^2 \underline{M} + j\omega \underline{B} + \underline{K}]^{-1} \quad (3.22)$$

When the inverse of this theoretical transfer matrix is multiplied with the experimental transfer matrix \underline{H}^e one should get the unity matrix \underline{I} as an answer. However, the experimental transfer matrix will contain errors so that the result of the multiplication will be:

$$\underline{H}^e \cdot [-\omega^2 \underline{M} + j\omega \underline{B} + \underline{K}] = \underline{I} + \underline{S} \quad (3.23)$$

where \underline{S} is a matrix containing the errors. The matrices \underline{K} and \underline{B} will have to satisfy this relationship with a matrix \underline{S} which has to be as small as possible. This problem will be solved by using a minimization scheme based upon the least squares method. For this purpose Eq. (3.23) is divided into a real and imaginary part:

$$\left[\begin{array}{cc} \underline{H}_{Re}^e & + j \underline{H}_{Im}^e \end{array} \right] \cdot \left[-\omega^2 \underline{M} + j\omega \underline{B} + \underline{K} \right] = \underline{I} + \underline{S}_{Re} + j \underline{S}_{Im} \quad (3.24)$$

This can be written as:

$$\left[\begin{array}{cc} \underline{H}_{Re}^e & -\omega \underline{H}_{Im}^e \\ \underline{H}_{Im}^e & \omega \underline{H}_{Re}^e \end{array} \right] \cdot \left[\begin{array}{c} \underline{K} \\ \underline{B} \end{array} \right] = \left[\begin{array}{c} \underline{I} + \underline{S}_{Re} + \omega^2 \underline{H}_{Re}^e \underline{M} \\ \underline{S}_{Im} + \omega^2 \underline{H}_{Im}^e \underline{M} \end{array} \right] \quad (3.25)$$

$$\text{or: } (\underline{A} \underline{X} - \underline{E}) = \underline{R} \quad (3.26)$$

$$\text{with: } \underline{A} = \left[\begin{array}{cc} \underline{H}_{Re}^e & -\omega \underline{H}_{Im}^e \\ \underline{H}_{Im}^e & \omega \underline{H}_{Re}^e \end{array} \right], \quad \underline{X} = \left[\begin{array}{c} \underline{K} \\ \underline{B} \end{array} \right],$$

$$\underline{E} = \left[\begin{array}{c} \underline{I} + \omega^2 \underline{H}_{Re}^e \underline{M} \\ \omega^2 \underline{H}_{Im}^e \underline{M} \end{array} \right] \quad \text{and} \quad \underline{R} = \left[\begin{array}{c} \underline{S}_{Re} \\ \underline{S}_{Im} \end{array} \right]$$

The unknown matrix \underline{X} has to be calculated by minimizing the following expression:

$$\underline{R}^T \underline{R} = (\underline{A} \underline{X} - \underline{E})^T \cdot (\underline{A} \underline{X} - \underline{E}) \quad (3.27)$$

which results in:

$$(\underline{A}^T \underline{A}) \cdot \underline{X} = \underline{A}^T \underline{E} \quad (3.28)$$

This expression must be valid for every spectral line of the transfer matrix. By summing Eq. (3.28) over all angular frequencies ω it follows:

$$\left\{ \sum_{\omega} (\underline{A}^T \underline{A}) \right\} \cdot \underline{X} = \sum_{\omega} (\underline{A}^T \underline{E}) \quad (3.29)$$

$$\text{or: } \underline{A}_{tot} \underline{X} = \underline{R}_{tot} \quad (3.30)$$

so that the stiffness matrix and the damping matrix can be found as follows:

$$\left[\begin{array}{c} \underline{K} \\ \underline{B} \end{array} \right] = \underline{X} = \underline{A}_{tot}^{-1} \underline{R}_{tot} \quad (3.31)$$

These experimental matrices are most likely not symmetric matrices which of course they should be. The matrices are made symmetric by putting the mean values of the coefficients k_{ij} and k_{ji} (b_{ij} and b_{ji}) at their places in the matrices. In this way an experimental stiffness matrix \underline{K}^e will be obtained which can be compared with the analytical stiffness matrix.

Measurements were carried out to obtain the 25 frequency response functions of the experimental transfer matrix \underline{H}^e . The frequency range of interest was from 0 Hz to 2500 Hz which contained spectral lines with $\Delta f = 2.9$ Hz. For the estimation of the stiffness matrix \underline{K}^e not all spectral lines were taken into account. Only those spectral lines which were located at peaks of \underline{H}^e were used because the other spectral lines are of relatively minor importance to the summation of Eq. (3.29). Nevertheless, a satisfying result of the calculations of the stiffness and damping matrices could not be obtained with the method described. Possibly the least squares method needs further improvement or has to be replaced by a better method.

However, the measured frequency response functions provided five natural frequencies of the shaft-bearing test rig. The natural frequencies that belong to the rotational eigenmodes were 145 Hz and 132 Hz for the rotations around the x-axis and y-axis respectively. The equation of motion (3.20) with the calculated bearing stiffness matrix resulted in natural frequencies for these directions of 152 Hz and 120 Hz respectively. This gives a strong indication that the proposed theoretical model predicts the moment stiffness coefficients, which are diagonal elements in the stiffness matrix, sufficiently accurate. Therefore, it is judged that the use of the theoretical model for the prediction of the six-dimensional bearing stiffness matrix in Chapters 4 and 5 is justified. For the time being it can only be concluded that the experimental identification method of the bearing stiffness matrix is not yet complete and needs further refinement.

3.5 Stiffness and damping matrices of fluid film bearings

The stiffness and damping matrices of radial fluid film bearings has been subject to investigations all over the world. Especially the radial stiffness matrix with four stiffness elements (k_{xx} , k_{xy} , k_{yx} and k_{yy}) has been widely published (/3.9/, /3.10/, /3.11/, /3.12/ and /3.20/). They deduced the oil-film forces from the basic Reynolds equation in order to get the linearised stiffness coefficients. This is done under the assumptions that the bearings are sufficiently short to ignore one term of the Reynolds

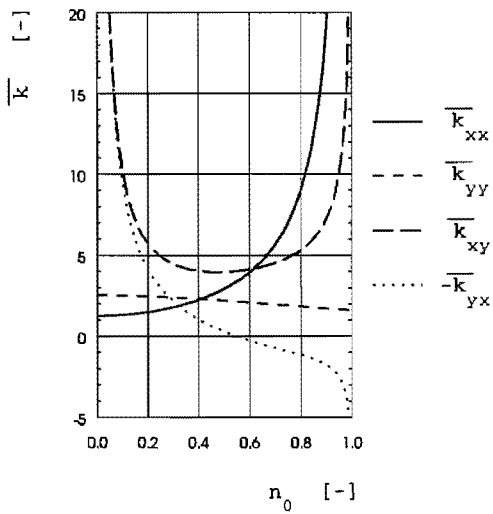


Figure 3.7:
Stiffness coefficients of
fluid film bearings.

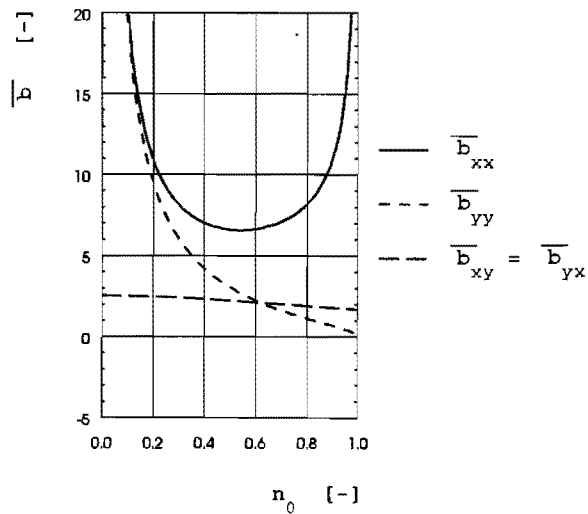


Figure 3.8:
Damping coefficients of fluid film
bearings.

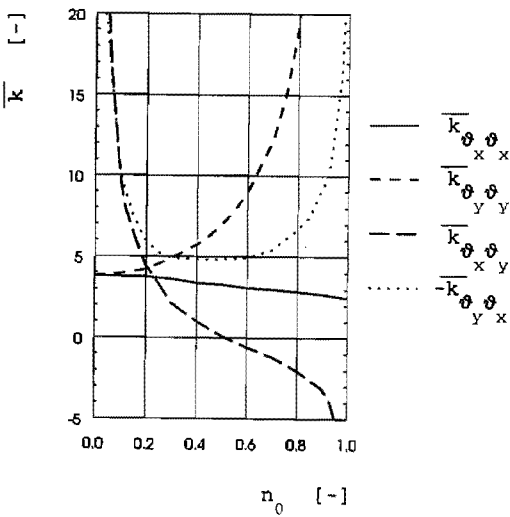


Figure 3.9:
Moment stiffness coefficients of
fluid film bearings.

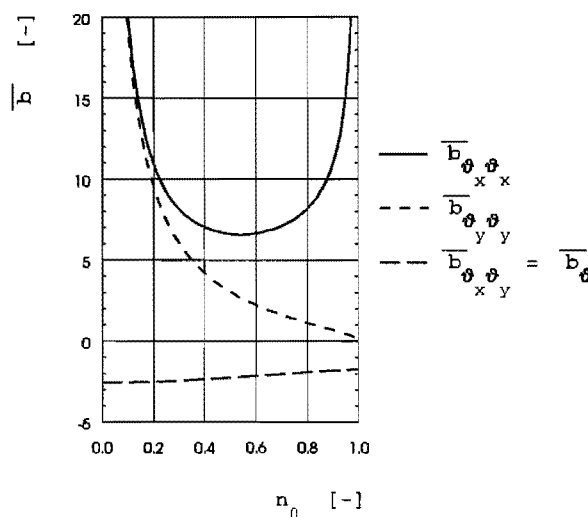


Figure 3.10:
Moment damping coefficients of
fluid film bearings.

equation. Also, it is assumed that there is no pressurized oil supply to the bearings and that the viscosity is constant throughout the lubricant film. The results are conveniently represented in graphs with dimensionless parameters as function of the static eccentricity ratio e_0 . Figs. 3.7 and 3.8 give examples from /3.9/.

In Figs. 3.7 and 3.8 the dimensionless stiffness coefficients \overline{k}_{ij} and the dimensionless damping coefficients \overline{b}_{ij} are presented. They are made dimensionless by multiplying the stiffness coefficients k_{ij} by C/F and the damping coefficients b_{ij} by $\omega C/F$. Where C is the bearing clearance, ω is the angular velocity of the shaft and F is the radial force on the fluid film bearing in the x-direction.

The radial and axial stiffnesses and damping coefficients of fluid film bearings can be easily derived from these figures. However, as said before, literature for deriving the moment stiffness and damping coefficients is extremely scarce. Fig. 3.9 shows the graphs for the moment stiffness coefficients of fluid film bearings according to Kikuchi /3.2/. Here the coefficients are made dimensionless by multiplying the moment stiffness coefficients $k_{\phi_i \phi_j}$ by $60C/(FL^2)$ and the damping coefficients $b_{\phi_i \phi_j}$ by $60\omega C/(FL^2)$. In the publication of Mukherjee and Rao /3.3/ these coefficients were made dimensionless by using the factors $C/(FLD)$ and $\omega C/(FLD)$ respectively, where D is the diameter of the bearing. Since the graphs of Kikuchi are based upon a bearing with $D/L = 40/24$, this means that the graphs of Kikuchi have exactly 100 times higher stiffness and damping coefficients. Nevertheless, when for this factor is corrected both investigators come to the same results.

The Figs. 3.7 through 3.10 were used to obtain the stiffness and damping coefficients of the fluid bearings which were used in the test rig of Chapter 5 of this thesis. The fluid film bearings were only used for the double helical gear set and had the following proportions:

	pinion	wheel	
D	80.250	95.200	mm
L	56	70	mm
Δr	125	100	μm
n	1500	500	rev/min
$\omega=2\pi n/60$	157.1	52.4	rad/s
F	20763	20763	N
$\eta(60^\circ\text{C})$	0.049	0.049	Nsm^{-2}
h_0	22	17	μm
$e=\Delta r-h_0$	103	83	μm
$n_0=e/\Delta r$	0.82	0.83	-

With resulting stiffness matrices:

$$K_{\text{pinion}} \cong K_{\text{wheel}} = \frac{F}{C} \cdot \begin{bmatrix} 0.11 & 0.06 & 0 & 0 & 0 & 0 \\ 0.01 & 0.02 & 0 & 0 & 0 & 0 \\ 0 & 0 & 0 & 0 & 0 & 0 \\ 0 & 0 & 0 & 0.03 \cdot LD & -0.02 \cdot LD & 0 \\ 0 & 0 & 0 & -0.02 \cdot LD & 0.22 \cdot LD & 0 \\ 0 & 0 & 0 & 0 & 0 & 0 \end{bmatrix}$$

and damping matrices:

$$B_{\text{pinion}} \cong B_{\text{wheel}} = \frac{F}{\omega C} \cdot \begin{bmatrix} 0.09 & 0.02 & 0 & 0 & 0 & 0 \\ 0.02 & 0.01 & 0 & 0 & 0 & 0 \\ 0 & 0 & 0 & 0 & 0 & 0 \\ 0 & 0 & 0 & 0.09 \cdot LD & -0.02 \cdot LD & 0 \\ 0 & 0 & 0 & -0.02 \cdot LD & 0.01 \cdot LD & 0 \\ 0 & 0 & 0 & 0 & 0 & 0 \end{bmatrix}$$

Note:

In Chapter 5 only the stiffness matrices will be implemented in a Finite Element Method model of the test gearbox with the double helical gears. The damping matrices can not be implemented in the finite element analysis which uses the modal analysis approach in the frequency domain. Because this approach was used in the FEM analysis of Chapters 4 and 5, the damping matrices have not been incorporated. However, experiments on the transmission of structure-borne sound via fluid film bearings have shown that they may dissipate more vibration power than that they transmit for excitation by a shaft in bending, see /3.21/. Therefore, this approach may appear to be not appropriate when fluid film bearings have to be modeled.

The differences in vibration transmission through bearings will be investigated in Chapter 5 by replacing the fluid film bearings by roller bearings. This will be done in the FEM calculations and will be investigated experimentally as well. However, the FEM calculations could only be performed when symmetrical matrices were used for numerical reasons. The stiffness matrices of the fluid film bearings are not symmetrical ($k_{xy} \neq k_{yx}$) and therefore they had to be made symmetrical in order to use them in FEM calculations. This is done by taking the mean value of k_{xy} and k_{yx} in these matrices. Together with the not included damping matrices in the FEM model it might seem useless to perform these calculations. However, they will be performed because it represents the present-day state of the art.

3.6 Summary

The stiffness matrix of a rolling element bearing can be calculated with the theory presented in this chapter. The stiffness matrix contains not only radial and axial stiffness coefficients but also has moment stiffness coefficients. Generally speaking, until very recently, in the literature these moment stiffness coefficients are not used when dynamical calculations are performed on rotor-bearing structures. However, these moment stiffness coefficients have to be considered to be of great importance when vibration transmission to housings is of interest.

The theory of this chapter makes it possible to calculate the complete stiffness matrix of rolling element bearings such as ball bearings, angular contact bearings, roller bearings and tapered roller bearings. The calculation method of Lim /3.1/ is used for this purpose. However, it has been improved for the cases of roller bearings and of tapered roller bearings.

The stiffness matrix of a ball bearing has been calculated as an example of this calculation method and has been partially verified experimentally. The predicted rotational natural frequencies of a shaft-bearing test rig proved to be in very good agreement with the measurements. Therefore, it could be concluded that the moment stiffness coefficients of the bearing, which are diagonal elements in the stiffness matrix, were correctly calculated.

As will be seen later on in this thesis, especially these moment stiffness coefficients of the bearing will prove to play an important role in the vibration transmission from gears to gearbox housing.

The stiffness and damping matrices of fluid film bearings have been taken from the literature. However, literature for deriving the moment stiffness and damping coefficients is extremely scarce. The stiffness matrices of the gear test rig of Chapter 5 that were presented for illustrative reasons proved to be unsymmetrical. In the work of Chapter 5 they were made symmetrical to include them in our FEM modeling. However, it is impossible to implement the damping matrices in these FEM models because only one damping factor can be assigned for the whole structure. This is a result of the method that was used for the FEM calculations of transfer functions. Perhaps another calculation method should be used which is able to implement the damping matrices of the fluid film bearings in the FEM modeling correctly.

4. VIBRATIONAL BEHAVIOUR AND SOUND RADIATION OF GEARBOX HOUSINGS

Finite Element Method (FEM) calculations have been performed on a variety of models of gearbox housings. Starting with a simplified empty gearbox housing and adding step by step complications, eigenfrequencies and their eigenmodes are predicted. In addition, Modal Analysis measurements on these housings have been performed. Agreements and discrepancies between FEM results and Experimental Modal Analysis results are discussed in this chapter. This shows the usefulness of FEM with respect to predicting eigenfrequencies and eigenmodes of gearbox housings.

To investigate the modeling of bolted connections, calculations and measurements have been performed on an empty box-like structure which is made out of one piece, and on an empty box-like structure which is bolted together. The same routine is repeated for a gearbox with and without shafts and bearings inside the housing. The work will be evaluated to obtain a clearer picture on the expectations which will be realistic when using this type of computational modeling.

Forced vibrations transfer functions from excitation point to the housing surface are calculated and measured. As input a point force excitation is taken and as output the surface-averaged mean square velocity level L_v of the gearbox housing surface is calculated.

For sound radiation by the gearbox housing a very simplified modeling will be discussed.

4.1 Introduction

In the previous chapters the generation of vibrations at the gear mesh (Chapter 2) and the vibration transmission properties of bearings (Chapter 3) have been investigated. In this chapter the modeling of two main blocks in the vibration and sound transmission chain are investigated (see Fig. 4.1). First the vibration transmission in the gearbox housing will be studied by the use of the transfer function TF. It will be defined as the ratio of the surface-averaged mean square velocity of the housing and the mean square angular velocity of the gears or alternatively the mean square force applied on the housing or gear mesh. Next the modeling of the sound radiation from the housing will be studied. This will be defined as the ratio of the radiated sound power and the surface-averaged mean square velocity of the housing surface.

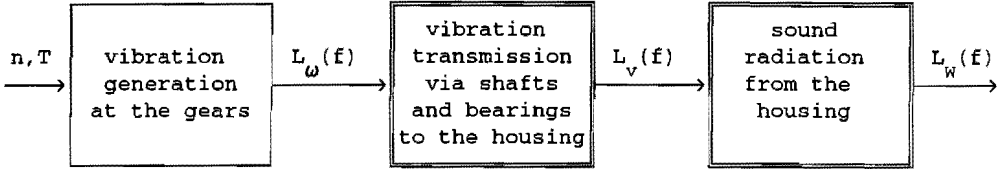


Figure 4.1:
Sound generation scheme of a gear transmission.

The main purpose of this chapter is to investigate whether FEM calculations can predict these velocity levels accurately enough to be used as a design tool for low noise gear transmissions. This will be studied by calculating and measuring eigenfrequencies and their vibration modes of simple structures that look like gearbox housings and of a scale model gearbox. Also comparisons will be made between computed and measured forced vibration responses.

The gearbox housing can be modeled as a transfer system between input (vibrational level $L_{\omega}(f)$ at the gear mesh of the scale model gearbox or force level $L_P(f)$ at a certain position of the box-like structures) and output (surface-averaged mean square velocity on the housing surface $L_V(f)$). The transfer function of the structure is frequency dependent and can be determined by either calculations or by experimental techniques. Given the size and the excitation frequencies of many gearboxes, the dynamic behaviour of the gearboxes which determines the noise production is often dominated by a rather small number of vibration modes. Therefore, computational and experimental methods which take this modal behaviour into account properly are more appropriate than methods such as the Structural Energy Analysis (SEA), which ignore a detailed modal modeling. Therefore, the modeling methods that will be considered are the Finite Element Method (FEM) for computational purposes and Experimental Modal Analysis (EMA) for experimental purposes. If the data resulting from these methods turns out too detailed for design purposes, appropriate data reduction can easily be obtained.

The Finite Element Method is a numerical tool that can be used at an early stage in the design process of a gearbox. In contrast, the Experimental Modal Analysis (see Chapter 1) has to be performed on an existing gearbox

housing. From the design engineer point of view it will be clear that FEM is preferable to EMA. FEM gives the possibility to perform numerical experiments without the need for a physical model. The question rises to what extent and for what purposes the results of FEM calculations will be valid. The FEM model has to be as complicated as necessary to describe the dynamic behaviour of the structure properly. The designer has to know how far he has to go with modeling of details. A small but incomplete FEM model will result in acceptable computation time but may provide useless answers. A very detailed model might give accurate answers but would probably require an immense computer memory and impractical long calculation times.

In the literature extensive experimental studies were undertaken (see e.g. /4.1/ and /4.2/). However, attempts to correlate these tests with computational predictions were limited. One reason may be the complexity of the housing geometry involved, which makes the use of FEM complex and expensive. Some examples for gear transmissions are reported in /4.3/ and /4.4/ which illustrate the complexity of the proper use of FEM in gear transmission technology. However, they use very simple FEM models with no interior shafts nor gears and often the gearbox housing plates are modeled separately. Therefore, the use of FEM analysis as a design tool for low noise gear transmissions is still limited and should be investigated more thoroughly. This is the main intention of the work following in this chapter.

In this chapter a compromise will be sought between simplicity and size of the FEM models and the expected accuracy of the results. Modeling aspects will be studied by using a step by step approach starting with a very simple (gearbox-) housing model. This approach results in FEM models with a size that can be analyzed within acceptable time limits and still provide reliable answers. The final step in this chapter using FEM modeling is the investigation of a complete gearbox with geared transmission and bearing stiffness matrices. But before testing the reliability of FEM for such a complex structure, the calculation method will be evaluated for some simpler structures.

This is done by starting with a simple box-like housing without any bearings or shafts. After comparison between the calculation and Modal Analysis measurements on the simple model, the next step is taken. A housing which consists of two box-like parts bolted together is then subjected to investigation. After that, a more complex gearbox scale model is taken as study object, without and with gearbox interior elements.

The sound radiation block of Fig. 4.1 will only be modeled for $L_v(f)$ data summed up over 1/3-octave bands which usually contain several eigenfrequencies of vibration modes of the gearbox. Approximate data for $L_w(f)-L_v(f)$ will be used as is common practice in SEA applications. The rationality of this approach will be discussed in section 4.7.

4.2 Unsupported simple box-like structure

The frequency range of interest in the FEM calculations was set to 0 up to 4 kHz. This frequency range is determined by the spectrum of the angular velocity level $L_w(f)$ of a gear transmission which can be calculated using the method described in Chapter 2 of this thesis. This vibration spectrum contains the tooth frequency and its higher harmonics.

The FEM calculations provide frequency response functions which can be highly dependent on the structural behaviour, i.e. eigenfrequencies and their vibration modes. To investigate the practical value of FEM calculations for designing low noise gearboxes this method is applied to a simple (gearbox) housing.

This structure consists of no more than five plates with thickness of 8 mm and a foot of 15 mm thickness that are welded together. This gearbox housing should rather be called a box model as preparation of modeling more complex housing structures. Fig. 4.2 shows the dimensions of the housing. The housing has no bottom in order to be able to bolt two of these housings together for the purpose of calculations and measurements on a more complex structure, for which the results will be presented later in this chapter.

To exclude any uncertainties in boundary conditions the housing was unsupported by putting it on soft rubber elements. A more stiff support of the housing would introduce the problem as to how to model it in the FEM calculations. This will be done in the next section of this chapter. The FEM calculations were performed using 647 shell elements. The bending wavelength of a plate of the same dimension as the top plate and at a frequency of 4000 Hz was used to choose the mesh dimensions. The model has at least four elements within one wavelength at 4000 Hz, by which a good visual presentation is guaranteed at any eigenfrequency of the structure so that they can be distinguished when modal analysis results are available.

In the frequency range up to 4000 Hz, 35 mode shapes were calculated /4.5/ apart from six rigid body modes at eigenfrequencies of 0 Hz. A few mode

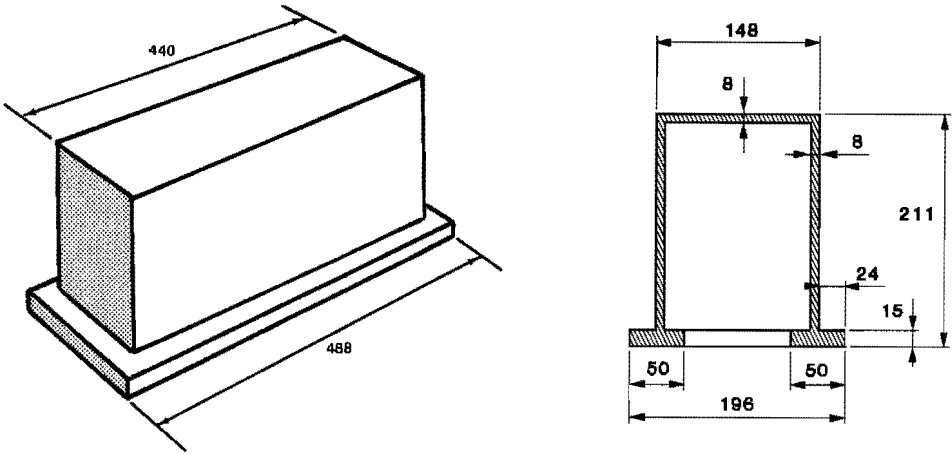


Figure 4.2:

Simple gearbox housing (dimensions in mm).

The total mass of the steel structure is 24.5 kg.

shapes are shown in Fig. 4.3. The eigenfrequency of 641 Hz is the lowest non-zero eigenfrequency. All examples in Fig. 4.3 show plate-like vibration modes.

For experimental usage two identical box-like structures were made according to Fig. 4.2. For both gearboxes model analysis techniques have been used to determine their modes and eigenfrequencies. In both cases 30 modes were found in the frequency range up to 4000 Hz. The other 5 eigenmodes were not found in the modal analysis which is possibly due to the fact that the position of the accelerometer coincided with a nodal line of zero vibration. By comparing the eigenfrequencies of the corresponding modes of these two box-like models it turned out that the differences are very small, within 1 percent. From this it can be concluded that the manufacturing of these simple structures had no noticeable influence on the measured eigenfrequencies and modes.

The degree of agreement between the numerical (FEM) and the experimental eigenfrequencies is shown in Fig 4.4 /4.6/. The mode shapes were compared with each other and the corresponding frequencies were plotted against each other in this figure. The mean relative difference between calculated and measured eigenfrequencies is 5 percent which is very acceptable. Hence, the Finite Element Method is an accurate tool in predicting modes and eigenfrequencies of this simple, unsupported box model.

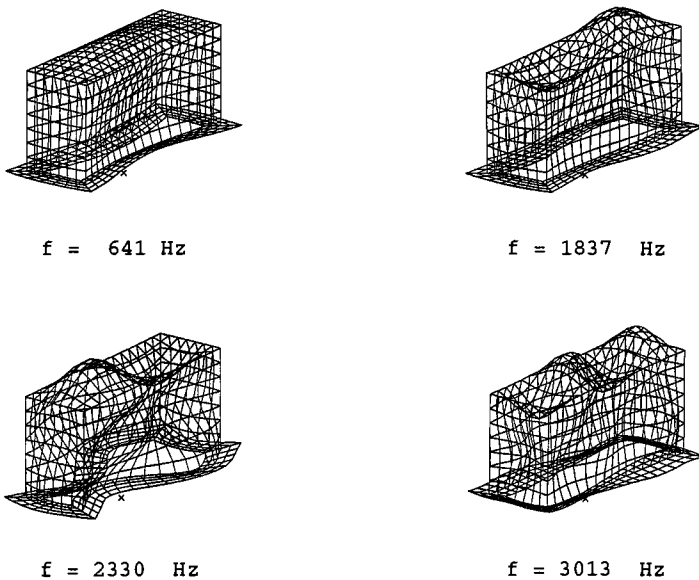


Figure 4.3:
 Mode shapes at a few eigenfrequencies of the simple gearbox housing.

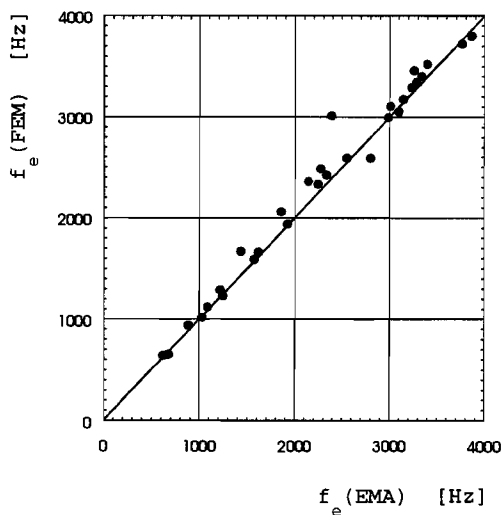


Figure 4.4:
 Numerical (FEM) and experimental (EMA) eigenfrequencies of corresponding modes of the simple unsupported gearbox housing /4.6/.

The following point that will be considered is whether the FEM is able to predict transfer functions accurately as well. For a real gearbox this transfer function will be defined as the surface-averaged mean square velocity of the housing divided by the mean square angular velocity $\tilde{\omega}^2(f)$ at the input. However, the simple box-like structures which contain no gears will be excited by a force spectrum, therefore the transfer function $TF_P(f)$ is written as:

$$\begin{aligned}
 TF_P(f) &= 10 \log \left(\frac{\overline{\tilde{v}^2(f)} \cdot F_0^2}{\tilde{F}^2(f) \cdot v_0^2} \right) = 10 \log \left(\frac{\overline{\tilde{v}^2(f)}}{v_0^2} \right) - 10 \log \left(\frac{\tilde{F}^2(f)}{F_0^2} \right) = \\
 &= L_v(f) - L_F(f) \quad [\text{dB}] \quad (4.1)
 \end{aligned}$$

where we use $v_0 = 5 \cdot 10^{-8}$ m/s and $F_0 = 1$ N.

Other definitions are possible as well, but for the purpose of this study the surface-averaged mean square velocity is defined as the response quantity.

To investigate the utility of FEM for predicting the transfer function, a first validation was made for the simple box-like structure of Fig. 4.2. The excitation force was applied at the top plate for one validation and was applied at the front plate for another. The velocity level $L_v(f)$ was calculated by averaging the computed $v_{\text{rms}}^2(f)$ over the housing area. The values of $v_{\text{rms}}^2(f)$ were computed at equidistant frequencies ($\Delta f = 4.88$ Hz). To model the damping, decay times T_{60} on the box were measured for every 1/3-octave band which contains eigenfrequencies. The decay time is defined as the time in which the root mean square acceleration response decreased 60 dB after switching off a vibration exciter /4.7/. This estimation method was practical thanks to the low damping of the structure (i.e. long T_{60}):

$$\eta = \frac{2.2}{\bar{f}_{\text{band}} T_{60}} \quad (4.2)$$

On the basis of the measurements the loss factor η for the calculations of the forced response was set at 0.0026 for the 500 Hz 1/3-octave band and decreased to $\eta = 0.0010$ for the frequency band of 3150 Hz /4.8/.

The computational predictions of the forced velocity level were carried out taking into account the responses of various collections of nodes. The

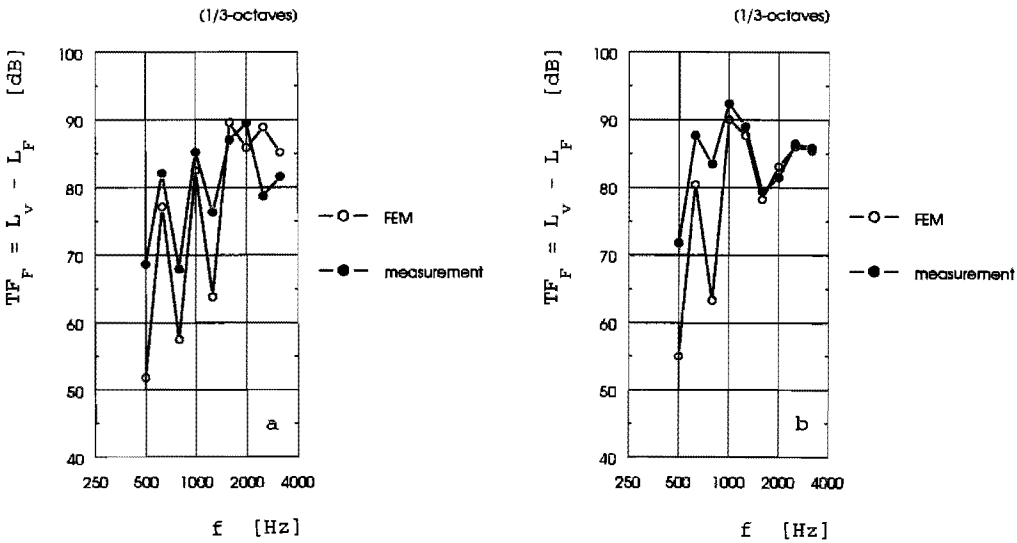


Figure 4.5:

Measured and calculated transfer functions TF_F of the unsupported simple gearbox housing /4.6/. Force input at a point of the top plate (a) and force input at the front plate (b). Both excitation points lie somewhat out of the centre of the plates to ensure that many eigenmodes are excited.

numbers of nodes that were used were respectively 18, 36, 48 and 94 to find a convergency point for the results. This proved to occur for 36 nodes. For the experimental determination of $L_v(f)$ 166 measurement points were used. Now, in contrast to the results in Fig. 4.4 less good agreement is seen between calculations and measurements in Fig. 4.5. At low frequencies the 1/3-octave bands contain only one or none eigenfrequency of the housing. It can be seen that for these low frequencies the comparison between measurement and calculations is not satisfactory. From 1000 Hz on the measurements and calculations are in better agreement.

In bands where no resonances are present the computed results are underestimations. This might be caused by neglecting the modes with eigenfrequencies above 4 kHz. The rigid body modes determine the mass-like behaviour at low frequencies. The high frequency modes may contribute to the local deformations in frequency bands where resonant modes are lacking. However, the overall response is determined by the peaks and not by the low level bands so that these deviations may turn out to be acceptable. In the band of 630 Hz where one resonance is present a deviation of 8 dB occurs when the force is applied at the front plate of the structure. The reason is unknown. Also the 2500 Hz 1/3-octave band of Fig. 4.5-a shows a

remarkable difference between calculation and measurement. This may be due to the fact that the number of vibration modes in this frequency band for FEM is different than for EMA as can be seen in Fig. 4.4 where two dots are far away from the ideal line.

The Finite Element Method is thus a reasonably reliable tool for predicting modes, eigenfrequencies and velocity levels for simple, unsupported box-like structures as the one in this section in cases that the frequency bands contain at least one eigenfrequency. The only parameter that has to be estimated or measured accurately is the loss factor of the structure. When this parameter is known, the results of FEM calculations of the velocity levels might be acceptable when the structure is excited at frequency bands containing eigenfrequencies. If octave bands are used instead of 1/3-octave bands somewhat better results will be obtained since the number of vibration modes per band will increase. However, octave bands give less information about the frequency dependency of the dynamic behaviour of the structure. This is why 1/3-octave band results are used in this thesis. From the designers point of view the results can often be presented in octave bands. In many practical applications of gear transmissions the running speed and thereby the tooth frequency will vary considerably. Then the strong frequency dependent vibration transfer function $TF_F(f) = L_V(f) - L_F(f)$ calls for the use of larger frequency bands to obtain averaged results of $L_V(f)$. On the other hand when the velocity levels $L_V(f)$ of a gear transmission operating under a constant speed is of interest, the use of narrow frequency bands has to be preferred.

4.3 Supported simple box-like structure

In the previous section the reasonable accuracy of FEM predictions for dynamical behaviour was shown for the case of the simple (gearbox) housing without any boundary conditions. However, in practice gearboxes make contact with the surrounding world by bolting them to a supporting structure. The question of how to model these bolted joints of gearbox housings in the FEM analysis is the topic of investigation described in this section.

For this purpose the simple gearbox housing was bolted to a large frame with eight bolts. Experimental Modal Analysis was performed and FEM calculations were carried out using three different boundary conditions for the gearbox feet. For all three boundary conditions the nodes at the positions of the eight bolts were fixed in all six degrees of freedom. The differences followed from the boundary conditions for the other element nodes of the bottom flange:

- 1) no kinematic constraints
- 2) all remaining node motions were suppressed in normal direction
- 3) all remaining node motions were suppressed in all six degrees of freedom

The first boundary condition also allows free movement of the bottom flange perpendicular to the joint except at the bolts. This is not correct in practice since the frame to which the gearbox is mounted restricts this movement. But on the other hand the other two boundary conditions are possibly too restrictive for this movement. The third boundary condition restricts the movements of the bottom flange in all directions which will lead to higher eigenfrequencies of the gearbox housing. Whether or not these three different boundary conditions have great influence on the calculated eigenfrequencies of the structure can be seen in Fig. 4.6. Of the 29 calculated eigenmodes in the frequency range up to 4000 Hz only 11 modes could be identified from the measurements. The mode shapes of these frequencies were compared to obtain Fig 4.6 from which it can be seen that the differences between the three boundary conditions used in the FEM analysis are small. It should be noticed that two eigenfrequencies almost coincide at 1167 Hz and 1176 Hz. Most of the calculated eigenfrequencies are somewhat higher than the measured ones, probably due to a slight over-estimation of the stiffness in the FEM model. The mean differences compared

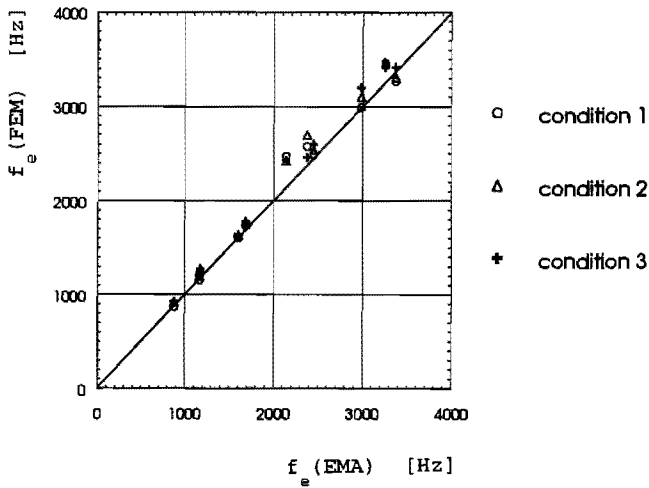


Figure 4.6:

Numerical (FEM) and experimental (EMA) eigenfrequencies of corresponding modes of the simple gearbox housing supported at the bottom flange by using three different boundary conditions in the FEM calculations.

to the measured frequencies are 4, 6 and 5 percent respectively for the three boundary conditions. From this it may be concluded that all three boundary conditions are equally good.

For further calculations the third boundary condition will be taken. Since the differences between the three are very small this choice was made because the first and second set of boundary conditions showed for unknown reasons a few zero energy modes (or hour-glass modes /4.9/).

For the calculation of the velocity level $L_v(f)$ the frequency range of interest is from 0 to 4000 Hz, where 29 eigenfrequencies are present. The loss factor η was estimated by using some modal loss factors resulting from the EMA on the gearbox housing. The decay time measurement method of the previous section could not provide accurate estimates due to too short decay times T_{60} which resulted after the impact hammer excitation. It turned out that a frequency independent damping coefficient ξ ($= \eta/2$) of 0.002 had to be used in the FEM calculations /4.8/. This is a somewhat higher damping coefficient than which was used in the previous section where the structure was unsupported.

The resulting velocity levels for two excitation points are presented in Fig 4.7. These two excitation points are the same as in the previous section, i.e. at the top plate and at the front plate. The figure shows a

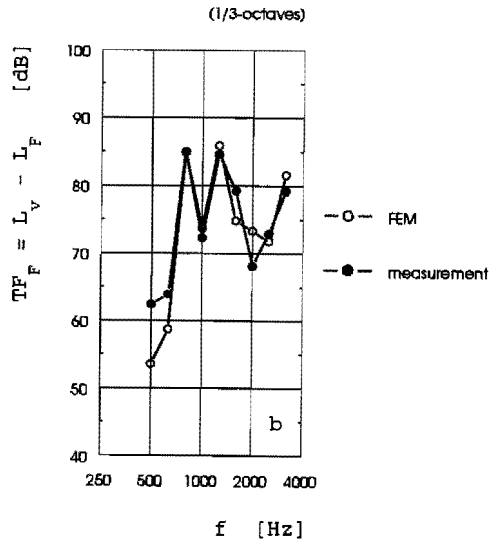
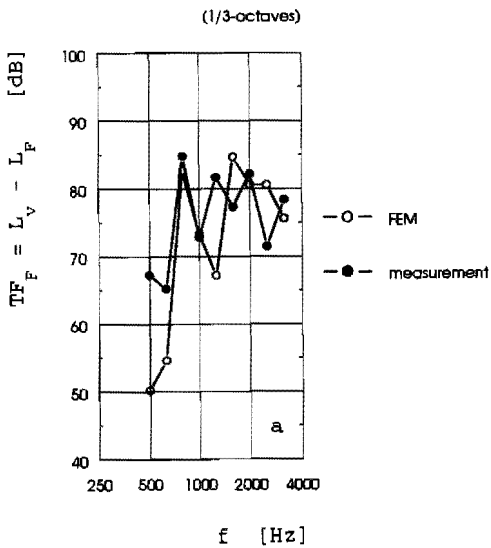


Figure 4.7:

Measured and calculated transfer functions TF_F of the supported simple gearbox housing /4.6/. Force input at the top plate (a) and force input at the front plate (b).

good resemblance between the calculated and measured levels, especially for the higher frequency bands where more eigenfrequencies per band are present. When octave bands are used instead of 1/3-octave bands, the results for the 1kHz-band and the 2 kHz-band are very good. However, the 500 Hz-band still shows large differences due to the fact that no vibration modes correspond with eigenfrequencies in this frequency band. Nevertheless, this is not very important since the overall velocity level $L_V(f)$ is dominated by the higher frequency bands which contain resonant modes. From this it can be concluded that frequency bands without eigenfrequencies will give less good predictive results, possibly because the FEM modeling contains no eigenmodes above 4 kHz which are responsible for the local deformations. It can also be concluded that the uncertainty about the computed eigenfrequencies of the vibration modes recommends the use of 1/3-octave bands or octave bands.

The Finite Element Method is therefore a good tool for calculating velocity levels of simple rigidly mounted gearbox housings. The support can be modeled in a rather simple way by restricting all six degrees of freedom at the nodes of the housing FEM model that make contact in the joint zone. However, the FEM predictions of forced responses can only be reliable when realistic damping factors ξ are known.

4.4 Two assembled box halves

Normally speaking, a gearbox housing is bolted to a frame as discussed in the previous section. However, this is not the only bolted joint of a gearbox housing. The majority of the industrial gearboxes consist of a lower and an upper gearbox housing part which are bolted together. In order to know the influence of these joints on the FEM calculation accuracy, two identical simple gearbox housings of sections 4.2 and 4.3 were bolted together at their bottom flanges. This assembly was dynamically free from the surroundings and in practice realized by putting it on soft rubber elements. It was used for measurements and calculations of modes and eigenfrequencies. Due to the larger dimensions of this gearbox assembled structure, the number of eigenfrequencies in the frequency range up to 4000 Hz turned out to increase significantly compared to that of the separate structure discussed before. For computational reasons it was decided to look at a smaller frequency range of 0 to 2000 Hz. In this frequency range 24 eigenfrequencies were calculated of which 19 could be assigned to measured vibration modes.

The measurements (EMA) were carried out with and without a paper gasket of 0.15 mm thickness between the flanges of the box structure. The gasket had a very small influence on the measured eigenfrequencies. At the most 3 percent and on the average 1 percent relative difference was seen between the individual corresponding modes. However, the loss factor η was influenced by the gasket as Fig. 4.8 shows. These values of η were obtained with the measurements of decay times per 1/3-octave band. Slightly higher values (approximately 10 percent) for the loss factor were measured over the total frequency range when the gasket was applied. However, the differences are not significant when the velocity level $L_v(f)$ will be calculated. The expected differences in the predicted $L_v(f)$ due to the gasket will not extend 1 dB since a doubled loss factor influences 1/3-octave bands levels of $L_v(f)$ by approximately 3 dB and in Fig. 4.8 it can be seen that the differences are much smaller than this factor two.

The correlation between the calculated and measured eigenfrequencies is not influenced by the loss factor. However, the calculation (FEM) of the eigenfrequencies of the two assembled box halves is not as straightforward as in the previous sections. A realistic bolted joint FEM-model with GAP-elements would be preferable to calculate the joint behaviour accurately. However, a simplification of this FEM-model will be used since a realistic FEM-model

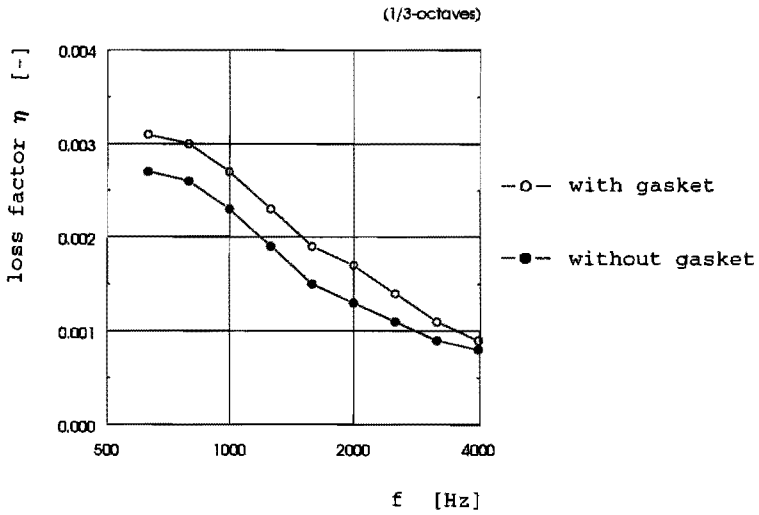


Figure 4.8:

Measured loss factors of the two assembled box halves with and without a paper gasket of 0.15 mm thickness.

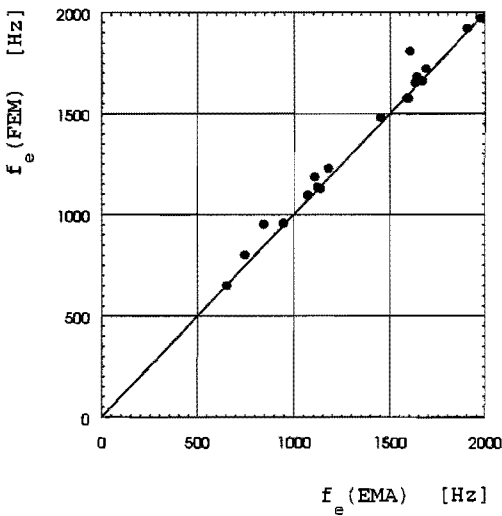


Figure 4.9:

Numerical (FEM) and experimental (EMA) eigenfrequencies of corresponding modes of two assembled box halves /4.6/.

would consume too much valuable computer memory and execution time. The joint was modeled by assuming that no joint exists at all; as if the gear-box housing is welded together to one piece. This is the simplest possible model of such a joint and it is interesting to investigate how well this modeling of the joint describes the dynamical behaviour of the structure. Fig. 4.9 shows the numerical and experimental eigenfrequencies of the two assembled box halves. It can be concluded that the FEM model predicts slightly too high eigenfrequencies. The largest relative error is 11 percent, while the mean relative error is not more than 3 percent. Therefore, the joint modeling used is assumed to be an acceptable model for the bolted joint.

The calculations and measurements for the transfer function $TF_F(f)$ were performed for three excitation directions at the same point of the structure. The point is located at the joint where a bearing could be positioned when the housing would contain gears. At this point a radial force, an axial force and a moment were applied in order to simulate a bearing stiffness matrix which transmits these possible excitation directions. The reciprocity principle was used to obtain the measured point-to-point transfer functions needed. This reciprocity principle for mechanical systems says for example:

$$H_{12}(f) = \frac{v_2(f)}{F_1(f)} = \frac{v_1(f)}{F_2(f)} = H_{21}(f) \quad (4.3)$$

$$\text{or: } H_{12}(f) = \frac{v_2(f)}{M_1(f)} = \frac{\omega_1(f)}{F_2(f)} = H_{21}(f) \quad (4.4)$$

In this way the measurement for the moment input with velocity level $L_v(f)$ as output could be realized by measuring the angular velocities ω at the 'bearing point' when an impact hammer produced input force impulses F at selected points on the surface of the structure. Two accelerometers were used at the joint to measure the angular accelerations. The signals were subtracted from each other to obtain the angular accelerations and to derive the corresponding angular velocity level spectra. Fig. 4.10 shows transfer functions $TF_F(f)$ and $TF_M(f)$ resulting from the experiments and from the FEM model for the three excitation directions at the bearing position. Fig. 4.10-c is based upon a moment being applied. This is the reason for levels being different from those in the other two figures.

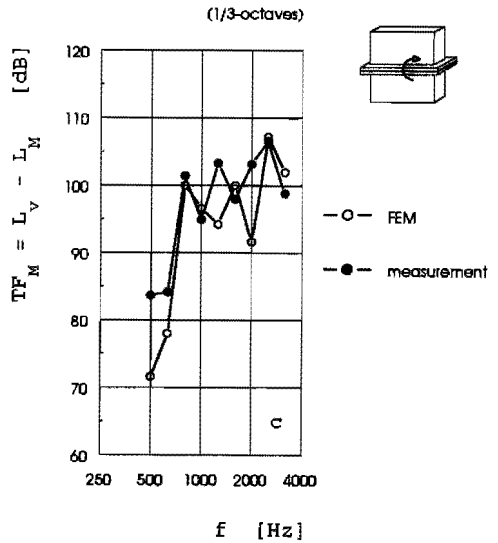
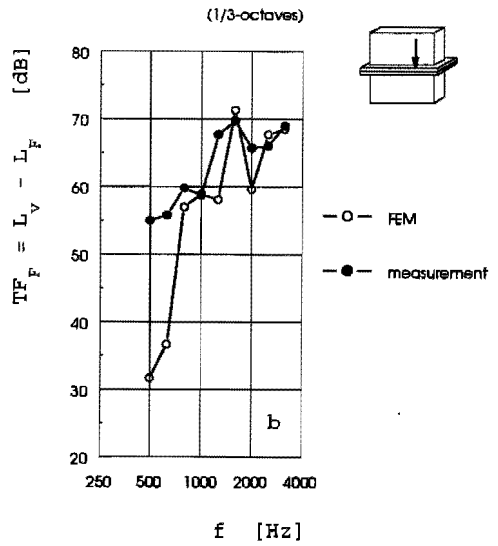
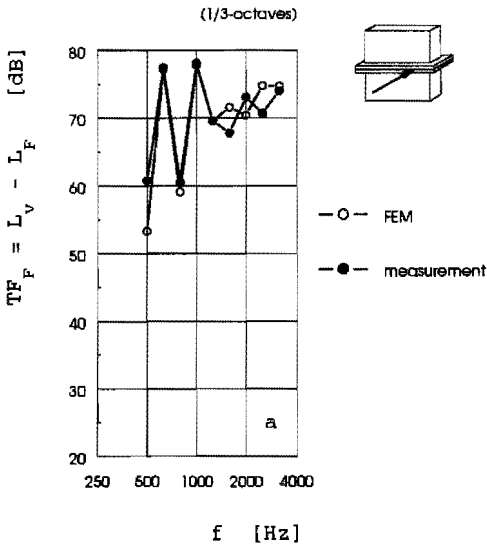


Figure 4.10:

Measured and calculated transfer functions TF_F and TF_M of the two assembled box halves for three different excitation directions.

Apart from the lower frequency range, where the eigenfrequency density is low, the predictions made by the Finite Element Method are in good agreement with the measurements. In the 500 Hz frequency band no eigenfrequencies of the structure are present so that the incompleteness of the FEM model is probably responsible for the underestimation by the calculation. When octave bands would be calculated for $TF_F(f)$ and $TF_M(f)$, the results would be somewhat better. However, the 500 Hz band of Fig. 4.10-b and the 1 kHz band of Fig. 4.10-b and 4.10-c will still show a difference between calculation and measurement.

Fig. 4.10-b and 4.10-c are closely related because the radial force of Fig. 4.10-b was applied at a distance of $a = 15$ mm from the heart line of the front plate. This introduces a radial force as well as a moment of magnitude $F_{\text{rad}} \cdot a$. Assuming that the result of Fig. 4.10-b is mainly determined by the moment excitation, Fig. 4.10-c could be estimated as follows:

$$\begin{aligned}
 \text{TF}_{\text{Fig. 4.10-c}}^{\text{M}}(f) &\cong 10 \log \left(\frac{\overline{\tilde{v}^2}(f) \cdot F_0^2 \cdot \ell_0^2}{F_{\text{rad}}^2(f) \cdot a^2 \cdot v_0^2} \right) = \text{TF}_{\text{Fig. 4.10-b}}^{\text{F}}(f) - 20 \log(a/\ell_0) = \\
 &= \text{TF}_{\text{Fig. 4.10-b}}^{\text{F}}(f) + 36.5 \text{ dB} \quad (4.5)
 \end{aligned}$$

where $\ell_0 = 1$ m

The importance of the angular excitation of the structure by a bearing force or moment is hereby clearly shown. The moment stiffness coefficients of a bearing seem therefore essential for accurate predictions of velocity levels of gearbox housings and for this reason they have to be known or calculated (see Chapter 3 of this thesis) preliminary to FEM calculations of transfer functions $\text{TF}_{\omega}^{\text{v}} = L_{\text{v}} - L_{\omega}$.

The rather good agreement between the predicted and measured eigenfrequencies of corresponding modes and predicted and measured forced responses justifies the simplified modeling of the bolted connection of the two box halves. Of course, again, a reliable estimation of modal loss factors is another requirement for a good prediction of forced responses.

4.5 Empty gearbox model

The experience gained in the previous sections was used in a FEM analysis of a realistic gearbox housing model. This gearbox housing is a somewhat simplified version of a scale model (at 80 percent scale) of the gearbox of Chapter 5 on which extensive vibration and sound measurements have been performed. In this section the gearbox housing model is considered empty, i.e. without any shafts or bearings. Fig. 4.11 shows the dimensions of the gearbox housing model. The usual joint between upper and bottom case section has been omitted, i.e. the gearbox model was build as a single structural component just like the FEM model of section 4.4. This was

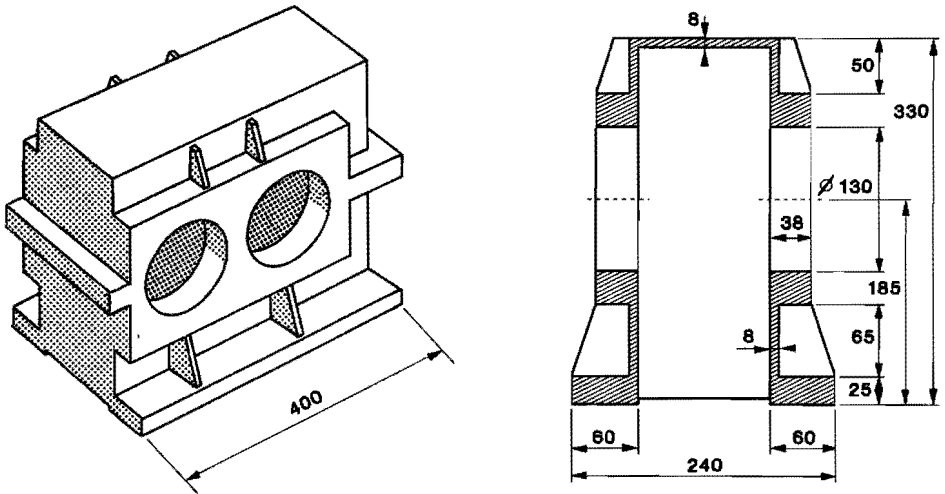
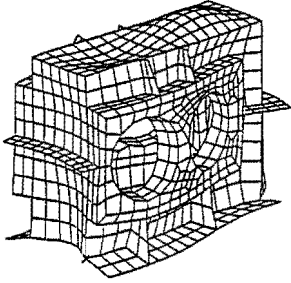


Figure 4.11:
Gearbox housing model (dimensions in mm).

realized by welding the parts of the gearbox model together so that a one-piece structure was created without any bolted joints. In order to be able to connect a shaker to the shafts in a later experiment (see the next section of this chapter) the gearbox model has no bottom plate.

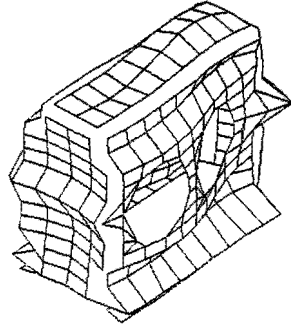
The FEM model consists of 570 4-node shell elements for the 8 mm plates of the structure and of 460 8-node brick elements for the thicker parts (38 mm). The total FEM model contains 1370 nodes. The connection between shell elements and bricks was carefully made by ensuring correct force and moment transmissibility between these elements. The gearbox model is dynamically free from the surrounding, which is realized in practice by putting the housing on soft rubber elements.

The FEM calculations were performed for the frequency range up to 4000 Hz where 42 eigenfrequencies and mode shapes were found after 11 iterations /4.10/. The first non-zero eigenfrequency was found at 387 Hz, the second at 703 Hz and the third at 1119 Hz. This means that the 1/3-octave bands up to 1250 Hz are sparsely filled with eigenfrequencies of the gearbox housing. In fact the bands of 400 Hz, 630 Hz, 1000 Hz and 1250 Hz are occupied by only one eigenfrequency, and the 1/3-octave bands of 500 Hz and 800 Hz have none at all. Therefore, resulting velocity levels $L_v(f)$ at these frequency bands are predominated by none or a single resonant mode. Since the predictions are expected to improve in accuracy when more modes



$f = 1777 \text{ Hz}$

FEM calculation



$f = 1894 \text{ Hz}$

EMA measurement

Figure 4.12:

Calculated and measured mode shape of the empty gearbox model.

are present in a 1/3-octave band, the comparison between calculations and measurements will be expected to give better results for the higher frequencies, i.e. 1600 Hz and more.

The FEM calculations and the EMA measurements were linked together by searching for similar vibration modes by visual inspection. 42 FEM modes were calculated and 27 clear EMA modes were measured of which 25 could be assigned to FEM modes. As an example the calculated mode shape at 1777 Hz is shown in Fig. 4.12 together with the corresponding measured mode shape at 1894 Hz.

The Experimental Modal Analysis was carried out with the help of LMS software using Single Degree Of Freedom (SDOF) curve fit procedures to estimate the modal parameters. This was done by peak picking in the sumblock of all measured transfer functions. Only peaks were picked that could be clearly distinguished among others. This meant that small peaks and peaks with frequencies close together were not taken into consideration so that not all calculated eigenmodes were extracted from the experiments.

The numerical (FEM) and experimental (EMA) eigenfrequencies of the empty gearbox model are shown in Fig. 4.13. Here it can be seen that the calculated eigenfrequencies are too small, on average 10 percent. This was thought to be a result of the fact that the FEM model was not stiff enough,

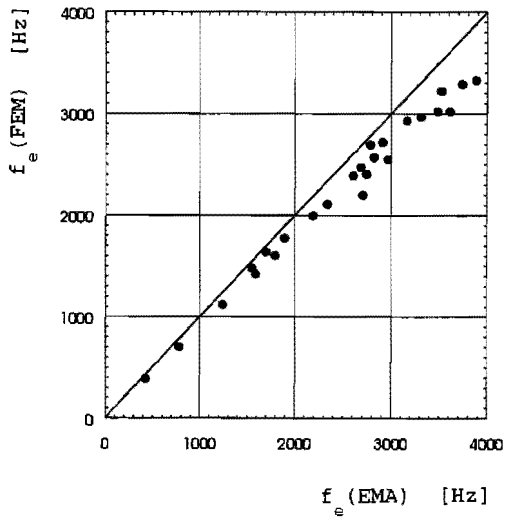


Figure 4.13:

Numerical (FEM) and experimental (EMA) eigenfrequencies of corresponding modes of the empty gearbox model.

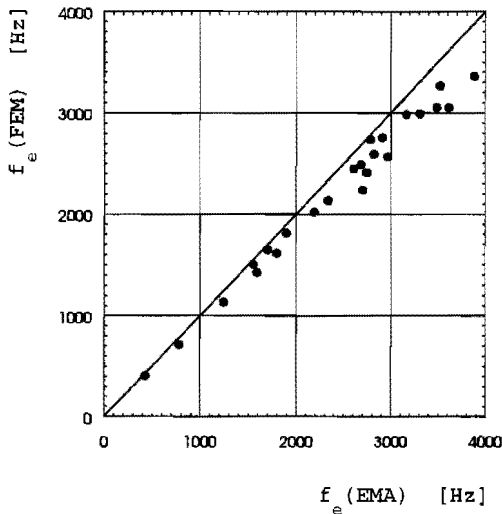


Fig. 4.14:

Numerical (FEM) and experimental (EMA) eigenfrequencies of corresponding modes of the empty gearbox model after altering the FEM-model (brick elements instead of shell elements at the position of the bolt joint).

especially the rim which replaces the bolted joining. This rim has a cross section of 30 mm x 30 mm and was modeled with shell elements instead of brick elements.

The calculations have been repeated after modifying the FEM model. The joint was modeled with brick elements by which the number of nodes and consequently the necessary calculation time increased slightly. The new results are shown in Fig. 4.14 where it can be seen that especially at higher frequencies the calculations and the measurements are still not in good agreement with each other. The points in the figure have an average difference with the ideal 45 degree line of 9 percent which is an improvement of only 1 percent. Therefore, the more complex FEM-model does not improve the results as much as was hoped. This shows the difficulty of modeling a gearbox housing correctly in order to obtain valid eigenfrequencies.

Nevertheless, further calculations have been performed using this "stiffened" FEM-model such as the prediction of the velocity level $L_v(f)$ of the gearbox. Fig. 4.15 shows the calculated and measured transfer functions $TF_F(f)$ for the case of an axial force excitation at the thicker part of the structure between the two bearing openings at the front plate. The figure shows how well the FEM model predicts the resulting vibrations at the surface of the gearbox model, if one looks at a frequency band which contains at least a few eigenfrequencies. Therefore, it can be concluded

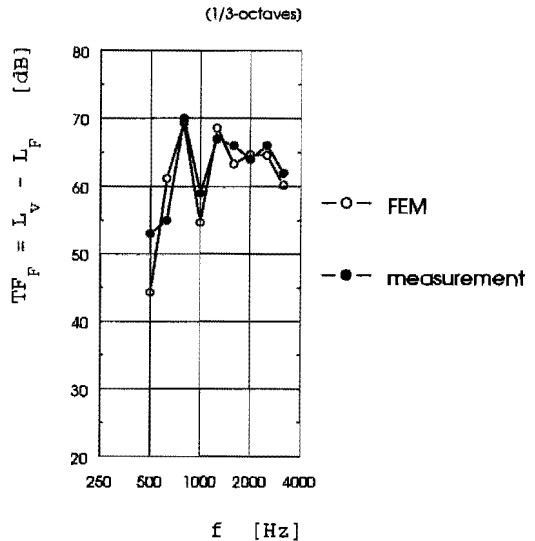


Figure 4.15:
Measured and calculated
transfer functions TF_F of
the empty gearbox model.

that the exact values of the eigenfrequencies does not have too much influence on the calculated velocity levels in frequency bands where at least a few eigenfrequencies are present.

Furthermore, the excitation point is positioned at a thick part of the gearbox model while the excitation points in the previous sections of this chapter were situated at thin plates. This means that at frequencies below the first eigenfrequency or at a 1/3-octave band where no vibration modes are present, the local distortions close to the excitation point are probably less present. And hence, that the vibration modes with eigenfrequencies above 4 kHz would probably not play an important part in describing the behaviour of the structure at these lower frequencies.

4.6 Gearbox model with shafts and ball bearings

The final part of our investigations on the potential use of FEM for prediction of structural responses of gearboxes will be described in this section. Again calculations and measurements were performed on the gearbox model as described in the previous section. However, now the model complexity was increased by adding two shafts and four appropriate ball bearings. The shafts were connected with each other with a rod by which a radial force could be applied between the two shafts to simulate a static tooth force. In the experiments a static radial force was applied which was checked by the use of strain gauges which were put on the rod in order to measure the tensile stress.

First the two shafts were axially loaded to an axial force of 4000 N followed by a radial force of 20000 N. The axial and radial forces together build up a force vector for each of the four ball bearings so that the bearing stiffness matrices could be calculated by using the computer algorithm of Chapter 3. The ball bearings had the following dimensions:

	pinion shaft	wheel shaft
ball bearing type	SKF 6312	SKF 6215
shaft diameter [mm]	60	75
house diameter [mm]	130	130
width [mm]	31	25
number of elements	8	11
element diameter [mm]	22.22	17.46

The resulting bearing stiffness matrices were as follows:

Pinion shaft:

$$[K]_{bm} = \begin{bmatrix} 5.05 \cdot 10^8 & 0 & 0 & 0 & -5.48 \cdot 10^6 & 0 \\ 0 & 5.74 \cdot 10^8 & -7.10 \cdot 10^7 & 4.89 \cdot 10^6 & 0 & 0 \\ 0 & -7.10 \cdot 10^7 & 1.29 \cdot 10^8 & -1.12 \cdot 10^6 & 0 & 0 \\ 0 & 4.89 \cdot 10^6 & -1.12 \cdot 10^6 & 1.70 \cdot 10^5 & 0 & 0 \\ -5.48 \cdot 10^6 & 0 & 0 & 0 & 1.22 \cdot 10^5 & 0 \\ 0 & 0 & 0 & 0 & 0 & 0 \end{bmatrix}$$

Wheel shaft:

$$[K]_{bm} = \begin{bmatrix} 5.66 \cdot 10^8 & 1.42 \cdot 10^4 & -6.10 \cdot 10^3 & 5.27 \cdot 10^2 & -6.86 \cdot 10^6 & 0 \\ 1.42 \cdot 10^4 & 6.46 \cdot 10^8 & -8.26 \cdot 10^7 & 6.08 \cdot 10^6 & -5.27 \cdot 10^2 & 0 \\ -6.10 \cdot 10^3 & -8.26 \cdot 10^7 & 1.59 \cdot 10^8 & -1.46 \cdot 10^6 & 2.71 \cdot 10^2 & 0 \\ 5.27 \cdot 10^2 & 6.08 \cdot 10^6 & -1.46 \cdot 10^6 & 2.45 \cdot 10^5 & -1.32 \cdot 10^1 & 0 \\ -6.86 \cdot 10^6 & -5.27 \cdot 10^2 & 2.71 \cdot 10^2 & -1.32 \cdot 10^1 & 1.73 \cdot 10^5 & 0 \\ 0 & 0 & 0 & 0 & 0 & 0 \end{bmatrix}$$

The implementation of the bearing stiffness matrices in the FEM model was given special attention. Each bearing stiffness matrix describes the stiffness between two points of the gearbox FEM model. It is obvious that one point lies in the centre of the bearing, i.e. the centre of the shaft. This point is part of the shaft and transmits gear shaft vibrations through the bearing stiffness matrix to the gearbox housing.

The other point which belongs to the housing structure is positioned at the same location in the centre of the bearing opening. These two points are connected through the stiffness matrix which couples three displacements and two rotations of both the shaft and the gearbox housing.

The connection of the 'shaft point' to the shaft will be clear since the shaft is modeled by beam elements so that this point is part of one beam element. However, the connection of the 'housing point' to the housing is more complicated. The 'housing point' was modeled as being part of a very stiff and relatively massless beam element in the middle of the bearing opening. This beam element is connected with the gearbox housing by a number of relatively stiff and massless rods which form a star configuration. First the FEM calculations were performed with a connection of the bearings to a rigid support instead of a flexible gearbox housing to see

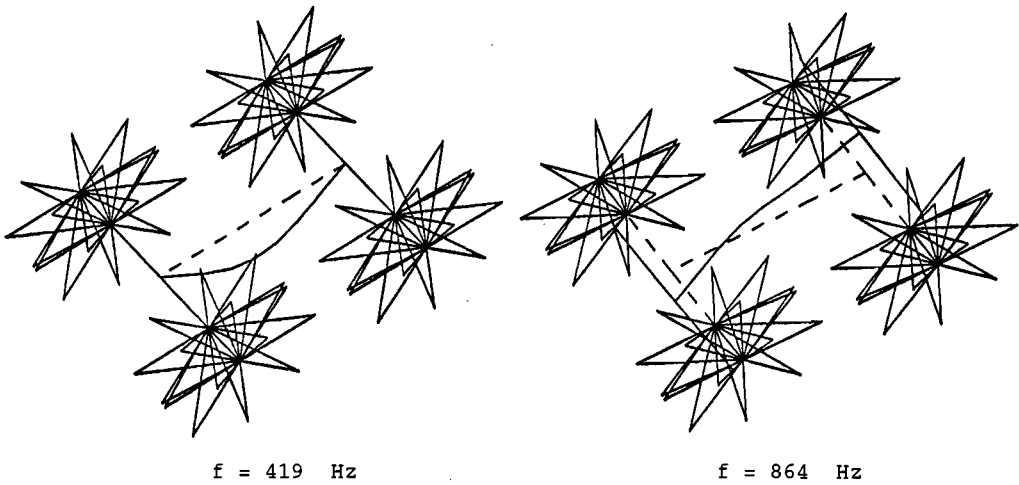


Figure 4.16:

Interior of the gearbox model at an eigenfrequency of 419 Hz (on the left) and 864 Hz (on the right) /4.8/. The relatively stiff and massless rods are situated at the 'stars'.

whether the bearing stiffness matrices could be implemented correctly. Fig. 4.16 shows this FEM model without the gearbox housing at a mode shape of 419 Hz and 864 Hz. The dotted lines show the undeformed positions of the shafts. It can clearly be seen that the gearbox interior (i.e. the rotating elements) moves while the rods stay in their initial places. The first eigenfrequency was encountered at 419 Hz and there are 12 modes with eigenfrequencies in the frequency range up to 4 kHz /4.8/. At the eigenfrequency of 419 Hz the connecting rod bends and the shafts rotate around the bearing axis without moment stiffness while at an eigenfrequency of 864 Hz the two shafts and the connecting rod move as a whole on the stiffnesses of the bearings. For higher eigenfrequencies the gearbox interior moves on the bearing stiffnesses or shows bending motions of the three shafts.

As a next step this gearbox interior was added to the FEM model of the gearbox model, only two modes were found at which mainly the interior moves. These were for the first eigenfrequency of 420 Hz and for the third eigenfrequency of 884 Hz. The other 45 modes were mainly gearbox housing modes.

In the Experimental Modal Analysis only 25 clear mode shapes could be distinguished of which 19 could be appointed to calculated mode shapes

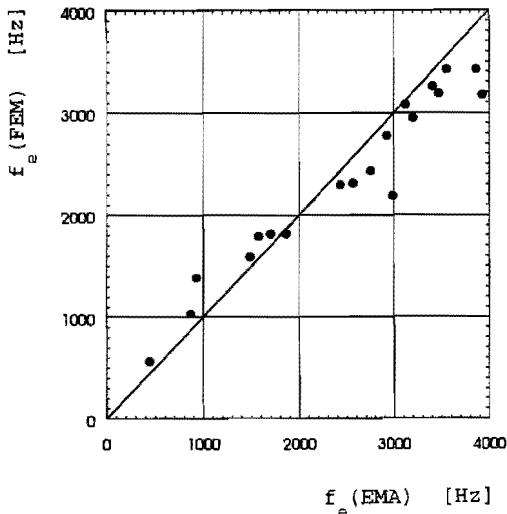


Figure 4.17:

Numerical (FEM) and experimental (EMA) eigenfrequencies of corresponding modes of the gearbox model with shafts and bearings inside.

/4.11/. The measurements which were performed after the calculations had been carried out showed peaks with high damping. Furthermore, many peaks were close together, which made their identification difficult. For these reasons the SDOF curve fitting could not give reliable estimations of the modal parameters so that a Multi Degree Of Freedom (MDOF) routine was used. The LMS modal analysis software supports three different MDOF routines of which the Least Square Complex Exponential method was used. The measurements were carried out in the same way as was done for the empty gearbox model using 399 points at the gearbox model surface.

The 19 measured eigenmodes were gearbox housing modes and the calculated gearbox interior modes with eigenfrequencies of 420 Hz and 884 Hz were not present. Fig. 4.17 shows the numerical (FEM) and experimental (EMA) eigenfrequencies of these 19 mode shapes with an (absolute) average difference of 13 percent. Below 2 kHz the Finite Element Method predicts slightly too high eigenfrequencies as where it predicts too low eigenfrequencies above 2 kHz. Therefore, the FEM model describes the dynamical behaviour of the gearbox model not very well when eigenfrequencies and mode shapes are considered.

The prediction of velocity levels at the gearbox surface, as a result of a force excitation at the 'meshing point' of the interior, is the next step

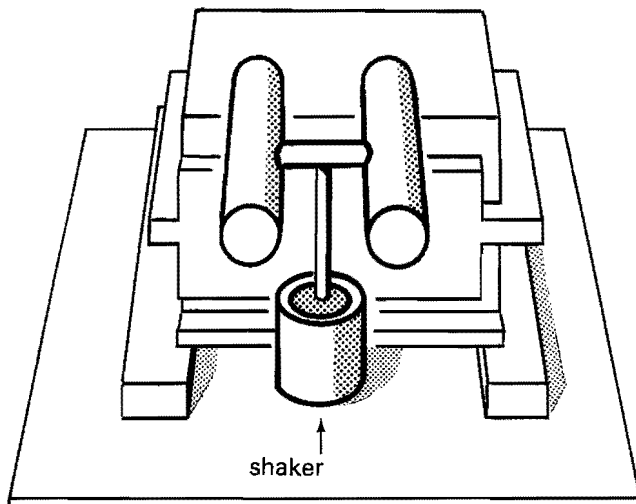


Figure 4.18:

Excitation of the gearbox model at the meshing point by a shaker.

in the calculation process. The transfer function $TF_F(f)$, which describes the relationship between force excitation at the meshing point and the surface velocity level $L_v(f)$ of a gearbox, is a crucial part of the sound generation mechanism. When the excitation level at the gear mesh is known (see Chapter 2) this relationship can be used in order to calculate the velocity level at the gearbox surface. .

In order to simulate a gear mesh excitation, the interior of the gearbox model was excited at the rod between the two shafts. For this purpose a shaker was used as is shown in Fig. 4.18. The velocity level $L_v(f)$ was calculated by using as many as 183 points to obtain the spatially averaged velocity level as accurately as possible. The measurements were carried out with considerable less points (20) for time-saving reasons. Fig. 4.19 shows the measured and calculated transfer functions $TF_F(f) = L_v(f) - L_F(f)$ in 1/3-octave bands. The high levels at 1 kHz and 1.6 kHz which are predicted by the FEM model were not found during measurements. This is probably due to the fact that the damping coefficient used in the FEM calculations was too small. It was set at a frequency independent value of 0.002 after a few response functions had been measured.

The full Experimental Modal Analysis of the structure was carried out after the FEM calculations were performed. The modal damping coefficient of the single corresponding FEM vibration mode in the 1 kHz band proved to be as large as 0.014. This is seven times as large as was assumed for the FEM

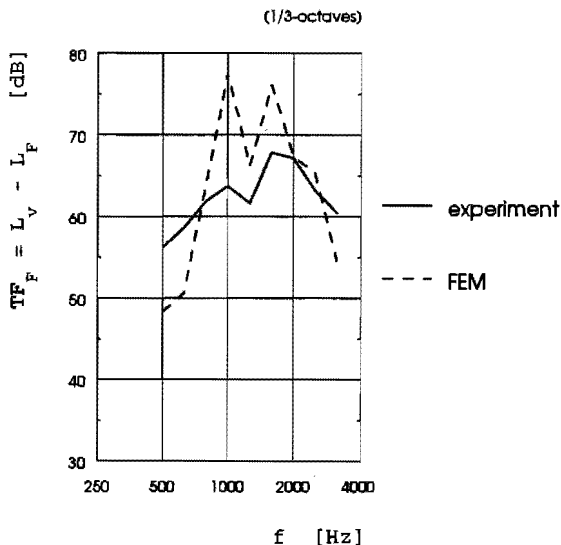


Figure 4.19:

Measured and calculated transfer functions TF_F of the gearbox model with shafts and bearings.

calculations. When taking this difference in damping coefficient in account, the calculated transfer function of the 1 kHz band can be corrected with $-10\log(7) = -8.5$ dB to a value of 69.1 dB instead of 77.6 dB as Fig. 4.19 shows. From this it may be concluded that correct damping coefficients are very important for accurate FEM calculations of the transfer function.

Also the fact that only 19 of the 45 calculated modes could be identified by the use of EMA, gives an indication that only modes with small damping coefficients could be distinguished. The other 16 modes calculated with FEM proved to have even higher damping coefficients than the 19 modes that could be appointed to calculated modes. In the FEM calculation these 16 modes contribute probably too much to TF_F . The experimental observations show that the damping coefficient of the gearbox model with shafts and bearings is highly dependent on the vibration modes and is certainly not frequency independent as was assumed for the FEM calculations.

This shows how difficult it is to predict $TF_F(f)$ of such a complex structure with shafts and bearings. The empty gearbox model can be modeled quit well, but when shafts and bearings are added to the model and crudely estimated frequency dependent damping values are used, the FEM predictions prove to be rather poor.

A gearbox is normally excited at the tooth frequency and its higher harmonics as is pointed out in Chapter 2 of this thesis. It will be shown in Chapter 5 that for the used gearbox variants, the tooth frequency determines the overall velocity level and the radiated sound power level at given operational conditions, i.e. running speed n and torque load T . Therefore, for predicting the overall velocity level L_v only the levels of $L_\omega(f)$ (or $L_F(f)$ for force excitation) and the transfer function $TF_\omega(f) = L_v(f) - L_\omega(f)$ (or $TF_F(f) = L_v(f) - L_F(f)$) have to be known at the tooth frequency. The overall velocity level can be calculated by combining source strength and transmission data. In the case of the gearbox model which is a 80 % scale model of the test gearbox of Chapter 5, which is run from zero to 1500 rev/min (gear pinion) with corresponding tooth frequencies of zero to 600 Hz, the gearbox model is assumed to be excited at tooth frequencies which lie $1/0.8 = 1.25$ times higher. This means that the gearbox model would be subject to tooth frequencies from zero up to 750 Hz.

When this is taken into account and when calculations at the tooth frequency are performed using both calculated and measured curves of Fig. 4.19, then the resulting overall vibration levels L_v would consistently differ by roughly 8 dB for tooth frequencies up to 710 Hz which is the upper boundary for the 1/3-octave band of 630 Hz. For tooth frequencies up to 750 Hz the differences are considerably less: 2 dB.

The conclusion is that this type of FEM calculations are not yet good enough to predict accurate overall velocity levels which are relevant for the sound production of a gearbox. This is seen from the fact that the differences between calculation and measurement of Fig. 4.19 are too large for a large part of the frequency range of vital interest, i.e. up to 750 Hz. This frequency range covers frequency bands which contain no or only a few eigenfrequencies. From the studies which were made in this chapter it follows that the prediction of the transfer function $TF_F(f)$ in this frequency range needs further investigations.

In the frequency range above the tooth frequency the calculated transfer function of the gearbox model shows higher levels than those measured. For this frequency range a better estimation or measurement of the damping coefficient seems the answer to the improvement of the theoretical modeling of the transfer function. However, this frequency range is of less practical importance when vibration transfer functions are concerned of gear transmissions because, as will be seen in Chapter 5, the tooth frequency typically determines the overall vibration and sound levels.

4.7 Sound radiation

The last part of the vibration and sound transmission chain of gear transmissions is the sound radiation by the vibrating gearbox housing as is shown in Fig. 4.20. Although it may be said that the mechanism of generation of sound by surface vibration is common to all kind of sources, the effectiveness of radiation in relation to the amplitude of vibration may vary widely for different types of sources. For a vibrating surface in order to radiate sound effectively, it must not only be capable of compressing or changing the density of the fluid with which it is in contact, but must do so in such a manner as to produce significant density changes in the fluid remote from the surface. Surfaces vibrating in contact with air displace air volume at the interface. Consequently it is sensible to investigate the sound field generated by the air volume displacement produced by a small element of a vibrating surface. By the principle of superposition one would expect to be able to construct the field by summation of the fields from elementary sources distributed over the entire surface. Although such an exercise seems simple at first, it is generally not so, because the field generated by an elementary source depends upon the geometry of the whole surface of which it is a part, and upon the presence of any other bodies in the surrounding air. However, there are many cases of practical importance to which a relatively simple theoretical expression applies with reasonable accuracy.

Especially for rather compact box-like structures Föller and a number of other researchers from the Technical University of Darmstadt have developed powerful approximation models, which enable a quick estimation of the sound power when the vibration levels on the radiating surface are known (/4.12/, /4.13/ and /4.14/). The main results of their work will be quoted here and applied to compare with some of our experimental results to prove their relevance and accuracy. Also the advantages and the limitations of this type of modeling will be evaluated (see Chapter 6).

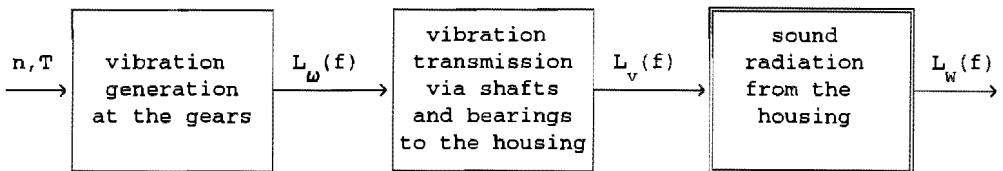


Figure 4.20:
Sound generation scheme of a gear transmission.

It is shown in books on acoustics (see e.g. /4.14/ and /4.15/) that the sound power of a uniform radially pulsating sphere of radius R at frequency f can be written as

$$P = 2\pi\rho c R^2 v_R^2 \frac{(f/f_s)^2}{1 + (f/f_s)^2} \quad [W] \quad (4.6)$$

where v_R is the radial velocity amplitude at the surface and f_s is the transitional frequency of a pulsating sphere.

$$f_s = \frac{c}{2\pi R} \quad [\text{Hz}] \quad (4.7)$$

Eq. (4.6) shows the following properties:

1. At frequencies below f_s ($f \ll f_s$) the emitted sound power is small. The reason is that at these low frequencies the inertia of the surrounding air is too small to generate pulsating compression. This occurs only at higher frequencies. At low frequencies the air close to the sphere is locally just moving in and out.

2. For $f \gg f_s$ the term $(f/f_s)^2 / (1 + (f/f_s)^2)$ of Eq. (4.6) approaches unity. The term $2\pi\rho c R^2 v_R^2$ thus represents the maximum emitted sound power. The power level at $f = 2 \cdot f_s$ is 1.0 dB less. From this frequency on the radiated sound power level deviates less than 1 dB from the maximum radiated power.

3. When the transitional frequency f_s of a pulsating sphere is increased with the excitation frequency f kept constant, the radiated sound power P decreases. Eq. (4.7) shows that f_s increases for decreasing R. Therefore, to minimize the radiation of sound power by a pulsating sphere the dimensions have to be as small as possible.

The radiation efficiency σ of a structure is defined as:

$$\sigma \stackrel{\text{def}}{=} \frac{P}{\rho c S \cdot \overline{v^2}} \quad [-] \quad (4.8)$$

where $\overline{v^2}$ is the surface-averaged mean square velocity of the surface area S. For the pulsating sphere the rms velocity is $\tilde{v} = v_R / \sqrt{2}$ and the total surface area $S = 4\pi R^2$. Identical velocities occur at every point of the

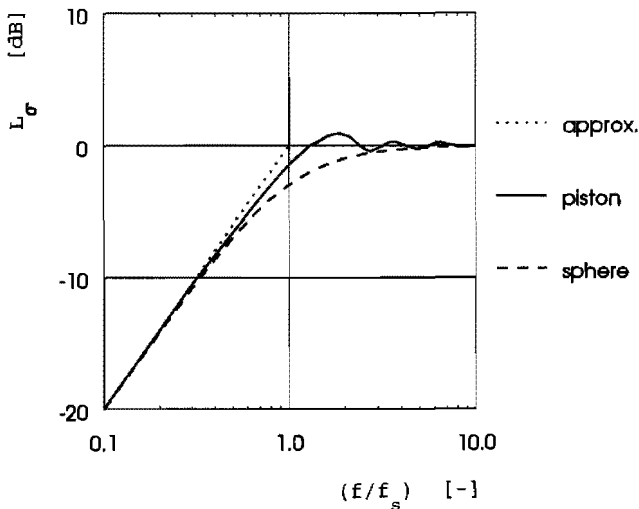


Figure 4.21:

Radiation index $L_\sigma = 10 \log \sigma$ of a pulsating sphere (radius R) and a baffled piston (radius a) with $R = a/\sqrt{2}$.

sphere so that $\tilde{v}^2 = \tilde{v}^2 = v_R^2/2$. Therefore, using Eqs. (4.6) and (4.8) the radiation efficiency of a pulsating sphere can be written as:

$$\sigma_s = \frac{(f/f_s)^2}{1 + (f/f_s)^2} \quad [-] \quad (4.9)$$

Fig. 4.21 shows the radiation index $L_\sigma = 10 \log \sigma$ of the pulsating sphere as function of the normalized frequency (f/f_s) . For $f > f_s$ the radiation index approaches to 0 dB. For lower frequencies it is almost equal to the straight dotted line which represents the approximation $\sigma \cong (f/f_s)^2$ so that in this frequency range L_σ increases with 20 dB per decade. Often this approximation with two straight lines is used instead of Eq. (4.9) and by doing so a maximum error of 3 dB occurs at $f = f_s$. Here a doubling of the actual radiated sound power is predicted using the approximation.

The model of a rigid circular disc vibrating transversely to its plane in a coplanar rigid baffle is called a baffled piston. The radiation index can be expressed in a similar manner as was done for the pulsating sphere. For a piston with radius a , the result is closely equal to that for a sphere when $a = R\sqrt{2}$. For this value of radius a it holds that $f_s = f_p$, because:

$$f_p = \frac{c\sqrt{2}}{2\pi a} = \frac{c}{\sqrt{2}\pi S} \quad [\text{Hz}] \quad (4.10)$$

The result is shown in Fig. 4.21 where it can be seen that the curves for both radiators are closely equal. However, the radiation index of the baffled piston reaches values greater than 0 dB due to extra energy radiated by the edges of the piston into the radial direction.

For both cases the radiation index becomes close to 0 dB when half the wavelength λ becomes about as large as the maximum distance between opposite parts of the source. For a sphere one has: $\pi R = 0.5\lambda$ at $f = f_s$ and for a piston: $2a = 0.5\lambda$ at $f = f_p$. Large structures are therefore better sound radiators at low frequencies than small structures.

Somewhat more complex radiation mechanisms are present for plate-like structures. For the purpose of estimating their sound radiation characteristics, many structures of practical interest may be modeled rather accurately by rectangular flat plates. Flexural-mode patterns of such rectangular panels take the general form of adjacent regions of roughly equal area and shape, which vary alternately in vibrational phase and are separated by nodal lines of zero vibration. The radiation efficiency depends on the ratio of acoustic wavenumber to structural wavenumber. When the structural bending wavelengths are smaller than the corresponding wavelengths in air, the sound radiation efficiency is below unity. This is due to the cancellation of the sound pressures by adjacent plate regions. The corresponding regions of opposite phase of the panel constitute dipoles or quadrupoles that are much less efficient sound radiators than pure volume velocity (monopole) sources. Hence, the low-frequency radiation efficiency is far less than the baffled piston equivalent. This cancellation effect decreases as frequency increases and the acoustic wavenumber approaches the structural wavenumber.

The radiation efficiencies of the pulsating sphere and of the baffled piston can be obtained analytically, but this is not generally possible for structures like gearbox houses. It is normally impossible to find a simple analytical expression for the radiation efficiency corresponding to arbitrary single-frequency excitation, because a number of modes will respond simultaneously, each vibrating with a different amplitude and phase. Therefore, it is more usual to try to estimate the average radiation efficiency of the modes having their eigenfrequencies within a certain frequency band.

For this purpose it is necessary to assume a distribution of vibration amplitudes, or energies, over the modes. On this basis the model for the radiation index of plate-like structures such as gearbox housings can be divided in three parts of the frequency range; one for a baffled piston at low frequencies, one for full radiation at high frequencies and an optional one for plates with acoustic cancellation at intermediate frequencies. As examples the radiation indices of the model gearbox of the previous section and of the test gearbox of chapter 5 will be discussed.

The plates of a gearbox housing are acoustically coupled when they may not be considered as separate uncorrelated sound sources. At low frequencies the small and thick plated gearbox housing of the previous section and the gearbox housing of Chapter 5 will form such acoustically coupled structures. An approximation of the radiation efficiency can be made according to /4.12/. This approximation is shown in Fig. 4.22 where the radiation index $L_{\sigma}(f)$ is shown as an example. The estimated radiation index is the minimum of two curves: $L_{\sigma'_p}$ and $L_{\frac{\sigma'_{p1}}{\sigma'_p}}$. The solid curve for $\sigma'_p(f)$ is the radiation index of an equivalent baffled piston which can be constructed as follows. At the mean critical frequency \overline{f}_c the point P can be calculated as

$$\sigma'_p(\overline{f}_c) = 1.13 \cdot \overline{U} \cdot \overline{f}_c / c \quad (4.11)$$

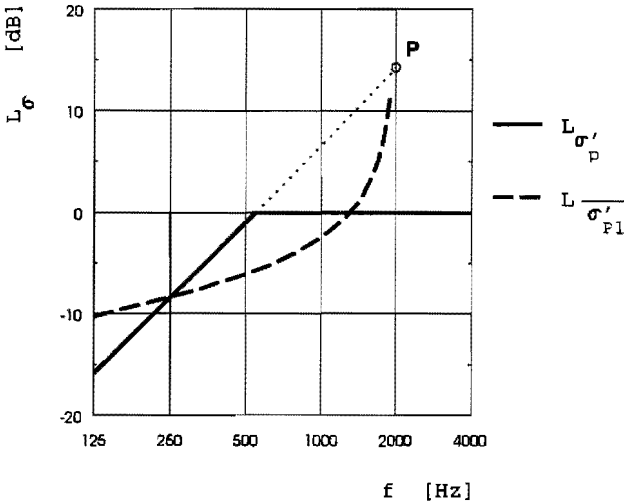


Figure 4.22:

The approximation curves for the radiation index of a box-like structure.

For this example the mean critical frequency \overline{f}_c is 2000 Hz.

A straight line with a slope of 25 dB/decade can be constructed through point P. The part of this line below 0 dB is the estimated radiation index at low frequencies. For frequencies where this line exceeds the 0 dB level, the estimated radiation index is taken to be 0 dB.

The mean perimeter \bar{U} of the plates of the gearbox housing and the mean critical frequency \bar{f}_c have to be known in order to calculate point P. The mean critical frequency \bar{f}_c can be calculated as follows:

$$\bar{f}_c = \left(\frac{\bar{U}}{U/f_c^{3/2}} \right)^{2/3} \quad [\text{Hz}] \quad (4.12)$$

For steel and aluminium the critical frequency f_c of a homogeneous plate is only dependent on the thickness of the plate: $f_c \cong 12/h$ Hz, when h is in meters. Eq. (4.12) can be used for box-like structures with plates of various thicknesses to obtain a mean critical frequency \bar{f}_c of the structure.

Above a certain frequency the plates of the housing are acoustically uncoupled and acoustic cancellation can occur. The broken curve in Fig. 4.22 is more complicated and can be calculated by using the radiation efficiencies of the separate plates of the structure for the case of acoustic cancellation. This results in a mean radiation efficiency $\bar{\sigma}'_{Pl}$ of the plates which is defined as follows:

$$\bar{\sigma}'_{Pl} = \frac{\sum \sigma'_{Pl_i} S_i \bar{v}_i^2}{\sum S_i \bar{v}_i^2} \quad (4.13)$$

The individual radiation efficiencies σ'_{Pl_i} of the plates are:

$$\sigma'_{Pl_i} = \frac{Uc}{4\pi^2 S_i f_{c_i}} \cdot \frac{(1-\alpha_i^2) \ln((1+\alpha_i)/(1-\alpha_i)) + 2\alpha_i}{(1-\alpha_i^2)^{3/2}} \quad (4.14)$$

$$\text{with } \alpha_i = (f/f_{c_i})^{1/2}$$

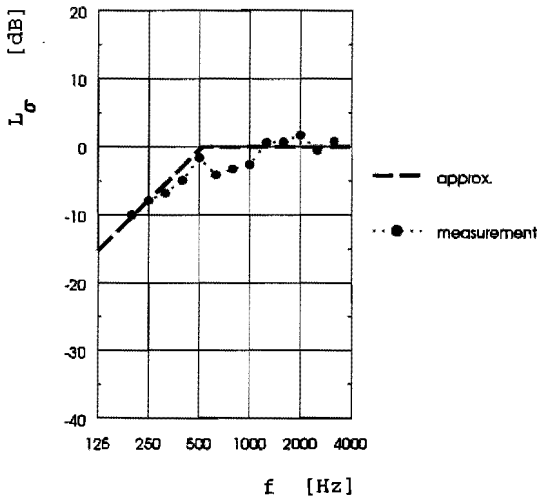


Figure 4.23:
Radiation index L_σ of the
model gearbox of section 4.6.

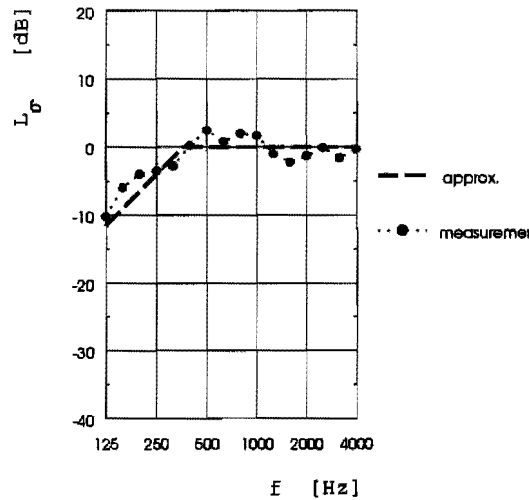


Figure 4.24:
Radiation index L_σ of the
test gearbox of Chapter 5.
(see also section 5.5)

However, when the plate area S decreases or the plate thickness h increases, the radiation efficiency $\overline{\sigma'_{Pl}}$ will increase to 1 ($= 0$ dB) so that for thick and compact housings the radiation efficiency is only determined by $\overline{\sigma'_P}$ at frequencies below $\overline{f_c}$ and no acoustic cancellation occurs. This is true when the following relation holds:

$$\frac{c^2}{\overline{S_P} \cdot \overline{f_c}^2} > 1.31 \quad (4.15)$$

with $\overline{S_P}$ the mean plate area.

The model gearbox of the previous section and the test gearbox of Chapter 5 are examples of such compact housings. The radiation indices of these gearboxes are shown in Figs. 4.23 and 4.24 respectively. The calculations which were performed to obtain these results are presented in Appendix E. Fig. 4.23 shows the calculated approximation for the gearbox model together with the measured radiation index. The measurement of L_σ consisted of a sound power level measurement according to DIN 45635 /4.16/ with nine microphone positions and a measurement of the velocity level L_v . The radiation index was calculated as follows:

$$\frac{P(f)}{P_0} = \frac{\rho c S \overline{v^2}(f)}{\rho c S_0 v_0^2} \cdot \sigma(f)$$

$$\text{or: } 10 \log \left(\frac{P(f)}{P_0} \right) = 10 \log \left(\frac{S}{S_0} \right) + 10 \log \left(\frac{\overline{v^2}(f)}{v_0^2} \right) + 10 \log(\sigma(f)) \quad [\text{dB}]$$

$$\text{or: } L_\sigma(f) = L_w(f) - L_v(f) - L_s \quad [\text{dB}] \quad (4.16)$$

$$\text{with } P_0 = 1 \cdot 10^{-12} \text{ W, } S_0 = 1 \text{ m}^2 \text{ and } v_0 = 5 \cdot 10^{-8} \text{ m/s.}$$

The total area of the gearbox model surfaces is 0.408 m^2 so that $L_s = -3.9$ dB. $L_w(f)$ and $L_v(f)$ were obtained with a shaker attached to the gearbox model interior (i.e. rotating elements) as described in section 4.6. White noise which covered the complete frequency range of interest was used as input signal. The resulting measured radiation index shows rather good agreement with the predicted radiation index as can be seen in Fig. 4.23.

Since the mean critical frequency $\overline{f_c}$ of the test gearbox of Chapter 5 is about 450 Hz and the tooth frequency of the meshing gears reaches as high as 600 Hz, the radiation index $L_\sigma(f)$ of the test gearbox is estimated to be 0 dB for the frequency range of main interest. This frequency range is namely determined by the tooth frequency and its higher harmonics up to 4 kHz. Its calculated and measured radiation index is shown in Fig. 4.24 where it can be seen that the radiation index is about 0 dB for frequencies above 365 Hz.

According to Eq. (4.8) the sound power level $P = \rho c S \overline{v^2} \sigma$. Therefore, it is the product of $\overline{v^2} \cdot \sigma$ which has to be minimized in order to design low noise gear transmissions. If a box-like structure, such as the test gearbox of Chapter 5, composes of plates with a radiation index $L_\sigma \cong 0$ dB would be modified in such a way that $L_\sigma \ll 0$ dB, this would imply severe modification of the stiffness of the housing. Therefore, probably $\overline{v^2}$ would increase and no significant reduction of $\overline{v^2} \cdot \sigma$ and thus of the radiated sound power would be obtained. Therefore, the use of the Boundary Element Method for calculating the sound radiation of this kind of gear transmissions, instead of the use of the described estimation method, would be unnecessarily cumbersome and not necessarily more accurate.

When noise reduction measures are of interest in the design of low noise gear transmissions, it must be concluded that none or only small benefit can be obtained from the point of view of the radiation index optimization in case of small and compact gearboxes. The reason is, as could be seen from the given examples, that in the frequency range of main excitation the radiation efficiency is at its maximum value and can not easily be reduced, because this would imply drastic changes in the housing stiffness. Other measures are likely to have a greater impact on the noise reduction such as minimizing the internal excitations (L_{ω}) and the vibration transmission towards the surface of the gearbox housing by altering the housing structure or using another bearing type.

4.8 Summary

From the literature no publications are known where predictions of the vibrational response of gearbox housings with gears and shafts are verified. This chapter investigates the computation of the free and forced vibrations of box-like structures with and without gears and bearings. This is accompanied with experimental modal analysis to examine the validity of calculated FEM results. It turns out that the FEM models require rather detailed meshes but that certain simplifications are allowed. For example, the bolt joints between upper and lower casing may be modeled by assuming a one-pieced gearbox structure and the gearbox feet can be modeled with foot node motions of which all six degrees of freedom have been suppressed. The importance of the use in the FEM modeling of full bearing stiffness matrices, has been made plausible. However, it was concluded that the prediction of forced responses of gearboxes with shafts and bearings inside is at present insufficiently accurate for design purposes and needs further investigations.

Since the investigations of this chapter show that the modeling of empty gearbox housings is rather accurate in terms of eigenfrequencies, eigenmodes and forced vibrations, it seems for the time being useful to study optimization of gearbox housings without the gears, shafts and bearings inside and for force and moment excitations at the bearing positions to get low velocity responses on the housing surface.

The modeling of the sound radiation efficiency of a gearbox housing was briefly investigated. The radiation efficiency proved to be equal to unity

for a large part of the frequency range of interest for compact gearbox housings as the one that is used in Chapter 5. This value approximates the maximum value which will be found for a box-like structure. The radiation efficiency decreases only at frequencies well below the prevailing tooth frequencies. Therefore, it would seem obvious to try to reduce the radiation efficiency of the gearbox housing structure. However, such a reduction would require rather unrealistic structural changes of the gearbox housing. Therefore, it was concluded that there is no room for noise level reductions in high power compact gear transmissions by reducing the radiation efficiency of the gearbox structure. Other noise reduction measures are likely to be more successful such as minimizing the internal excitations of meshing gears and the vibration transmission to the surface of the gearbox housing by modifying the housing structure or using another bearing type.

5. EXPERIMENTS

This chapter presents the results of noise and vibration measurements on a gear test rig. The test rig contains a single stage gear transmission in which different sets of gears have been installed, namely single and double helical gears with different profile corrections. Also different types of bearings have been installed.

One objective of the experiments is to investigate to what extent the results predicted by theoretical models developed in this thesis are confirmed. This concerns both the effect on noise of alteration of a single component and the quantitative analysis of the whole noise and vibration transmission chain. In addition the results give also a good indication of the bandwidth of sound power levels within which a certain gearbox can be optimized by an appropriate selection of components. This type of information may enable designers to evaluate the cost-effectiveness of certain measures.

5.1 Introduction

Noise and vibration control by predictive modeling ideally requires a computational model of the entire gearbox system, its attachments and other connected structures. This is due to the fact that the dynamics of each of the components, which serve as vibrational energy transfer paths, may have significant effects on the overall system dynamics. For example, the discrete frequency excitations generated by the meshing gears are transmitted through various structural parts such as the shafts, bearings, housing, mounts and other attachment points as said before in Chapter 4. There are no examples in the literature that offer a rigorous treatment on the overall gearbox dynamics which includes dynamic interactions between gear-shaft system, support bearings, gearbox housing, gearbox mounts and noise radiation. In most cases one or more components are modeled in detail and the other components are modeled with only a few degrees of freedom or are assumed uncoupled from the rest of the gearbox /5.1/.

This thesis makes contributions to an improved situation of modeling by looking in detail at the various parts of the sound generation and transmission chain and by using them for the overall sound power level prediction of a gear transmission.

The sound generation and transmission chain has been described in the previous sections of this thesis. It was divided into three parts: the vibration source (Chapter 2), the vibration transfer through bearings into the gearbox housing (Chapters 3 and 4) and the sound radiation (section 4.7). For all these separate parts theoretical calculations were performed and to some extent they were verified by experiments to investigate the relevance of the strategies followed.

In this chapter the three parts will be combined in order to investigate the behaviour of a complete gear transmission. For the purpose of experimental verification a test rig was developed on which various experiments were carried out. The test rig allowed well controlled measurements of vibration levels and sound power levels at different operational conditions such as running speed and torque load. Tests were carried out on four single helical and one double helical gear set. The single helical gears all had the same geometry but had different profile corrections. One of the single helical gear sets was used for experiments with different kinds of rolling element bearings. The double helical gears were used for two experiments, one with roller bearings and one with fluid film bearings. For all these gear sets the angular velocity levels at the gears, the velocity levels at the gearbox housing surface and the sound power level were measured. The measurements were used to partially validate the proposed theories of this thesis and also to evaluate the relative importance of certain low-noise design options in view of cost-effectiveness considerations.

5.2 The test rig

A single stage, high precision gear transmission was designed for the experiments. As this thesis focuses on high precision gears under high loads, the transmission had to meet the requirement that the unloaded Transmission Error (T.E.) had to be negligible, because it is assumed that the tooth deflections are several times as large as the profile errors. To realize this, the gears were hardened and ground in order to get within DIN-class 5, so that the maximum tooth profile errors were no more than a few micrometers. The tooth deflections were in the order of magnitude of 40 μm at a maximum tooth load of 41500 N, which corresponds with a torque load of 2000 Nm at the pinion and 6000 Nm at the gear wheel.

To exclude unwanted non-periodical signals in the measurements each

measurement existed of many data samples which were averaged. The transmission gear ratio was chosen to be an integer ($i = 3$). In this way the data samples which had a constant time length of 0.41 seconds could be taken quickly after each other by using a trigger point at the gear wheel. After each completed rotation of the wheel the same teeth meet in the gear mesh due to the integer transmission gear ratio. However, an integer transmission gear ratio is seldomly used in practice because it emphasizes the unloaded T.E. But as the unloaded T.E. of the test gearbox is very small in comparison to the tooth deflections, it is of no importance to the test rig situation.

The gears were designed for large tooth deflections as can be seen from the gear dimensions and operational conditions which are given in Appendix F. The reason for this choice is that this will result in a relatively small unloaded T.E. in comparison to the loaded T.E. The gearbox contains a pinion and a wheel which transmit 300 kW power at maximum torque load and running speed. These loads and speeds can be established accurately at any given value as will be described later on in this section.

The test gearbox was connected to a similar gearbox in a back to back configuration as is shown in Fig. 5.1. This auxiliary gearbox has the same transmission gear ratio of 3.0 but with different tooth numbers to prevent coinciding tooth frequencies of both gearboxes. The contribution of the auxiliary gearbox to the dynamic behaviour of the test gearbox, i.e. to the velocity levels $L_{\omega}(f)$ and $L_v(f)$ and to the sound power level $L_W(f)$ could hereby be eliminated. The ratio of the tooth frequencies of test and auxiliary gearbox is in proportion to the tooth numbers of the pinions respectively the wheels, namely 24 to 19 (or 72 to 57), independent of the speed.

$$f_{\text{tooth.test}} / f_{\text{tooth.auxiliary}} = 24/19 = 72/57 = 1.26 \quad (5.1)$$

In the measured narrow-band spectra these tooth frequencies and their harmonics could clearly be distinguished. The unwanted contributions of the auxiliary gearbox could be removed from the spectra by setting the corresponding spectral lines at $n \cdot f_{\text{tooth}}$ to the mean values of the adjacent narrow-band levels. After this 'spectrum cleaning' the 1/3-octave band spectra were calculated. However, this procedure proved to be necessary only for the tooth frequency of the auxiliary gearbox and now and then for a higher harmonic of this tooth frequency when it coincided with a eigenfrequency of the test gearbox structure. Mainly, this was thanks to the

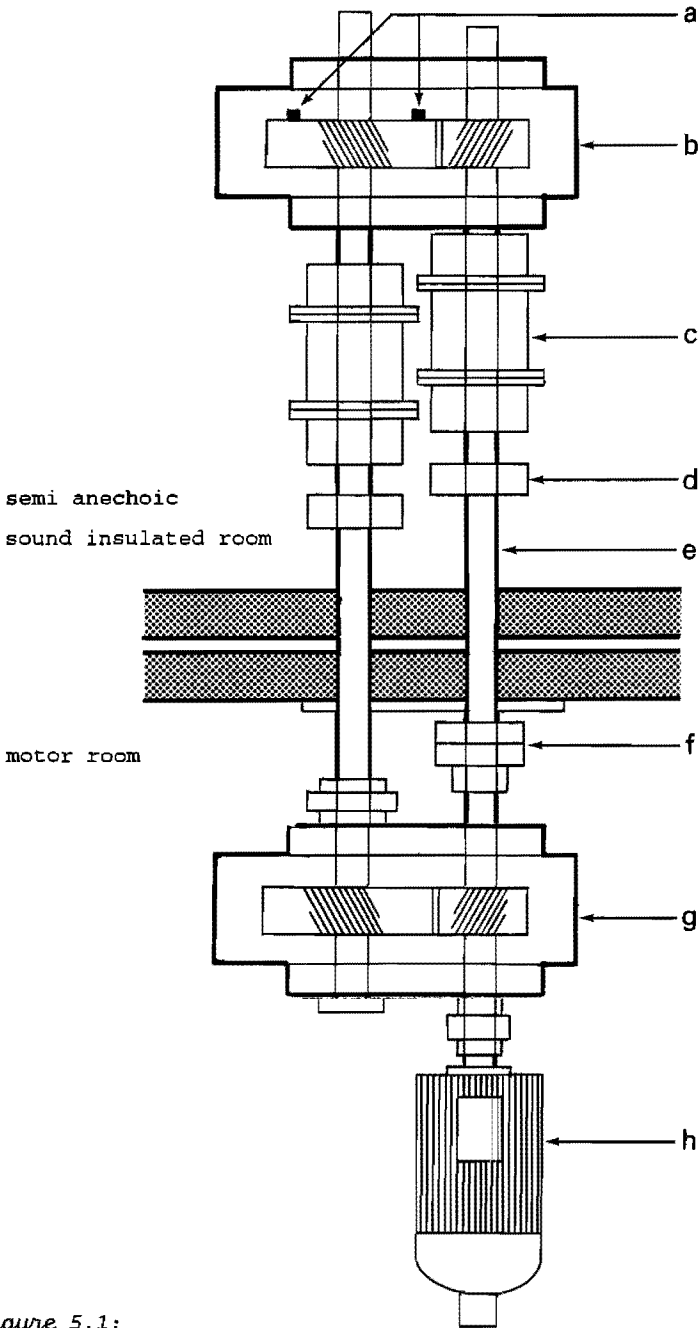


Figure 5.1:

Test rig with back to back arrangement of two gearboxes. The test gearbox was installed in a semi anechoic sound insulated room.

a. accelerometers, b. test gearbox, c. flexible coupling, d. supporting bearing, e. quill shaft, f. torque coupling, g. auxiliary gearbox, h. electric motor

long and torsionally flexible quill shafts between the two gearboxes that supplied a low eigenfrequency of the back to back test rig of about 50 Hz. The tooth frequencies and their harmonics are in practice always much higher than 50 Hz and therefore with these flexible shafts a good vibration isolation was created between the two gearboxes for these high frequencies. The test rig was driven by an electric motor which was attached to the pinion shaft of the auxiliary gearbox as is shown in Fig. 5.1. As it concerns a back to back test rig the electric motor only has to provide the energy losses of the test rig. While a maximum power of 300 kW could be transmitted through the test gearbox the electric motor only has to deliver a few percent of this power. The motor was chosen to have a maximum power of 20 kW which proved to be sufficient under any given operational condition. The running speed of the electric motor could be set to any value between 0 and 1500 rev/min by the use of a frequency controlled power unit. The torque load could be adjusted at standstill by the use of the specially designed torque coupling which is positioned at the pinion quill shaft near the auxiliary gearbox. This coupling consists of two flanges with a rolling element bearing inside connecting the two flanges. The flanges can be bolted to each other at any given angular position giving the test rig a specified torque load at the pinion quill shaft with at the same time a three times larger torque load at the wheel shaft. Steel profiles of 2 meter length were bolted to the flanges to provide the angular displacement. At one profile a load of 0 to 100 kg could be hung while the other profile was lifted until the first profile was in equilibrium. At that position the torque loads are known under the condition that the test rig frictional resistance is negligible. This is the reason for choosing the rolling element bearing between the flanges. The applied torque loads were also monitored by the use of strain gauges which were fixed on the pinion quill shaft.

The pinion and wheel quill shafts were connected to the test gearbox by flexible couplings which allow slight movements in five degrees of freedom. In this way the test gearbox is provided with a pure torque load and with no other unwanted moments or forces. This guarantees that the boundary conditions were as they were assumed to be in the dynamical calculations of Chapter 2.

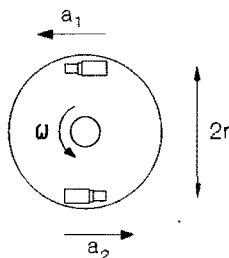
The sound power level of the test gearbox was measured with eight microphones positioned on a fictitious box-like area around the test gear unit. To get test circumstances for reliable sound power measurements the test

gearbox was installed in a semi anechoic sound insulated room. This room was vibration isolated from the building using rubber isolators. To eliminate any background noise caused by the auxiliary gearbox and by the electric motor, these were installed in a separate motor room. As can be seen in Fig. 5.1 the two quill shafts were led through a double brick wall. Care was taken to prevent any harmful mechanical contact. At both walls an array of lip seals on the shafts was used to prevent as much as possible sound transmission from the motor room into the test room.

5.3 Angular velocity level $L_{\omega}(f)$ at the gears

The first part of the sound generation and transmission chain of gear transmissions is the vibration production at the gear mesh. As stated in Chapter 2 of this thesis these vibrations are a result of the time variable tooth stiffness and the engagement shocks. The dynamical behaviour of the gears with their bearings and connected shafts was predicted by the lumped parameter model described in Chapter 2. It resulted in an angular velocity level $L_{\omega}(f)$ at the gears which is dependent on the gear dimensions as well as on the operational conditions such as running speed and torque load. To facilitate the validation of the predictions the angular velocity level $L_{\omega}(f)$ was calculated and measured at the wheel which provides more space for the attachment of accelerometers than the pinion.

For the measurements the accelerometers were positioned in opposite positions and directions near the rim of the wheel at a radius of 136 mm. They measured the circumferential accelerations (see sketch). Both accelerometers recorded the vibrations of the wheel plus the change in gravitational acceleration which provided a sinusoidal signal at the rotation frequency superimposed on the gear vibrations. This unwanted gravitational acceleration was eliminated by summation of both time signals and dividing them by two:



$$\frac{d\omega}{dt} = \frac{a(t)}{r} = \frac{a_1(t) + a_2(t)}{2r} \quad [\text{rad/s}^2] \quad (5.2)$$

The angular velocity $\omega(f)$ was obtained after an integration of $d\omega/dt$. Four data blocks with 4096 points each were taken to get a smooth estimate of the mean square angular velocity $\tilde{\omega}^2(f)$. The angular velocity level $L_\omega(f)$ is defined in Eq. (2.61).

The measurement data were obtained as a narrow-band frequency spectrum with $\Delta f = 2.44$ Hz from 0 to 5000 Hz from which a 1/3-octave band spectrum was calculated. Since an analog low pass filter was used that suppressed responses above 4.5 kHz, the resulting spectra show 1/3-octave bands up to 4 kHz.

Fig. 5.2 shows the measured angular velocity level $L_\omega(f)$ of the single helical gear set with profile correction A (which will be called gear set A from now on) at three different running speeds and maximum torque load of 2000 Nm (see Appendix F for detailed information about the test gears used). At the tooth frequency a high peak can be observed for each speed. The spectra are dominated by the 1/3 octave band in which the tooth frequency lies. The relationship between the running speed n_1 (or simply called n) of the pinion and the tooth frequency is straightforward:

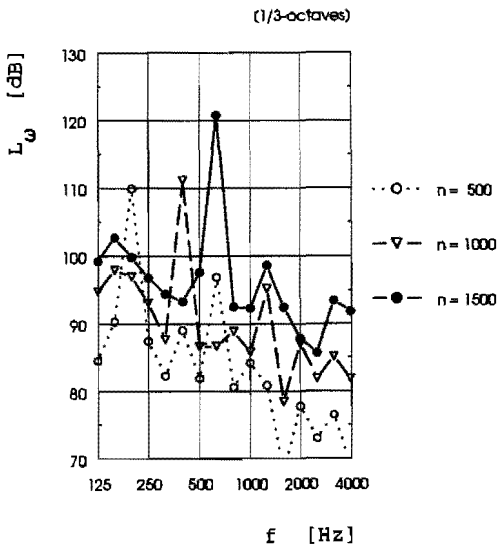


Figure 5.2:
Measured angular velocity level L_ω of gear set A at maximum torque load ($T = 2000$ Nm) for three different running speeds of the pinion.

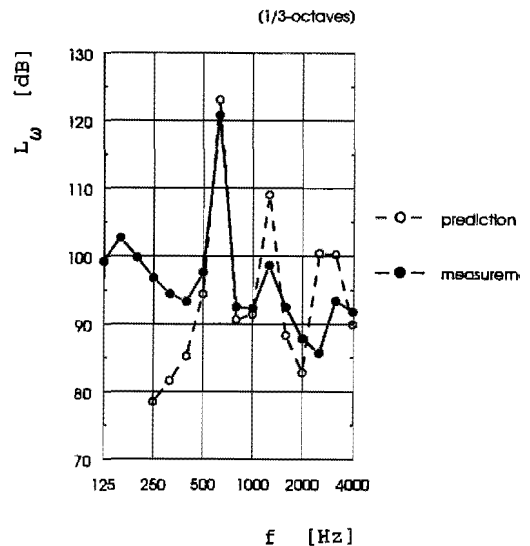


Figure 5.3:
Predicted and measured angular velocity level L_ω of gear set A at maximum load and speed ($T = 2000$ Nm and $n = 1500$ rev/min).

$$f_{\text{tooth}} = n_1 \cdot z_1 / 60 = n \cdot 24 / 60 = n \cdot 0.4 \quad (5.3)$$

in the case of the single helical gear sets). Therefore, the tooth frequencies in Fig. 5.2 are 200, 400 and 600 Hz respectively. It can be seen that the vibration levels at all 1/3-octave bands increase with the running speed n .

Fig. 5.3 shows the measured and calculated angular velocity level $L_\omega(f)$ at maximum power of 300 kW of gear set A. The calculation using the modeling of Chapter 2, predicts high peak levels at the frequency bands of the tooth frequency and its higher harmonics. The measured vibration levels at the second and third harmonic of f_{tooth} are smaller than those predicted. However, these higher order frequency bands are of less importance because the tooth frequency band determines the overall angular velocity level L_ω . It will be shown in the next sections that the peak at the tooth frequency determines the overall vibration level and thereby is of main interest for further calculations. The predicted peak at the tooth frequency of Fig. 5.3 differs by 2.3 dB from the measured level. Somewhat larger differences between measured and calculated levels were obtained for many other operational conditions of the gear unit as is shown in Fig 5.4.

Fig. 5.4 shows the angular velocity level L_ω of gear set A as function of the running speed of the pinion. In this Figure only the angular velocity levels of the 1/3-octave band in which the tooth frequency lies are taken

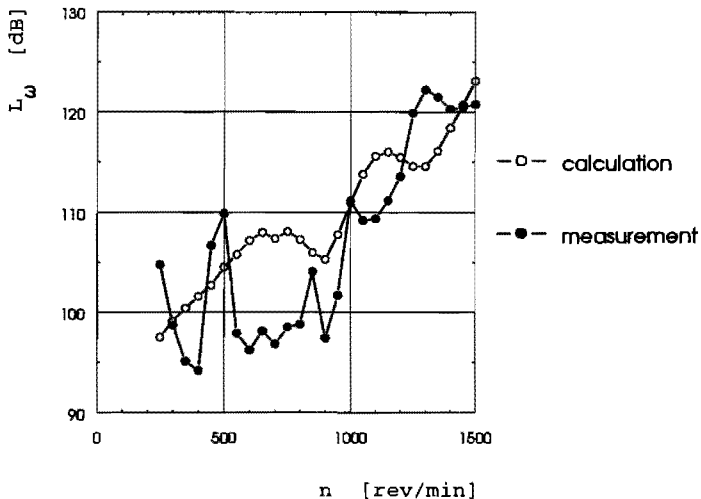


Figure 5.4:

Measured and calculated angular velocity level L_ω at tooth frequency of gear set A as function of the running speed n of the pinion ($T = 2000 \text{ Nm}$).

into account. This is justified by the fact that the tooth frequency dominates the overall angular velocity level.

The three curves of Fig. 5.2 are reduced to three points in Fig. 5.4 which are situated at $n = 500, 1000$ and 1500 rev/min. These levels are 109.9, 111.2 and 120.8 dB respectively. The figure also shows that the curves are not particularly smooth but have peaks due to resonances. Because the measurements were taken at r.p.m. intervals of 50 rev/min, the measured curve in Fig. 5.4 has a limited resolution.

With increasing running speed the angular velocity level fluctuates sometimes by 10 dB. This figure shows the dependence of the angular velocity level on the running speed of a gear transmission. In the literature most investigators leave this feature out when presenting their results. Mostly, conclusions are drawn from measurements at maximum operational conditions without considerations of structural resonances as they can be seen in Fig. 5.4.

From Fig. 5.4 it can be seen that the calculated L_{ω} also shows the influence of resonances but at different running speeds than those that were measured. However, especially in the noisy speed range above 800 rev/min (see Fig. 5.15) the mean level of the measured and calculated angular velocity levels are about the same and the differences not more than a factor of about 2. The figure shows that the calculations are useful when the maximum level is taken. For those gear transmissions which are being operated at varying running speeds, a calculated maximum angular velocity level seems to be a useful tool for predicting the vibration generation of gear transmissions.

The differences in measured and calculated angular velocity levels are at least partially due to the fact that the lumped parameter model of Chapter 2 is incomplete. The main reason is the assumption of a rigid gearbox housing. The lumped parameter model uses the bearing stiffnesses but neglects the flexibility of the housing. This is certainly incorrect in view of the test results that have been reported in section 4.6.

Whether or not the calculation method is still useful to predict the effects of modifications of the gears or bearings on noise production will be investigated in later sections of this chapter.

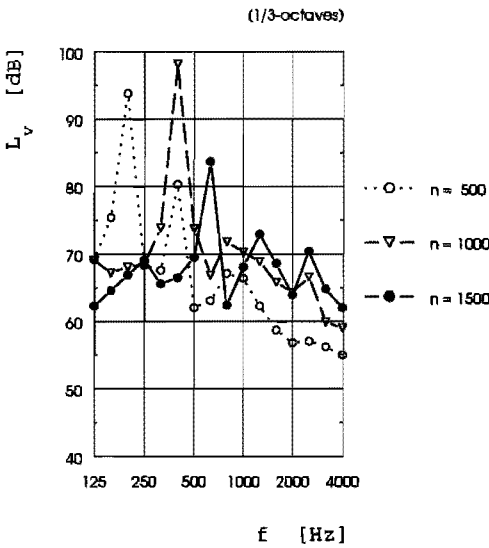


Figure 5.5:
Measured velocity level L_v of the housing for gear set A at maximum torque load ($T = 2000$ Nm) for three different running speeds of the pinion.

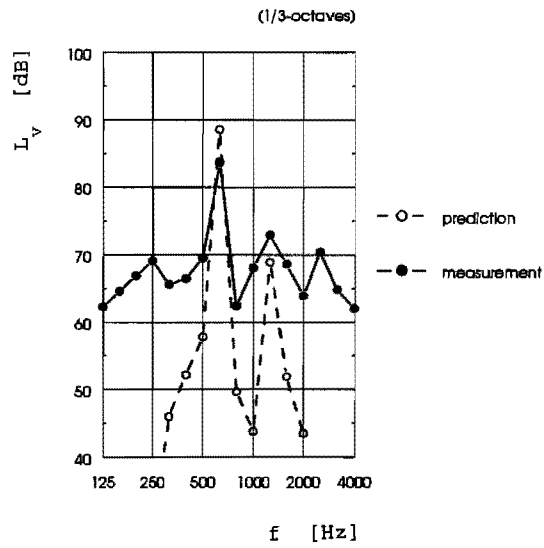


Figure 5.6:
Predicted and measured velocity level L_v of the housing for gear set A at maximum torque load and running speed ($T = 2000$ Nm and $n = 1500$ rev/min).

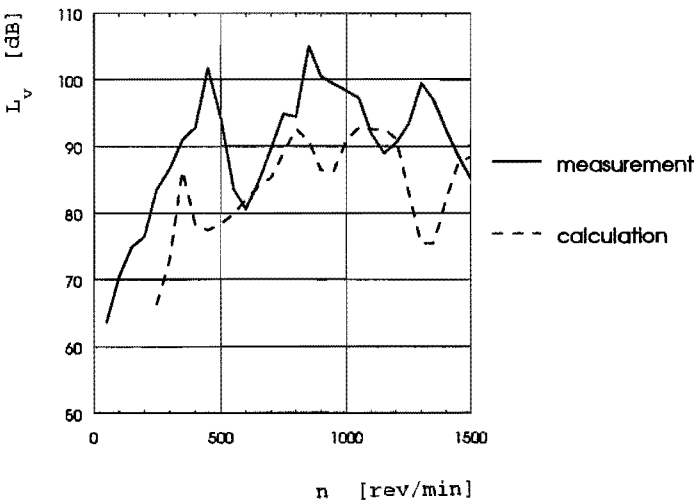


Figure 5.7:
Measured and calculated velocity level L_v at tooth frequency of the housing for gear set A as function of the running speed n of the pinion at maximum torque load ($T = 2000$ Nm).

5.4 Velocity level $L_v(f)$ at the gearbox housing surface

The second part of the sound generation and transmission chain of gear transmissions is the vibration transfer from the gears into the gearbox housing which will initiate vibrations at the gearbox surface with a velocity level $L_v(f)$ as described in Chapter 4. The velocity level of the test gearbox was measured with eight accelerometers distributed over the gearbox housing surface. Each accelerometer position was assigned to a certain surface area S_i of the housing. The surface weighted velocity level $L_v(f)$ over eight partial areas results from the following equation:

$$L_v(f) = 10 \log \left(\frac{\overline{\tilde{v}^2}(f)}{v_0^2} \right) = 10 \log \left(\sum_{i=1}^8 \gamma_i \cdot \frac{\tilde{v}_i^2(f)}{v_0^2} \right) \quad [\text{dB}] \quad (5.4)$$

$$\text{with } v_0 = 5 \cdot 10^{-8} \text{ m/s}$$

$$\gamma_i = S_i / S_{\text{tot}}$$

Just like in the previous section, the velocity data were analysed using a narrow-band spectrum with $\Delta f = 2.44$ Hz. From this narrow-band spectrum a 1/3-octave band spectrum was calculated as, for example, Fig. 5.5 shows for gear set A. The same operational conditions are taken as in the previous section, using maximum torque load $T = 2000$ Nm and running speeds $n = 500$, 1000 and 1500 rev/min. The 1/3-octave bands in which the tooth frequency (200, 400 and 600 Hz) and their second harmonic (400, 800 and 1200 Hz) lie show clear peaks for the three curves.

Again the 1/3-octave band in which the tooth frequency lies, dominates the overall velocity level as was observed in the previous section for the angular velocity level $L_\omega(f)$. Nevertheless, the velocity levels $L_\omega(f)$ and $L_v(f)$ show relative differences due to the dynamical behaviour of the bearings and the gearbox housing. The angular velocity level $L_\omega(f)$ of Fig. 5.2 increases with increasing running speed. In contrast, the velocity level $L_v(f)$ of Fig. 5.5 shows a smaller peak for $n = 1500$ rev/min at the tooth frequency of 600 Hz than for lower running speeds. The highest measured overall velocity level is not reached at the maximum speed but at $n = 850$ rev/min as Fig. 5.7 shows. This figure illustrates the strong dependency of the velocity level on the structural behaviour of the gearbox. Three speeds result in high measured levels at maximum torque load, these are 450, 850 and 1300 rev/min which correspond with tooth frequencies of 180, 360 and 550 Hz. They coincide with eigenfrequencies of the gearbox.

At this place it should be noticed that the high velocity levels at the lower running speeds will not necessarily result in high sound power levels. The lower value of the radiation index of the test gearbox which is shown in Fig. 4.24, will decrease the sound power level below frequencies of 366 Hz. But more important is the A-weighting of the sound power level which decreases the levels at frequencies well below 1kHz significantly. Fig. 5.6 shows the predicted and measured velocity level $L_v(f)$ at maximum operational conditions, i.e. 300 kW power. Again the tooth frequency and its second harmonic are clearly distinguishable. The prediction was done using the FEM calculation of the transfer function $TF_\omega(f)$, using the calculated angular velocity level $L_\omega(f)$ of the wheel as input and with $L_v(f)$ as output.

$$TF_\omega(f) = 10 \log \left(\frac{\overline{v}^2 \cdot \omega_0^2}{\omega^2 \cdot v_0^2} \right) = L_v(f) - L_\omega(f) \quad [\text{dB}] \quad (5.5)$$

The FEM calculations were carried out using a sinusoidal torque with amplitude of 1 Nm and frequency f which was applied at the wheel centre point. The velocity levels $L_v(f)$ and $L_\omega(f)$ were calculated in order to obtain the transfer function $TF_\omega(f)$ according to Eq. (5.5). The calculations were performed using a frequency independent modal damping coefficient ξ of 0.04 and using eight positions at the gearbox housing surface and one on the centre of the gear wheel. The damping coefficient of 0.04 was an averaged result of measured modal damping factors of a few frequency response functions of the gearbox housing. The eight points on the gearbox surface corresponded with the eight positions at which the measurements were carried out.

This transfer function was calculated for narrow-bands and was added to the calculated angular velocity level $L_\omega(f)$ according to Eq. (5.5). This resulted in a narrow-band spectrum of a velocity level $L_v(f)$ from which the 1/3-octave band spectrum was calculated.

Fig. 5.7 shows the running speed dependency of the measured and predicted velocity level L_v at the 1/3-octave band in which the tooth frequency lies. This is justified by the fact that the tooth frequency dominates the overall velocity level. It can be seen from this figure that the levels of the measurements are on average higher than those predicted. This is in accordance with what was found in Chapter 4 (see e.g. Figs. 4.5, 4.7, 4.10 and 4.19) where the predicted transfer function $TF_F(f)$ in the frequency

range of interest was too small. This frequency range is determined by the tooth frequency and lies in a region where no or only a few eigenfrequencies of the structure are present in a 1/3-octave band. A partial reason for these too low levels is possibly the neglect of modes with eigenfrequencies above 4 kHz as was stated in Chapter 4. Even when the maximum measured and predicted velocity levels are compared, a difference of about 10 dB is found.

The FEM calculation of the transfer function $TF_{\omega}(f)$ between angular velocity level $L_{\omega}(f)$ at the gear wheel and the velocity level $L_v(f)$ at the surface of the gearbox housing provides hereby not an accurate tool for predicting the vibration transfer between gear shafts and the gearbox housing surface. The low frequency modeling of the housing behaviour and the implementation of shafts and bearing stiffness matrices to the FEM model seems to be the bottle-neck for these kind of predictions as was also concluded for the scale model of Chapter 4. Therefore, more investigations should be made to improve the FEM modeling of gearbox housings with and without shafts and bearings.

5.5 Sound power level $L_w(f)$ of the test gearbox

For the purpose of sound power measurements a fictitious box was defined around the test gear transmission at 0.5 meter from its surfaces. According to DIN 45635 /5.2/ this measurement box should be at a distance of 1.0 meter from the gearbox but this would mean that the top and side areas of the measurement box came very close to the ceiling and walls of the semi anechoic sound insulated room. Therefore, it was decided to take a smaller measurement box. Special attention was paid to the fact that at these short distances from the noise source, the air pressure and velocity waves could be out of phase so that simple sound pressure measurements would not be sufficient to calculate the total emitted sound power of the gearbox. For this reason sound intensity measurements were performed simultaneously with the sound pressure measurements. At several operational conditions of the gear transmission it turned out that both measurements gave exactly the same results for the radiated sound power estimation. This meant that the smaller measurement box was still sufficiently large for sound power determination, using sound pressure measurements, so that the more complex sound intensity method could be omitted for the rest of the sound measurements.

The fictitious measurement box has four planes since the gearbox stands on a frame and the input and output shafts are shielded by a wooden box, both covered externally with sound insulating materials. Hence, four planes are left on which six microphones should be positioned according to DIN 45635, one at the middle of every plane and two in the corners of the box. Furthermore, DIN 45635 prescribes that the number of microphones should always be larger than the maximum difference in dB between the measured sound pressure levels. After a few measurements it was decided that according to this rule eight microphone positions were sufficient.

The sound power level $L_w(f)$ could be derived from the eight sound pressure measurements in the following way:

$$L_w(f) = 10 \log \left(\frac{\tilde{P}^2(f)}{P_0^2} \right) = 10 \log \left(\sum_{i=1}^8 \frac{\tilde{P}_i^2(f) \cdot S_i}{P_0^2 \cdot S_0} \right) \quad [\text{dB}] \quad (5.6)$$

$$\text{with } P_0 = 1 \cdot 10^{-12} \text{ W, } p_0 = 2 \cdot 10^{-5} \text{ N/m}^2 \text{ and } S_0 = 1 \text{ m}^2$$

The eight microphone positions were at almost equal distances to each other so that all surface areas S_i could be assumed to be the same: $S_i = S/8$. This leads to a further simplification of Eq. (5.6) since the total area of the measurement box is 3.95 m^2 :

$$L_w(f) = 10 \log \left(\sum_{i=1}^8 \frac{\tilde{P}_i^2(f)}{P_0^2} \right) - 3.1 \text{ dB} \quad (5.7)$$

Measurement results at different operational conditions of gear set A were processed according to Eq. (5.7). The results are shown in Fig. 5.8 for three running speeds at maximum torque load. The 1/3-octave bands in which the tooth frequency and its second harmonic lie can be distinguished clearly in the figure. Just like in the previous section with the velocity level $L_v(f)$, the overall sound power level $L_w(f)$ at maximum running speed is not the highest. The resemblance of Fig. 5.5 and Fig. 5.8 is remarkable but not unexpected since the sound radiation index $L_{\sigma}(f)$ is about zero dB for the whole frequency range of these figures as was shown in Chapter 4 of this thesis (see Fig. 4.24).

The predicted sound power level at maximum running speed and torque load is shown in Fig. 5.9 together with the results of the measurements. The

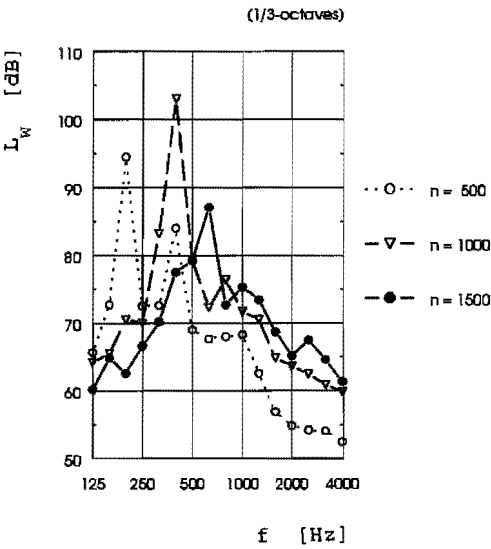


Figure 5.8:
 Measured sound power level L_W of gear set A at maximum torque load ($T = 2000 \text{ Nm}$) for three different running speeds of the pinion.

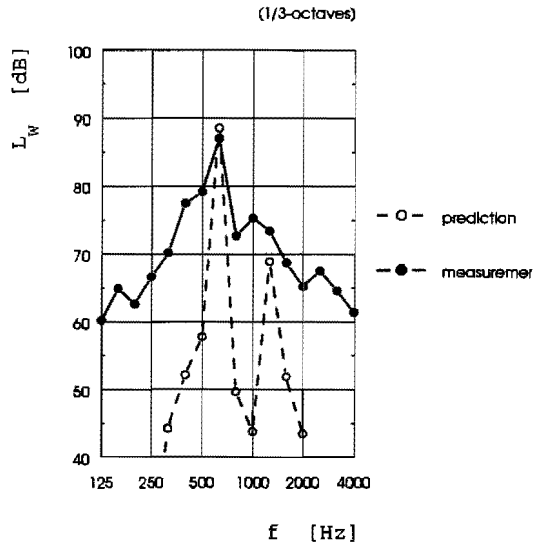


Figure 5.9:
 Predicted and measured sound power level L_W of gear set A at maximum torque load and running speed ($T = 2000 \text{ Nm}$ and $n = 1500 \text{ rev/min}$).

predicted curve resulted after calculation of the angular velocity level $L_\omega(f)$ and the velocity level $L_v(f)$ and by assuming a sound radiation efficiency $\sigma(f)$ of unity. Therefore, the prediction is entirely based upon theory apart from the fact that a frequency independent measured loss factor η of the structure was used for the calculation of $L_v(f)$. Hereby, the complete sound transmission chain has been described mathematically.

Fig. 5.10 shows the measured and predicted overall sound power level L_W of gear set A as function of running speed. Just like in the previous section this figure resembles Fig. 5.7 by showing three extremities around $n = 500$, 950 and 1350 rev/min . When comparing these two figures one should take notice of the difference in quantity which belong to the vertical axes. The sound power level was A-weighted to obtain a quantity which is in rather general use as a dose measure in relation to noise annoyance or hearing damage. This results in lower levels compared to linear (i.e. unweighted) levels, especially for the left part of the figure where the tooth frequency is low. At these low frequencies the A-weighting has a significant decreasing effect.

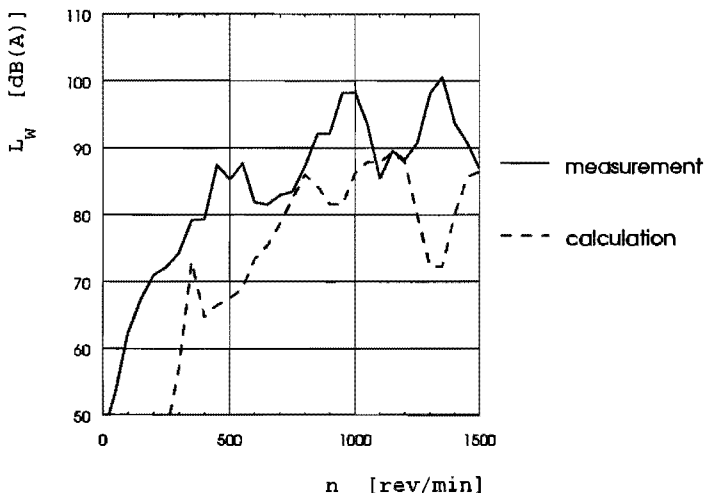


Figure 5.10:

Measured and calculated A-weighted sound power level L_w of gear set A as function of the running speed n of the pinion ($T = 2000 \text{ Nm}$).

Fig. 5.10 shows a tendency which is known from the literature (/5.3/, /5.4/), namely that the sound power level increases approximately with 6 dB(A) per speed doubling. However, especially for running speeds above 400 rev/min rather large fluctuations are seen because of resonances.

When considering $n = 500$ with $L_w = 80 \text{ dB(A)}$ as reference point, the "speed law" would imply an increase from a level of 74 dB(A) at 250 rev/min, to 86 dB(A) at 1000 rev/min and to 89 dB(A) at 1500 rev/min in Fig. 5.10. This trend can be seen although a rather large scatter of 5 to 10 dB(A) is seen as well.

The actual values of the calculated and measured sound power levels as they are shown in Fig. 5.10 are not well matched. However, it should be said that gear transmissions are often driven at various speeds and torque loads so that resonances will define the sound power level of a particular gear transmission when classifications have to be made. For this purpose one should look at the maximum measured and calculated sound power levels which are 100.5 dB and 89.4 dB respectively. From this it is clear that the calculations predict a seriously underestimated sound power level.

The unweighted measured sound power levels and the measured velocity levels have also been used for determining the sound radiation index $L_p(f)$ of the

gearbox. For this purpose Eq. (4.16) has been used with an area level L_s of -1.0 dB. Because the measurements of $L_v(f)$ and of $L_w(f)$ were taken at r.p.m. intervals of 50 rev/min, the radiation index was averaged over 30 running speeds. The result is shown in Fig. 4.24 which confirms the simplified model that was used for the prediction of the radiation index of the compact gearbox housing.

This section shows that the sound power level of the test gearbox is strongly dependent on the running speed and that the sound power level can be predicted by the proposed theory of this thesis with only moderate accuracy. Figs. 5.7 and 4.19 indicate that at the relatively low tooth frequency an underestimation of the velocity and sound power levels occurs due to an incorrect calculated transfer function. Therefore, the main factor that still needs more investigations seems to be the transfer function $TF_w(f)$ at low frequencies.

Nevertheless, a big step forward has been made in predicting sound power levels of gear transmissions. It is now possible to predict the sound power level by only using drawing board knowledge. It is therefore possible to estimate to some extent the influence on the velocity level and the sound power level of structural measures without actually building and testing the gearbox alternatives.

5.6 Scatter in sound power levels for a single gearbox variant

Before proceeding with the results of further measurements some practical considerations have to be discussed to put the forthcoming measurements in their perspective. The accuracy and repeatability of the measurements at the test rig have to be investigated. Also the assumed negligible profile faults or unloaded Transmission Error have to be verified. This is done in order to distinguish significant differences in later experiments and to be able to relate them to the changes made in bearing types or tooth profile corrections used. Therefore, the random scatter in measured levels for a single gearbox variant has to be known first.

For this purpose sound power measurements have been performed on the same gear transmission at different days of the week. The results are shown in Fig 5.11 where the differences between two measurement days are given. As function of the running speed the differences are shown and they are as they should be, namely oscillating around zero dB with a small mean value

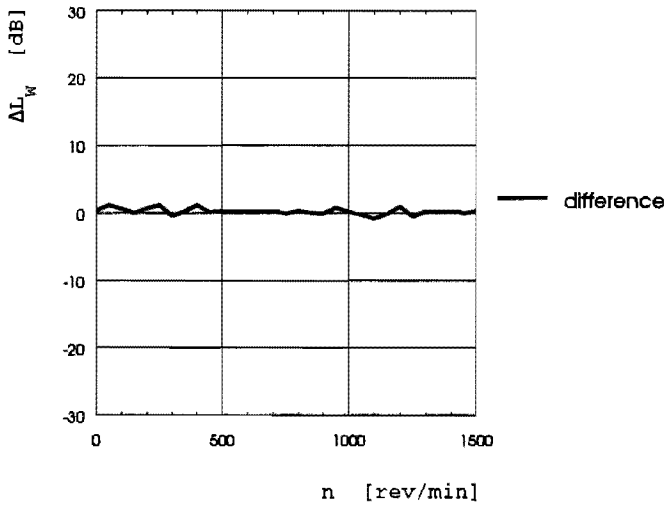


Figure 5.11:

Difference in sound power level L_W for two measurements, with exactly the same operational conditions ($T = 2000 \text{ Nm}$), taken on different days of the week.

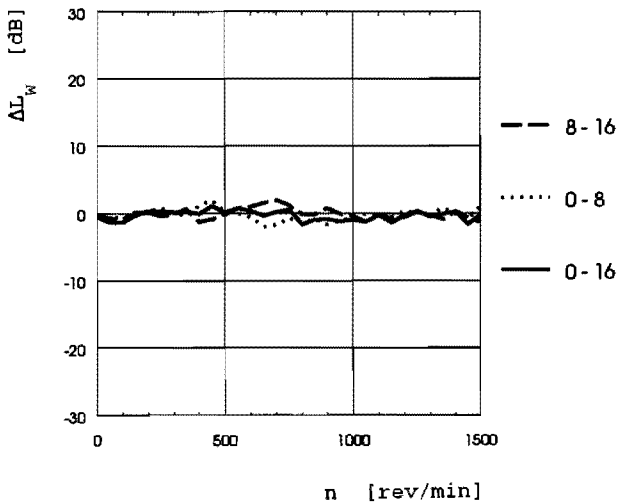


Figure 5.12:

Difference in measured sound power level L_W for three different gear positions to show the influence of the unloaded Transmission Error ($T = 2000 \text{ Nm}$).

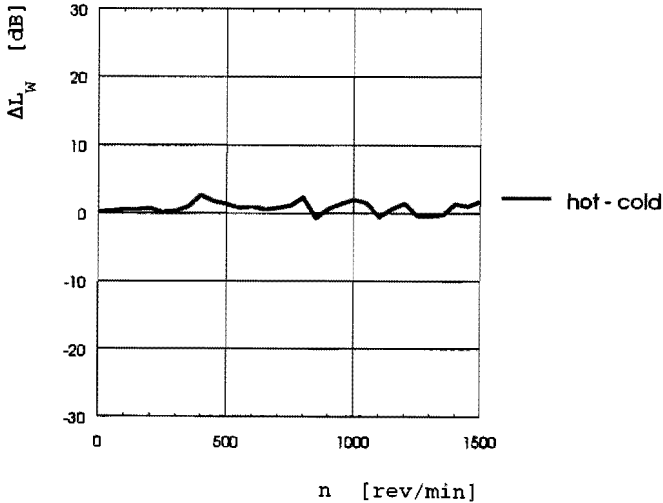


Figure 5.13:

Difference in measured sound power level L_w at the single helical gear set with ball bearings for two temperatures (20 and 80 °C) of the gearbox oil, i.e. for different viscosity of the oil ($T = 2000 \text{ Nm}$).

of +0.3 dB and with a small standard deviation of 0.5 dB. From this it can be concluded that the repeatability of the sound power measurements is very good.

Fig. 5.12 shows the sound power level differences for three different pinion-wheel configurations. Since the transmission gear ratio is exactly 3.0 the same teeth of pinion and wheel meet every rotation of the wheel. The influence of the unloaded Transmission Error can therefore be investigated by removing and turning the pinion through an angle relatively to the wheel and then assembling them together again. This was done for 1/3 and 2/3 revolutions of the pinion which corresponds with 8 and 16 teeth of the pinion relative to the wheel. The mean differences in sound power level were 0.3 dB with a standard deviation of 0.8 dB. Taking Fig. 5.11 into account, this means that these differences are not significant. From this it may be concluded that the unloaded Transmission Error of the test gears is well distributed over all teeth of the pinion and the wheel and that the positions of pinion and wheel is irrelevant to the measurements. Nevertheless, the positions of pinion and wheel were always kept the same in the measurements of section 5.8, where the influence of rolling bearing elements is investigated with the same test gears.

Fig. 5.13 shows the influence of the oil temperature on the sound power level. Measurements were carried out at the start of a day where the oil temperature was equal to the surrounding air temperature which was about 20 degrees Celsius. At the end of that day, after intense operation of the test rig, the measurement was repeated with a much higher oil temperature of about 80 degrees Celsius. The temperature difference corresponds with a difference in oil viscosity between 0.48 Nsm^{-2} at room temperature and 0.023 Nsm^{-2} at high temperature. This can be interpreted as if another oil was used. At low temperatures slightly lower sound power levels were measured as could be expected since the oil viscosity is higher with corresponding higher damping properties. The mean difference over the speed range of zero to 1500 rev/min of the pinion is 0.8 dB which is just above the standard deviation of Fig. 5.11. Therefore, this is a significant result when measurement accuracy is concerned, but it is rather insignificant when sound reduction measures are concerned. A low oil temperature or a high viscosity oil would not result in a remarkable sound reduction of gear transmissions.

5.7 Profile corrections and their influence on L_w

Profile corrections were discussed in Chapter 2 of this thesis. They may influence the dynamical behaviour of the gearbox interior (i.e. the rotating elements) by changing the engagement shocks of the gears. According to the theory appropriate profile corrections should reduce the velocity level and hence the sound power level of a gear transmission. This is also known from practice and many articles in the literature describe this feature. However, the amount of vibration reduction and sound power reduction in dB(A) is not mentioned in these articles, or only in a few practical examples. This thesis wants to calculate the level reductions beforehand and verify them by measurements.

For this purpose four identical sets of pinion and wheel were manufactured with different profile corrections. An uncorrected set was not included because this seemed irrelevant since almost all high precision gear sets, which form the topic of this thesis, have some kind of profile correction. The four profile corrections are described in Appendix F and they are indicated as correction (or set) A, B, C and D.

Correction A has been proposed by the gearing manufacturers and hence is based on experience. It consists of tip relief corrections on pinion and

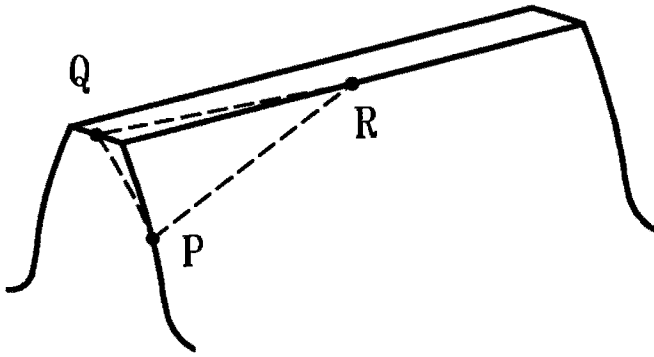


Figure 5.14:

Three-dimensional profile correction of gear set D.

wheel of $31\ \mu\text{m}$ and $13\ \mu\text{m}$ over a length of $4.1\ \text{mm}$ and $1.3\ \text{mm}$ respectively. This gear set has been used in the previous sections of this chapter and can be seen as the reference gear set with which the other corrections will be compared.

Correction B resulted from calculations made with the newly developed computer program of Chapter 2. It resulted in a tip relief of the pinion of $40\ \mu\text{m}$ over $4.8\ \text{mm}$ and of the wheel of $15\ \mu\text{m}$ over $1.4\ \text{mm}$. Supplementary a profile width correction was established over half the tooth width of the pinion with maximum relief at the edge of $9\ \mu\text{m}$.

Correction C was meant for illustrative purposes to show the influence of too small a tip relief respectively too large a torque load. This was realized with a pinion tip relief of $18\ \mu\text{m}$ over $2.0\ \text{mm}$ and an uncorrected wheel.

Correction D has an experimental character by combining a tip relief and a tooth width correction. Fig. 5.14 shows this three-dimensional profile correction. The tip relief has a triangular shape on the tooth surface with two triangular points on the tip of the tooth (Q and R) and one along the tooth profile at the tooth edge (point P). The line P-R is chosen in such a way that this line becomes a contact line of the meshing teeth at one moment. Therefore, line P-R is parallel to the lines of contact which lie at the base helix angle β_b . Both pinion and wheel are equipped with these three-dimensional profile corrections. Depending on the torque and rotation directions, two meshing teeth of pinion and wheel will meet at point Q of pinion or wheel. In our case this is the wheel since the torque and

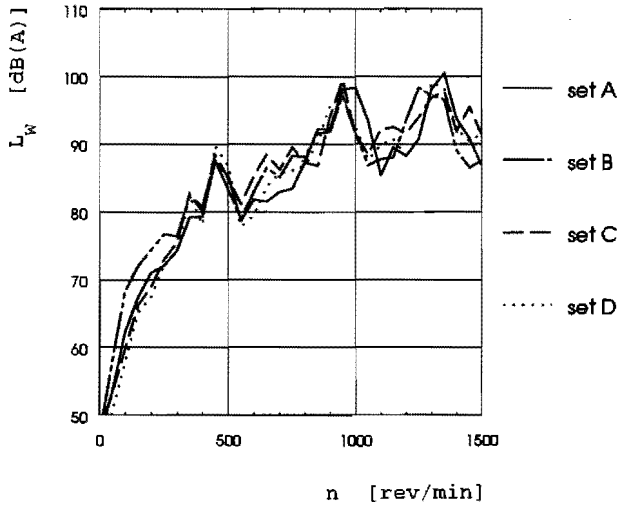


Figure 5.15:

Measured A-weighted sound power level L_w of the four single helical gear sets at maximum torque load ($T = 2000 \text{ Nm}$).

rotation direction on the driving pinion are both clockwise when looking from the electric motor to the test gearbox (see Fig. 5.1). During meshing this contact point will progress along the tooth surfaces in the corrected area with contact lines parallel to P-R until they reach P-R. At this point the mesh is uncorrected so that the route from Q to P-R of the wheel determines the engagement shock. The same arguments apply to the disengagement shock where the route from P-R to Q of the pinion is responsible.

Fig. 5.15 shows the results of sound power level measurements with increasing running speed for these four gear sets. They all have resonances at 450, 950 and 1300 rev/min but the relative differences are small. From $n = 800 \text{ rev/min}$ up to 1500 rev/min the sound power levels are as large as 90 dB(A) or more and here the mean differences between the sets are as follows:

		measurements		calculations		
		standard		standard		
		mean	deviation	mean	deviation	
L_{w_setB}	- L_{w_setA}	: -0.9	4.0	-0.4	0.2	dB
L_{w_setC}	- L_{w_setA}	: +0.4	4.1	+2.9	0.2	dB
L_{w_setD}	- L_{w_setA}	: -0.3	3.1	-5.1	0.2	dB

The calculated differences are a result of differences in L_w at the tooth frequency because it was assumed that the vibration transmission through the shafts, bearings and housings as well as the sound radiation efficiency is not influenced by changing the tooth profile correction. The differences between measurements and calculations are rather large, especially in case of the three dimensional profile correction D where a mean sound power level reduction was expected of 5.1 dB.

The mean measured differences are within 1 dB of the sound power level of the gear set with correction A. Since the standard deviation of a sound power measurement within the same gear set is about 0.5 dB, as shown in the previous section, it can only be concluded that the sound power level over the speed range is on the average only slightly or not influenced by the applied profile corrections.

However, the standard deviations of the individual measurements indicate a stronger fluctuation with running speed, as can be seen in Fig. 5.15. At a certain running speed, sound power level differences between the gear sets occur of 5 dB or even more. The differences between the four gear sets can also be shown when the maximum sound power levels are compared. These levels are:

$$\begin{array}{ll} \max(L_{W_setA}) = 100.5 \text{ dB(A)} & \max(L_{W_setB}) = 98.3 \text{ dB(A)} \\ \max(L_{W_setC}) = 99.5 \text{ dB(A)} & \max(L_{W_setD}) = 99.2 \text{ dB(A)} \end{array}$$

The measurements clearly show that the actual shape of the profile correction has a small influence on the sound power level. However, it should be mentioned that the amount of correction (i.e. tip relief) of the gear sets used is the same except for gear set C. This gear set shows on average a slightly higher sound power level over the speed range of interest. Similar calculations have been performed for an uncorrected gear set which resulted in a predicted sound power level that on average is 3.5 dB higher than that of gear set A.

For these gears the expected reduction in vibration and sound power level due to the 3-D tooth profile correction could not be confirmed. Although this is in contrast with expectations on the basis of the modeling described in Chapter 2, this is a very important practical result. With the present understanding no definitive explanation can be given for it, but it can be suspected that the finite stiffness of the housing has an important influence on L_w , which up to now has been neglected in dynamic models such as described in Chapter 2.

5.8 Rolling element bearings

The vibration transmission from the gears to the gearbox housing is influenced by the stiffness and damping properties of the bearings. In Chapter 3 of this thesis the stiffness matrices were introduced of several types of bearings such as ball bearings, roller bearings, taper roller bearings and fluid film bearings. However, given the chosen calculation method, the damping properties of the bearings could not be properly implemented in the FEM calculations of the transfer functions of the gearbox.

The gear sets in the previous sections of this chapter were equipped with ball bearings. The two bearings on the pinion shaft were of the type SKF 6316 and on the wheel of type SKF 6219. Both bearings have the same outer diameter of 170 mm but have different inner diameters of 80 mm and 95 mm respectively.

One single helical gear set was selected to do measurements with several rolling element bearings attached to it. For this purpose gear set B was used. Four sets of rolling element bearing types were used with of course the ball bearings type SKF 6316 and SKF 6219 as one of them. Ball bearings are commonly used in gear transmissions and therefore they are taken as reference for the rest of this section.

The second bearing type is the single row angular contact ball bearing which was used in combination with a ball bearing. On every shaft an angular contact ball bearing was situated at the shaft side where the axial force is encountered by the bearings. With the single helical gears this axial force is a result of the tooth helix angle β and could become as large as 8272 Newton at maximum torque load. This axial load was encountered by the angular contact ball bearings of pinion (SKF 7316B) and wheel (SKF 7219B). The other two ball bearings had only radial forces to encounter. The angular contact ball bearings were situated at the front (pinion) and at the back (wheel) of the gearbox.

The third bearing type was a double row self-aligning roller bearing which was used at all four bearing positions. These bearings were of the type SKF 21316CC for the pinion and SKF 22219CC for the wheel shaft. Double row self-aligning roller bearings are expensive but are used here and there in gearing practice to enable the gear shafts to bend freely especially in cases where these shafts are flexible. The construction of this bearing type allows limited rotations around coordinate axes perpendicular to the shaft axis.

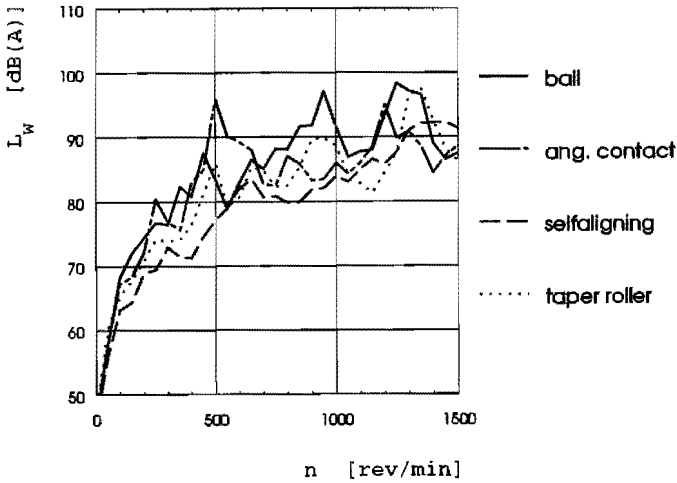


Figure 5.16:

Measured A-weighted sound power level L_w for gear set B with four different rolling element bearings ($T = 2000 \text{ Nm}$). 1. ball bearings, 2. single row angular contact ball bearings, 3. double row self-aligning roller bearings and 4. taper roller bearings.

The fourth bearing type is the taper roller bearing which was also used in combination with ball bearings. The same reasons apply as for the angular contact ball bearings to use only two of such bearings. Four taper roller bearings would give too much bearing air in the axial unloaded bearings which can result in an unwanted radial movement of the gears with excessive vibrations as a result.

Figs. 5.16 and 5.17 show the results of the sound power level measurements for the four configurations of gear set B (for $T = 2000 \text{ Nm}$). The differences are larger than those encountered in the previous section where the influence of profile corrections was investigated. Here, the sound power level differences are up to 15 dB which is considerable. This is mainly due to changes in resonance frequencies caused by the different bearing stiffness matrices. The mean differences with regard to the ball bearing set, over the speed range of 800 to 1500 rev/min are:

	mean	standard deviation	
$L_{w_angular}$	-4.2	4.5	dB
$L_{w_selfaligning}$	-5.1	6.0	dB
$L_{w_tapered\ roller}$	-3.6	4.1	dB

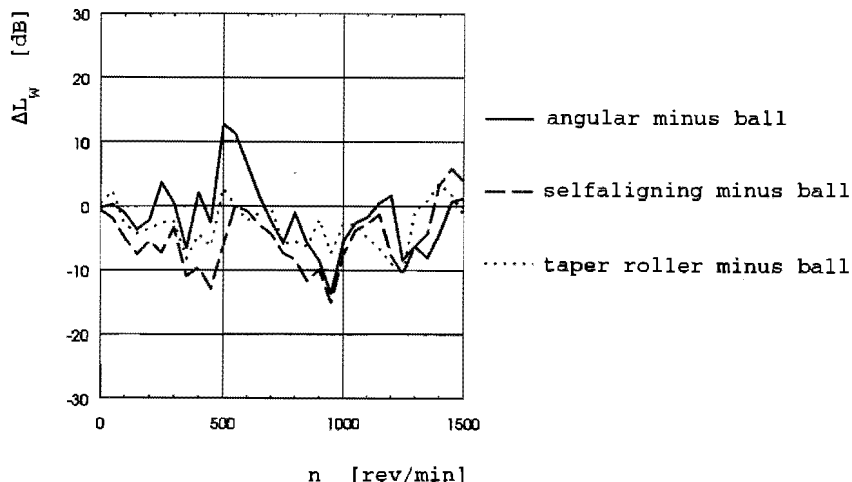


Figure 5.17:

Differences in measured sound power level L_W relative to gear set B with ball bearings ($T = 2000 \text{ Nm}$).

However, the angular contact ball bearing configuration shows an excessive peak around 500 rev/min which is probably due to a resonant vibration mode of the gears in axial direction. For the rest of the speed range it is somewhat quieter than the ball bearing configuration resulting in a mean difference of -4.2 dB. However, at $n = 950 \text{ rev/min}$ the difference is 13.7 dB in favour of the angular ball bearing.

The other two bearing configurations show better results with the double row self-aligning roller bearings as being the best with an average sound power level difference of -5.1 dB with regard to the ball bearing configuration. The tapered roller bearing configuration gives a somewhat less distinct improvement on the sound power level, but still by 3.6 dB on average.

When looking at the maximum sound power levels per bearing configuration the following values are obtained from Fig. 5.16:

$$\begin{aligned}
 \max(L_{W_{\text{ball}}}) &= 98.3 \text{ dB(A)} \\
 \max(L_{W_{\text{angular}}}) &= 95.1 \text{ dB(A)} \\
 \max(L_{W_{\text{selfaligning}}}) &= 92.3 \text{ dB(A)} \\
 \max(L_{W_{\text{tapered roller}}}) &= 97.4 \text{ dB(A)}
 \end{aligned}$$

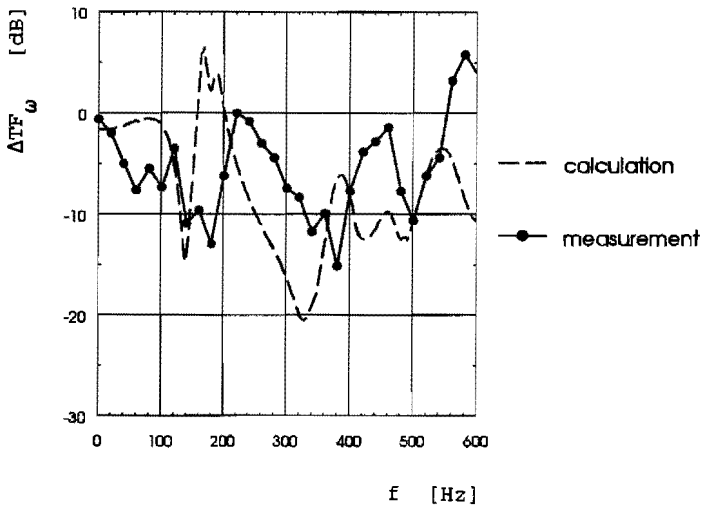


Figure 5.18:

Calculated and measured differences in the transfer function $TF_{\omega}(f)$ of the gearbox between the ball bearing configuration and the double row self-aligning roller bearing configuration.

The double row self-aligning roller bearing configuration is clearly the most quiet of the four, with a difference of 6.0 dB(A) in comparison with the ball bearing configuration.

The maximum difference in favour of the double row self-aligning roller bearing is -15.1 dB. This probably is a result of the zero stiffness for angular displacements for this kind of rolling element bearing. Angular displacements excite the gearbox housing in a way at which the housing responds easily with bending waves on the surface. This is prevented by the use of these bearings in gear transmissions. The absence of any peak in the sound power level of Fig. 5.16 for the double row self-aligning roller bearing variant confirms this statement.

A FEM model of the test gearbox was equipped with stiffness matrices of the ball bearings according to Chapter 3 and also equipped with the stiffness matrices of the double row self-aligning roller bearings. Because the latter is not discussed in chapter 3, the stiffness matrix of the ball bearings was used with zero moment stiffness coefficients instead of the stiffness coefficients of the ball bearing. Both FEM models provided the transfer function $TF_{\omega}(f)$ between the wheel angular velocity level $L_{\omega}(f)$ and the gearbox housing velocity level $L_v(f)$ according to Eq. (5.5). Fig. 5.18 shows the differences between these two calculated transfer functions. It

shows a mean difference of 7.3 dB with a standard deviation of 4.5 dB in favour of the FEM model with the double row self-aligning roller bearings. The measured differences in $TF_{\omega}(f)$ are shown in the figure as well. This is done by assuming that the tooth frequency is mainly responsible for the overall velocity levels L_{ω} and L_v so that the pinion speed of 1500 rev/min corresponds with the frequency of 600 Hz in Fig. 5.18. Apart from a slight frequency shift both curves show a similar frequency dependency. The figure shows that the FEM models predict the transfer function differences in a rather good manner. The zero moment stiffness coefficients of the double row self-aligning roller bearings can hereby be made responsible for the advantageous difference. Although more expensive it seems a very effective way of reducing the radiated sound power of a gear transmission by the use of self-aligning bearings.

Concluding, it seems that the FEM calculations can be used to investigate effects of noise reduction measures which are related to the vibration transmission block of the sound generation scheme of Fig. 1.1. The influences on the transfer function of different bearings (i.e. stiffness matrices) or modifications of the (empty) gearbox housing can hereby be investigated. For this purpose the FEM model of a gear transmission has to be sufficiently accurate, i.e. a high number of elements has to be used, and the dynamical calculations have to be carried out with appropriate measured or estimated damping factors.

5.9 Double helical gears with roller bearings and fluid film bearings

Another way of transmitting 300 kW with a transmission gear ratio of 3.0 is by the use of double helical gears instead of single helical gears. The manufacturing of double helical gears is more complex and hence more expensive but it gives certain advantages as well. The main advantage is the fact that double helical gears do not exert any axial force upon the gearbox housing. The axial force components of the two helical parts of the gears cancel each other out. This makes it possible to use a bearing construction that, in theory, gives no axial vibration input into the housing. The pinion bearings were combined radial and thrust bearings to restrict axial movements of the gears while both wheel bearings can freely move in axial direction. The wheel is axially positioned by the double helix of the gear mesh.

A second advantage of double helical gears is that by the absence of an axial force component on the bearings, fluid film bearings can be used in the test rig. In the experiments the tooth force has to be applied during standstill of the test rig and this means that fluid film bearings will make metallic contact. To enable a start-up of the test rig these metallic contacts have to be minimized since they give rise to friction which has to be conquered. This is not possible with single helical gears because the axial or thrust bearings would increase the friction by an enormous amount. When only radial bearing forces are present the contact areas are much smaller with consequently less friction. At every start-up of the test rig this friction has to be conquered which results in a slight bearing damage. For this reason the number of start-ups was restricted to a few and special attention was paid to the selection of fluid film bearing types.

The double helical gears were tested with fluid film bearings and with single row cylindrical roller bearings in the same gearbox as was used in the previous sections of this chapter. The fluid film bearings are of the type Glyco E-135-80 for the pinion and Glacier 095 KSA 070 for the wheel. These are two-part bearings with 1 mm white metal as bearing material. The pinion thrust bearings are only used to position the gears axially so that no axial force is present and hence no friction is introduced at start-up. The fluid film bearings were supplied with oil (Shell Omala 150) by the use of a small oil pump which was installed outside the semi anechoic sound insulated room.

The roller bearings were of the type SKF NJ 316 and SKF NU 2219 for pinion and wheel respectively. Here the pinion bearings have two rims on the outer ring and one on the inner ring to prevent axial movements in the same way as the fluid film bearings do. The wheel bearings have plain inner rings to enable axial movements of the wheel which of course are restricted by the double helix of the gear mesh.

The two parts of the double helical gears on which the teeth lie are separated by a distance of 54 mm to enable the grind stone to enter. Both parts have face widths of 25 mm (pinion) and 23 mm (wheel) with the same number of teeth as the single helical gears of the previous sections of this chapter to give the same tooth frequencies at the measurements. The helix angle has been increased to 33 degrees to ensure an overlap ratio ϵ_{β} that exceeds unity. This resulted in the use of a smaller module $m = 3.5$ mm

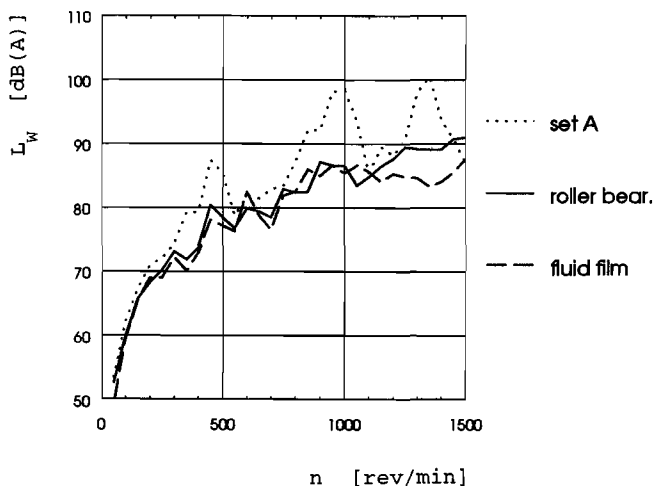


Figure 5.19:

Measured A-weighted sound power level L_w of the double helical gear set with roller bearings and with fluid film bearings as function of the running speed n at maximum torque load ($T = 2000$ Nm). Also the measured A-weighted sound power level is shown of the gear set A with ball bearings.

instead of $m = 4.0$ mm for the single helical gears.

Fig. 5.19 shows the results from sound measurements of the double helical gear set with roller bearings and with fluid film bearings for the maximum torque load of 2000 Nm and also the results of the single helical gear set A with ball bearings. At low running speeds the sound power curves of the double helical gears are similar to each other but from 1100 rev/min on the gears with fluid film bearings are significantly more silent, up to 5.9 dB at 1350 rev/min. Over the speed range of interest (i.e. $n = 800$ to $n = 1500$ rev/min.) the mean difference is 1.9 dB in favour of the gears with the fluid film bearings in comparison with the roller bearings, with a standard deviation of 3.0 dB.

The differences between the single helical gear set and the double helical gear sets is very remarkable. On average the double helical gear sets have a lower sound power level of 5.3 dB for the roller bearing configuration and 7.2 dB for the fluid film bearing configuration in the speed range of interest. Even when the single helical gear set B is taken with the double row self-aligning roller elements the differences are in favour of the double helical gear sets (0.2 dB for the roller element bearing

configuration and 2.1 dB for the fluid film bearing configuration). When the maximum sound power levels are taken to classify the different bearing configurations, the following levels are obtained:

$$\begin{aligned}\max(L_{W_{\text{ball}}}) &= 100.5 \text{ dB(A)} \\ \max(L_{W_{\text{selfaligning}}}) &= 92.3 \text{ dB(A)} \\ \max(L_{W_{\text{roller element}}}) &= 91.0 \text{ dB(A)} \\ \max(L_{W_{\text{fluid film}}}) &= 87.7 \text{ dB(A)}\end{aligned}$$

The possible sound power level reductions that can be obtained by changing the gear transmission design from single helical gears to double helical gears and by changing the bearing types are hereby clearly shown. For the test gearbox of this chapter a maximum difference in sound power level was obtained of 12.8 dB(A) in favour of the double helical gear set with fluid film bearings.

Furthermore, the large sound power level fluctuations with varying running speed which are seen in Fig. 5.19 for the single helical gear set are not present in the results of the double helical gear sets. They show very smooth curves as function of the pinion speed. From these curves the previously mentioned relation between running speed and sound power level (i.e. 6 dB(A) increase per speed doubling) can be seen clearly.

FEM calculations have been performed on the double helical gear sets with roller bearings and with fluid film bearings using the bearings stiffness matrix according to Chapter 3. Fig. 5.20 shows the differences in Transfer Functions $TF_{\omega}(f)$ of these two variations. However, in contrast to Fig. 5.18 the calculations are not satisfactory at all. This is probably due to the fact that the damping properties of the fluid film bearings, which were ignored at the FEM calculations for computational reasons, have a great influence on the transfer function. This asks for further investigations in order to be able to predict differences in $TF_{\omega}(f)$ between the roller bearing and the fluid film bearing configurations. Also effects of the non-symmetry of the stiffness matrices as they are derived with the graphs given in Chapter 3 need further investigations.

As additional illustration of the dependency of the sound power level on the operational conditions Fig. 5.21 shows the influence of the torque load (or tooth load) on the sound power level at six different running speeds n .

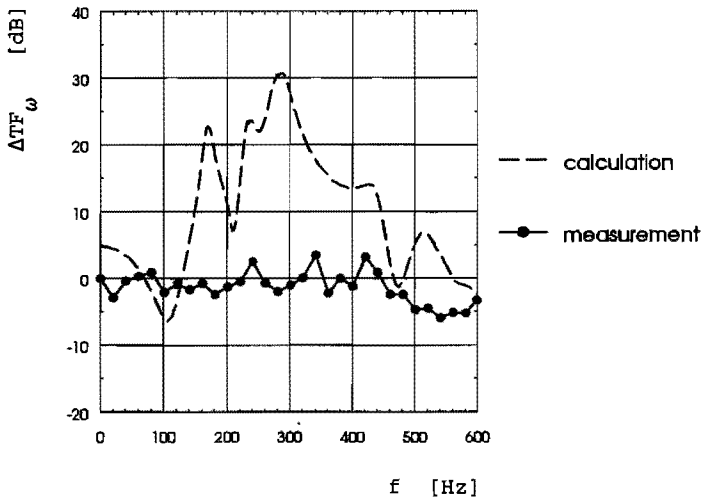


Figure 5.20:

Calculated and measured differences between the Transfer Functions $TF_{\omega}(f)$ of the double helical gear set with roller bearings and with fluid film bearings at maximum torque load ($T = 2000 \text{ Nm}$).

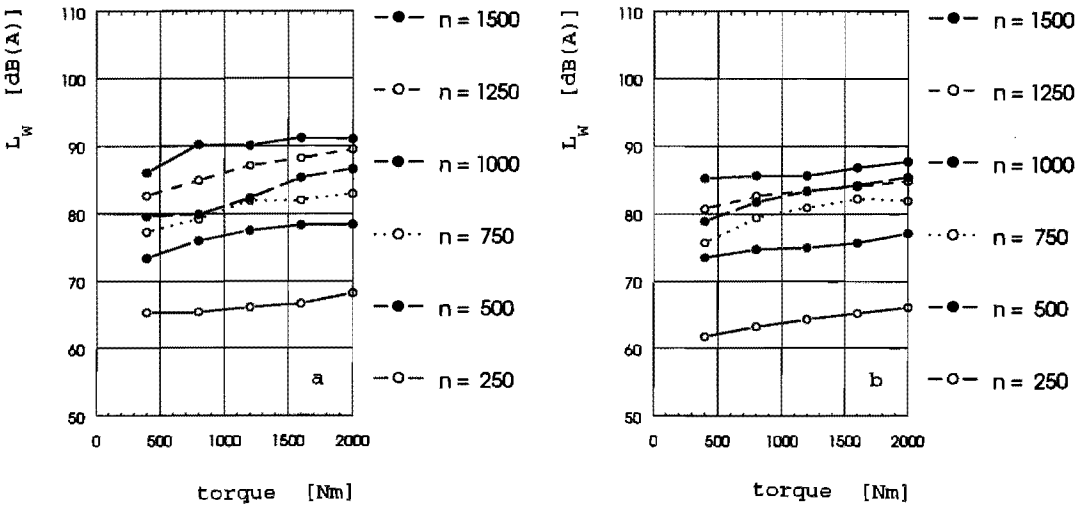


Figure 5.21:

Measured A-weighted sound power level L_w of the double helical gear set with roller bearings (a) and with fluid film bearings (b) as function of the transmitted torque load.

The results of the roller bearings are presented on the left of this figure (a) and the results of the fluid film bearings on the right (b). Both figures are similar and they more or less support the assumptions mentioned in the literature (/5.3/, /5.4/) that states a dependency of the sound power level to the transmitted torque load of the following kind. With every doubling of the transmitted torque load, the sound power level increases with 3 dB(A) on average. However, the curves of Fig. 5.21 confirm this statement only for higher torque loads. When the transmitted torque load T is being increased from 1000 to 2000 Nm (which is a doubling) the sound power level increases by 3.4 dB(A). The same relation holds for the gear set with fluid film bearings, from which resulted a similar increase of 2.7 dB(A).

In conclusion, it seems that the use of double helical gears forms a very good alternative for single helical gears to achieve low noise gear transmissions. The difference in maximum measured sound power levels of the standard single helical gear set A with ball bearings and the double helical gear set with roller bearings was 9.5 dB(A). A further noise reduction was measured for the double helical gear set with fluid film bearings of 12.8 dB(A) relative to the standard single helical gear set.

5.10 Summary

The theoretical models which were developed in the previous chapters of this thesis could be verified to some extent with the help of a test rig with a single stage gear transmission which was built for the measurement of angular velocity levels at the wheel, velocity levels at the gearbox housing and sound power levels. The three parts of the sound generation and transmission chain were measured, being the vibration generation at the gear mesh, the bearing and housing dynamical behaviour and the sound radiation. This was done for the so-called gear set A which has tip relief corrections on the pinion as well as on the wheel according to gear manufacturer's standard practice.

The angular velocity level $L_{\omega}(f)$ was calculated with help of the lumped parameter model which was introduced in Chapter 2. It showed resonances as function of the running speed but at different speeds than those that were measured. The mean level of the measured and calculated velocity levels are

about the same, but differences up to a factor two are found at maximum torque load in the high speed range of the gearbox (i.e. $n = 800$ up to 1500 rev/min.). The results of the calculations are useful when the maximum level over a certain speed range is taken. Since many gear transmissions are being operated at varying running speeds, a calculated averaged velocity level is not a very useful tool for predicting the vibration generation of gear transmissions but the maximum velocity level is. However, the predicted levels are not very accurate when the speed dependency is taken into account. This is probably caused by the assumption of a rigid gearbox housing support of the bearings in the lumped parameter model.

The FEM calculation of the transfer function $TF_{\omega}(f)$ between angular velocity level $L_{\omega}(f)$ at the gear wheel and the surface averaged velocity level $L_v(f)$ at the surface of the gearbox housing provides not an accurate tool for predicting the vibration transfer between gear shafts and the gearbox housing surface. The proper modeling of the coupling between the shafts and the housing seems to be the bottle-neck for these kind of predictions.

The sound power level of the test gearbox proved to be strongly dependent on the operational conditions (i.e. running speed and torque load). The sound power level can be predicted by the proposed theory of this thesis with rather low accuracy. A main factor which still needs more investigations seems to be the low frequency behaviour prediction of the vibration transmission from shafts to gearbox housing surface. This concerns both the modeling of the housing dynamics and the estimation of modal damping values.

Nevertheless, a big step forward has been made in predicting effects of alterations in the structure of gear transmissions. For example the positive influence of the double row self-aligning roller bearings on the transfer function could be predicted rather well. The zero moment stiffness coefficients of the bearing could be made responsible for this favourable effect. The sound transmission behaviour of fluid film bearings could not be modeled accurately in this study.

The sound power measurements on a single gearbox variant could be reproduced very accurately as an averaged value of 0.3 dB with a standard deviation of 0.5 dB shows. It was also confirmed that the unloaded Transmission Error had no influence on the measurements, as was assumed at

the start of this thesis. This shows the quality of the test rig and puts all measurements in their perspective.

The influence of the viscosity of the gearbox oil was investigated by measuring at different oil temperatures. An averaged difference of 0.8 dB was measured which means that the gear transmission with high viscosity oil produces slightly less noise. Nevertheless, this difference is so small that the use of a high viscosity oil to obtain significant sound reductions seems not realistic.

Sound power measurements of different kinds of profile corrections clearly showed that the actual shape of the profile correction had a small influence on the sound power level. A reduction of the maximum sound power level by 2.2 dB(A) could be realized by using calculated tip reliefs instead of the standard profile correction which was prescribed by a gear manufacturer. However, it should be mentioned that the amount of correction (i.e. tip relief) does have influence, because an uncorrected gear set would on average produce 3.5 dB more than the corrected gear sets. From this it could be concluded that when the amount of tip relief is correctly chosen for the prevailing tooth force, no significant gain can be obtained by the use of sophisticated profile corrections such as the three dimensional profile correction which was used during the measurements. This important result was not in agreement with the expectations on the basis of the modeling in Chapter 2. As a partial explanation it is suggested that the lumped parameter model used in Chapter 2 for the gearbox interior (i.e. the rotating elements) is incorrect.

Measurements were performed on a single helical gear set with several kinds of rolling element bearings attached on the pinion and wheel shafts of the test gearbox. Ball bearings were taken as reference in these measurements because this kind of rolling element bearing is widely used in gear transmissions. This gear set proved to give rise to the highest sound power level. Tapered roller bearings were slightly better by 0.9 dB(A) for the maximum sound power level. The use of single row angular contact ball bearings decreased the maximum sound power level by 3.2 dB(A). The best results were obtained with double row self-aligning roller bearings which resulted in a maximum sound power level that was 6.0 dB(A) lower than the one of with ball bearings. This good result can be explained by the fact that these bearings have a zero moment stiffnesses. This reduces the

transmission of vibrations into the gearbox housing which would directly give rise to bending waves in the housing surface. Although more expensive it seems a very effective way of reducing the radiated sound power of a gear transmission by the use of self-aligning bearings.

Measurements have been performed on a double helical gear set with single row cylindrical roller bearings and with fluid film bearings. At low running speeds no noticeable differences in sound power level could be detected for these two bearing configurations. However, at higher running speeds the sound power level differences increased up to 5.9 dB at most. The maximum sound power level of the roller bearings configuration was 91.0 dB(A) and that of the fluid film configuration was 87.7 dB(A). From this it can be concluded that fluid film bearings have a favourable effect on the sound power level. When a comparison is made between the standard single helical gear set with ball bearings and the double helical gear set with fluid film bearings the noise reduction is impressive. The difference between the maximum sound power levels of these two gear transmission variants is as large as 12.8 dB(A).

6. EVALUATION

A brief evaluation of the foregoing study is presented and design guidelines are given.

6.1 Theoretical achievements

In the foregoing study much attention was paid to the development and testing of computational tools for the purpose of designing low noise gear transmissions. The work concerned both the influence of the tooth geometry and of the tooth flank profile corrections on the origin of the vibrations and noise. Furthermore, the transmission of the vibrations via shafts and bearings to the outer surfaces of the gearbox housing were studied, where the vibrations are causing sound radiation into the surrounding air.

6.1.1 Prediction of gear vibrations

An important step was the development of a computer program for the fast calculation of the time variable tooth stiffness and the engagement and disengagement shocks. These phenomena are considered to be the main vibration sources in high quality gear transmissions. The computer program is based upon an analytical model instead of a time consuming Finite Element Method model which is used by many other investigators. The analytical model is much faster and is applicable for any gear transmission with spur gears, single helical gears or double helical gears.

The basis for this analytical model was taken from other investigators and it was extended to a multi purpose computer program that calculates tooth deflections, tooth force distributions and the time variable tooth stiffness of a gear pair. Moreover, a model was included which describes the engagement and disengagement shocks of the tooth pairs. This model is based upon the actual geometry of the tooth profile corrections and the amount of tooth deflections that result from the applied torque load.

The new model is considered to form a valuable addition to the gearing technology because it can help the gear designer to effectively outline a gear transmission with respect to the tooth geometry in order to produce low noise gear transmissions. Nevertheless, further developments appear to be needed as it comes to predicting the vibrations of the gear wheels accurately.

In the present study the prediction of the gear wheel vibrations was

obtained by integrating the data for the time variable tooth stiffness and for the engagement and disengagement shocks with a dynamic model for the gearbox interior. This is a lumped parameter model for the gear wheels, shafts and bearings and is based on the assumption that a rigid gearbox housing provides the boundary conditions for the bearings.

However, Finite Element studies in Chapter 4 reveal that dynamic boundary conditions at the interface of housing and bearing have a severe influence on the dynamic behaviour of the gearbox interior. As a consequence one may expect prediction errors for gear wheel vibrations when assuming rigid boundaries for the lumped parameter model of the gearbox interior.

Another indication for this error source is found in Chapter 5 where the predicted angular vibrations of a gear wheel are compared with measurement results (see Figure 5.4). The differences between the predicted and measured values show a large scatter as a function of running speed. Nevertheless, the results are not useless. Especially for the higher speeds (≥ 1000 rev/min) the averaged angular velocity levels are predicted quite well and the differences remain within 6 dB, i.e. a factor 2 in magnitude.

A further indication for the incompleteness of the present modeling is found in section 5.7, where measured sound power levels have been compared for single helical gears with different tooth profile corrections. It was found, for example, that the noise reduction for a 3D-profile correction was significantly less than expected on the basis of the predicted reduction in gear wheel vibrations.

Although the foregoing study has revealed that there are still some shortcomings in the prediction model for gear wheel vibrations, we consider the approach developed in this thesis as basically sound and as a good step forward in the development of cost-effective computational modeling. However, further research is needed to investigate when and how more elaborate modeling of the dynamics of the gearbox interior has to be incorporated.

6.1.2 Vibration transmission from gears to the housing

As a further important step in computational modeling an extensive study has been made of the coupled dynamical behaviour of the gearbox interior and the housing. The modeling aims at calculating a system transfer function between the angular velocity level at a gear wheel as input and the surface-averaged mean square velocity level on the housing as an

output. The transfer system consists of the assembly of wheels, shafts, bearings and housing structure. The modeling approach taken in this thesis is that the system is assumed to be linear and that the Finite Element Method is the most promising tool for obtaining the desired transfer function. For the actual calculation the Modal Analysis approach has been followed. Much attention has been paid to the modeling of the stiffness matrices for bearings, especially for ball and roller bearings.

With respect to the modeling of the housing a step by step approach was followed comparing computational and experimental results for structures with increasing complexity.

From the results of the present study a number of lessons can be learned. Both computational and experimental results have made it plausible that the inclusion of moment stiffnesses in the bearing stiffness matrix is essential for a proper modeling of vibration transmission. With respect to the modeling of the housing structure it was shown that rather detailed meshes are required, but that nevertheless certain simplifications are allowed. For example, the bolt joints between upper and lower casing may be modeled by assuming a one-pieced gearbox structure and the gearbox feet which are attached to a stiff supporting structure may be modeled by suppressing the contact node vibrations for all six degrees of freedom.

With respect to the transfer functions for forced vibration the present study shows both promising as well as disappointing agreements between computational and experimental results. For an empty gearbox housing the predicted transfer function agrees quite well with measured results in frequency bands which contain several eigenfrequencies (see Figs. 4.5, 4.7, 4.10 and 4.15). However, at lower frequencies the prediction tends to give significant underestimations of the transfer functions, which might be an indication for incompleteness of the modal model. This point requires further attention because it concerns a range which often covers tooth frequencies.

For a gearbox model with shafts and bearings the predicted transfer functions did agree less favourably with experimental results. A main uncertainty follows from the estimation of damping factors. Moreover, from a methodological point of view it needs further investigation whether or not the followed Modal Analysis approach in the FEM computations in this thesis is appropriate. Certainly for the modeling of fluid film bearings, ignoring the proper implementation of the damping matrices, seems to lead

to useless predictions (see Fig. 5.20). On the other hand the prediction in Chapter 5 of the effect of replacing the ball bearings by double row self-aligning roller bearings on the housing vibrations seems more promising (see Fig. 5.18). However, further research is needed to improve the accuracy of the predictions.

In summary it may be concluded that with the presented work the results of FEM predictions of gearbox housing vibrations remain rather uncertain with respect to their accuracy. A major topic for further research is the improved modeling of the coupling between the gearbox interior (i.e. the rotating elements) and the housing. Both for modes dominant in the interior and for modes dominant on the housing the "coupled" eigenfrequencies may deviate very much from the "uncoupled" eigenfrequencies. Nevertheless, when averaging over running speeds the effect of replacing ball bearings by self-aligning bearings was predicted reasonably correct.

6.1.3 Sound radiation from the housing surface

In the present study a simple model for obtaining the radiation efficiency of the housing was used. Comparison between predictions and experiments proved that this modeling was quite accurate. Moreover, it was observed that for the rather compact gearboxes which were investigated in this study, the radiation efficiency was close to its maximum value, i.e. unity, for the range of prevailing tooth frequencies. This also implies that the radiation efficiency will not be subject to large changes when structural modifications would be made to reduce the vibration response of the housing. Therefore, from a designers point of view it would be sufficient to have tools available for optimization towards a low vibration response of the housing.

However, this will not be necessarily the case for less compact gearboxes, i.e. bigger and relatively less stiff housings. In that case it might be incorrect to ignore the effect of structural optimization changes on the sound radiation efficiency. Then still it would be advisable to explore the use of simplified modeling as known, for example, from the Statistical Energy Analysis approach. It is suspected that the cost-effectiveness of introducing a much more demanding Boundary Element Method modeling will be disappointing in the majority of applications.

6.2 Practical results

The extensive experimental program reported in this study has provided results which are of great practical value for the designer of low noise gear transmissions. These results concern the effectiveness of tooth profile corrections, the evaluation of alternative bearings for a gearbox with single helical gears and the evaluation of replacing single helical gears in combination with ball bearings by double helical gears in combination with other types of bearings. Although certain design changes may lead to the use of more expensive components, a larger noise reduction may save additional so-called secondary noise reduction measures. This makes such design changes cost-effective options for certain applications.

The results reported in this thesis concern data over a wide range of speed and torque load. Especially the dependency of certain effects on running speed is striking. This is often not observed in other publications, because many investigators have published measured results at a single or a small number of operational conditions to test their theoretical predictions. This tends to obscure the important effects of such conditions as running speed and torque load upon the dynamical behaviour of the gearbox.

6.2.1 Tooth profile corrections

For a gearbox with single helical gears with ball bearings, the radiated noise was measured for four different tooth profile corrections including a sophisticated 3D-correction. The major observation was that the differences in radiated sound power levels between the four variants were not more than 2 dB. Especially, for the 3D-correction this was disappointing in view of the predicted larger reduction. Possible reasons have been discussed already in 6.1.1. An uncorrected gear pair was not part of the measurements because most high power gear transmissions have corrected gears. With the correct amount of tip relief, corresponding with the tooth deflections for the prevailing tooth force, no further gain could be established by the use of sophisticated tooth profile corrections such as the three dimensional tooth profile correction which was used during the measurements.

For the designer this seems to suggest that expensive variants of tooth profile corrections may be avoided in favour of more effective measures. However, care should be taken in generalizing this statement to gears that deviate strongly from those under study in this thesis. Especially, for

gears with a larger width, a strongly uneven force distribution along the tooth width probably necessitates the use of 3D-profile corrections. Use of the design tool described in Chapter 2 of this thesis, may then still be most favourable, for the time being, in terms of cost-effectiveness.

6.2.2 Bearing variants

The bearing choice can have a very significant influence on the radiated sound power level of a gearbox. When the design of the gear transmission allows different kind of bearings to be used, it should be recommended to use bearings with low values for moment stiffnesses. Such bearings are for example the double row self-aligning roller bearings which were used in some tests of Chapter 5. Compared to a variant with ball bearings this lead to a reduction of the maximum sound power level of 6 dB.

Another and more expensive alternative is the use of double helical gears with roller bearings. This variant has, in theory, no axial force input to the gearbox housing and has a larger mass of the wheels. In the tests of Chapter 5 this resulted in a 9 dB lower maximum sound power level in comparison with the single helical gears with ball bearings. This favourable result was obtained in spite of the non-zero moment stiffnesses of the roller bearings, probably because the moment excitation played a less important role due to a higher bending stiffness of the shafts. However, when the flexibility of the shafts decreases, due to another gear transmission design, self-aligning bearings should be used to cancel out any moment excitation to the gearbox housing.

The measured noise reduction was even more increased when fluid film bearings were used instead of the roller bearings. A reduction of 13 dB of the maximum sound power level was observed in comparison with the single helical gears with ball bearings variant.

From these observations it is concluded that at least for rather small size and compact high power gear transmissions, for noise reduction purposes, priority should be given to alternative combinations of gears and bearings rather than to more advanced tooth profile corrections.

SUMMARY

This thesis presents new contributions to the modeling of the sound generating and transmission mechanisms of a gearbox with parallel shafts and to the experimental evaluation of noise reduction measures. The complete chain of vibration generation at the gears, of vibration transmission through bearings to the gearbox housing and of the sound radiation to the surrounding air is investigated.

In Chapter 2 attention is paid to the gears as the primary source of vibrations and noise. A computer program based on analytical modeling has been developed for fast calculations of the force distributions at the teeth and of the time variable tooth stiffness. Furthermore, the time variable tooth stiffness and the profile corrections are used as input for calculating the angular velocity (vibration) level at the gears which is the main vibration phenomenon in high quality gear transmissions. For this purpose a new dynamic model has been used which describes the engagement and disengagement shocks as function of tooth load and the amount of profile correction. Different types of 2D and 3D profile corrections can be used as input for these calculations.

Chapter 3 describes a method for calculating the stiffness matrix of ball bearings taken from the literature. Further developments of this method have been made for roller bearings. The stiffness matrix includes radial, axial and moment stiffness coefficients as well as their cross terms. The moment stiffness coefficients are of particular interest because they are assumed to have a significant influence on the vibration transmission of gearboxes. In addition the stiffness and damping matrices of fluid film bearings are presented as found in the literature.

In Chapter 4 Finite Element Method (FEM) calculations are presented for gearbox housings with and without bearings and shafts. A step by step approach is followed, from a simple empty box-like structure to a scale model of a gearbox, to investigate the usefulness of FEM calculations for the prediction of eigenfrequencies, eigenmodes and forced responses. In addition Experimental Modal Analysis (EMA) measurements are presented of these housings to evaluate the relevance of the FEM results.

The last part of the chain of the vibration and sound generation of gear transmissions is the modeling of the sound radiation efficiency of a gearbox housing. A simplified modeling method is briefly discussed and the radiation efficiency is proved to be close to its maximum value (i.e. unity) for a large part of the frequency range of interest for compact gearbox housings. It is concluded that extensive numerical calculations of this radiation efficiency are superfluous and moreover that significant reduction of it by design measures is not practically feasible. Therefore, the fundamental strategy for gear noise reduction in compact highly loaded gearboxes should be the reduction of gear vibrations, of transmission to the housing and of the housing vibration response but not the reduction of the radiation efficiency.

Chapter 5 presents the results of experiments carried out on a gear test rig. The proposed modeling methods of this thesis are tested to some extent and important results on practical noise reduction measures are obtained. The proposed model for calculating the angular velocity levels at the gears is reasonably good for the high speed range with respect to its magnitude. However, the predicted advantage of a sophisticated 3D-correction is not observed in the experiment. This and other experimental and computational results leads to a critical appraisal of the degree of completeness of the model of Chapter 2.

The FEM calculations of the transfer function between angular velocity level and the surface-averaged velocity level at the gearbox housing did not give very precise predictions. A major topic for further research is the improved modeling of the coupling between the gearbox interior (i.e. the rotating elements) and the housing. However, the prediction of the difference in vibration response between two gearbox alternatives such as a variant with ball bearings and another with double row self-aligning roller bearings was quite promising.

With respect to the effectiveness of noise reduction measures, sound power measurements for different kind of profile corrections on a single helical gear set are presented. They show a disappointingly small difference between the maximum sound power levels of these gearbox variants of only 2 dB. In addition, the influence on the sound power level of several kinds of rolling element bearings is shown. Here a maximum difference was measured of 6 dB in favour of the double row self-aligning roller bearing.

Furthermore, measurements on a double helical gear set with cylindrical roller bearings and with fluid film bearings are presented. They show an impressive improvement of the maximum sound power level by almost 13 dB when the single helical gear set with 'standard' profile correction A and ball bearings is compared with the double helical gear set with fluid film bearings.

Finally, in Chapter 6, an evaluation is made of the achievements in this study with respect to computational models. It is discussed which further developments and investigations are needed. Furthermore, the experiments are evaluated with respect to practical consequences for design decisions. It is also discussed whether or not the findings of this study may be extrapolated to less compact gearboxes.

SAMENVATTING

Dit proefschrift presenteert nieuwe bijdragen aan de modellering van het geluidopwekkend en -doorleidend mechanisme van een tandwielkast met parallelle assen en van experimentele resultaten van geluidverminderende maatregelen. De gehele keten van het ontstaan van trillingen in de tandengrijping, van de doorleiding van trillingen via lagers naar de tandwielkast en van de geluidsafstraling naar de omringende lucht wordt onderzocht.

In hoofdstuk 2 wordt aandacht besteed aan de tandwielen die als primaire trillingsbron worden beschouwd. Een computerprogramma is ontwikkeld dat gebaseerd is op een analytische modellering welke op een snelle wijze de tandkrachtverdelingen en de tijdsafhankelijke vertandingsstijfheid berekent. Een ander computerprogramma dat ontwikkeld is, gebruikt de tijdsafhankelijke vertandingsstijfheid en de profielkorrekties als invoergegevens voor de berekening van rotatie trillingsniveaus van de tandwielen van hoge kwaliteit tandwielkasten. Hiervoor is een nieuw rekenmodel geïntroduceerd dat de intree- en uitreestoot beschrijft als functie van de tandkracht en de profielkorrekties. Verschillende soorten profiel correcties (2D en 3D) kunnen worden toegepast als invoergegeven van dit programma.

Hoofdstuk 3 beschrijft een methode uit de literatuur om de stijfheidsmatrix van een groefkogellager te berekenen. Deze methode is uitgebreid voor cilinderlagers en kegellagers. De stijfheidsmatrix bevat radiale, axiale en moment stijfheidscoëfficiënten alsook hun kruistermen. De moment stijfheidscoëfficiënten verdienen bijzondere aandacht omdat hiervan vermoed wordt dat ze een belangrijke invloed hebben op de trillingsdoorleiding in tandwielkasten. Tevens worden in dit hoofdstuk de stijfheid en demping matrices gepresenteerd van glijlagers zoals ze in de literatuur gevonden zijn.

In hoofdstuk 4 worden Eindige Elementen Methode (EEM) berekeningen gepresenteerd van tandwielkasten met en zonder assen en tandwielen. Een stap voor stap methode wordt gevolgd, van een lege doosachtige kast tot aan een schaalmodel van een tandwielkast, om de bruikbaarheid te onderzoeken van de EEM resultaten van eigenfrequenties, eigenmodes en overdrachtsfuncties.

Tevens worden resultaten van Experimentele Modale Analyse (EMA) metingen van deze kasten gegeven om de toepasbaarheid van de EEM resultaten aan te tonen.

Het laatste deel van de keten van de trillings- en geluidsofwekking van tandwielkasten is de modellering van de geluidsafstraling. Dit wordt beknopt beschreven waarbij de afstraalfactor, voor een groot gedeelte van het frequentiegebied dat van belang is voor compacte tandwielkasten, dicht bij zijn maximum waarde van 1 blijkt te liggen. Er wordt geconcludeerd dat uitgebreide numerieke berekeningen van de afstraalfactor overbodig zijn en dat een belangrijke vermindering van de afstraalfactor niet praktisch uitvoerbaar is door veranderingen in het ontwerp aan te brengen. De fundamentele strategie voor geluidsvermindering van compacte hoog belaste tandwielkasten moet dan ook worden gericht op de vermindering van de tandwieltrillingen, van de trillingsdoorleiding naar het huis en van de huisresponsie en niet op het verminderen van de afstraalfactor.

Hoofdstuk 5 geeft de resultaten van experimenten die uitgevoerd zijn op een testopstelling. De voorgestelde modelleringsmethoden van dit proefschrift worden tot op zekere hoogte getest en enkele belangrijke resultaten van praktische geluidsreductie maatregelen worden beschreven. Het voorgestelde model voor de berekening van de hoeksnelheid trillingsniveaus van de tandwielen blijkt met betrekking tot zijn grootte redelijk goed voor het hoge toerentalgebied. De voorspelde geluidsreductie ten gevolge van een gecompliceerde drie-dimensionale profielcorrectie wordt echter niet gevonden in de experimenten. Dit en andere experimentele en voorspelde resultaten leiden tot een kritische waardebeoordeling van de belangrijkheid van het model van Hoofdstuk 2.

De EEM berekeningen van de overdrachtsfunctie tussen hoeksnelheid trillingsniveau en het oppervlakte-gewogen snelheidsniveau op het kastoppervlak leverde geen erg precieze voorspellingen. Een belangrijk onderwerp voor verder onderzoek is de verbetering van de modellering van de koppeling tussen het binnenwerk van een tandwieloverbrenging en de tandwielomkast. De voorspelling was echter zeer goed betreffende het verschil in overdrachtsfuncties van twee tandwielkast alternatieven, zoals de variant met groefkogellagers en die met dubbelrijige tonlagers.

Geluidmetingen voor verschillende soorten profielcorrecties van een enkel schuine tandwielset zijn gegeven. Zij tonen een teleurstellend klein verschil van slechts 2 dB van het maximum geluidvermogeniveau tussen deze varianten. Tevens wordt de invloed getoond op het geluidvermogeniveau van verschillende soorten wentellagers. Hier wordt een maximum verschil gemeten van 6 dB in het voordeel van de dubbelrijige tonlager variant. Verder worden resultaten van metingen gegeven van een pijlvertanding met cilinderlagers en met glijlagers. Zij tonen voor de onderzochte tandwielkast configuratie een indrukwekkende vermindering van het geluidvermogeniveau van bijna 13 dB voor de glijlager variant in vergelijking met de enkel schuine tandwielset met standaard profielcorrectie en groefkogellagers.

Hoofdstuk 6 geeft een evaluatie van hetgeen bereikt is in dit proefschrift met betrekking tot de rekenmodellen. Er wordt beschreven welk verder onderzoek noodzakelijk is. Tevens worden de experimenten besproken met betrekking tot hun praktische consequenties voor ontwerp vraagstukken. Er wordt ook bekeken in hoeverre de bevindingen van dit proefschrift geldig zijn voor andere, minder compacte tandwielkasten, in welke mate de gehele trillings- en geluidketen is opgelost en wat er in de toekomst nog gedaan zou moeten worden. Tevens worden regels gepresenteerd voor het ontwerpen van trillings- en geluidarme tandwielkasten.

APPENDIX A:

CONTENTS OF THE SCHMIDT-MATRIX

The contents of the matrix **A** and vectors **b** and **c** are presented in this Appendix. They are needed to calculate the eight unknown constants to describe the deflection of a cantilever plate. The equation $\mathbf{A} \cdot \mathbf{b} = \mathbf{c}$ looks as follows (Schmidt /2.3/):

$$\begin{bmatrix}
 a_{11} & a_{12} & a_{13} & a_{14} & a_{15} & a_{16} & a_{17} & a_{18} \\
 a_{21} & a_{22} & a_{23} & a_{24} & a_{25} & a_{26} & a_{27} & a_{28} \\
 a_{31} & a_{32} & a_{33} & a_{34} & a_{35} & a_{36} & a_{37} & a_{38} \\
 a_{41} & a_{42} & a_{43} & a_{44} & a_{45} & a_{46} & a_{47} & a_{48} \\
 a_{51} & a_{52} & a_{53} & a_{54} & a_{55} & a_{56} & a_{57} & a_{58} \\
 a_{61} & a_{62} & a_{63} & a_{64} & a_{65} & a_{66} & a_{67} & a_{68} \\
 a_{71} & a_{72} & a_{73} & a_{74} & a_{75} & a_{76} & a_{77} & a_{78} \\
 a_{81} & a_{82} & a_{83} & a_{84} & a_{85} & a_{86} & a_{87} & a_{88}
 \end{bmatrix}
 \cdot
 \begin{bmatrix}
 A_1 \\
 B_1 \\
 C_1 \\
 D_1 \\
 A_r \\
 B_r \\
 C_r \\
 D_r
 \end{bmatrix}
 =
 \begin{bmatrix}
 c_1 \\
 c_2 \\
 c_3 \\
 c_4 \\
 c_5 \\
 c_6 \\
 c_7 \\
 c_8
 \end{bmatrix}
 \tag{A-1}$$

The contents of vector **b** is unknown: $A_1, B_1, C_1, D_1, A_r, B_r, C_r, D_r$.

In principle the contents of matrix **A** and vector **c** are known. There are two different possibilities for filling up **A** and **c**. They depend on the values of the stiffnesses S_1, S_2 and S_3 .

Firstly for

$$\left(\frac{S_2}{S_1} \right)^2 > \frac{4S_3}{S_1} \tag{A-2}$$

then **A** looks like:

$$a_{11} = a_{12} = r_1^2 ; a_{13} = a_{14} = r_2^2 ; a_{15} = a_{16} = a_{17} = a_{18} = 0$$

$$a_{21} = r_1^3 - 2(1-\nu)\alpha r_1 / h_p^2 ; a_{22} = -a_{21} ; a_{23} = r_2^3 - 2(1-\nu)\alpha r_2 / h_p^2 ; a_{24} = -a_{23}$$

$$a_{25} = a_{26} = a_{27} = a_{28} = 0$$

$$a_{31} = e^{r_1 \xi} ; a_{32} = e^{-r_1 \xi} ; a_{33} = e^{r_2 \xi} ; a_{34} = e^{-r_2 \xi}$$

$$a_{35} = -a_{31} ; a_{36} = -a_{32} ; a_{37} = -a_{33} ; a_{38} = -a_{34}$$

$$a_{41} = r_1 a_{31} ; a_{42} = -r_1 a_{32} ; a_{43} = r_2 a_{33} ; a_{44} = -r_2 a_{34}$$

$$a_{45} = -a_{41} ; a_{46} = -a_{42} ; a_{47} = -a_{43} ; a_{48} = -a_{44}$$

$$a_{51} = a_{52} = a_{53} = a_{54} = 0$$

$$a_{55} = r_1^2 e^{r_1 b} ; a_{56} = r_1^2 e^{-r_1 b} ; a_{57} = r_2^2 e^{r_2 b} ; a_{58} = r_2^2 e^{-r_2 b}$$

$$a_{61} = a_{62} = a_{63} = a_{64} = 0$$

$$a_{65} = e^{r_1 b} a_{21} ; a_{66} = e^{-r_1 b} a_{22} ; a_{67} = e^{r_2 b} a_{23} ; a_{68} = e^{-r_2 b} a_{24}$$

$$a_{71} = (e^{r_1 \xi} - 1)/r_1 ; a_{72} = -(e^{-r_1 \xi} - 1)/r_1 ; a_{73} = (e^{r_2 \xi} - 1)/r_2$$

$$a_{74} = -(e^{-r_2 \xi} - 1)/r_2 ; a_{75} = (e^{r_1 b} e^{r_1 \xi} - 1)/r_1 ; a_{76} = -(e^{-r_1 b} e^{-r_1 \xi} - 1)/r_1$$

$$a_{77} = (e^{r_2 b} e^{r_2 \xi} - 1)/r_2 ; a_{78} = -(e^{-r_2 b} e^{-r_2 \xi} - 1)/r_2$$

$$a_{81} = (r_1^{-2} - S_2/S_3)(e^{r_1 \xi} - 1) - \xi/r_1 ; a_{82} = (r_1^{-2} - S_2/S_3)(e^{-r_1 \xi} - 1) + \xi/r_1$$

$$a_{83} = (r_2^{-2} - S_2/S_3)(e^{r_2 \xi} - 1) - \xi/r_2 ; a_{84} = (r_2^{-2} - S_2/S_3)(e^{-r_2 \xi} - 1) + \xi/r_2$$

$$a_{85} = (e^{r_1 b} e^{r_1 \xi} - 1)(r_1^{-2} - S_2/S_3) + e^{r_1 b} (\xi - b)/r_1$$

$$a_{86} = (e^{-r_1 b} e^{-r_1 \xi} - 1)(r_1^{-2} - S_2/S_3) + e^{-r_1 b} (b - \xi)/r_1$$

$$a_{87} = (e^{r_2 b} e^{r_2 \xi} - 1)(r_2^{-2} - S_2/S_3) + e^{r_2 b} (\xi - b)/r_2$$

$$a_{88} = (e^{-r_2 b} e^{-r_2 \xi} - 1)(r_2^{-2} - S_2/S_3) + e^{-r_2 b} (b - \xi)/r_2$$

and c looks like:

$$c_1 = c_2 = c_3 = c_4 = c_5 = c_6 = c_8 = 0 ; c_7 = \frac{F(j)}{S_3}$$

Secondly for

$$\left(\frac{s_2}{s_1} \right)^2 < \frac{4s_3}{s_1} \quad (\text{A-3})$$

then \mathbf{A} looks like:

$$a_{11} = p^2 - q^2 ; a_{12} = 2qp ; a_{13} = a_{11} ; a_{14} = -a_{12}$$

$$a_{15} = a_{16} = a_{17} = a_{18} = 0$$

$$a_{21} = p^3 - 3q^2p - 2p(1-\nu)\alpha/h_p^2 ; a_{22} = -q^3 + 3p^2q - 2q(1-\nu)\alpha/h_p^2$$

$$a_{23} = -a_{21} ; a_{24} = a_{22} ; a_{25} = a_{26} = a_{27} = a_{28} = 0$$

$$a_{31} = e^{p\xi} \cos(q\xi) ; a_{32} = e^{p\xi} \sin(q\xi) ; a_{33} = e^{-p\xi} \cos(q\xi) ; a_{34} = e^{-p\xi} \sin(q\xi)$$

$$a_{35} = -a_{31} ; a_{36} = -a_{32} ; a_{37} = -a_{33} ; a_{38} = -a_{34}$$

$$a_{41} = e^{p\xi} (p \cos(q\xi) - q \sin(q\xi)) ; a_{42} = e^{p\xi} (q \cos(q\xi) + p \sin(q\xi))$$

$$a_{43} = e^{-p\xi} (-p \cos(q\xi) - q \sin(q\xi)) ; a_{44} = e^{-p\xi} (q \cos(q\xi) - p \sin(q\xi))$$

$$a_{45} = -a_{41} ; a_{46} = -a_{42} ; a_{47} = -a_{43} ; a_{48} = -a_{44}$$

$$a_{51} = a_{52} = a_{53} = a_{54} = 0$$

$$a_{55} = e^{pb} ((p^2 - q^2) \cos(qb) - 2qp \sin(qb))$$

$$a_{56} = e^{pb} ((p^2 - q^2) \sin(qb) + 2qp \cos(qb))$$

$$a_{57} = e^{-pb} ((p^2 - q^2) \cos(qb) + 2qp \sin(qb))$$

$$a_{58} = e^{-pb} ((p^2 - q^2) \sin(qb) - 2qp \cos(qb))$$

$$a_{61} = a_{62} = a_{63} = a_{64} = 0$$

$$a_{65} = pa_{55} - qa_{56} - e^{pb} (1-\nu) 2\alpha (p \cos(qb) - q \sin(qb)) / h_p^2$$

$$a_{66} = qa_{55} + pa_{56} - e^{pb} (1-\nu) 2\alpha (q\cos(qb) + p\sin(qb)) / h_p^2$$

$$a_{67} = -pa_{57} - qa_{58} + e^{-pb} (1-\nu) 2\alpha (p\cos(qb) + q\sin(qb)) / h_p^2$$

$$a_{68} = qa_{57} - pa_{58} - e^{-pb} (1-\nu) 2\alpha (q\cos(qb) - p\sin(qb)) / h_p^2$$

$$a_{71} = e^{p\xi} (p\cos(q\xi) + q\sin(q\xi)) - p ; a_{72} = e^{p\xi} (p\sin(q\xi) - q\cos(q\xi)) + q$$

$$a_{73} = e^{-p\xi} (-p\cos(q\xi) + q\sin(q\xi)) + p ; a_{74} = e^{-p\xi} (-p\sin(q\xi) - q\cos(q\xi)) + q$$

$$a_{75} = e^{pb} (p\cos(qb) + q\sin(qb)) - a_{71} - p ; a_{76} = e^{pb} (p\sin(qb) - q\cos(qb)) - a_{72} + q$$

$$a_{77} = e^{-pb} (q\sin(qb) - p\cos(qb)) - a_{73} + p ; a_{78} = e^{-pb} (-p\sin(qb) - q\cos(qb)) - a_{74} + q$$

$$a_{81} = e^{p\xi} (\cos(q\xi) v + 2\bar{q}\bar{p}\sin(q\xi)) - \bar{p}(\xi + \bar{p}) + \bar{q}^2 + S_2/S_3$$

$$a_{82} = e^{p\xi} (\sin(q\xi) v - 2\bar{q}\bar{p}\cos(q\xi)) + \bar{q}(\xi + \bar{p}) + \bar{q}\bar{p}$$

$$a_{83} = e^{-p\xi} (\cos(q\xi) v - 2\bar{q}\bar{p}\sin(q\xi)) + \bar{p}(\xi - \bar{p}) + \bar{q}^2 + S_2/S_3$$

$$a_{84} = e^{-p\xi} (\sin(q\xi) v + 2\bar{q}\bar{p}\cos(q\xi)) + \bar{q}(\xi - \bar{p}) - \bar{q}\bar{p}$$

$$a_{85} = e^{pb} (\cos(qb) (\bar{p}(\xi - b) + v) + \sin(qb) (\bar{q}(\xi - b) + 2\bar{q}\bar{p})) - e^{p\xi} (\cos(q\xi) v + 2\bar{q}\bar{p}\sin(q\xi))$$

$$a_{86} = e^{pb} (\sin(qb) (\bar{p}(\xi - b) + v) - \cos(qb) (\bar{q}(\xi - b) + 2\bar{q}\bar{p})) - e^{p\xi} (\sin(q\xi) v - 2\bar{q}\bar{p}\cos(q\xi))$$

$$a_{87} = e^{-pb} (\cos(qb) (\bar{p}(b - \xi) + v) + \sin(qb) (\bar{q}(\xi - b) - 2\bar{q}\bar{p})) - e^{-p\xi} (\cos(q\xi) v - 2\bar{q}\bar{p}\sin(q\xi))$$

$$a_{88} = e^{-pb} (\sin(qb) (\bar{p}(b - \xi) + v) - \cos(qb) (\bar{q}(\xi - b) - 2\bar{q}\bar{p})) - e^{-p\xi} (\sin(q\xi) v + 2\bar{q}\bar{p}\cos(q\xi))$$

$$\text{with: } v = \bar{p}^{-2} - \bar{q}^{-2} - S_2/S_3 ; \bar{p} = p/(p^2 + q^2) ; \bar{q} = q/(p^2 + q^2)$$

and c looks like:

$$c_1 = c_2 = c_3 = c_4 = c_5 = c_6 = c_8 = 0 ; c_7 = \frac{F(j)}{S_3} (q^2 + p^2)$$

APPENDIX B:

TOOTH PROFILE FORM OF INVOLUTE GEARS

Equations to calculate the profile form of an involute gear are presented in this Appendix. These formulas are taken from Roosmalen /B.1/ in which Bronner /1.5/ is taken as an example for spur gears. The formulas are extended for the more general case of helical gears. The fillet curve (or trochoid) can be determined by newly developed formulas.

The profile of a gear tooth can be divided into four parts. These are:

- 1 - tip
- 2 - involute
- 3 - trochoid or fillet curve
- 4 - root

Due to symmetry only one half of the tooth profile needs to be calculated. This will be the right hand part. In the following the four parts are being described as function of x and y . The tooth form is part of a Cartesian coordinate system as shown in Fig. B.1. The origin of this coordinate system coincides with the gear centre point.

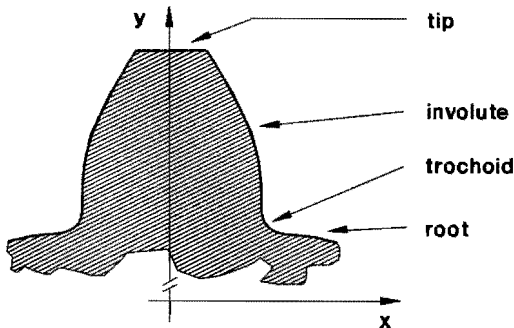


Figure B.1:

Profile form of an involute gear tooth.

This profile form is based on the rack with which it is manufactured. The dimensional properties of the rack are essential to the tooth profile form. Fig. B.2 gives the parameters that describe the form of the rack.

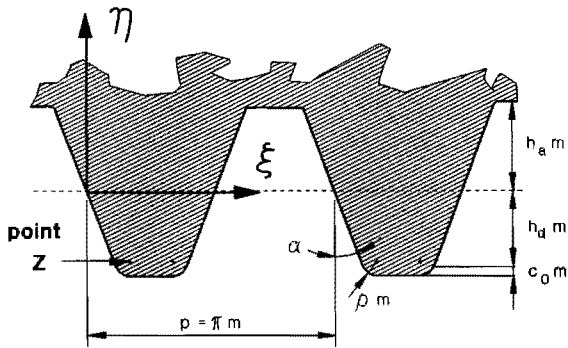


Figure B.2:
Rack dimensions.

Mathematically the four parts of the tooth profile can be described as follows:

1) tip

$$r_{\text{tip}} = m(z/2 + h_a + x - k) \quad [\text{m}] \quad (\text{B-1})$$

with	m	module	[m]
	z	number of teeth	[-]
	h_a	addendum coefficient	[-]
	x	addendum modification factor	[-]
	r_{tip}	tip radius	[m]
	k	addendum reduction factor	[-]

2) involute

$$\begin{cases} x_1 = r_0 \sin(\varphi + \vartheta) + [x m \sin(\alpha_t) - r_0 \varphi \cos(\alpha_t)] \cos(\alpha_t - \varphi - \vartheta) \\ y_1 = r_0 \cos(\varphi + \vartheta) + [x m \sin(\alpha_t) - r_0 \varphi \cos(\alpha_t)] \sin(\alpha_t - \varphi - \vartheta) \end{cases} \quad (\text{B-2})$$

with	r_0	pitch radius	[m]
	α_t	transverse pressure angle	[rad]
	ϑ	$\pi/2z$	[rad]
	φ	parameter	[rad]

$$\frac{r_0 + xm}{r_0 \tan(\alpha_t)} - \sqrt{\left\{ \frac{r_{tip}}{r_b} \right\}^2 - 1} \leq \varphi \leq \frac{4(h_d - x \cos(\alpha_t^2))}{z \sin(2\alpha_t)} \quad (B-3)$$

with r_b base circle radius [m]
 h_d dedendum coefficient [-]

pressure angle α' at radius r :

$$\alpha'(r) = \arccos\left(\frac{r_b}{r}\right) - \frac{r_0 + xm}{r_0} \tan(\alpha_t) + \sqrt{\left\{ \frac{r}{r_b} \right\}^2 - 1} - \frac{\pi}{2z} \quad (B-4)$$

3) trochoid or fillet curve

$$\begin{cases} x_t = (\xi_z - r_0 \varphi) \cos(\varphi + \theta) + (\eta_z + r_0) \sin(\varphi + \theta) + m\rho \cos(u - \varphi - \theta) \\ y_t = -(\xi_z - r_0 \varphi) \sin(\varphi + \theta) + (\eta_z + r_0) \cos(\varphi + \theta) + m\rho \sin(u - \varphi - \theta) \end{cases} \quad (B-5)$$

with ξ_z coordinate (Fig. B.2) [m]
 η_z coordinate (Fig. B.2) [m]
 ρ radius factor (Fig. B.2) [-]
 u parameter [-]

$$\alpha_t - \arcsin\left[\sin(\alpha_t) \sin(\beta)\right] \leq u \leq \frac{\pi}{2} - \beta \quad (B-6)$$

$$\varphi(u) = \frac{1}{r_0} \left\{ \xi_z + \eta_z \frac{\sin(\beta) - \cos(u)}{\sin(u)} + m\rho \left(\tan(\beta) - \frac{\sin(\beta) \cos(\beta)}{1 - \sin(\beta) \cos(u)} \right) \right\} \quad (B-7)$$

4) root

$$r_{root} = m(z/2 - h_d - c_0 + x) \quad (B-8)$$

with r_{root} root circle radius [-]
 c_0 see Fig. B.2 [-]

APPENDIX C:

STIFFNESS MATRIX AND OTHER VARIABLES OF THE LUMPED PARAMETER MODEL OF CHAPTER 2

The stiffness matrix $[S_{\text{tooth}}(t)]$ has dimension 15×15 . It contains non-zero elements in the upper left 12×12 corner. This corner looks like:

$$\begin{bmatrix} k_{xx} & k_{xy} & -k_{xz} & 0 & 0 & r_1 k_{x\phi_z} & -k_{xx} & -k_{xy} & k_{xz} & 0 & 0 & r_2 k_{x\phi_z} \\ k_{xy} & k_{yy} & -k_{yz} & 0 & 0 & r_1 k_{y\phi_z} & -k_{xy} & -k_{yy} & k_{yz} & 0 & 0 & r_2 k_{y\phi_z} \\ -k_{xz} & -k_{yz} & k_{zz} & 0 & 0 & -r_1 k_{z\phi_z} & k_{xz} & k_{yz} & -k_{zz} & 0 & 0 & -r_2 k_{z\phi_z} \\ 0 & 0 & 0 & 0 & 0 & 0 & 0 & 0 & 0 & 0 & 0 & 0 \\ 0 & 0 & 0 & 0 & 0 & 0 & 0 & 0 & 0 & 0 & 0 & 0 \\ r_1 k_{x\phi_z} & r_1 k_{y\phi_z} & -r_1 k_{z\phi_z} & 0 & 0 & r_1^2 k_{\phi_z\phi_z} & -r_1 k_{x\phi_z} & -r_1 k_{y\phi_z} & r_1 k_{z\phi_z} & 0 & 0 & r_1 r_2 k_{\phi_z\phi_z} \\ -k_{xx} & -k_{xy} & k_{xz} & 0 & 0 & -r_1 k_{x\phi_z} & k_{xx} & k_{xy} & -k_{xz} & 0 & 0 & -r_2 k_{x\phi_z} \\ -k_{xy} & -k_{yy} & k_{yz} & 0 & 0 & -r_1 k_{y\phi_z} & k_{xy} & k_{yy} & -k_{yz} & 0 & 0 & -r_2 k_{y\phi_z} \\ k_{xz} & k_{yz} & -k_{zz} & 0 & 0 & r_1 k_{z\phi_z} & -k_{xz} & -k_{yz} & k_{zz} & 0 & 0 & r_2 k_{z\phi_z} \\ 0 & 0 & 0 & 0 & 0 & 0 & 0 & 0 & 0 & 0 & 0 & 0 \\ 0 & 0 & 0 & 0 & 0 & 0 & 0 & 0 & 0 & 0 & 0 & 0 \\ r_2 k_{x\phi_z} & r_2 k_{y\phi_z} & -r_2 k_{z\phi_z} & 0 & 0 & r_1 r_2 k_{\phi_z\phi_z} & -r_2 k_{x\phi_z} & -r_2 k_{y\phi_z} & r_2 k_{z\phi_z} & 0 & 0 & r_2^2 k_{\phi_z\phi_z} \end{bmatrix}$$

where $r_1 = r_{g1}$ and $r_2 = r_{g2}$

$$k_{xx} = S_t(t) \cos^2(\beta_b) \sin^2(\alpha'_t)$$

$$k_{x\phi_z} = S_t(t) \sin(\alpha'_t) \cos^2(\beta_b)$$

$$k_{xy} = S_t(t) \cos^2(\beta_b) \sin(\alpha'_t) \cos(\alpha'_t)$$

$$k_{y\phi_z} = S_t(t) \cos(\alpha'_t) \cos^2(\beta_b)$$

$$k_{xz} = -S_t(t) \sin(\beta_b) \cos(\beta_b) \sin(\alpha'_t)$$

$$k_{z\phi_z} = -S_t(t) \sin(\beta_b) \cos(\beta_b)$$

$$k_{yy} = S_t(t) \cos^2(\beta_b) \cos^2(\alpha'_t)$$

$$k_{\phi_z\phi_z} = S_t(t) \cos^2(\beta_b)$$

$$k_{yz} = -S_t(t) \sin(\beta_b) \cos(\beta_b) \cos(\alpha'_t)$$

$$k_{zz} = S_t(t) \sin^2(\beta_b)$$

Non zero elements of the matrix $[S_{\text{shafts}}]$ are:

$$S_{\text{shafts}}(6,6) = \frac{\pi G}{32} (d^4/\ell)_{\text{shaft2}} \quad [\text{Nm/rad}]$$

$$S_{\text{shafts}}(12,12) = \frac{\pi G}{32} (d^4/\ell)_{\text{shaft3}} \quad [\text{Nm/rad}]$$

$$S_{\text{shafts}}(13,13) = \frac{\pi G}{32} \left[(d^4/\ell)_{\text{shaft1}} + (d^4/\ell)_{\text{shaft2}} \right] \quad [\text{Nm/rad}]$$

$$S_{\text{shafts}}(14,14) = \frac{\pi G}{32} \left[(d^4/\ell)_{\text{shaft3}} + (d^4/\ell)_{\text{shaft4}} \right] \quad [\text{Nm/rad}]$$

$$S_{\text{shafts}}(15,15) = \frac{\pi G}{32} (d^4/\ell)_{\text{shaft1}} \quad [\text{Nm/rad}]$$

$$S_{\text{shafts}}(6,13) = S_{\text{shafts}}(13,6) = -\frac{\pi G}{32} (d^4/\ell)_{\text{shaft2}} \quad [\text{Nm/rad}]$$

$$S_{\text{shafts}}(12,14) = S_{\text{shafts}}(14,12) = -\frac{\pi G}{32} (d^4/\ell)_{\text{shaft3}} \quad [\text{Nm/rad}]$$

$$S_{\text{shafts}}(13,15) = S_{\text{shafts}}(15,13) = -\frac{\pi G}{32} (d^4/\ell)_{\text{shaft1}} \quad [\text{Nm/rad}]$$

The bearing stiffness coefficients are calculated with the computer program mentioned in Chapter 3. The non zero elements of $[S_{\text{bearing}}]$ are:

$$S_{\text{bearing}}(1,1) = 5.3 \cdot 10^8 \text{ N/m} \quad S_{\text{bearing}}(7,7) = 5.3 \cdot 10^8 \text{ N/m}$$

$$S_{\text{bearing}}(2,2) = 7.3 \cdot 10^8 \text{ N/m} \quad S_{\text{bearing}}(8,8) = 5.7 \cdot 10^8 \text{ N/m}$$

$$S_{\text{bearing}}(3,3) = 1.6 \cdot 10^8 \text{ N/m} \quad S_{\text{bearing}}(9,9) = 1.3 \cdot 10^8 \text{ N/m}$$

$$S_{\text{bearing}}(4,4) = 5.2 \cdot 10^6 \text{ Nm/rad} \quad S_{\text{bearing}}(10,10) = 3.7 \cdot 10^6 \text{ Nm/rad}$$

$$S_{\text{bearing}}(5,5) = 3.8 \cdot 10^6 \text{ Nm/rad} \quad S_{\text{bearing}}(11,11) = 3.4 \cdot 10^6 \text{ Nm/rad}$$

The values of the parameters in the formulas, for the case of the gearbox interior of the test rig with single helical gears, are:

$T_{15} = 2000$	Nm
$\alpha'_t = 20,410$	degr.
$\beta_b = 11,267$	degr.
$r_{g1} = 0,045992$	m
$r_{g2} = 0,137976$	m
$m_{g1} = 28,0$	kg
$m_{g2} = 86,0$	kg
$I_{xg1} = I_{yg1} = 0,550$	$\text{kg}\cdot\text{m}^2$
$J_{g1} = 0,0240$	$\text{kg}\cdot\text{m}^2$
$I_{xg2} = I_{yg2} = 0,260$	$\text{kg}\cdot\text{m}^2$
$J_{g2} = 0,430$	$\text{kg}\cdot\text{m}^2$
$J_{c1} = 0,0520$	$\text{kg}\cdot\text{m}^2$
$J_{c2} = 0,450$	$\text{kg}\cdot\text{m}^2$

APPENDIX D:

CONTENTS OF THE ROLLING ELEMENT BEARING STIFFNESS MATRIX

The contents of the symmetrical ball bearing stiffness matrix $[K]_{bm}$ can be derived from Eqs. (3.1) - (3.10) when considering

$$\frac{\partial A_j}{\partial \delta_x} = \frac{(\delta^*)_{rj}}{A_j} \cos(\psi_j) \qquad \frac{\partial A_j}{\partial \beta_x} = \frac{(\delta^*)_{zj}}{A_j} r_j \sin(\psi_j)$$

$$\frac{\partial A_j}{\partial \delta_y} = \frac{(\delta^*)_{rj}}{A_j} \sin(\psi_j) \qquad \frac{\partial A_j}{\partial \beta_y} = -\frac{(\delta^*)_{zj}}{A_j} r_j \cos(\psi_j)$$

$$\frac{\partial A_j}{\partial \delta_z} = \frac{(\delta^*)_{zj}}{A_j} \qquad \frac{\partial A_j}{\partial \beta_z} = 0$$

It then follows

$$k_{bxx} = K_n \sum_j \frac{(A_j - A_0)^n}{A_j^3} \left\{ \frac{nA_j (\delta^*)_{rj}^2}{A_j - A_0} + (\delta^*)_{zj}^2 \right\} \cos^2(\psi_j) \qquad (C-1a)$$

$$k_{bxy} = K_n \sum_j \frac{(A_j - A_0)^n}{A_j^3} \left\{ \frac{nA_j (\delta^*)_{rj}^2}{A_j - A_0} + (\delta^*)_{zj}^2 \right\} \sin(\psi_j) \cos(\psi_j) \qquad (C-1b)$$

$$k_{bxz} = K_n \sum_j \frac{(A_j - A_0)^n}{A_j^3} \left\{ \frac{nA_j}{A_j - A_0} - 1 \right\} (\delta^*)_{rj} (\delta^*)_{zj} \cos(\psi_j) \qquad (C-1c)$$

$$k_{bx\theta_x} = K_n \sum_j \frac{(A_j - A_0)^n}{A_j^3} \left\{ \frac{nA_j}{A_j - A_0} - 1 \right\} r_j (\delta^*)_{rj} (\delta^*)_{zj} \sin(\psi_j) \cos(\psi_j) \qquad (C-1d)$$

$$k_{bx\theta_y} = K_n \sum_j \frac{(A_j - A_0)^n}{A_j^3} \left\{ 1 - \frac{nA_j}{A_j - A_0} \right\} r_j (\delta^*)_{rj} (\delta^*)_{zj} \cos^2(\psi_j) \qquad (C-1e)$$

$$k_{byy} = K_n \sum_j^z \frac{(A_j - A_0)^n}{A_j^3} \left\{ \frac{nA_j (\delta^*)_{rj}^2}{A_j - A_0} + (\delta^*)_{zj}^2 \right\} \sin^2(\psi_j) \quad (C-1f)$$

$$k_{byz} = K_n \sum_j^z \frac{(A_j - A_0)^n}{A_j^3} \left\{ \frac{nA_j}{A_j - A_0} - 1 \right\} (\delta^*)_{rj} (\delta^*)_{zj} \sin(\psi_j) \quad (C-1g)$$

$$k_{by\theta_x} = K_n \sum_j^z \frac{(A_j - A_0)^n}{A_j^3} \left\{ \frac{nA_j}{A_j - A_0} - 1 \right\} r_j (\delta^*)_{rj} (\delta^*)_{zj} \sin^2(\psi_j) \quad (C-1h)$$

$$k_{by\theta_y} = -k_{bx\theta_x} \quad (C-1i)$$

$$k_{bzz} = K_n \sum_j^z \frac{(A_j - A_0)^n}{A_j^3} \left\{ \frac{nA_j (\delta^*)_{zj}^2}{A_j - A_0} + (\delta^*)_{rj}^2 \right\} \quad (C-1j)$$

$$k_{bz\theta_x} = K_n \sum_j^z \frac{(A_j - A_0)^n}{A_j^3} \left\{ \frac{nA_j (\delta^*)_{zj}^2}{A_j - A_0} + (\delta^*)_{rj}^2 \right\} r_j \sin(\psi_j) \quad (C-1k)$$

$$k_{bz\theta_y} = -K_n \sum_j^z \frac{(A_j - A_0)^n}{A_j^3} \left\{ \frac{nA_j (\delta^*)_{zj}^2}{A_j - A_0} + (\delta^*)_{rj}^2 \right\} r_j \cos(\psi_j) \quad (C-1l)$$

$$k_{b\theta_x\theta_x} = K_n \sum_j^z \frac{(A_j - A_0)^n}{A_j^3} \left\{ \frac{nA_j (\delta^*)_{zj}^2}{A_j - A_0} + (\delta^*)_{rj}^2 \right\} r_j^2 \sin^2(\psi_j) \quad (C-1m)$$

$$k_{b\theta_x\theta_y} = -K_n \sum_j^z \frac{(A_j - A_0)^n}{A_j^3} \left\{ \frac{nA_j (\delta^*)_{zj}^2}{A_j - A_0} + (\delta^*)_{rj}^2 \right\} r_j^2 \sin(\psi_j) \cos(\psi_j) \quad (C-1n)$$

$$k_{b\theta_y\theta_y} = K_n \sum_j^z \frac{(A_j - A_0)^n}{A_j^3} \left\{ \frac{nA_j (\delta^*)_{zj}^2}{A_j - A_0} + (\delta^*)_{rj}^2 \right\} r_j^2 \cos^2(\psi_j) \quad (C-1o)$$

$$k_{bi\theta_z} = k_{b\theta_i\theta_z} = 0 \quad ; \quad i = x, y, z \quad (C-1p)$$

where $(\delta^*)_{rj}$, $(\delta^*)_{zj}$ and A_j are defined by Eqs. (3.2) - (3.4).

The contents of the symmetrical roller bearing stiffness matrix $[K]_{bm}$ can be derived from Eqs. (3.5), (3.6), (3.8), (3.10), (3.13) and (3.14).

It follows:

$$k_{bxx} = nK_n \cos^2(\alpha_0) \sum_j^z \delta_j^{n-1} \cos^2(\psi_j) \quad (C-2a)$$

$$k_{bxy} = \frac{n}{2} K_n \cos^2(\alpha_0) \sum_j^z \delta_j^{n-1} \sin(2\psi_j) \quad (C-2b)$$

$$k_{bxz} = \frac{n}{2} K_n \sin(2\alpha_0) \sum_j^z \delta_j^{n-1} \cos(\psi_j) \quad (C-2c)$$

$$k_{bx\theta_x} = \frac{n}{4} K_n \sin(2\alpha_0) \sum_j^z r_j \delta_j^{n-1} \sin(2\psi_j) \quad (C-2d)$$

$$k_{bx\theta_y} = -\frac{n}{2} K_n \sin(2\alpha_0) \sum_j^z r_j \delta_j^{n-1} \cos^2(\psi_j) \quad (C-2e)$$

$$k_{byy} = nK_n \cos^2(\alpha_0) \sum_j^z \delta_j^{n-1} \sin^2(\psi_j) \quad (C-2f)$$

$$k_{byz} = \frac{n}{2} K_n \sin(2\alpha_0) \sum_j^z \delta_j^{n-1} \sin(\psi_j) \quad (C-2g)$$

$$k_{by\theta_x} = \frac{n}{2} K_n \sin(2\alpha_0) \sum_j^z r_j \delta_j^{n-1} \sin^2(\psi_j) \quad (C-2h)$$

$$k_{by\theta_y} = -k_{bx\theta_x} \quad (C-2i)$$

$$k_{bzz} = nK_n \sin^2(\alpha_0) \sum_j^z \delta_j^{n-1} \quad (C-2j)$$

$$k_{bz\theta_x} = nK_n \sin^2(\alpha_0) \sum_j^z r_j \delta_j^{n-1} \sin(\psi_j) \quad (C-2k)$$

$$k_{bz\theta_y} = -nK_n \sin^2(\alpha_0) \sum_j^z r_j \delta_j^{n-1} \cos(\psi_j) \quad (C-2l)$$

$$k_{b\theta_{x x}} = nK_n \sin^2(\alpha_0) \sum_j^z r_j^2 \delta_j^{n-1} \sin^2(\psi_j) \quad (C-2m)$$

$$k_{b\theta_{x y}} = -\frac{n}{2} K_n \sin^2(\alpha_0) \sum_j^z r_j^2 \delta_j^{n-1} \sin(2\psi_j) \quad (C-2n)$$

$$k_{b\theta_{y y}} = nK_n \sin^2(\alpha_0) \sum_j^z r_j^2 \delta_j^{n-1} \cos^2(\psi_j) \quad (C-2o)$$

$$k_{bi\theta_z} = k_{b\theta_{i z}} = 0 \quad ; \quad i = x, y, z \quad (C-2p)$$

APPENDIX E:

RADIATION EFFICIENCY OF TWO GEARBOX HOUSINGS

The radiation efficiency of two gearbox housings will be estimated in this Appendix using the method described in section 4.7 of this thesis. The two gearbox housings of interest are the housings of the test gearbox of Chapter 5 and its 80 percent scale model of Chapter 4. The frequency dependent radiation efficiency is the link between the vibration level at the surface of the housing and the produced sound power level.

Before the calculation method for estimating the radiation efficiency of a gearbox as described in Chapter 4 can be used, the surface areas and perimeters of the individual plates of the gearbox have to be known. For this purpose the gearbox housing has to be modeled as if it consists of a number of plates which are homogeneous, i.e. have a constant thickness h . Of course, this is not the case for actual gearbox housings which often have ribs. This means that some simplifications may be necessary for the purpose of modeling.

In Fig. E.1 both housings are shown. It has been supposed that the housings can be divided into a number of homogeneous plates. These plates will only differ by their thickness, perimeters and areas. The perimeters of these plates are chosen to be at either edges of the housings, the flange between upper casing and lower casing or the boundary between two plates of different thickness. The top plate is a single plate while the two sides of

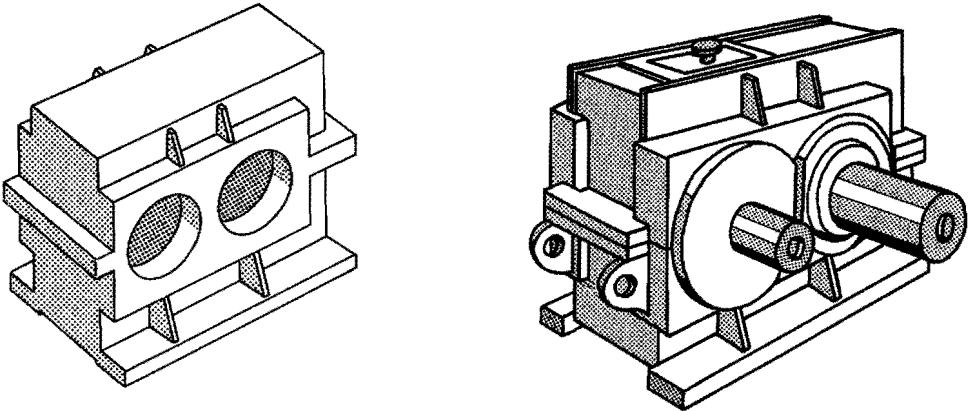


Figure E.1:

Gearbox housings of the 80 percent scale model (on the left) and of the test gearbox of Chapter 5 (on the right).

the housings were divided in two plates each. The front and back parts of the housings were divided in a thin plate at the lower housing part, a thin plate at the upper housing part and a thick plate which contains the bearing openings. These openings are part of the plate area because for both housings these openings are covered by flanges.

The approximation of the radiation index of the complete housing can be done according to Fig. 4.22 by looking at the homogeneous plates of the gearbox housing. Point P can be calculated with the use of Eq. (4.11) for which the mean perimeter \overline{U} and the mean critical frequency \overline{f}_c (Eq. (4.12)) have to be calculated.

For reasons of simplicity the L-shaped plates at the front and back of the gearboxes are considered to be rectangular with the surface area of the L-shaped plates and the ribs are not taken into account. The foot plates of the test gearbox housing were mounted to a supporting structure so that these plates do not contribute to the sound radiation. In contrast, the scale model of section 4.6 was put on soft rubber elements so that the foot plates do take part and have to be taken into account for the approximation of the radiation efficiency of the scale model housing. This leads to the following dimensions and frequencies for the 80 percent scale model:

	S [m ²]	U [m]	h [m]	f _c [Hz]
top	0.0544	1.07	0.008	1500
side up	0.0177	0.532	0.008	1500
side low	0.0224	0.602	0.008	1500
front up	0.0243	0.922	0.008	1500
front low	0.0303	0.952	0.008	1500
front	0.0657	1.07	0.038	316
foot	0.0240	0.920	0.025	480

$$\overline{S}_p = 0.423/13 = 0.0326 \text{ m}^2 \qquad \overline{U} = 11.1/13 = 0.852 \text{ m}$$

$$\overline{f}_c = \left[\frac{\overline{U}}{U/f_c^{3/2}} \right]^{2/3} = 643 \text{ Hz} \qquad (4.12)$$

$$\sigma'_p(\overline{f}_c) = 1.13 \cdot \overline{U} \cdot \overline{f}_c/c = 1.80 \qquad (4.11)$$

point P: $10 \log(\sigma'_p(\overline{f}_c)) = 2.6 \text{ dB at } 643 \text{ Hz}$

The dimensions of the test gearbox of Chapter 5 and the resulting frequencies are:

	$S [m^2]$	$U [m]$	$h [m]$	$f_c [Hz]$
top	0.0833	1.32	0.010	1200
side up	0.0281	0.670	0.010	1200
side low	0.0340	0.740	0.010	1200
front up	0.0442	1.21	0.010	1200
front low	0.0494	1.23	0.010	1200
front	0.106	1.36	0.065	185

$$\overline{S}_p = 0.606/11 = 0.0551 \text{ m}^2 \qquad \overline{U} = 11.7/11 = 1.07 \text{ m}$$

$$\overline{f}_c = \left(\frac{\overline{U}}{U/f_c^{3/2}} \right)^{2/3} = 433 \text{ Hz} \qquad (4.12)$$

$$\sigma'_p(\overline{f}_c) = 1.13 \cdot \overline{U} \cdot \overline{f}_c/c = 1.52 \qquad (4.11)$$

point P: $10\log(\sigma'_p(\overline{f}_c)) = 1.8 \text{ dB}$ at 433 Hz

The radiation index of the housings below the mean critical frequency \overline{f}_c can be constructed by applying a line through point P with a gradient of 25 dB/octave. This line crosses the $L_{\sigma} = 0 \text{ dB}$ line at 508 Hz for the scale model housing and at 366 Hz for the test gearbox housing. The radiation index of the equivalent baffled piston is zero for higher frequencies and drops down to -15.2 dB and -11.7 dB at $f = 125 \text{ Hz}$ for the scale model housing and the test gearbox housing respectively.

Whether the radiation index of these housings is also partially determined by the radiation efficiency $\overline{\sigma'_{p1}}$, as Fig. 4.22 indicates, can be investigated by checking when Eq. (4.15) holds:

$$\frac{c^2}{\overline{S}_p \cdot \overline{f}_c^2} > 1.31 \qquad (4.15)$$

For both housings this equation holds because the left hand side of Eq. (4.15) is 8.79 and 11.4 respectively for the scale model housing and the test gearbox housing. This means that both radiation indices can be modeled by the two straight solid lines for $L_{\sigma'_p}$, as shown in Fig. 4.22.

APPENDIX F:

GEOMETRY AND PROFILE CORRECTIONS OF FIVE TEST GEAR SETS

The test gears used in Chapter 5 are four identical single helical gear sets and one double helical gear set. The four single helical gear sets differ only by the amount and form of the profile corrections. In fact, to represent these four sets physically, only two gear sets were needed because both tooth flanks were used. Between measurements the pinion could be turned over 180 degrees around an axis perpendicular to the gear shaft axis. With the same torque direction as before, the other tooth flanks come into contact with identical gear geometry apart from the profile corrections. Thus, only three gear sets were used for the experiments. The single helical gears had the following dimensions:

		pinion	wheel	
transmitted power	P		300	kW
centre distance	a		200	mm
module	m		4	mm
number of teeth	z	24	72	-
gear ratio	i		3.000	-
maximum running speed	n	1500	500	rev/min
pressure angle	α		20.000	degr.
helix angle	β		12.000	degr.
addendum modification factor	x	0.50000	0.48728	-
tooth width	B	66	62	mm
quality (DIN 3962)	Q	5	5	-
material		17CrNiMo6	17CrNiMo6	
oil		Shell Omala 150		
addendum coefficient	h_a	1.00	1.00	-
dedendum coefficient	h_d	1.40	1.40	-
rack radius factor	ρ	0.40	0.40	-

Which gives the following geometry of the single helical gears:

pitch diameter	d	98.145	294.434	mm
outer diameter	d_o	109.668	305.855	mm
root diameter	d_r	90.945	287.132	mm

base diameter	d_b	91.983	275.949	mm
addendum reduction	$k \cdot m$		-0.239	mm
transverse contact ratio	ϵ_α		1.441	-
overlap ratio	ϵ_β		1.026	-
total contact ratio	ϵ_{tot}		2.467	-
maximum velocity	v		7.709	m/s
circumferential tooth load	F		38918	N
axial tooth load	F_{ax}		8272	N
torque	T	1910	5730	Nm
transverse pressure angle	α_t		20.410	degr.
operating transverse pressure angle	α_{wt}		23.099	degr.
helix angle on the base circle	β_b		11.267	degr.

The double helical gears had the following dimensions:

		pinion	wheel	
transmitted power	P		300	kW
centre distance	a		200	mm
module	m		3.5	mm
number of teeth	z	24	72	-
gear ratio	i		3.000	-
maximum running speed	n	1500	500	rev/min
pressure angle	α		20.000	degr.
helix angle	β		33.000	degr.
addendum modification factor	x	0.00000	-0.09020	-
tooth width	B	2x25	2x23	mm
quality (DIN 3962)	Q	5	5	-
material		17CrNiMo6	17CrNiMo6	
oil		Shell Omala 150		
addendum coefficient	h_a	1.00	1.00	-
dedendum coefficient	h_d	1.40	1.40	-
rack radius factor	ρ	0.40	0.40	-

Which gives the following geometry of the single helical gears:

pitch diameter	d	100.159	300.476	mm
outer diameter	d_o	107.156	306.841	mm
root diameter	d_r	90.359	290.044	mm
base diameter	d_b	91.879	275.637	mm
addendum reduction	$k \cdot m$		-0.001	mm
transverse contact ratio	ϵ_α		1.333	-
overlap ratio	ϵ_β		2x1.114	-
total contact ratio	ϵ_{tot}		2.447	-
maximum velocity	v		7.867	m/s
circumferential tooth load	F		38136	N
external axial tooth load	F_{ax}		0	N
torque	T	1910	5730	Nm
transverse pressure angle	α_t		23.460	degr.
operating transverse pressure angle	α_{wt}		23.250	degr.
helix angle on the base circle	β_b		30.783	degr.

The single helical gears had four different profile corrections which are named correction A, B, C and D.

Correction A has been proposed by a gear manufacturer which is based on experience. It consists of tip relief corrections on pinion and wheel. The maximum tip relief of the pinion was prescribed to be 24 to 31 μm over a length of 2.0 to 2.7 mm along the line of action. After grinding the gears profile measurements were performed which showed a tip relief of 31 μm over a length of 4.1 mm along the line of action. The wheel showed a tip relief of 13 μm (should be 29 to 36 μm) over a length of 1.3 mm (2.7 to 3.4 mm). This means that the grinding of the gears was not completely done as it should be, but the resulting gears were used in the experiments anyway and in the numerical analyses according to Chapter 2 the measured profile corrections were used.

Correction B results from calculations with the developed computer program of Chapter 2. It resulted in tip reliefs of pinion (30 to 37 μm over a

length of 2.5 to 3.2 mm) and of the wheel (29 to 36 μm over a length of 2.7 to 3.4 mm) with a correction in tooth width direction at the pinion of 4 to 11 μm over half the tooth width (33 mm). The profile measurements revealed a tip relief at the pinion of 40 μm over 4.8 mm and a tip relief at the wheel of 15 μm over 1.4 mm. The width correction was exactly as intended namely 9 μm over 32 mm.

Correction C was meant for illustrative reasons to show the influence of a too small tip relief respectively a too large tooth load. They were prescribed to be 12 to 19 μm over 0.9 to 1.6 mm at the pinion and 11 to 18 μm over 1.0 to 1.7 mm at the wheel. The profile measurements revealed tip reliefs of 18 μm over 2.0 mm (pinion) and of 0 μm over 0 mm (wheel).

Correction D has an experimental character by combining a tip relief and a tooth width correction in one. Fig. F.1 shows this three-dimensional profile correction. The tip relief has a triangular shape on the tooth surface with two triangular points on the tip of the tooth (one at the very end: Q) and the third point along the tooth profile at the very end (P). The line P-R is chosen in such a way that this line becomes a contact line of the gears at one stage in the mesh. Therefore, line P-R is parallel to the lines of contact which lie under an angle of β_b . Both pinion and wheel are equipped with these three-dimensional profile corrections. Depending on the torque and rotational directions, two meshing teeth of pinion and wheel

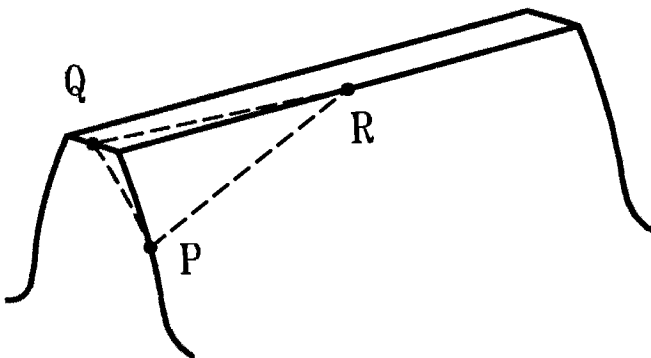


Figure F.1:
Three-dimensional profile correction of gear set D.

will meet at point Q of pinion or wheel (in the experiments of Chapter 5 it is the wheel). During meshing this contact point will progress along the tooth surfaces in the corrected area with contact lines parallel to P-R until they reach P-R. At this point the mesh is uncorrected so that the route from Q to P-R of the wheel determines the engagement shock that the gears will encounter. The same arguments apply to the disengagement shock where the route from P-R to Q of the pinion is responsible.

The maximum amount of relief occurs at point Q and it measured 30 μm for the pinion and 37 μm for the wheel. The length at the line of action from point Q to P measured 5.2 mm and 6.0 mm respectively while the length in tooth width direction was 25 mm (pinion) and 30 mm (wheel) respectively.

The double helical gear set was corrected with a tip relief of 20 μm over 2.2 mm (pinion) and of 42 μm over 3.3 mm (wheel). This profile correction was laid out on both helices on only one tooth flank side of each gear because the corrections were not of prime importance in this particular investigation. The double helical gear set was meant to show the difference in roller bearings and fluid film bearings on the dynamical behaviour and sound generation of the gear transmission.

REFERENCES

Chapter 1:

- 1.1 VDI-Richtlinie 2159, VDI-Handbuch Lärminderung, 1983
- 1.2 Niemann, G., Winter, H., "Maschinenelemente", Berlin, Springer Verlag, 1975
- 1.3 Akamatsu, T., et al., "Untersuchung der Geräusche von Zahnradgetrieben", Toyota Gijutsu, Vol. 24, 383-391, 1975
- 1.4 Sigg, H., "Profile and longitudinal corrections on involute gears", AGMA paper 109.16, 1965
- 1.5 Bronner, H., "Einfluss von Flankenkorrekturen auf Zahnkraft und Verformung bei Geradverzahnung". PhD thesis, University of Stuttgart, 1980
- 1.6 Roosmalen, A. van, "Een model voor de berekening van tandstijfheden van tandwieloverbrengingen met rechte tanden", MSc thesis, University of Eindhoven, 1986
- 1.7 Toppe, A., "Untersuchungen über die Geräuschanregung bei Stirnrädern unter besonderer Berücksichtigung der Fertigungsgenauigkeit", PhD thesis, TH Aachen, 1966
- 1.8 Lachenmaier, S., "Auslegung von evolventischen Sonderverzahnungen für schwingungs- und geräuscharmen Lauf von Getrieben", PhD thesis, TH Aachen, 1983
- 1.9 Pittroff, H., "Geräuscharmheit durch schwingungsstabiles Konstruieren rotierender Bauteile", VDI-Berichte Nr. 278, 43-59, 1977
- 1.10 White, M., "Rolling element bearing vibration transfer characteristics: effect of stiffness", Journal of applied mechanics, Vol. 46, 677-684, 1979
- 1.11 Gargiulo, E., "A simple way to estimate bearing stiffness", Machine Design, 107-110, july 1980
- 1.12 Ophey, L., "Experimentelle Ermittlung der Steifigkeit und Dämpfung radial belasteter Wälzlager", Fertigungstechnik Nr. 79, 32-35, 1981
- 1.13 Kraus, J. et al., "In situ determination of rolling bearing stiffness and damping by modal analysis", Journal of Vibration Acoustics Stress and Reliability in Design, Vol. 109, 235-240, 1987
- 1.14 Lim, T., "Force and moment transmissibilities through rolling element bearings in a single-stage rotor system", Proceedings of the 8th Int. Modal Analysis Conference, Florida, 704-710, 1990

- 1.15 Lim, T., "Vibration transmission through rolling element bearings. Part I: Bearing stiffness formulation. Part II: System studies". Journal of Sound and Vibration, Vol. 140, Nr. 1, 1991
- 1.16 Holmes, R., "The vibration of a rigid shaft on short sleeve bearings", Journal Mechanical Engineering Science, Vol. 2, No. 4, 337-341, 1960
- 1.17 Lund, J. et al., "Rotor-bearing dynamics design technology, Part III: Design handbook for fluid film type bearings", Mechanical Technology Incorporated Technical Report AFAPL-TR-65-45, 1965
- 1.18 Rao, J.S., "Rotor dynamics", Wiley Eastern, New Delhi, 1983
- 1.19 Goodwin, M., "Dynamics of rotor-bearing systems", Unwin-Hyman, London, 1989
- 1.20 Parkins, D.W., "Theoretical and experimental determination of the dynamic characteristics of a hydrodynamic journal bearing", Journal of Lubrication Technology, Transactions of the ASME, Vol. 101, 129-139, 1979
- 1.21 Burrows, C.R., Sahinkaya, M.N., "Frequency-domain estimation of linearized oil-film coefficients", Journal of lubrication technology, Transactions of the ASME, Vol. 104, 210-215, 1982
- 1.22 Kikuchi, K., "Analysis of unbalance vibration of rotating shaft system with many bearings and disks", Bulletin of the JSME, Vol. 13, No. 61, 864-872, 1970
- 1.23 Mukherjee, A., Rao, J.S., "Stiffness and damping coefficients of an inclined journal bearing", Mechanism and Machine Theory, Vol. 12, 339-355, 1977
- 1.24 Haven, J. van, Wachte, L. de, Vanhonacke, P., "Modal analysis on standard gear units", ASME paper 80-C2/DET-79, 1980
- 1.25 Kato, M. et al., "Sound power measurement of gearbox by intensity method", Second world congress on gearing, Paris, France, Vol. 1, 653-662, 1986
- 1.26 Sung, H., Nefske, D., "Engine vibration and noise reduction using a crank-block system model", SAE paper No. 891129, 1989
- 1.27 Drago, R.J., "How to design quiet transmissions", Machine Design, 175-181, december 1980
- 1.28 Lyon, R.H., "Machinery noise and diagnostics", Butterworth, 1987
- 1.29 Lu, L.K.H., Rockwood, W.B. et al., "An integrated gear system dynamics analysis over a broad frequency range", The shock and vibration bulletin, No. 55, Part 3, 1-11, 1985

- 1.30 Cremer, L., Heckl, M., Ungar, E.E., "Structure-borne sound", Springer-Verlag Berlin Heidelberg New York, 1988
- 1.31 Fahy, F., "Sound and structural vibration. Radiation, transmission and response", Academic press, 1985
- 1.32 Chiang, T., Badgley, R.H., "Reduction of vibration and noise generated by planetary ring gears in helicopter aircraft transmissions", Journal of Engineering for Industry, november, 1149-1158, 1973
- 1.33 Weber, W., "Vorausberechnung der Schalleistung einer Baureihe von einstufigen Stirnradgetrieben mittels akustischer Modellgesetze", VDI-Berichte 629, 41-56, 1987

Chapter 2:

- 2.1 Weck, M., Imdahl, M., Tenberge, H., Wittke, W., "Auslegung geräuscharmer Verzahnungen mit modernen Berechnungsmethoden", VDI-Z special Antriebstechnik, 66-70, april 1994
- 2.2 Bronner, H., "Einfluss von Flankenkorrekturen auf Zahnkraft und Verformung bei Geradverzahnung". PhD thesis, University of Stuttgart, 1980
- 2.3 Schmidt, G., "Berechnung der Wälzpressung schrägverzahnter Stirnräder unter Berücksichtigung der Lastverteilung", PhD thesis, University of München, 1973
- 2.4 Smith, J.D., "Gears and their vibrations. A basic approach to understanding gear noise", Marcel Dekker the MacMillan Press Ltd., 1983
- 2.5 Flaczek, T., "Lastverteilung und Flankenkorrektur in gerad- und schrägverzahnten Stirnradstufen", PhD thesis, TU München, 1988
- 2.6 Roosmalen, A. van, "Een model voor de berekening van tandstijfheden van tandwieloverbrengingen met rechte tanden", MSc thesis, University of Eindhoven, 1986
- 2.7 Roosmalen, A. van, 1991, 'Verslag 'eerste' fase 1986-1989', internal publication, University of Eindhoven, 1991
- 2.8 Weber, E., Banaschek, K., "Formänderung und Profilirücknahme bei gerad- und schrägverzahnten Rädern", Schriftenreihe Antriebstechnik 11, 1953
- 2.9 Kagawa, T., "Deflection and moment due to a concentrated edgeload on a cantilever plate of finite length", Proc. 11th Japan National Congress for Appl. Mech., 1961
- 2.10 Hayashi, K., "Load distribution on the contact line of helical gear teeth". Bulletin of ISME, Bd. 6, Nr. 22, 336-353, 1963

- 2.11 Press, W., et al., "Numerical recipes, the art of scientific computing", Cambridge university press, 1988
- 2.12 Lachenmaier, S., "Auslegung von evolventischen Sonderverzahnungen für schwingungs- und geräuscharmen Lauf von Getrieben", PhD thesis, TH Aachen, 1983
- 2.13 Sigg, H., "Profile and longitudinal corrections on involute gears", AGMA paper 109.16, 1965

Chapter 3:

- 3.1 Lim, T., "Vibration transmission through rolling element bearings. Part I: Bearing stiffness formulation. Part II: System studies". Journal of Sound and Vibration, Vol. 140, Nr. 1, 1991
- 3.2 Kikuchi, K., "Analysis of unbalance vibration of rotating shaft system with many bearings and disks", Bulletin of the JSME, Vol. 13, No. 61, 864-872, 1970
- 3.3 Mukherjee, A., Rao, J.S., "Stiffness and damping coefficients of an inclined journal bearing", Mechanism and Machine Theory, Vol. 12, 339-355, 1977
- 3.4 White, M., "Rolling element bearing vibration transfer characteristics: effect of stiffness", Journal of applied mechanics, Vol. 46, 677-684, 1979
- 3.5 Gargiulo, E., "A simple way to estimate bearing stiffness", Machine Design, 107-110, july 1980
- 3.6 Ophey, L., "Experimentelle Ermittlung der Steifigkeit und Dämpfung radial belasteter Wälzlager", Fertigungstechnik Nr. 79, 32-35, 1981
- 3.7 Kraus, J. et al., "In situ determination of rolling bearing stiffness and damping by modal analysis", Journal of Vibration Acoustics Stress and Reliability in Design, Vol. 109, 235-240, 1987
- 3.8 Lim, T., "Force and moment transmissibilities through rolling element bearings in a single-stage rotor system", Proceedings of the 8th Int. Modal Analysis Conference, Florida, 704-710, 1990
- 3.9 Holmes, R., "The vibration of a rigid shaft on short sleeve bearings", Journal Mechanical Engineering Science, Vol. 2, No. 4, 337-341, 1960
- 3.10 Lund, J. et al., "Rotor-bearing dynamics design technology, Part III: Design handbook for fluid film type bearings", Mechanical Technology Incorporated Technical Report AFAPL-TR-65-45, 1965
- 3.11 Rao, J.S., "Rotor dynamics", Wiley Eastern, New Delhi, 1983

- 3.12 Goodwin, M., "Dynamics of rotor-bearing systems", Unwin-Hyman, London, 1989
- 3.13 Parkins, D.W., "Theoretical and experimental determination of the dynamic characteristics of a hydrodynamic journal bearing", Journal of Lubrication Technology, Transactions of the ASME, Vol. 101, 129-139, 1979
- 3.14 Burrows, C.R., Sahinkaya, M.N., "Frequency-domain estimation of linearized oil-film coefficients", Journal of lubrication technology, Transactions of the ASME, Vol. 104, 210-215, 1982
- 3.15 Mundt, R., "Ueber die Berührung fester elastischer Körper, eine allgemein verständliche Darstellung der Theorie van Heinrich Hertz", SKF, Schweinfurt
- 3.16 Gupta, P.K., "Advanced dynamics of rolling elements", Springer-Verlag Berlin Heidelberg New York Tokyo, 1984
- 3.17 Harris, T.A., "Rolling bearing analysis", New York, John Wiley, 1966
- 3.18 Eschmann, P., Hasbargen, L., Weigand, K., "Ball and roller bearings", New York: John Wiley, 1985
- 3.19 Press, W., et al., "Numerical recipes, the art of scientific computing", Cambridge university press, 1988
- 3.20 Glienicke, J., "Feder- und Dämpfungskonstanten von Gleitlagern für Turbomaschinen und deren Einfluss auf das Schwingungsverhalten eines einfachen Rotors", PhD thesis, TH Karlsruhe, 1966
- 3.21 Verheij, J.W., "Using structural energy flow measurements to study sound transmission through a propeller shaft-bearing structure to underwater", Proceedings of the fourth international congress on intensity techniques, Publications CETIM, Senlis (France), aug. 31 to sept. 2, 415-422, 1993

Chapter 4:

- 4.1 Lim, T.C., Singh, R., "A review of gear housing dynamics and acoustics literature", NASA contractor report 185148, 1989
- 4.2 Kato, M. et al., "Sound power measurement of gearbox by intensity method", Second world congress on gearing, Paris, France, Vol. 1, 653-662, 1986
- 4.3 Badgley, R.H., Chiang, T., "Reduction of vibration and noise generated by planetary ring gears in helicopter aircraft transmission", ASME paper 72-PTG-11, 1972
- Also in Journal of Engineering Industry, 1149-1158, 1973

- 4.4 Inoue, K., Townsend, D.P., Coy, J.J., "Optimum design of a gearbox for low vibration", Journal of Mechanical Design, Vol. 115, 1002-1107, 1993
- 4.5 Verest, J.F.M., "Het gebruik van de Eindige Elementen Methode ten behoeve van het voorspellen van de geluidproductie van tandwielkasten", internal publication Technical University Eindhoven, 1990
- 4.6 Schroën, H.G.H., "Metingen aan eenvoudige tandwielkasthuizen en vergelijking met EEM-berekeningen", internal publication Technical University Eindhoven, 1991
- 4.7 Ewins, D.J., "Modal testing: theory and practice", Research Studies Press, 1984
- 4.8 Verest, J.F.M., "Overdrachtsbepaling voor kastkonstrukties ten behoeve van geluidproductie", internal publication Technical University Eindhoven, 1991
- 4.9 Bathe, K.J., "Finite element procedures in engineering analysis", Prentice-Hall Inc., Englewood Cliffs, New Jersey, 1982
- 4.10 Verest, J.F.M., "Eindige Elementen Methode berekeningen voor drie kastkonstrukties", internal publication Technical University Eindhoven, 1991
- 4.11 Vries, A.F. de, "Experimentele verificatie van het dynamische gedrag van een model tandwielkast", internal publication Technical University Eindhoven, 1994
- 4.12 Föller, D., "Maschinengeräusche, Vorhaben Nr. 36, Das Geräuschverhalten typischer Maschinenstrukturen, erstes Teilabschlußbericht. Die Geräuschabstrahlung von Platten und kastenförmigen Maschinengehäusen", Forschungshefte Forschungskuratorium Maschinenbau E.V. Heft 78, 1979
- 4.13 Müller, H.W., et.al., "Praxisreport Maschinenakustik", FKM-Forschungsheft 102, Frankfurt a. Main, Forschungskuratorium Maschinenbau e.V., 1983
- 4.14 Kollmann, F.G., "Maschinenakustik. Grundlagen, Meßtechnik, Berechnung, Beeinflussung", Springer-Verlag, 1993
- 4.15 Fahy, F., "Sound and structural vibration. Radiation, transmission and response", Academic Press, 1985
- 4.16 DIN 45635, "Geräuschmessung an Maschinen", part 1, 16 and 23

Chapter 5:

- 5.1 Inoue, K., Townsend, D.P., Coy, J.J., "Optimum design of a gearbox for low vibration", Journal of Mechanical Design, Vol. 115, 1002- 1007, 1993
- 5.2 DIN 45635, "Geräuschemessung an Maschinen", part 1, 16 and 23
- 5.3 Hösel, Th., "Geräuschuntersuchungen an schrägverzahnten Stirnrädern mit Evolventenverzahnung", PhD thesis, University of München, 1965
- 5.4 Roosmalen, A. van, "Geluidproductie van tandwieloverbrengingen; een kritisch overzicht van prognoseregels en van de invloed van ontwerpparameters", VROM-rapport GD-HR-14-01, 1988

Appendix B:

- B.1 Roosmalen, A. van, "Verslag eerste fase", NOVEM-project Geluidarme tandwieloverbrengingen, internal publication, University of Eindhoven, 1989

DANKBETUIGING

Dit onderzoek werd gefinancierd door de Technische Universiteit Eindhoven en het Ministerie van Volkshuisvesting, Ruimtelijke Ordening en Milieu (VROM) die het toezicht op de uitvoering overliet aan NOVEM. De nederlandse tandwiel-industrie, gebundeld in NERATRANS, heeft de twee tandwieloverbrengingen (Hfdst. 5) kostenloos gefabriceerd.

Diverse mensen hebben een bijdrage geleverd aan het onderzoek. Op deze plaats wil ik hen bedanken.

Han Verest leverde een grote bijdrage (hfdst. 4 en 5) door het uitvoeren van berekeningen met de Eindige Elementen Methode. We hebben menige discussie gevoerd over de toepasbaarheid van deze rekenmethode op tandwielkasten. Hij heeft met een niet aflatende inzet en interesse mede de doorslag gegeven voor het slagen van dit promotie onderzoek.

Erik Schroën was een zeer grote steun bij de praktische uitvoering van Modale Analyse experimenten (Hfdst. 4) en van de meetopstelling (Hfdst. 5). Hij ontwierp en realiseerde de opstelling met een ongeëvenaard enthousiasme en welgemeende stelligheid.

Bijzondere dank gaat uit naar mijn dagelijkse begeleider Rens Kodde. Zijn inbreng op dit werk is van onschatbare waarde. Hij heeft de uitvoering van de experimenten intensief begeleid en was bovenal een steun bij kleine en grote problemen. Hij was van begin tot eind betrokken bij het onderzoek en leverde bijdragen op allerlei gebied zoals vak-inhoudelijk, financieel en menselijk en daarnaast bij het corrigeren van dit proefschrift.

De bovengenoemde mensen hebben samen met Huub Wouters altijd gezorgd voor een nuttig besteedde lunch pauze, waarin allerlei zaken van het onderzoek besproken werden.

In de loop van het onderzoek hebben mij vele studenten geholpen met hun opdrachten, stages en afstudeerwerken. Van hen wil ik met name bedanken Geert Lamers, René Bouwman, Jacek Cieslik, Ruud Reynders, Danny Heuvelmans, Twan de Vries, Robert Bezemer, Jeroen Meulendijk en Edwin Staps. Zij hebben het mogelijk gemaakt om het onderzoek in een vrijwel continue opeenvolging van projecten te doen slagen.

Voorts bedank ik Cees Rovers en Piet Kelderman die mij bereidwillig geholpen hebben bij het realiseren van de proefopstellingen voor de diverse

experimenten. Samen hebben we de praktische problemen altijd kunnen oplossen.

De totstandkoming van dit projekt werd geïnitieerd door prof.dr.ir. M.J.W. Schouten die mij dit promotie-onderzoek liet starten. Als tweede promotor leverde hij waardevolle suggesties bij het schrijven van het proefschrift. Mijn eerste promotor prof.dr.ir. J.W. Verheij waardeer ik zeer om zijn kritische benadering van het vak. Hij hield de rode draad van het onderzoek altijd scherp in het oog. Zijn suggesties tijdens de technische besprekingen hebben mij erg geholpen bij het planmatig uitvoeren van het onderzoek en bij het schrijven van dit proefschrift.

Met ir. J.B. Kerpestein heb ik meerdere malen gesprekken gevoerd over de tandwiel technische zaken van het onderzoek. Hij bezit de capaciteit om de problemen systematisch aan te pakken.

De figuren van dit proefschrift en het ontwerp van de kافت zijn mede tot stand gekomen met de hulp van oom Jan van der Vlis en mijn aanstaande Ingrid Festen.

Vanzelfsprekend gaat mijn dank uit naar mijn ouders die mijn studie mogelijk gemaakt hebben, en zeker wat betreft dit onderzoek hebben zij mij altijd gesteund en waren zeer geïnteresseerd in mijn werk.

Tot slot wil ik Ingrid op deze plaats bijzonder bedanken, want zonder haar steun en aanmoedigingen was dit proefschrift zeer waarschijnlijk nooit gereed gekomen.

CURRICULUM VITAE

16 maart 1962	geboren te Bommel
1974 - 1978	Scholengemeenschap Bommel, HAVO 1 tot en met 4
1978 - 1980	Canisius College te Nijmegen, VWO 5 en 6, diploma VWO
1980 - 1986	Technische Universiteit Eindhoven, diploma werktuigbouwkundig ingenieur, met lof
1986 - 1989	Technische Universiteit Eindhoven, Toegevoegd onderzoeker
1990 - 1993	Technische Universiteit Eindhoven, Universitair Docent Geluidarm Construeren

STELLINGEN BEHORENDE BIJ HET PROEFSCHRIFT

"DESIGN TOOLS FOR LOW NOISE GEAR TRANSMISSIONS"

1 De in de tandwielpraktijk bekende regel om een overlappingsquotiënt ε_{β} met een gehele waarde na te streven om tot een geluidarm ontwerp te komen is te beperkt. Het is voldoende om ε_{β} groter of gelijk aan 0.8 te nemen. Een gehele waarde voor ε_{β} is daarnaast inderdaad optimaal maar levert in het genoemde gebied niet veel extra op.

(Hoofdstuk 2)

2 Het toepassen van profielkorrekties bij relatief smalle tandwielen beïnvloedt de intree- en uittree-stoot op een gunstige wijze indien de maximale mate van correctie ongeveer gelijk is aan de optredende doorbuigingen van de tanden. Daarnaast brengt de exacte vorm van de profielkorrekties weinig tot geen verbetering met zich mee. Het investeren in moeilijk te vervaardigen (drie dimensionale) profielkorrekties heeft dan ook weinig zin.

(Hoofdstuk 2 en 5)

3 De in de literatuur vaak gebruikte karakterisering van lagerstijfheden met behulp van slechts radiale en axiale stijfheden is onvoldoende voor de beschrijving van de trillingsdoorleiding via lagers naar de tandwielkast. Hiervoor zijn ook momentstijfheden van belang. Zo heeft het toepassen van wentellagers met een lage momentstijfheid, zoals zich instellende tweerijige tonlagers, een zeer gunstige invloed op het doorgeleide geluidniveau van een tandwielkast.

(Hoofdstuk 3 en 5)

4 De Eindige Elementen Methode is het meest in aanmerking komende gereedschap om het trilgedrag van een compacte tandwielkast te berekenen. Het voorspellen van de ligging van de eigenfrequenties van de kast met binnenwerk blijkt vrij accuraat mogelijk, de voorspelling van snelheidsvelden op de kastwand daarentegen vooralsnog niet.

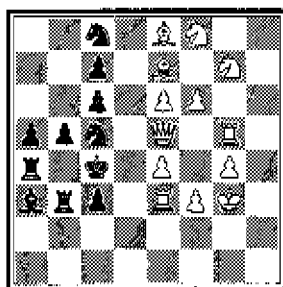
(Hoofdstuk 4)

5 Een goede konstruktieve maatregel om tot geluidarme tandwielkasten te komen is het toepassen van een pijlvertanding met glijlagers in plaats van een enkel-schuine vertanding met wentellagers. Dit is te verkiezen boven het zoeken naar de 'optimale' tandprofielcorrectievorm.

(Hoofdstuk 5)

- 6 De menselijke waarneming van de tandfrequentie in het geluidsspectrum van een tandwieloverbrenging betekent niet dat deze ook werkelijk aanwezig is in het spectrum. De mens kent namelijk een grondtoon toe aan een harmonisch complex, ook als deze grondtoon ontbreekt in het complex.
(J.J. Groen, Slechthorendheid en hoortoestellen, 1968)
- 7 Vooroordelen en generalisaties zijn er voor het gemak van hun gebruikers.
- 8 Golf wordt gekenmerkt door "fair play and gentlemanship". Dit wordt mede bereikt door het toepassen van een etiquette- en regelboek waarmee alle golfers bekend dienen te zijn. Een soortgelijk boek zou geen overbodige luxe zijn bij vele andere takken van sport.
- 9 De afstandsbediening van TV's is een bedreiging voor de volksgezondheid.
- 10 Het meest in het oog springende verschil tussen bromfiets en snorfiets is doorgaans niet de maximaal haalbare snelheid maar de kleur van het plaatje op het voorspatbord. Heroverweging van de valheimdraagplicht is daardoor noodzakelijk.
- 11 De lettercombinatie "dB" heeft in de praktijk veelal een negatieve klank en wordt vaak in verband gebracht met lawaai en overlast. Hierbij wordt voorbijgegaan aan de positieve eigenschappen zoals die tot uiting komen in iemands lievelingsmuziek of het onderstaande anagram.

A. van Roosmalen, P. le Grand
eerste plaatsing



2±

oplossing:

- | | |
|---------------|---------|
| 1. Pf5 dreigt | 2. Dd4 |
| 1. ...Tbwill. | 2. Dxc3 |
| 1. ...Bd4 | 2. Dxc5 |
| 1. ...Pxe4+ | 2. Dxe4 |
| 1. ...Pxe6 | 2. Dxe6 |

A.N.J. van Roosmalen
oktober 1994.